41st NOAA Climate Diagnostics and Prediction Workshop
Special Issue

Climate Prediction S&T Digest

doi:10.7289/V5JS9NH0

March 2017

NWS Science & Technology Infusion Climate Bulletin Supplement

Inside this issue:

NOAA's National Weather Service

Office of Science and Technology Integration
1325 East West Highway
Silver Spring, MD 20910

Climate Prediction Center
5830 University Research Court
College Park, MD 20740

Although the skill of current operational climate prediction is limited and the research on the topic presents many challenges, there are promises of improvement on the horizon. To accelerate advancement in climate services, an effective mechanism of S&T infusion from research to operation for application is much needed. This bulletin has been established to clarify science-related problems and relevant issues identified in operation, inviting our partners in the research community to work together on improvement of national climate prediction services.

Science and Technology Infusion Climate Bulletin
http://www.nws.noaa.gov/ost/climate/STIP/index.htm

National Weather Service
National Oceanic and Atmospheric Administration
U.S. Department of Commerce

PREFACE

It is with great pleasure that the Climate Prediction Center (CPC) and the Office of Science and Technology Integration (STI) offer you this synthesis of the 41st Climate Diagnostics and Prediction Workshop (CDPW). The CDPW remains a must attend workshop for the climate monitoring and prediction community. As is clearly evident in this digest, considerable progress is being made both in our ability to monitor and predict climate. The purpose of this digest is to ensure that climate research advances are shared with the broader community and also transitioned into operations. This is especially important as NOAA works to enhance climate services both across the agency and with external partners. We hope you find this digest to be useful and stimulating. And please drop me a note if you have suggestions to improve the digest.

I would like to thank Dr. Jiayu Zhou of the Office of Science and Technology Integration, for developing the digest concept and seeing it through to completion. This partnership between STI and CPC is an essential element of NOAA climate services.

David G. DeWitt
Director, Climate Prediction Center
National Centers for Environmental Prediction
NOAA's National Weather Service

CONTENTS

OVERVIEW

NOAA's 41st Climate Diagnostics and Prediction Workshop was held in Orono, Maine on 3-6 October 2016. The workshop was jointly hosted by the University of Maine Climate Change Institute and School of Earth and Climate Sciences and co-sponsored by the Climate Prediction Center (CPC) of the National Centers for Environmental Prediction (NCEP) and the Climate Services Branch (CSB) of the National Weather Service (NWS).

The workshop addressed topics in climate prediction, monitoring, and diagnostics, and focused on five major themes:

1. ENSO and recent climate anomalies;
2. The prediction, attribution, and analysis of high impact extreme climate events (drought, heat waves, severe weather, tropical cyclones) in the framework of climate variability and change and including the use of paleoclimate data;
3. Arctic climate variability and change, and linkages to lower latitudes. What paleoclimate data from the Arctic can tell us about our current and future climate;
4. Model and multi-model ensemble predictions and predictability. Strategies for calibration, consolidation, and optimal use of sources of predictability, including diagnostics of coupled model climate change projections for potential use in shorter timescale climate predictions;
5. Climatic events and risk management: knowledge and products to connect the diagnostics and predictions with preparedness and adaptation strategies.

The workshop featured daytime oral presentations, invited speakers, and panel discussions with a poster session event in one evening.

This Digest is a collection of extended summaries of the presentations contributed by participants. The workshop is continuing to grow and expected to provide a stimulus for further improvements in climate monitoring, diagnostics, prediction, applications and services.

Science and Technology Infusion Climate Bulletin
NOAA's National Weather Service
41st NOAA Annual Climate Diagnostics and Prediction Workshop
Orono, ME, 3-6 October 2016

OPENING ADDRESS

Contemporary Challenges in Short-Term Climate Forecasting

David G. DeWitt

Climate Prediction Center, NOAA/NWS/NCEP, College Park, MD

The Climate Prediction Center (CPC) continues to work to improve our suite of products and services in support of the National Weather Service (NWS) mission of protection of life and property and enhancement of the national economy. Demand from stakeholders for short-term climate prediction and monitoring products is steadily increasing and CPC is proactively meeting these new requests. Here I highlight some of the major initiatives that CPC is undertaking in order to meet stakeholder requests:

- Exploring the feasibility of producing prediction products in the week 3-4 timescale. Forecasts at this timescale are characterized by a small signal, large noise and have low predictability due to the decaying influence of atmospheric initial conditions and marginal influence from boundary conditions such as sea surface temperature, soil moisture, sea ice, *etc*. Consequently, forecasts of opportunity are likely to serve as the backbone for these outlooks. Currently, CPC is exploring the scientific potential and feasibility for producing week 3-4 outlooks for temperature and precipitation, Arctic sea ice forecasts, severe weather, tropical cyclone activity, and excessive heat.
- Development of user-friendly interactive tools for the temperature and precipitation outlooks. Two types of tools are being developed. The first allows stakeholders to view the three tercile categories for our probabilistic outlooks, while the second gives stakeholders the ability to tailor outlooks to their own risk profile.
- Exploring improvements to week two through seasonal precipitation forecasts in order to provide improved decision support services to the water resources community. Accurately forecasting precipitation is an incredibly difficult problem even on short-range weather timescales let alone longer timescales. CPC is exploring the potential for hybrid dynamical-statistical forecast techniques to improve over existing precipitation forecast tools.
- Forecasts for El Niño and its associated impacts during the 2015-216 period deviated in many ways from canonical patterns, especially for precipitation over the western United States. Understanding why this occurred and if it indicates lower predictability than previously assumed or missing or misrepresented processes in the dynamical models is an area of active research as CPC seeks to provide the most accurate and reliable prediction products to stakeholders.

Correspondence to: David DeWitt, 5830 University Research Court, Climate Prediction Center, NOAA/NWS/NCEP, College Park, Maryland; E-mail: david.dewitt@noaa.gov

1. 2015-16 EL NIÑO

41th NOAA Annual Climate Diagnostics and Prediction Workshop

3-6 October 2016, Orono, Maine

Science and Technology Infusion Climate Bulletin
NOAA's National Weather Service
41st NOAA Annual Climate Diagnostics and Prediction Workshop
Orono, ME, 3-6 October 2016

The 2015-16 El Niño

Michelle L'Heureux and CPC/IRI ENSO Forecast Team
Climate Prediction Center, NOAA/NWS/NCEP, College Park, Maryland

1. Evolution of the seasonal Niño SST indices during 2015-16

The El Niño of 2015-16 was among the strongest El Niño events observed since 1950, and took place almost two decades after the previous major event in 1997-98. NOAA Climate Prediction Center (CPC) issued an El Niño Advisory in March 2015. By early August 2015, seasonal Niño-3.4 sea surface temperature (SST) values were predicted by forecasters to be in excess of 2.0°C, which are values in the range of a Top 3 El Niño event.

These predictions verified as Niño 3.4 SST index were near record, peaking near 2.3°C for the average between November 2015-January 2016 (based on ERSSTv4 (Huang et al. 2015) and calculated as departures from the 1981-2010 monthly climatology; Fig. 1). The Niño-3.4 SSTs were at or in excess of +0.5°C for just over a year, between February-April (FMA) 2015 through April-June (AMJ) 2016. While the Niño-3.4 index values were impressive and competitive with the strongest El Niño events on record, two other Niño index regions clearly fell short of record setting. In particular, the easternmost Niño-3 SST and Niño-1+2 SST regions were cooler compared the 1997-98 event (Fig. 2). The latter region, near South America, also fell short of 1982-83 El Niño, and its amplitudes were more similar to the evolution of the 1972-73 event. As such, coastal Ecuador and Peru did not experience devastating rainfall and destruction as in 1982-83 and 1997-98 (personal communication, Ken Takahashi).

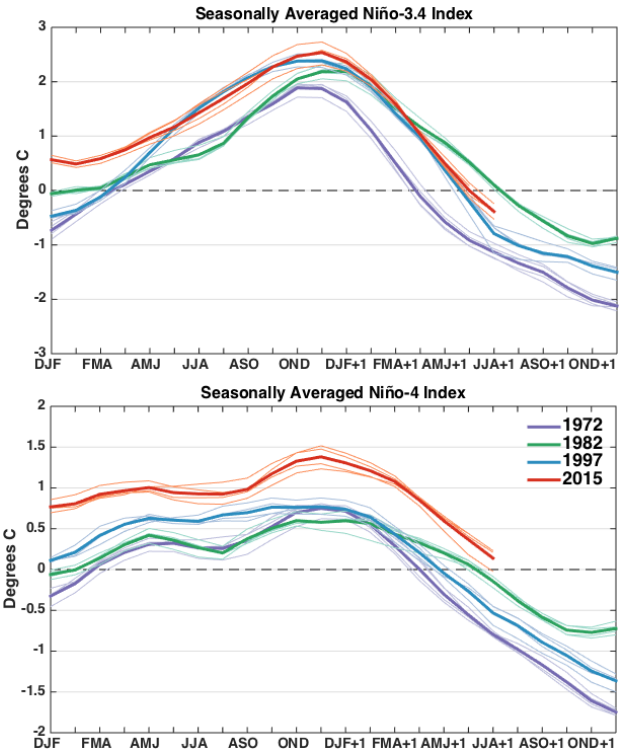

Fig. 1 Evolution of seasonal (3-month) averaged values of the Niño-3.4 SST index (top panel) and Niño-4 SST index (bottom panel) during 2015-16 (red), 1997-98 (blue), 1982-83 (green), and 1972-73 (purple). The Niño-3.4 region is 5°N-5°S, 170°-120°W and the Niño-4 region is 5°N-5°S, 150°-160°E. Thin lines correspond to the ERSSTv3b, ERSSTv4, COBE, and HadISST datasets and the thicker lines is the average of all datasets. Departures are formed by removing monthly means during 1981-2010.

In contrast, the westernmost Niño-4 SST region was clearly a record when compared to three previous major El Niño events (Fig. 1). Values in this region were near or in excess of +1.0°C from early 2015 through early 2016. While impressive relative to previous events, Niño-4 SST index values were similarly elevated during the more moderate El Niño of 2009-10 (Lee and McPhaden 2010). Overall, the 2015-16 El Niño event was exceptional for its anomalous warmth in the central and east-central equatorial Pacific Ocean, while remaining relatively cooler across the eastern Pacific Ocean.

2. Global temperature, precipitation, and circulation anomalies during DJF 2015-16

During December-February (DJF) 2015-16, above-average 500-hPa geopotential heights dominated the tropical latitudes and the mid-latitudes

Correspondence to: Michelle L'Heureux, Climate Prediction Center, NOAA/NWS/NCEP, 5830 University Research Court, College Park, MD; E-mail: michelle.lheureux@noaa.gov

of both hemispheres, with a large anticyclonic anomaly over Siberia during DJF 2015-16 (Fig. 3, top row). Associated with this pattern, strongly above-average temperatures prevailed over most of the globe, with particularly significant positive anomalies over the mid-to-high latitudes of the Northern Hemisphere (Fig. 3, middle row). The most significant regions of increased precipitation were located over the northwestern and southeastern United States, southern and eastern South America, southeast China, and just south of the equator in eastern Africa (Fig. 3, bottom row). Drier conditions were prominent over northern South America and around Indonesia.

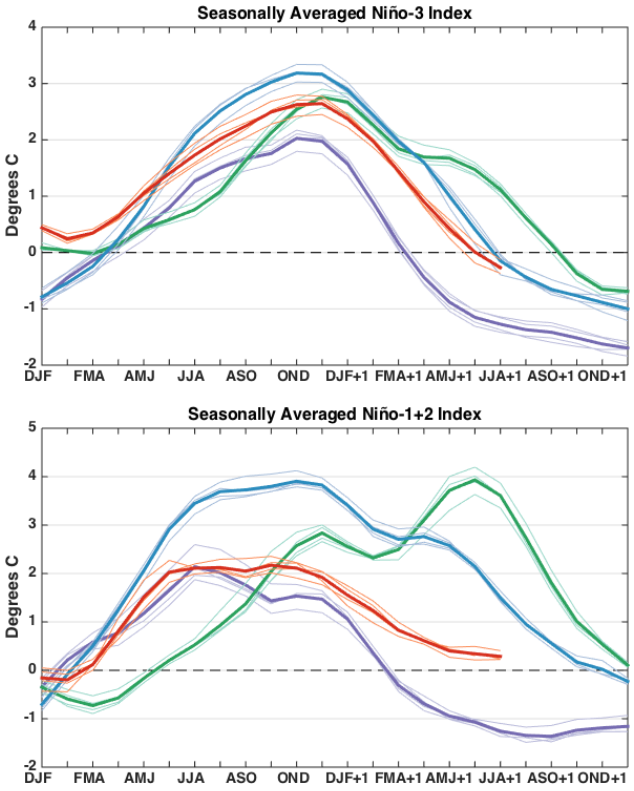

Fig. 2 Same as Figure 1, except for the Niño-3 SST index (top panel) and Niño- 1+2 SST index (bottom panel). The Niño-3 region is 5°N-5°S, 150°-90°W, and the Niño-1+2 region is 0°-10°S, 90°-80°W.

The aspects of the circulation that were perhaps most consistent with El Niño were the distinctive wave trains tracing a great circle route across the North and South Pacific Oceans. Anomalous cyclonic flow was observed in the Gulf of Alaska and middle latitudes of the South Pacific Ocean, with anomalous anticyclones poleward and east of the anomalous troughs over Canada and closer to West Antarctica. However, the cyclonic anomaly in the Gulf of Alaska and the anticyclonic anomaly near West Antarctica were shifted northward compared to the typical El Niño response. Over North America, the anomalous warmth projected well onto the El Niño pattern, but the observed anomalies were more intense and widespread than otherwise expected with El Niño. The anticipated pattern of below-average temperatures and heights over the southern tier of the United States did not emerge. Globally, many of the regions that typically experience warmer conditions during El Niño were also above average in 2015-16, and these anomalies were more prominent.

Relative to the temperature anomalies, precipitation was more consistent with El Niño during DJF 2015-16. However, there were some notable exceptions from the El Niño pattern, such as the lack of increased precipitation over the southwestern and south-central United States. Likewise, southernmost Africa was not as dry as one might expect in an El Niño during DJF - though dry conditions over southern Africa were more prominent during ASO through OND 2015 (not shown). In northern Australia, December brought significantly more rainfall than normal, though both January and February were very much below the median, which were in line with El Niño expectations.

3. Comparison with historical global temperature and precipitation anomalies

One way to quantify the match is to compute the spatial correlation coefficient between the observed pattern and a typical El Niño pattern (global domain shown in Fig. 3). To estimate the latter, detrended DJF climate anomalies are regressed onto standardized and detrended values of the DJF Niño-3.4 index from 1979-2014. Fig. 4 shows a scatterplot of correlation coefficients between the observed pattern and the El Niño regression pattern (with the spatial mean removed) for every DJF season between 1979-2016. Overall, it shows that the larger the Niño-3.4 index value (minus or plus), the larger the strength of the pattern fit with ENSO. This figure also demonstrates that DJF 2015-16 was within the expected historical spread, though the correlations were slightly lower than the significant El Niño events of 1997-98 and 1982-83. For DJF global temperature anomalies (Fig. 4, right panel), the spatial correlation coefficient is 0.33 (10% of the observed variance is explained by the ENSO pattern), while for precipitation anomalies (Fig. 4, left panel), the spatial

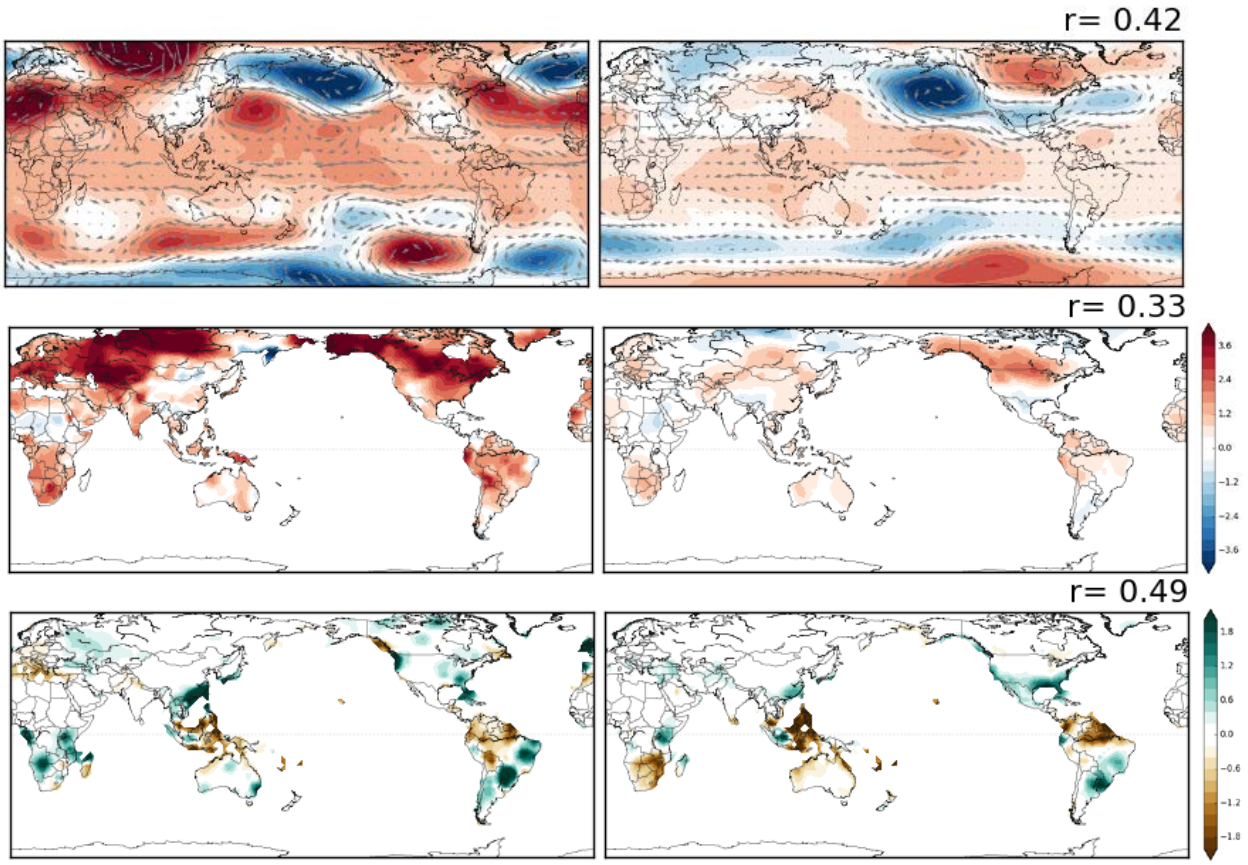

Fig. 3 December 2015-February 2016 anomalies of 500-hPa geopotential height and winds (top row), surface temperature (middle row), and precipitation (bottom row). The left column shows the observational data, while the right column shows the reconstruction for 2015/16 (weighted re- gression map of the Niño-3.4 index). The r-values show the spatial correlation coefficient between the observational and the reconstructed anomalies (cosine weighted by latitude). Geopotential height and wind data is from the NCEP/NCAR Reanalysis, the temperature is from the gridded GHCN+CAMS dataset (Fan and van den Dool, 2008), and precipitation data is from the gridded Precipitation Reconstruction Dataset (PREC) dataset (Chen *et al.*, 2002). Departures are formed by removing monthly means during 1981-2010.

correlation coefficient is 0.49 (24% of the variance is explained). While statistically significant, these values are not very large, and indicate that there was other variability during the Northern Hemisphere winter that was not well described by the ENSO linear regression pattern.

Acknowledgements. The NOAA/CPC ENSO forecast team: Anthony Barnston, Emily Becker, Gerry Bell, Tom Di Liberto, Jon Gottschalck, Mike Halpert, Zeng-Zhen Hu, Wanqiu Wang, Yan Xue. Portions are excerpted from the paper *Observing and Predicting the 2015-16 El Niño* online published in *Bulletin of American Meteorological Society* in 2016.

References

Huang, B., V. F. Banzon, E. Freeman, J. Lawrimore, W. Liu, T. C. Peterson, T. M. Smith, P. W. Thorne, S. D. Woodruff, and H.-M. Zhang, 2015: Extended Reconstructed Sea Surface Temperature Version 4 (ERSST.v4). Part I: Upgrades and intercomparisons. *J. Climate*, **28**, 911–930.

Chen, M., P. Xie, J. E. Janowiak, and P. A. Arkin, 2002: Global land precipitation: A 50-yr monthly analysis based on gauge observations. *J. Hydrometeor.*, **3**, 249–266.

Fan, Y., and H. van den Dool, 2008: A global monthly land surface air temperature analysis for 1948-present. *J. Geophys. Res.: Atmospheres*, **113**, D01103, doi:10.1029/2007JD008470.

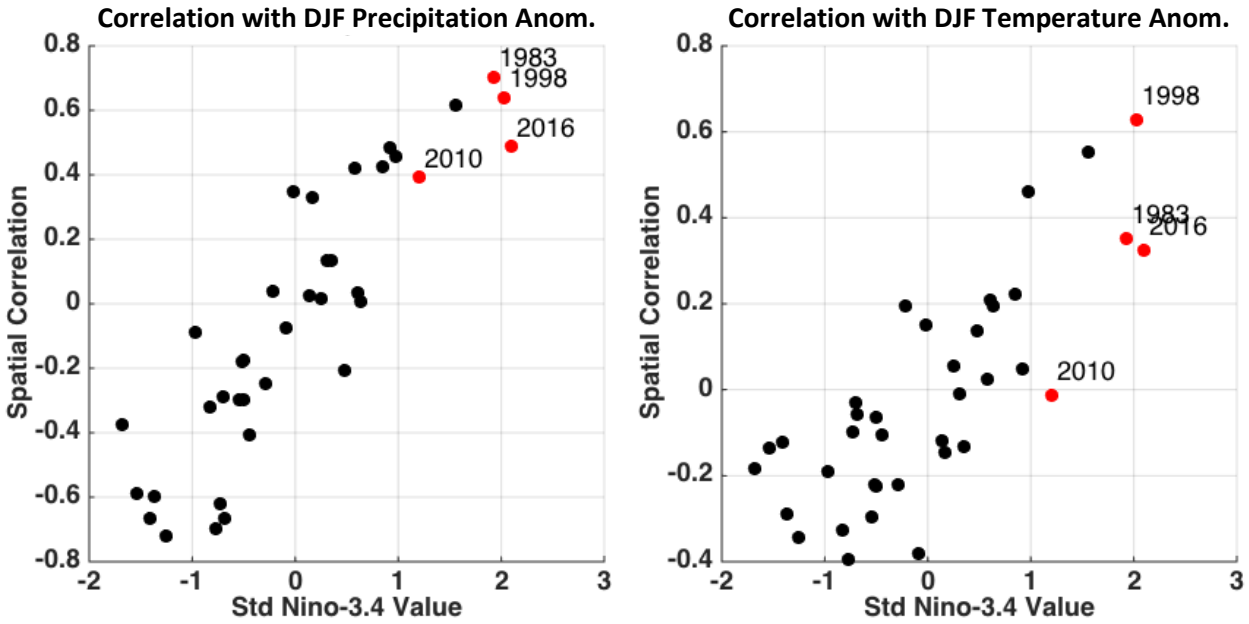

Fig. 4 The spatial correlation between the ENSO temperature (right panel) and precipitation (left panel) regression maps and observed anomalies (2015-16 shown in Figure 3). The correlation coefficient is on the ordinate and the seasonal average Nino-3.4 index value is on the abscissa. Each dot represents a single year between 1982-2016. The red dots indicate the 2015-16 El Nino, two other strong El Ninos in 1997-98 and 1982-83, and the 2009-10 El Nino, which is the El Nino prior to the 2015-16 event.

L'Heureux, M., K. Takahashi, A. B. Watkins, A. G. Barnston, E. J. Becker, T. E. Di Liberto, F. Gamble, J. Gottschalck, M. S. Halpert, B. Huang, K. Mosquera-Vasquez, and A. T. Wittenberg, 2016: Observing and predicting the 2015-16 El Niño. *Bull. Amer. Meteor. Soc.*, in press, doi: 10.1175/BAMS-D-16-0009.1.

Lee, T., and M. J. McPhaden, 2010: Increasing intensity of El Niño in the central-equatorial Pacific. *Geophys. Res. Lett.*, **37**, L14603, doi:10.1029/2010GL044007.

Science and Technology Infusion Climate Bulletin
NOAA's National Weather Service
41st NOAA Annual Climate Diagnostics and Prediction Workshop
Orono, ME, 3-6 October 2016

2015-16 El Niño Seasonal Weather Impacts from the OLR Event Perspective

Andrew M. Chiodi and D.E. Harrison

Joint Institute for the Study of the Atmosphere and Ocean, University of Washington, and NOAA/Pacific Marine Environmental Laboratory, Seattle, Washington

1. Introduction

El Niño-Southern Oscillation (ENSO) seasonal temperature and precipitation anomaly associations provide a useful basis for statistical seasonal weather forecasting in the seasons and regions where linkages between the tropical Pacific anomaly state and seasonal weather conditions are sufficiently strong in amplitude and consistent in character from one event to another ("robust"). Robust El Niño seasonal weather associations occur in boreal winter in many affected regions worldwide, when El Niño events reach peak amplitude in the tropical Pacific.

Outgoing-longwave-radiation (OLR) observations provide information about the development of deep atmospheric convection activity in the tropics. Changes in tropical convection patterns, along with the associated atmospheric heating anomalies, are believed to dynamically link the anomaly state of the tropical Pacific with its evident influence on weather conditions elsewhere.

Over the time for which satellite-based OLR information has been available (since 1974), most of the useful El Niño associations have been contributed primarily by the subset of El Niño years that are identifiable by their signature in tropical Pacific OLR (Chiodi and Harrison 2013, 2015; CH13 and CH15). The OLR El Nino index identifies 1982-83, 1986-87, 1991-92 and 1997-98 as "OLR El Niño" years. The U.S. regions with robust OLR El Niño wintertime temperature and precipitation associations were identified in the composite analysis of CH13, based on these four years. CH15 did the same for global (60°S to 60°N) precipitation over land. In both cases, the OLR El Nino composites were found to contain enough statistically significant anomaly (at 90 or 95% confidence) to reach field significance (at 90 or 95% confidence).

In contrast, composites based on the other "non-OLR El Nino years", which have event status based on the common El Niño definitions but not by OLR, yield little statistically significant winter weather anomaly at 90% or 95% confidence. Non-OLR El Niño year winter weather anomaly patterns exhibit a high degree of event-to-event variability, including over the regions where robust associations are found in the OLR El Niño case. The non-OLR El Niño wintertime temperature (U.S.) and precipitation (global and U.S.) composites do not pass field significance tests, even when compromising to the 66% confidence interval (CH13, CH15).

Three of the four previous OLR El Niño events (1982-83, 1991-92, 1997-98) were identifiable from the OLR information (OLR El Niño index) available by the end of fall of ENSO Year 0, in time to be of use to wintertime forecasting efforts, albeit at short lead. Should this type of behavior hold, monitoring tropical Pacific OLR conditions will provide means to usefully strengthen our ability to forecast winter weather in the strongly affected regions. It is not necessary to forecast OLR for this use.

The recent 2015-16 El Niño was identifiable as an OLR-event before winter (Fig. 1). Here we examine the extent to which the winter weather conditions seen in 2015-16 match those seen in the previous event composite (based on 1982-83, 1986-87, 1991-92 and 1997-98), over the strongly affected regions. These include the regions within Africa, South America and North America that were revealed to have robust precipitation associations by the CH15 composite analysis. We examine each of these three cases, but follow CH13 in offering a more detailed look at both wintertime temperature and precipitation associations over the U.S. (contiguous 48 States), rather than examine the entire North American continent. We also discuss the composite wintertime (Dec-Jan-Feb; DJF hereafter) tropical OLR anomaly pattern based on the four previous OLR El Nino events, as well as conditions observed in 2015-16.

Correspondence to: Andrew M. Chiodi, Joint Institute for the Study of the Atmosphere and Ocean, University of Washington, and NOAA/Pacific Marine Environmental Laboratory, Seattle, Washington; E-mail: andy.chiodi@noaa.gov

2. Data and methods

We use gauge-based gridded (1° latitude × 1° longitude) precipitation data from the Global Precipitation Climatology Center (GPCC; Schneider et al. 2015) for information on monthly precipitation anomaly over Africa and South America. GPCC precipitation data is available from http://gpcc.dwd.de. For temperature and precipitation information over the U.S., we use the U.S. Climate Divisional Data set made available by NOAA's National Centers for Environmental Information, at: https://www.ncdc.noaa.gov/monitoring-references/maps/us-climate-divisions.php.

These are the same precipitation and data sets used by CH15 and CH13. The base period used here to calculate the 2015-16 DJF seasonal weather anomalies is 1979-2015. The composites based on the previous four OLR El Niño events are shown here as they were published in CH15 and CH13, based on a 1974-2011 and 1979-2008 base period, respectively. We have confirmed that the composites remain qualitatively equivalent regardless of which of these three base periods is used to calculate anomalies from the mean seasonal cycle.

For up-to-date OLR information we use the NOAA OLR Climate Data Record (CDR), available with just a few days delay at http://olr.umd.edu/.

3. Tropical OLR anomaly

The wintertime (DJF) composite of tropical OLR anomaly based on the four previous El Nino years has a large amplitude and statistically significant (at 95%) negative anomaly (increased convection/atmospheric heating) spanning the eastern two-thirds of the equatorial Pacific Ocean basin (CH15 and Fig. 1). This composite also reveals significant positive OLR anomaly (decreased convection activity) over much of the far western tropical Pacific. The non-OLR composite (CH15; not shown here) has weaker OLR anomalies that reach statistical significance over a much smaller area, including near the Dateline. This difference in OLR behavior suggests that there is a much stronger tropical atmospheric heating anomaly at work in the OLR El Nino years than non-OLR El Niño years.

The 2015-16 DJF tropical OLR anomaly pattern resembles that seen in the OLR El Niño composite. This suggests that a similarly strong tropical atmospheric heating anomaly is at work in 2015-16 as well.

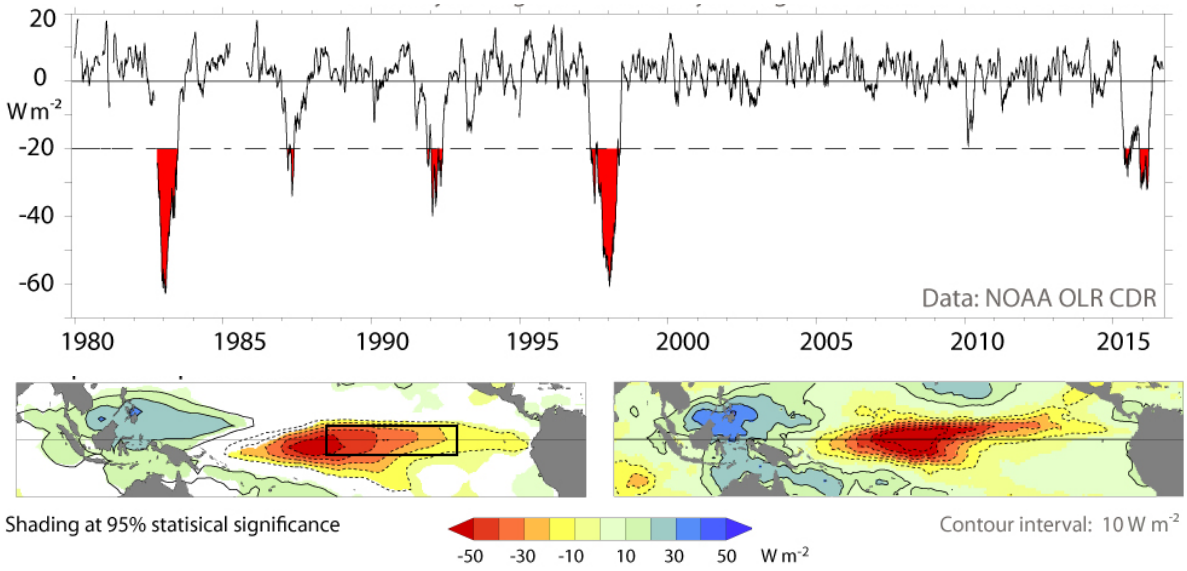

Fig. 1 Upper panel: The OLR El Niño index. The OLR anomaly is monthly mean and area averaged over 160°-110°W and 5°S-5°N. Bottom left: Composite DJF-averaged OLR anomaly based on the previous four OLR El Niño events. The box shows the OLR El Niño index averaging region. Bottom right: OLR anomaly averaged over the DJF period spanning December 2015 through February 2016.

4. El Niño DJF precipitation associations over Africa

Composite DJF precipitation anomaly over Africa based on the 4 previous OLR El Niño events is shown in the upper-right panel of Figure 2, along with the DJF average observed in 2015-16 (upper left panel). Statistically significant (90% level) wet and dry anomalies are seen over some southeastern (*e.g.* Tanzania) and southern (*e.g.* parts of South Africa, Mozambique and Zimbabwe) regions of the continent. Statistically significant dry anomaly is also seen over part of equatorial western Africa.

It is over these affected regions (where the composite is shaded) where we hypothesize that the OLR-perspective on El Niño can be used to strengthen our ability to forecast DJF precipitation during the OLR El Niño events. The 2015-16 DJF precipitation anomaly pattern matches the previous-event composite over these regions (Fig. 2, upper panels); in each case, a coherent dry-to-wet contrast is seen between the southern-to-southeastern part of the continent, and dry anomaly over equatorial western Africa.

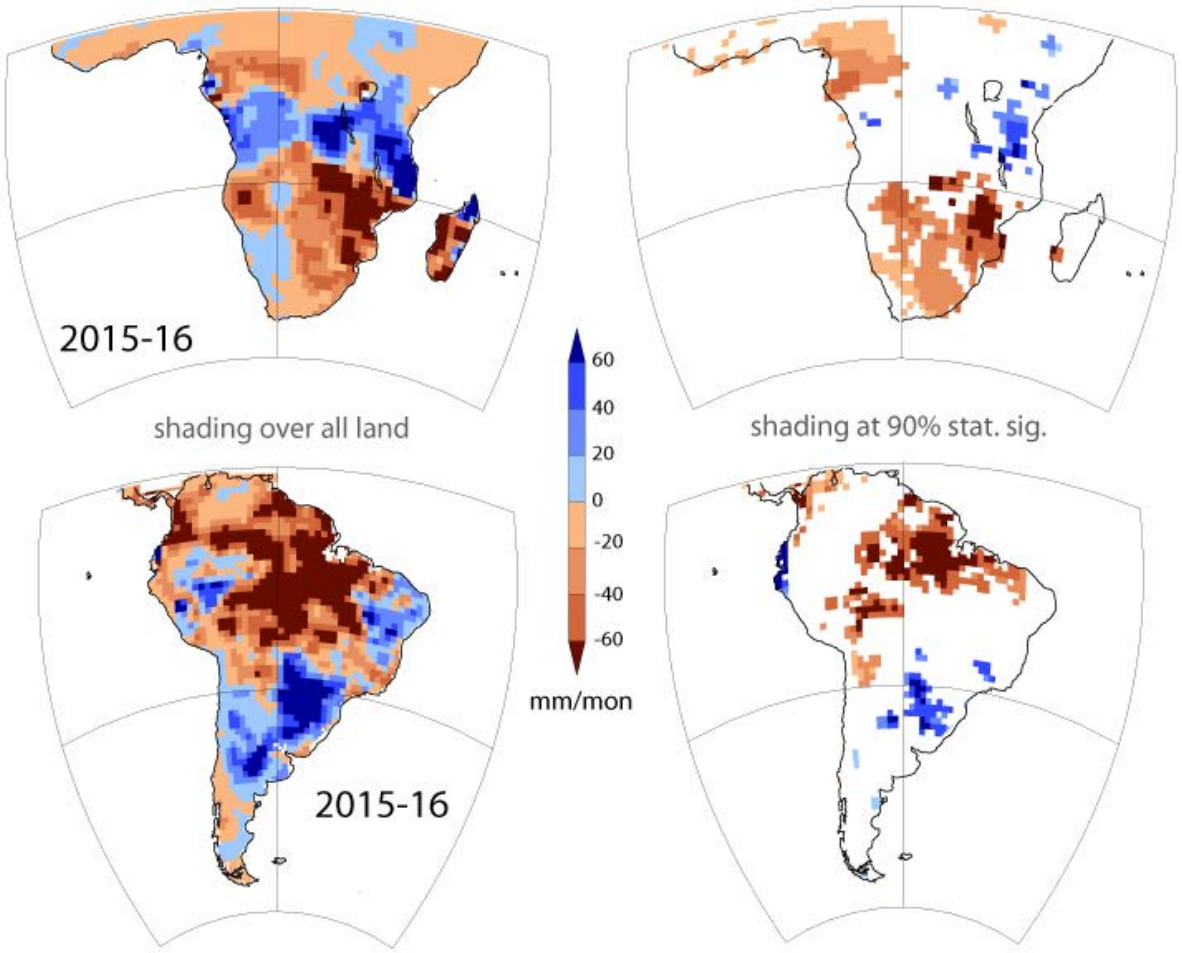

Fig. 2 Left side panels: DJF averaged precipitation anomalies observed during the recent 2015-16 OLR El Niño event. Right panels: Composite DJF precipitation anomalies based on the previous four OLR El Niño events, as described by Chiodi and Harrison (2015).

5. El Niño DJF precipitation associations over South America

The DJF precipitation composite based on the previous four OLR El Niño events reaches statistical significance (at 90%) over much of the Amazon river basin (dry) as well as over a smaller region in Southeastern South America (wet) (Fig. 2, lower panels). Some more localized statistically significant anomaly is also seen along the northwest coast, where dry anomaly is seen over the northwest coast of Columbia and wet anomalies are seen over Equador and Peru.

The two larger strongly-affected regions (Amazon Basin and Southeastern South America) exhibit 2015-16 DJF anomaly conditions that rather closely match those seen in the composite based on previous events. The 2015-16 case also matches the composite over the northwestern coast of Columbia, but not over Peru. Although more work is needed to explain the observed precipitation anomalies over Equador and Peru in 2015-16, there is a good overall match between the previous event composite and 2015-16 over South America.

6. El Niño DJF precipitation and temperature associations over the U.S.

The composite U.S. wintertime precipitation anomaly pattern based on the four previous OLR El Niño events reveals coherent and statistically significant (95%) wet anomalies over much of the southeast (Fig. 3, lower right). CH13 showed that each of the four individual event-years exhibited a broad swath of wet anomaly over this region. In 2015-16, DJF-averaged rainfall (Fig. 3, lower left) was substantially heavier than average over much of the southeast, but dryer than normal conditions were unexpectedly seen over Texas.

The OLR El Niño composite U.S. temperature anomaly pattern reveals statistically significant (95%) warm temperatures during DJF over much of the north central U.S (Fig. 3, upper right). The 2015-16 winter temperature anomaly also has >3°F temperature anomaly over this region (Fig. 3, upper left). We have confirmed that the warm anomaly over the north-central U.S. in DJF 2015-16 remains >3°F regardless of whether or not the linear trend in temperature over the study period is removed before the DJF anomaly is calculated. This result is also robust to changing the base period by 5-10 years. The OLR El Nino-associated wintertime warming amplitude over the north central U.S. is large compared to these other sources of variability.

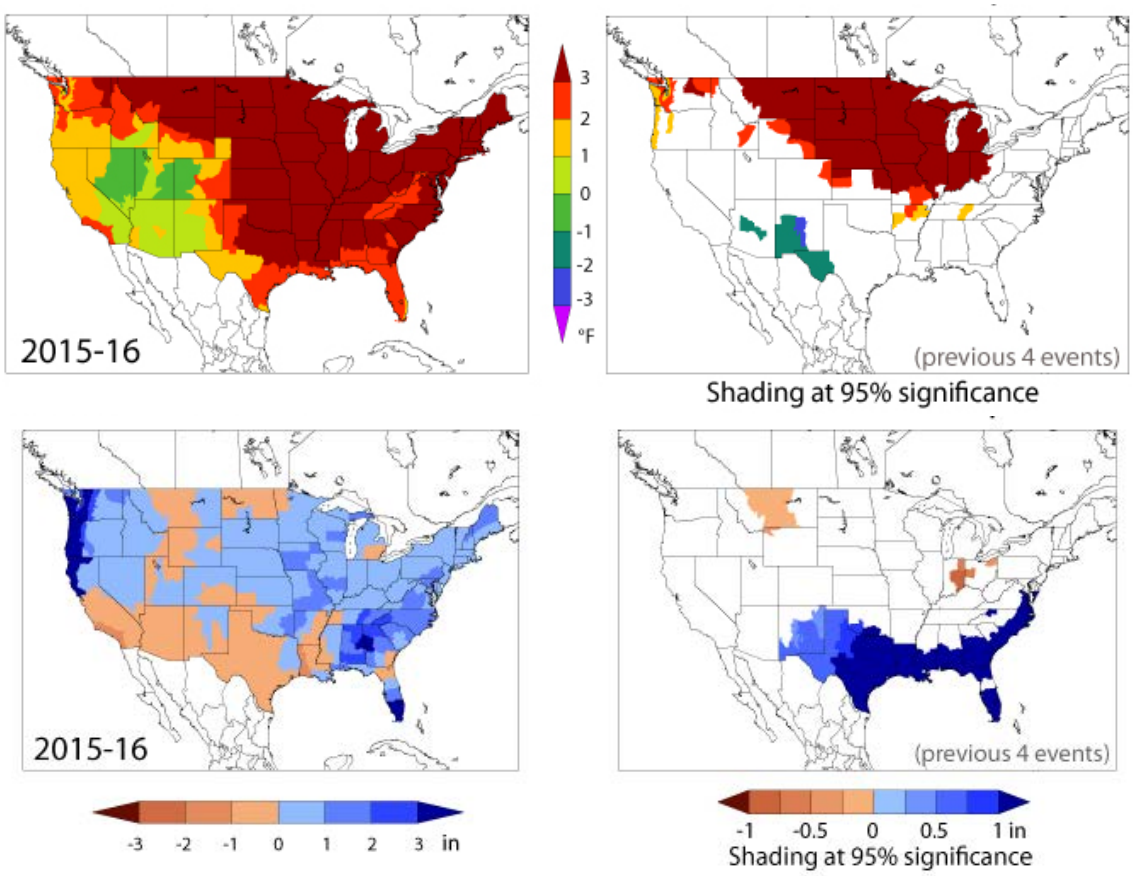

Fig. 3 DJF-averaged temperature (upper) and precipitation anomaly (lower) over the U.S. for the composite based on the previous four OLR El Niño events (right) and the 2015-16 event (left).

7. Summary

We have shown previously that most of the useful El Niño-winter weather anomaly associations worldwide have been contributed by the subset of El Niño years that are distinct based on tropical Pacific OLR. We have now experienced five such OLR El Nino years over the time for which satellite-based OLR information is available, with 2015-16 being the fifth. As was the case in most of the previous events, 2015-16 was distinguished by the OLR El Niño index before winter. We have previously hypothesized that this situation provides opportunity to strengthen our ability to forecast wintertime weather conditions over the regions where robust associations have been revealed by the prior events. Obviously, this requires that the associations remain consistent in future events. We have examined the extent to which the 2015-16 DJF weather anomalies are consistent with the previous-4-event composite over the regions where robust associations have been revealed by the composite.

The wintertime weather anomaly observed over the north central U.S. in 2015-16 well matches that seen in the composite of previous events in that a coherent patch of substantially (> 3°F) warm anomaly is seen in both cases. The observed 2015-16 DJF precipitation anomaly conditions also have the same character as those in the composite over about 75% of the regions previously identified as having robust associations (Peru and Texas being the exceptions). This basic agreement supports our hypothesis that the OLR-perspective on El Niño seasonal weather associations offers strengthened ability to make event-year winter weather forecasts in the robustly-affected regions.

Acknowledgements. This publication is partially funded by the Joint Institute for the Study of the Atmosphere and Ocean (JISAO) under National Oceanic and Atmospheric Administration (NOAA) Cooperative Agreement NA10OAR4320148, and by support from the Climate Observations Division of the NOAA Climate Program Office (FundRef number 100007298) as well as from NOAA's Pacific Marine Environmental Laboratory.

REFERENCES

Chiodi, A.M., and D.E. Harrison, 2013: El Niño impacts on seasonal U.S. atmospheric circulation, temperature, and precipitation anomalies: The OLR-event perspective. *J. Climate*, **23**, 822-837. doi: 10.1175/JCLI-D-12-00097.1

Chiodi, A.M., and D.E. Harrison, 2015: Global seasonal precipitation anomalies robustly associated with El Niño and La Niña events - An OLR perspective. *J. Climate* , **28**, 6133-6159. doi: 10.1175/JCLI-D-14-00387.1

Schneider, U., M. Ziese, A. Becker, A. Meyer-Christoffer, P. Finger, 2015: Global Precipitation Analysis Products of the GPCC. Global Precipitation Climatology Centre, 14 pp. ftp://ftp-anon.dwd.de/pub/data/gpcc/PDF/GPCC_intro_products_2008.pdf

Science and Technology Infusion Climate Bulletin
NOAA's National Weather Service
41st NOAA Annual Climate Diagnostics and Prediction Workshop
Orono, ME, 3-6 October 2016

Winter 2015/16 Atmospheric and Terrestrial Anomalies over North America: El Niño Response and Role of Noise

Mingyue Chen and Arun Kumar
[1]*Climate Prediction Center, NOAA/NWS/NCEP, College Park, Maryland*

ABSTRACT

In this study, attribution of the possible reasons for the observed 2015/16 winter precipitation anomalies that were opposite to the mean El Niño signal over the southwest North America were analyzed. The analysis focuses on the role of SST forcing and the contributions of atmospheric internal variability based on the ensemble forecasts of hindcasts and real-time forecasts from the NCEP Climate Forecasts System version 2 (CFSv2, Saha et al. 2014). We analyzed first the atmospheric response to forecast SSTs based on ensemble mean, specifically, to examine how well the 2015/16 winter NA atmospheric anomalies were predicted as an ensemble mean atmospheric response and if the pattern of 2015/16 winter anomalies in the forecast ensemble mean has been changed from that of the El Niño composite. Then we assessed the contribution of atmospheric noise based on individual forecast members, specifically, to examine how much the individual forecasts are differed from the ensemble means and if the observed 2015/16 winter atmospheric anomalies were within the envelope of variability in the ensemble forecast.

The results show that the pattern of 2015/16 winter North America atmospheric anomalies as an ensemble mean atmospheric response to SSTs compared favorably with the El Niño composite from the historical period and were much the same as the previous El Niño events of 1982/83 and 1997/98 with similar amplitude of ENSO SSTs. The major features include the 200mb height with sub-tropical Pacific jet toward the southwest NA, and the precipitation with positive anomalies over the southwest NA and negative across

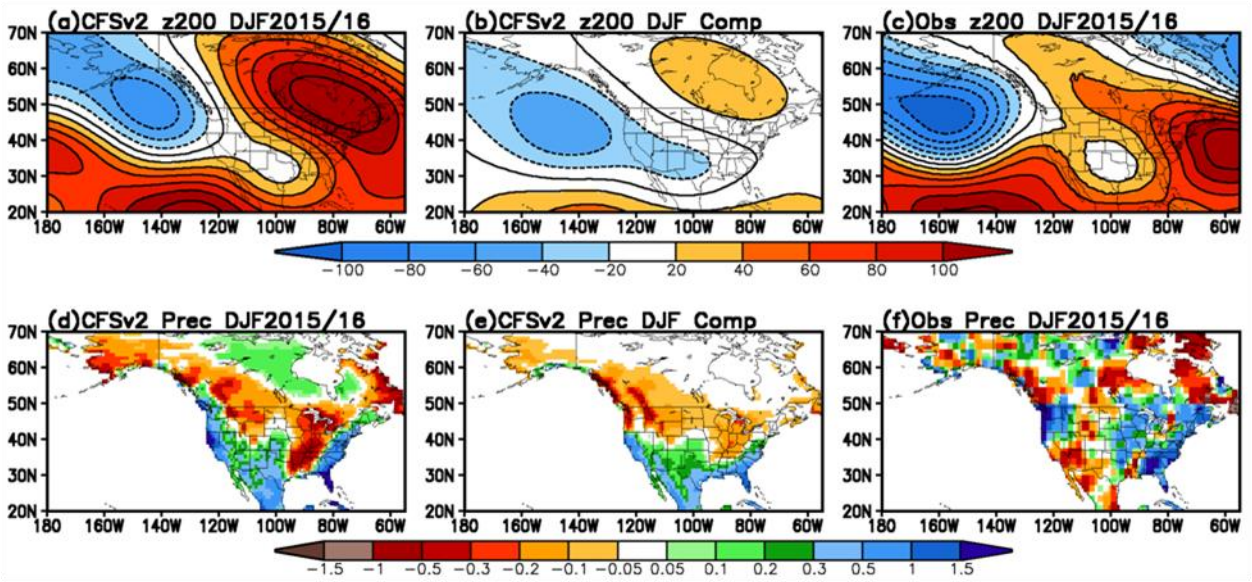

Fig. 1 The z200mb height (a, b, c) and precipitation (d, e, f) anomalies for the CFSv2 forecast ensemble mean of DJF2015/16 (a, d), the El Niño composite based on CFSv2 ensemble forecasts of DJF in1982-2014 (b, e), and the observations in DJF2015/16 (c, f). The unit is in m and mm/day for the 200mb height and precipitation, respectively. The observed precipitation is from (Janowiak and Xie 1999), and 200mb height from the CFSR (Saha *et al.* 2010).

Correspondence to: Mingyue Chen, Climate Prediction Center, NOAA/NWS/NCEP, 5830 University Research Court, College Park, MD; E-mail: mingyue.chen@noaa.gov

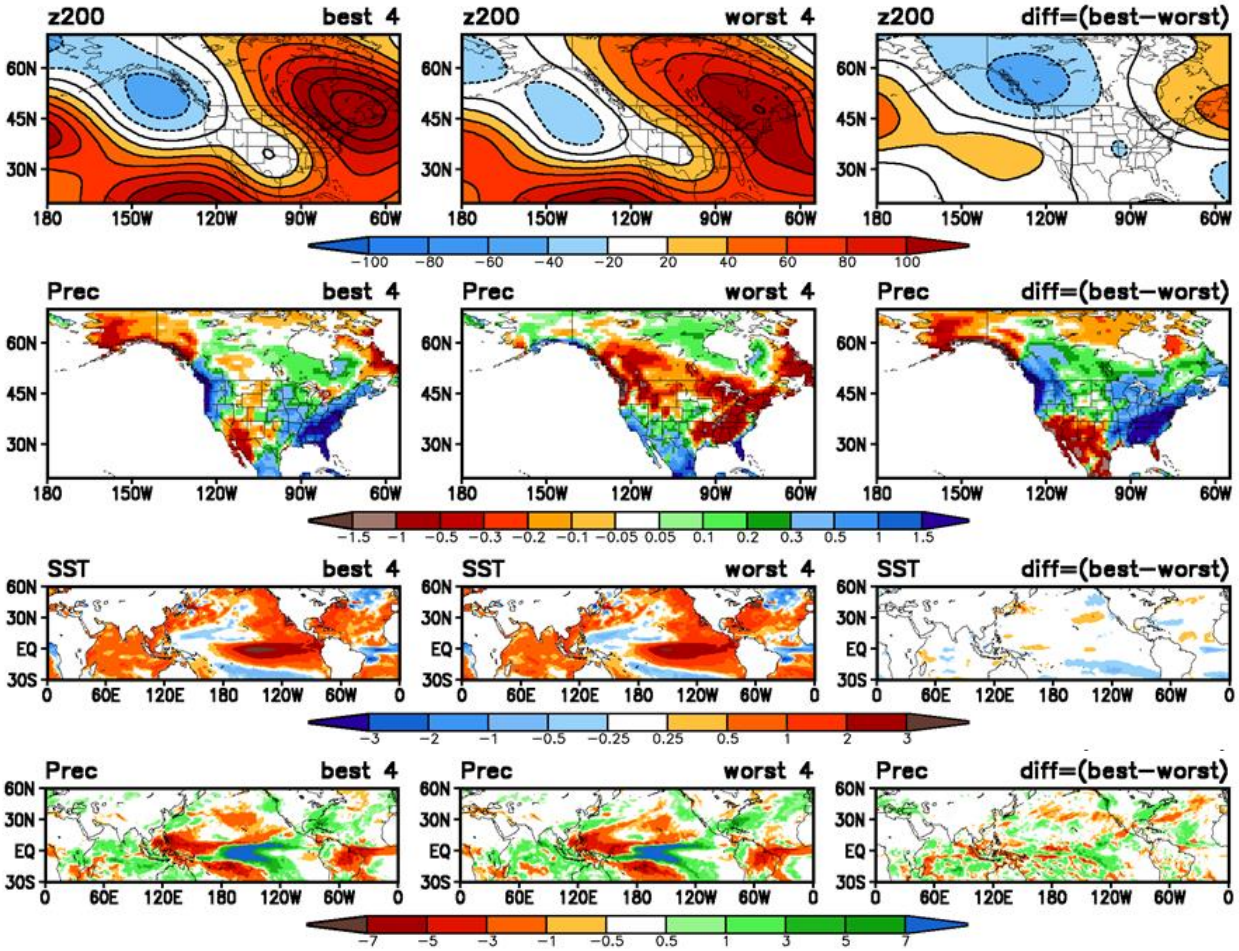

Fig. 2 Average of four best forecast members (the left panels), and four worst forecast members (the middle), and their differences (the right panels) for DJF2015/16 forecasts from CFSv2. The top row is for 200mb height (m) over the PNA; the 2nd row precipitation (mm/day) over North America, the 3rd row SST (K), and the 4th row precipitation (mm/day) over global region from 30°S to 60°N.

the northern NA (Fig. 1). Therefore, the tele-connection pattern and precipitation response pattern in winter 2015/16 had not changed from the mean El Niño signal. The observed negative precipitation anomalies over the southwest NA in DJF2015/16 were not the result of SST forced signal.

However, there are considerable variations in the outcome of 2015/16 winter precipitation over the North America from one forecast to another even though the SSTs are the same. Among the 40 forecasts in the analysis, the average of four members with highest correlation skill with the observation is very different from that of four members with lowest correlation skill with the observation, with their signs of forecasts anomalies opposite of each other (Fig. 2). The observed 2015/16 winter precipitation anomalies were well within the envelope of possible outcomes.

In conclusion, the reason why the observed 2015/16 winter precipitation anomalies over the southwest North America differed greatly from the El Niño composite was mainly due to the large contribution of the atmospheric internal variability (noise) which overwrote the atmospheric response (signal) to the ENSO SSTs. This unpredictable inherently nature of atmospheric variability leads to low predictability and prediction skill for the North America seasonal precipitation.

References

Janowiak, J. E., P. Xie, 1999: CAMS-OPI: A global satellite-rain gauge merged product for real-time precipitation monitoring applications. *J. Climate*, **12**, 3335-3342.

Saha, S., and Co-authors, 2010: The NCEP climate forecast system reanalysis. *Bull. Amer. Meteor. Soc.*, **91**, 1015-1057, doi:10.1175/2010BAMS3001.1

Saha, S., and Co-authors, 2014: The NCEP climate forecast system version 2. *J Climate*, **27**, 2185-2208. doi:10.1175/JCLI-D-12-00823.1

2. CLIMATE MODELING, MME, PREDICTION & PREDICTABILITY

41th NOAA Annual Climate Diagnostics and Prediction Workshop

3-6 October 2016, Orono, Maine

Science and Technology Infusion Climate Bulletin
NOAA's National Weather Service
41st NOAA Annual Climate Diagnostics and Prediction Workshop
Orono, ME, 3-6 October 2016

Do Statistical Pattern Corrections Improve Seasonal Climate Predictions in NMME Models?

Anthony G. Barnston[1] and Michael K. Tippett[2]

[1]*International Research Institute for Climate and Society (IRI), Columbia University, Palisades, New York*
[2]*Columbia University, New York, New York, and King Abdulaziz University, Jeddah, Saudi Arabia*

1. Introduction

The North American Multimodel Ensemble (NMME) contains global predictions of SST, surface air temperature, precipitation and other variables from 8 or more state-of-the-art coupled general circulation models (Kirtman 2014). In phase one of the NMME project, hindcasts of monthly average climate extending to up to 12 months into the future were created, spanning the 1982-2010 period. Here we seek to determine whether a commonly used multivariate statistical methods—namely, CCA—can improve the temporal anomaly correlation skill of the individual models, with the goal of improving the predictions of the multi-model ensemble. The anomaly correlation is used as the main metric because it measures the ability to reproduce the interannual variability of the climate, regardless of the presence of systematic errors that can be treated locally using simpler statistical methods.

2. Data and methods

The model hindcast data used here are available at the site http://iridl.ldeo.columbia.edu/SOURCES/.Models/.NMME. The 8 models used include (1) the COLA-RSMAS-CCSM4 model, (2) the NASA-GMAO-062012 model, (3) the GFDL-CM2pl-aer04 model, (4) the GFDL-CM2p5-FLOR-A06, model, (5) the GFDL-CM2p5-FLOR-B01 model, (6) the CMC1-CanCM3 model from Canada, (7) the CMC2-CanCM4 model from Canada, and (8) the NCEP-CFSv2 model. The model global hindcast data are on a 1-degree grid. The 8 models used provide varying numbers of ensemble members, ranging from 10 to 24. Here, the ensemble mean is used to represent the forecast signal, while the ensemble member spread, representing the forecast uncertainty, is not considered.

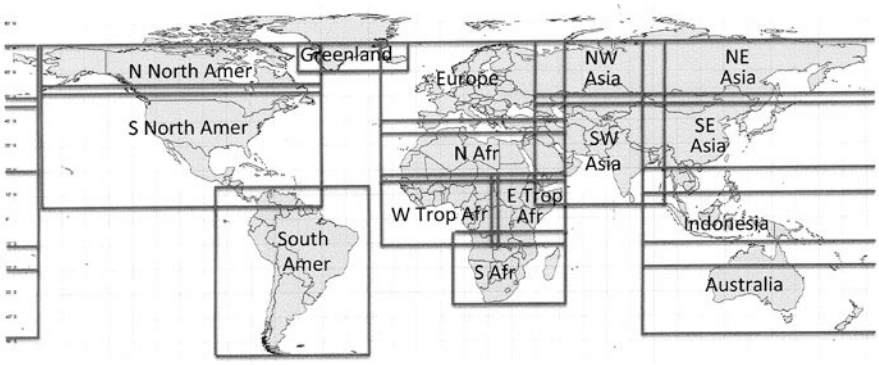

Fig. 1 The 15 slightly overlapping CCA target (predictands) areas, each of which uses a larger predictor area.

The verifying observations, also in a 1-degree grid and available on the above-mentioned web page, are CMAP-URD and GHCN-CAMS for precipitation and temperature, respectively, both created at the NOAA Climate Prediction Center. Most of our attention here is devoted to precipitation prediction.

In the CCA method used here, pre-orthogonalization (EOF analysis) is done separately on the model hindcasts (the X variable) and on the corresponding observations (the Y variable), and a truncated set of the principal component time series from these EOFs are used as input to the CCA. A cross-validation scheme is used, in which 3 consecutive years are withheld from both the pre-EOF and the CCA training sample, and the middle year of the three is predicted. The EOF analysis use the covariance matrix rather than the correlation matrix.

Correspondence to: Anthony G. Barnston, International Research Institute for Climate and Society (IRI), Columbia University, Palisades, New York; E-mail: tonyb@iri.columbia.edu.

The CCA is applied to 15 different regions of the globe (Fig. 1), with the idea that each region would be better treated with respect to the large-scale climate patterns pertinent to it but not necessarily other regions of the globe. The regions are defined so as to capture known leading modes of variability, such as those associated with ENSO. The corrected forecasts of each region will then be merged to form a global forecast.

While the temporal anomaly correlation is used as the main verification measure, the root mean squared error (RMSE) and the uncentered correlation are also computed to detect the presence of calibration issues before and after the CCA.

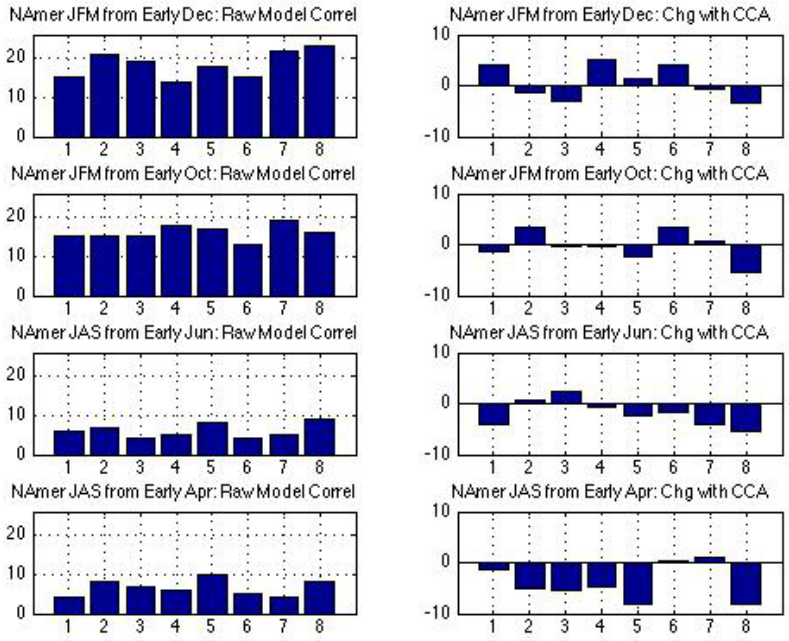

Fig. 2 Original anomaly correlation skill (left), and the change in skill due to the CCA (right). From top to bottom, the results are for (row 1) Jan-Mar precipitation forecasts from early Dec, (row 2) Jan-Mar forecasts from early Oct, (row 3) Jul-Sep forecasts from early Jun, and (row 4) Jul-Sep forecasts from early Apr. The order of the 8 models (horizontal axis) is as listed in the previous section (1:CCSM4, 2:NASA, 3:GFDL, 4:GFDL-FLORA, 5:GFDL-FLORB, 6:CMC1, 7:CMC2, and 8:CFSv2).

The regions overlap somewhat so that discontinuities in the forecasts at the boundaries can be smoothed with weightings reflecting the distance from the point in question to the nearest border of the two (or more) regions. The numbers of EOF modes used varies by region to approximately maximize skill, determined by skill sensitivity tests that vary the numbers of X, Y, and CCA modes. The globe as a single region was also used as a 16th "region", allowing for a skill comparison between the merged regional forecasts and the single globe forecast.

3. Results

Figure 2 shows, for the non-northern North America region (including the U.S.) for each of the 8 models, the original anomaly correlation skill, and then the change in skill from the CCA, for the Jan-Mar and Jul-Sep target seasons, each at 1.5-month lead and 3.5-month lead. The CCA corrections generally did not result in substantial skill improvements.

The upper right panel of Fig. 2 shows the CCA did improve the skill of the GFDL-FLOR-A model (model #4). Using this example, Fig. 3 shows the spatial distribution of anomaly correlation skill before and after the CCA correction, and the skill change due to the CCA. Skill was improved in various portions of the U.S., including the Midwest, northern Plains, and other pockets. However, as shown in Fig. 2, in the case of many of the other models for the two seasons and two lead times, average skill was not improved by the

Region	Skill Change	Region	Skill Change
N. North Amer	0.03	South Africa	0.04
S. North Amer	0.01	NW Asia	0.06
South Amer	-0.04	SW Asia	-0.06
Greenland	0.05	NE Asia	-0.01
Europe	-0.05	SE Asia	-0.06
North Africa	-0.04	Indonesia	0.01
W. Trop. Africa	-0.01	Australia	-0.14
E. Trop. Africa	-0.16	**Single Globe**	**-0.001**

Table 1 CCA-related change in anomaly correlation skill for precipitation forecasts for Jan-Mar made in early Dec, averaged over 8 models, for each of 15 individual regions and for the globe as a single region.

CCA.

One can use the CCA to statistically calibrate the forecasts for the entire globe as a single region, rather than merging the corrected forecasts of individual regions. While one might expect the merged skill result to be better than the single globe result (due to the individual attention given to each region), this is not found to be the case. For example, Table 1 shows the change in skill due to the CCA, averaged over all 8 models, for each region and for the globe as a single region, for precipitation forecasts of Jan-Mar made in early December. The average of the skills over the individual regions is slightly lower than the skill of the globe as a single region.

Skill comparisons for other seasons and lead times generally give similar results to that for short-lead forecasts for Jan-Mar, in that the CCA for the single globe does as well as, if not slightly better than, the individually tailored CCAs designed for each region and merged into a global forecast. A summary of these results is shown in Table 2 for the target seasons of Jan-Mar and Jul-Sep, each at 1.5 and 3.5 month lead times. In all cases, the merged CCAs from individual regions does not result as a positive change (or as small a negative change) in skill as the single globe CCA. The original model skills for the merging of individual regions does not exactly equal that of the single globe because the former does not obey area-weighting of skills, while the single globe does.

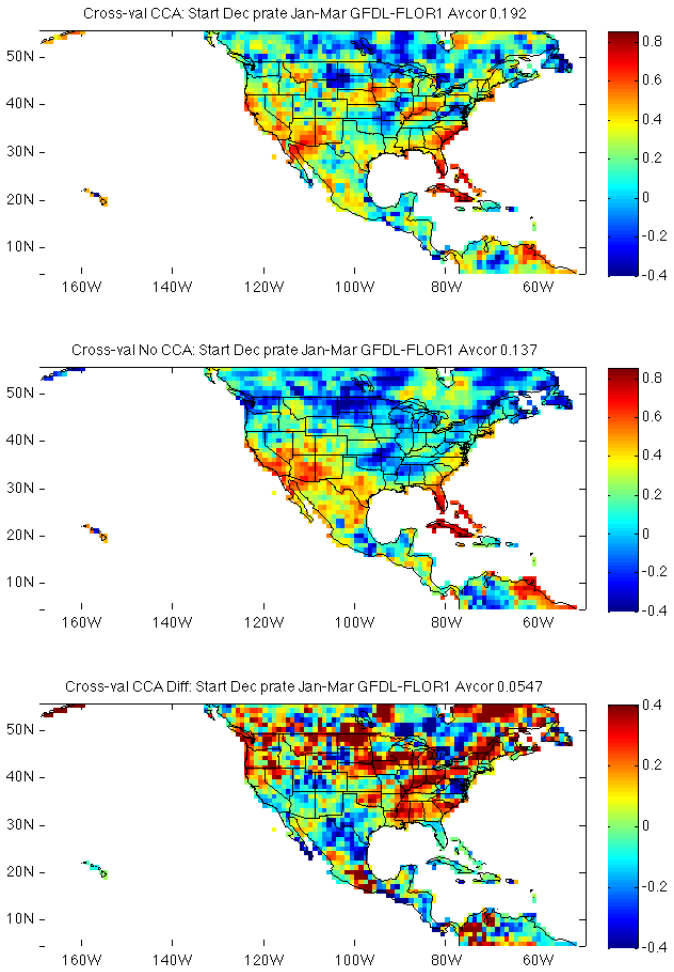

Fig. 3 Geographic distribution of temporal anomaly correlation skill over the non-northern North America region for precipitation forecasts by the GFDL-FLOR-A model for Jan-Mar made in early Dec. The middle panel shows the original skill, top panel the skill after the CCA correction, and bottom panel the skill improvement due to the CCA (note the different scale for the bottom panel).

While the analyses described so far have been limited to precipitation forecasts, a less extensive examination of temperature forecasts indicates an even less favorable result, with the CCA usually degrading the skill of the original uncorrected forecasts. Exceptions are found for temperature forecasts of Oct-Dec forecasts for eastern tropical Africa and Indonesia, where the CCA increases the anomaly correlation.

As complementary verification measures, the RMSE and the uncentered correlation between uncorrected and corrected and precipitation and temperature forecasts and the corresponding observations were also computed. In contrast to the anomaly correlation, both of these measures show a significant improvement following the CCA for both precipitation and temperature. This result suggests that systematic forecast errors that largely do not involve spatial pattern placement are present in the uncorrected forecasts—errors such as mean bias and amplitude bias.

4. Conclusions and discussion

The CCA corrections did not improve the skills of the precipitation forecasts of the individual models of the NMME as much as had been hoped. In fact, overall, a lack of systematic and substantial improvements is noted, with only slight improvements in about half of the cases.

Although the temporal anomaly correlation is not materially improved by the CCA, the RMSE and the uncentered correlations are notably improved. This indicates the presence of biases in the forecasts, such as mean bias and amplitude bias, which affect the two latter verification measures but not the anomaly correlation. One would expect the CCA to treat both local systematic biases and spatial placement errors together. Even if improving both types of errors, it might require retaining more EOF and CCA modes than if just one type of error were present. Mode truncation sensitivity tests were done, and the truncations resulting in approximately the best cross-validated correlation skills were selected.

Start ➔Target	Style	Original Model Skill	Change from CCA
Dec => JFM	Merge	0.149	-0.063
	Single Globe	0.153	-0.001
Oct => JFM	Merge	0.109	-0.009
	Single Globe	0.113	0.023
Jun => JAS	Merge	0.114	-0.014
	Single Globe	0.117	0.012
Apr => JAS	Merge	0.086	-0.009
	Single Globe	0.088	0.024

Table 2 Comparison of the effect on globally averaged anomaly correlation skill of the CCA when performed on individual regions and merged to a global precipitation forecast, and when performed on the globe as a single region. Results are shown for forecasts for Jan-Mar made in early Dec and early Oct, and forecast for Jul-Sep made in early Jun and early Apr.

A few explanations may be offered to account for the unimpressive ability of CCA to improve the model anomaly correlation skills:

i. A covariance matrix was used in the pre-EOFs, rather than a correlation matrix.
ii. The cross-validation may create a negative skill bias (Barnston and Van den Dool 1993), given the large areas of low skill in many of the regions.
iii. Local systematic biases (mean bias and amplitude bias) may be present to a greater extent in the model hindcasts than pattern placement biases. The CCA did improve local biases (seen in RMSE and uncentered correlation) but these improvements alone do not improve the anomaly correlation. Correction of pattern placement biases would be expected to improve the anomaly correlation.

Possible actions to be taken to address these results are:

i. Test the skill behavior when the correlation matrix rather than covariance matrix is used in the pre-EOFs.
ii. Consider a separate correction of local systematic errors prior to the CCA treatment. It is not clear that the CCA can successfully detect and treat spatial placement errors when there are also larger locally correctible systematic errors.
iii. For temperature, try using an alternative data set in place of the GHCN-CAMS. Although it is unlikely, it is possible there is a problem with GHCN-CAMS temperature data.

References

Barnston, A. G., and H. M. van den Dool, 1993: A degeneracy in cross-validated skill in regression-based forecasts. *J. Climate*, **6**, 963-977.

Kirtman B, and Coauthors, 2014: The North American Multi-Model Ensemble (NMME): Phase-1 seasonal to interannual prediction; Phase-2 toward developing intra-seasonal prediction. *Bull. Amer. Meteor. Soc.*, **95**, 585-601, DOI 10.1175/BAMS-D-12-00050.1

Science and Technology Infusion Climate Bulletin
NOAA's National Weather Service
41st NOAA Annual Climate Diagnostics and Prediction Workshop
Orono, ME, 3-6 October 2016

Exploring the Impact of SST on the Extended Range NCEP Global Ensemble Forecast System

Christopher Melhauser[2], Wei Li[2], Yuejian Zhu[1], Xiaqiong Zhou[2], Malaquias Peña[2], and Dingchen Hou[1]

[1]*Environmental Modeling Center, NOAA/NWS/NCEP, College Park, Maryland*
[2]*IMSG at EMC, College Park, Maryland*

1. Introduction

The National Oceanic and Atmospheric Administration (NOAA) is accelerating its efforts to improve its numerical guidance and prediction capability for the extended range - the weeks 3 & 4 period that bridges the gap between weather and climate. Operational global numerical guidance for weeks 3 & 4 and monthly prediction are currently available from NOAA's National Center for Environmental Prediction (NCEP) Climate Forecasting System Version 2 (CFSv2) coupled (ocean, sea-ice, land, atmosphere) model (Saha *et al.*, 2006; Saha *et al.*, 2010; Saha *et al*., 2014). Extending the NCEP Global Ensemble Forecasting System (GEFS) to cover the weeks 3 & 4 period provides additional benefits over the CFSv2 including a more frequent model upgrade cycle, higher model resolution, state-of-art flow-dependent initial perturbations from a hybrid data assimilation system, stochastic physics, and larger ensemble membership (80 perturbed members and 4 control runs for every 24-h period), all providing an improved sampling of forecast uncertainty.

In this study, an operational GEFS configuration is extended to 35 days and the forecast skill is evaluated. Various SST forcing experiments are performed to examine the impact of SST forcing on the extended-range forecast skill of global 2-m temperature, accumulated precipitation over the contiguous United States (CONUS), and Madden-Julian Oscillation (MJO; Madden and Julian, 1971) indices.

2. Methodology

The current operational configuration of GEFS uses the GFS Global Spectral Model v12.0.0 for integration four times per day (0000, 0600, 1200 and 1800 UTC) out to 16 days (Han and Pan 2011; Juang 2011, 2014). For days 0-8, GEFS has a spectral resolution of T_L574 (approximately 34 km) with 64 vertical levels and the horizontal resolution is reduced to T_L384 (approximately 52 km) for days 8-16. The horizontal resolution is further reduced to T_L254 (approximately 78 km) for days 16-35 for the extended GEFS runs in this study. The 20-member ensemble initial condition perturbations are selected from the operational hybrid NCEP Global Data Assimilation System (GDAS) 80-member Ensemble Kalman Filter (EnKF; Whitaker *et al.*, 2008; Wang *et al.* 2013; Kleist and Ide 2015) prior.

The SST configurations for this study consist of the operational GEFS 90 day e-folding of the observed RTG SST anomaly relaxed to climatology (CTL), an optimal Atmospheric Model Intercomparison Project (AMIP; Gates *et al.* 1999) configuration using the observed RTG SST analysis updated every 24-h during model integration (RTG), a 2-tier approach using the CFSv2 predicted SST updated every 24-h during model integration (CFS), and a 2-tier approach using biased corrected CFSv2 predicted SST updated every 24-h during model integration (CFS_BC). Detailed formulations for CTL and CFS_BC can be found in Appendix A.

All experiments span the fall and winter of 2013-14 and are initialized every 24 h starting 1 Sep 2013 and ending 28 Feb 2014. Over the experiment period, the MJO was weak or non-existent (Climate Prediction Center; http://www.cpc.ncep.noaa.gov/products/precip/CWlink/MJO/whindex.shtml) and ENSO neutral conditions persisted (Earth System Research Laboratory; http://www.esrl.noaa.gov/psd/enso/mei).

Correspondence to: Christopher Melhauser, IMSG at Environmental Modeling Center, NOAA/NWS/NCEP, 5830 University Research Court, College Park, MD; E-mail: christopher.melhauser@noaa.gov.

The forecast skill for 2-m temperature and accumulated precipitation are evaluated using a tercile (below-normal, normal, or above-normal with random chance being ⅓) probabilistic Heidke Skill Score (HKSS; *e.g.*, Wilks, 2011). The 2-m temperature is verified for land only against the 00 UTC GDAS analysis and the accumulated precipitation is verified for land only against the 00 UTC NCEP Climatologically Calibrated Precipitation Analysis (CCPA; Hou *et al.*, 2014) averaged or accumulated over days 8-14 (week 2) and days 15-28 (weeks 3 & 4).

The MJO is evaluated using the traditional real-time multivariate MJO (*i.e.* RMM) index (WH index; Wheeler and Hendon 2004, Gottschalck *et al.* 2010). The MJO forecast skill is defined as the bivariate anomaly correlation between the analysis and forecast RMM1 and RMM2. The long term climatology is calculated from the NCEP/NCAR Reanalysis 1 (http://www.esrl.noaa.gov/psd/data/gridded/data.ncep.reanalysis.html) and NCAR Interpolated Outgoing Longwave Radiation (http://www. esrl.noaa.gov/psd/data/gridded/data.interp_OLR.html) for the period of 1981-2010. The long term mean and average of the previous 120 days are removed from the forecast to eliminate long-term trends and seasonal variability.

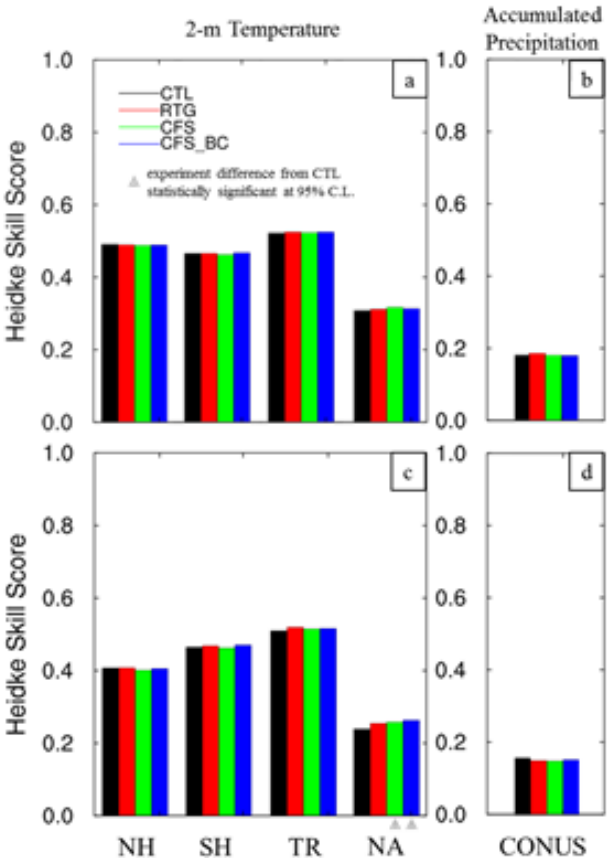

Fig. 1 Regional Heidke Skill Score for CTL (black), RTG (red), CFS (green), and CFS_BC (blue) calculated for week 2 (top row) and week 3 & 4 (bottom row) for 2-m temperature (a, c) and accumulated precipitation (b, d) averaged over the 6-month experiment period. The gray triangle indicates the difference of an experiment from CTL is statistically significant at the 95% confidence level.

3. Results and discussion

3.1 2-m temperature forecast skill

Over the fall and winter of 2013-14, the global land only 2-m temperature HKSS is regionally and lead time dependent. The tropics (TR) have the highest HKSS for both week 2 (Fig. 1a) and weeks 3 & 4 (Fig. 1b) with N. America (NA) having the lowest. Comparing between week 2 and weeks 3 & 4, the HKSS remains similar for the tropics and Southern Hemisphere (SH) with the Northern Hemisphere (NH) and NA dropping ~0.1-0.2. Within each region, the forecast skill for the SST forcing experiments is generally statistically indifferent from CTL for both week 2 and weeks 3 & 4. Both CFS and CFS_BC show a statistically significant improvement during weeks 3 & 4 over NA. It is interesting that RTG does not have a significant improvement over any land region compared to the other experiments, given this experiment is being forced the SST analysis. This suggests that there may be deficiencies in the forecast model which are limiting the spread of information from the ocean boundary to atmospheric land areas and the climatology of the SST analysis is most likely different than that of the model.

3.2 Accumulated precipitation forecast skill - CONUS

The CONUS accumulated precipitation HKSS shows no statistically significant difference between CTL and RTG, CFS, or CFS_BC for week 1 (not shown), week 2 (Fig. 1b), or weeks 3 & 4 (Fig. 1d). The magnitude of the HKSS falls off drastically after week 1 - approx. 0.55 at lead day 1 and 0.25 by lead day 7 (die off curves not shown). The aggregate accumulated week 2 HKSS is slightly higher than week 3 & 4, but overall, the results suggest minimal skill with the current model configurations, regardless of SST forcing.

3.3. MJO forecast skill

The forecast skill of MJO is a key metric when evaluating the capability of operational models for subseasonal forecasts (Kim *et al.* 2014; Shelly *et al.* 2014; Ling *et al.* 2014; Xiang *et al.* 2015). The MJO forecast skill in the operational version of GEFS is ~14.6 days (defined as the lead time when the bivariate anomaly correlation coefficient drops to 0.5) during the experimental period (Fig. 2). After week 2, MJO forecast skill quickly drops. Changing the prescribed SST to be closer to observations (RTG), the MJO forecast skill was improved up to ~2 days. For the weeks 3 & 4 range, the most skillful SST forcing is RTG with the CFS_BC being the most skillful scheme that could be practically used in operations. This implies that the MJO prediction skill is related to the accuracy of the representation of the SST. Therefore, without changing the model, it is found that improving the SST may potentially lead to an increase of the MJO skill.

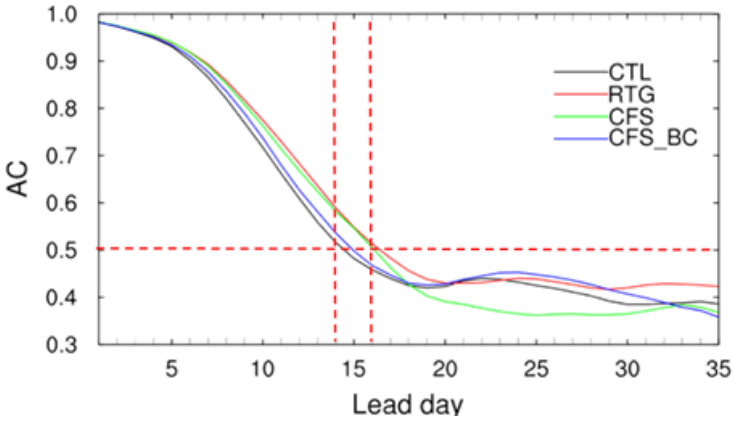

Fig. 2 MJO forecast skill (*i.e.* bivariate correlation between ensemble mean forecast and analysis data) as a function of lead time for the period of September 1, 2013 - February 28, 2014.

4. Summary

The NCEP GEFS is being extended from 16 to 35 days to cover the subseasonal forecast period. The impact of SST forcing on the extended range land only global 2-m temperature, CONUS accumulated precipitation, and MJO indices forecast skill were examined using various SST forcing configurations.

Extending the GEFS showed forecast skill over weeks 3 & 4 for temperature, but minimal to no skill for accumulated precipitation. Forcing the GEFS with an optimal SST configuration showed minimal to no improvement in land only 2-m temperature and accumulated precipitation. Minimal improvements using more realistic SST over the current operational SST configuration were found when validating over the Tropics, Northern Hemisphere, Southern Hemisphere, and North America. The bias corrected CFS_BC SST performed the best over NA with statistically significant improvements for 2-m temperatures. The minimal differences in skill between SST forcing experiments suggests that systematic model errors dominate at the extended period with model boundary condition forcing having a secondary impact. The MJO skill in operational GEFS is 14.6 days. Using more realistic SST (RTG, CFS, and CFS_BC), MJO skill increase by 10%.

Observations indicate that the fall and winter of 2013-14 has a generally weak MJO. Future work will focus on a two-year span that covers a stronger MJO period spanning 1 May 2014 to 31 May 2016 providing insight into the predictability from strong MJO and its relationship with 2-m temperature and CONUS accumulated precipitation from global teleconnections.

This summary is a subset from a study in preparation for publication (Zhu *et al.* 2017).

APPENDIX

SST Forcing Calculations

Operational GEFS SST Forcing (CTL)

The GEFS v11 operational SST forcing uses a 90-day e-folding of the RTG analysis at initialization, relaxed to climatology, calculated as

$$\mathrm{SST}_f^t = \left[\mathrm{SST}_a^{t_0} - \mathrm{SST}_c^{t_0}\right] e^{-(t-t_0)/90} + \mathrm{SST}_c^t$$

where *f* is the forecast, *a* the analysis, *c* is climatology, *t* is forecast lead time, and t_0 is the initial time.

Bias Corrected CFSv2 Predicted SST Forcing (CFS_BC)

The CFS_BC SST forcing is a hybrid of a persisted RTG anomaly at short lead times and bias corrected CFSv2 predicted SST at longer lead times. The CFSv2 predicted SST is bias corrected using both the CFSR climatology and CFSv2 model climatology. The persisted RTG anomaly is linearly combined with the bias corrected CFSv2 predicted SST over the 35 d period, calculated as

$$\mathrm{SST}_f^t = (1-w)\left[\mathrm{SST}_a^{t_0} - \mathrm{SST}_{cfsrc}^{t_0} + \mathrm{SST}_{cfsrc}^{t}\right] + w\left[\mathrm{SST}_{cfs}^{t} - \left(\mathrm{SST}_{cfs\_c}^{t} - \mathrm{SST}_{cfsrc}^{t}\right)\right]$$

where *f* is the forecast, a the analysis, *cfsrc* is the CFSR reanalysis climatology, *cfs* is the CFSv2 model forecast, *cfs_c* is the CFSv2 model climatology, *t* is forecast lead time, t_0 is the initial time, and *w* is defined as

$$w = (t - t_0)/35$$

References

Gates, W. and coauthors, 1999: An overview of the results of the Atmospheric Model Intercomparison Project (AMIP I). *Bull. Amer. Meteor. Soc.*, **80**, 29–55, doi: 10.1175/1520-0477(1999)080<0029:AOOTRO>2.0.CO;2.

Gottschalck, J., and Coauthors, 2010: A framework for assessing operational Madden–Julian oscillation forecasts: A CLIVAR MJO working group project. *Bull. Amer. Meteor. Soc.*, **91**, 1247–1258, doi:10.1175/2010BAMS2816.1.

Han, J. and H. Pan, 2011: Revision of convection and vertical diffusion schemes in the NCEP Global Forecast System. *Wea. Forecasting*, **26**, 520–533, doi: 10.1175/WAF-D-10-05038.1.

Hou, D., M. charles, Y. Luo, Z. Toth, Y. Zhu, R. Krzysztofowicz, Y. Lin, P. Xie, D. Seo, M. Pena, and B. Cui, 2014: Climatology-calibrated precipitation analysis at fine scales: Statistical adjustment of stage IV toward CPC gauge-based analysis. *J. Hydrometeor.*, **15**, 2542–2557, doi: 10.1175/JHM-D-11-0140.1.

Juang, H., 2011: A multiconserving discretization with enthalpy as a thermodynamic prognostic variable in generalized hybrid vertical coordinates for the NCEP Global Forecast System. *Mon. Wea. Rev.*, **139**, 1583–1607, doi: 10.1175/2010MWR3295.1.

Juang, H., 2014: A discretization of deep-atmospheric nonhydrostatic dynamics on generalized hybrid vertical coordinates for NCEP Global Spectral Model. NCEP Office Note 477, doi:10.7289/V5G73BM6.

Kim, H.-M., P. J. Webster, V. E. Toma, and D. Kim, 2014: Predictability and prediction skill of the MJO in two operational forecasting systems. *J. Climate*, **27**, 5364–5378, doi:10.1175/JCLI-D-13-00480.1.

Kleist, D. and K. Ide, 2015: An OSSE-based evaluation of hybrid variational–ensemble data assimilation for the NCEP GFS. Part II: 4DEnVar and hybrid variants. *Mon. Wea. Rev.*, **143**, 452–470, doi: 10.1175/MWR-D-13-00350.1.

Ling, J., P. Bauer, P. Bechtold, A. Beljaars, R. Forbes, F. Vitart, M. Ulate, and C. Zhang, 2014: Global versus local MJO forecast skill of the ECMWF model during DYNAMO. *Mon. Wea. Rev.*, **142**, 2228–2247, doi:10.1175/MWR-D-13-00292.1.

Madden, R. and P. Julian, 1971: Detection of a 40–50 day oscillation in the zonal wind in the tropical Pacific. *J. Atmos. Sci.*, **28**, 702–708, doi: 10.1175/1520-0469(1971)028<0702:DOADOI>2.0.CO;2.

Saha, S. and co-authors, 2006: The NCEP Climate Forecast System. *J. Climate*, **19**, 3483–3517, doi: 10.1175/JCLI3812.1.

Saha, S. and co-authors, 2010: The NCEP Climate Forecast System Reanalysis. *Bull. Amer. Meteor. Soc.*, **91**, 1015–1057, doi: 10.1175/2010BAMS3001.1.

Saha, S. and co-authors, 2014: The NCEP Climate Forecast System Version 2. *J. Climate*, **27**, 2185–2208, doi: 10.1175/JCLI-D-12-00823.1.

Shelly, A., P. Xavier, D. Copsey, T. Johns, J. M. Rodr´ıguez, S. Milton, and N. Klingaman, 2014: Coupled versus uncoupled hindcast simulations of the Madden-Julian Oscillation in the Year of Tropical Convection. *Geophys. Res. Lett.*, **41**, 5670–5677, doi:10.1002/2013GL059062.

Wang, X., D. Parrish, D. Kleist, and J. Whitaker, 2013: GSI 3DVar-based ensemble–variational hybrid data assimilation for NCEP Global Forecast System: Single-resolution experiments. *Mon. Wea. Rev.*, **141**, 4098–4117, doi: 10.1175/MWR-D-12-00141.1.

Wheeler, M.C and H. H. Hendon, 2004: An all-season real-time multivariate MJO index: Development of an index for monitoring and prediction. *Mon. Wea. Rev.*, **132**: 1917–1932, doi: 10.1175/1520-0493(2004)132<1917:AARMMI>2.0.CO;2.

Whitaker, J., T. Hamill, X. Wei, Y. Song, and Z. Toth, 2008: Ensemble data assimilation with the NCEP Global Forecast System. *Mon. Wea. Rev.*, **136**, 463–482, doi: 10.1175/2007MWR2018.1.

Wilks, D.S., 2011: Statistical methods in the atmospheric sciences. *Academic press*. Vol. 100, ISBN: 978-0-12-385022-5.

Xiang, B., M. Zhao, X. Jiang, S.-J. Lin, T. Li, X. Fu, and G. Vecchi, 2015: The 3–4-week MJO prediction skill in a GFDL coupled model. *J. Climate*, **28**, 5351–5364, doi:10.1175/JCLI-D-15-0102.1.

Zhu, Y., X. Zhou, M. Pena, W. Li, C. Melhauser, and D. Hou, 2017: Design and evaluation of sea surface temperature forcing on week 3&4 forecast skill using the NCEP Global Ensemble Forecasting System. *Wea. Forecasting*, in preparation.

Science and Technology Infusion Climate Bulletin
NOAA's National Weather Service
41st NOAA Annual Climate Diagnostics and Prediction Workshop
Orono, ME, 3-6 October 2016

Improved Climate Prediction Services for Australia

Robyn Duell, David Jones, Oscar Alves, and Andrew Watkins
Australian Bureau of Meteorology

The Bureau of Meteorology (the Bureau) has recently upgraded its climate prediction service. This upgrade focussed on improving user satisfaction and comprehension, and included a move from a statistical forecast system to a dynamical climate model (the Predictive Ocean Atmosphere Model for Australia - POAMA). Further substantial improvements to the service are now underway as a result of investment by the Australian Government and support from agricultural research and development groups.

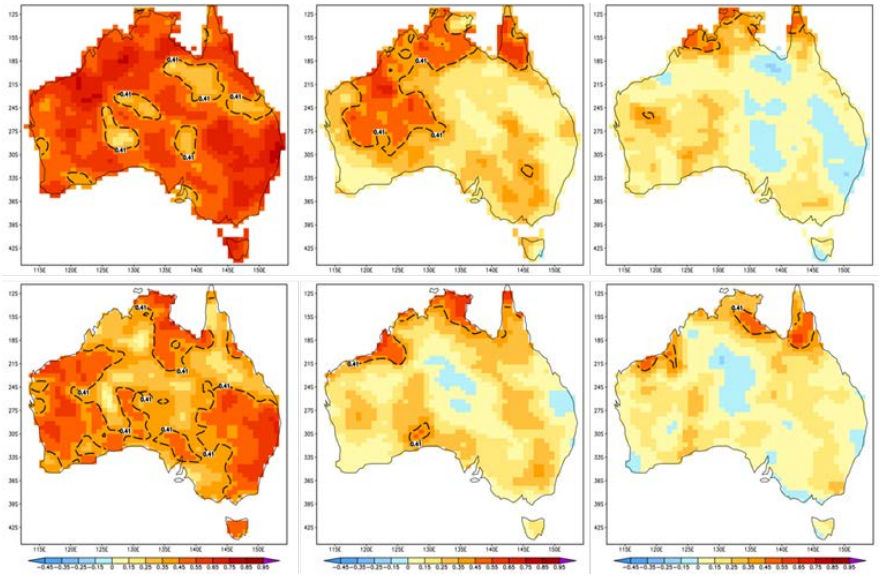

Fig. 1 Correlation skill for rainfall for ACCESS-S1 (top) and POAMA (bottom) for Week 1+2 (left), Week 2+3 (middle) and Week 3+4 (right).

These new improvements will be delivered to industry over the coming three years, and will include increasing model resolution, increasing model accuracy, issuing forecasts more frequently and issuing new weekly forecasts. The weekly forecasts will fill the gap between the Bureau's current seven day weather forecast and monthly and seasonal climate outlooks. For the first time the Bureau will be providing a service from days to weeks to months to seasons.

The new improvements have been made possible by the Bureau's recent purchase of a new Cray supercomputer and the introduction of a new modelling system (ACCESS-S, the Australian Community Climate and Earth–System Simulator – Seasonal) that is being developed in collaboration with the UK Met Office. Early analysis of the new modelling system over Australia indicates accuracy is significantly better than the current operational POAMA model on weekly timescales for rainfall (Fig.1) and temperature, and for minimum temperature on seasonal timescales. Similar skill to POAMA is achieved for rainfall and maximum temperature. ACCESS-S also outperforms POAMA for long lead predictions of ENSO (Fig. 2). Future development will focus on improving data assimilation, reducing model systematic errors and introducing a calibration component, all of which are expected to further

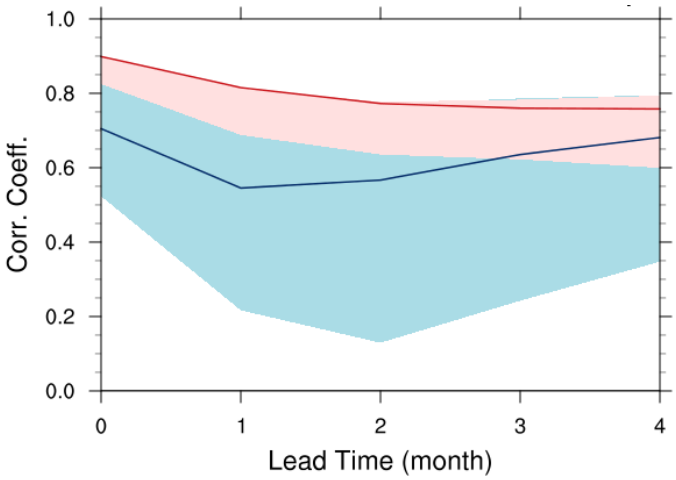

Fig. 2 Correlation skill for Niño3, initialized on 1 May.

Correspondence to: Robyn Duell, Australian Bureau of Meteorology, Melbourne, Australia;
E-mail: robyn.duell@bom.gov.au

increase model skill.

In addition to the introduction of a new modelling system, the improved service will also include changes in the communication and presentation of the model outputs, making outlooks more tailored to suit user needs.

The improved service will deliver better intelligence to Australian industry that will improve management of climate risks in Australia. Details of recent and upcoming service improvements were presented.

Visit the Bureau’s climate outlook service on the web: www.bom.gov.au/climate/ahead

Science and Technology Infusion Climate Bulletin
NOAA's National Weather Service
41st NOAA Annual Climate Diagnostics and Prediction Workshop
Orono, ME, 3-6 October 2016

Status of Week 3-4 Activities at the Climate Prediction Center

Jon Gottschalck[1], Adam Allgood[1], Steve Baxter[1], Muthu Chelliah[1], Dan Collins[1], Dan Harnos[1], Luke He[1], Michelle L'Heureux[1], Kyle MacRitchie[1,2], Peitao Peng[1], Matt Rosencrans[1], Augustin Vintzileos[3], and Qin Zhang[1]

[1]*Climate Prediction Center, NOAA/NWS/NCEP, College Park, Maryland*
[2]*Innovim LLC., Greenbelt, Maryland*
[3]*University of Maryland - ESSIC/CISC-MD*

The Week 3-4 outlook period is within a time range that primarily no longer benefits from predictability due to atmospheric initial conditions (*i.e.*, Week-2) and is at times in a range too short to reliably benefit from slowly evolving parts of the climate system (ocean, land, *etc.*) known to aid longer time scale prediction (monthly to seasonal outlooks). Consequently, the Week 3-4 time range often suffers from low predictability and it is important to understand this limitation to manage expectations for potential forecast skill. This article describes the current status of this activity at the Climate Prediction Center. The initial experimental product format is outlined followed by the current input to the experimental outlooks. Verification of the first year of experimental outlooks and user survey feedback to date is also described along with current development work.

The experimental product is released once per week every Friday at approximately 3 PM Eastern Time (ET). The first experimental outlook was released on September 18, 2015 and the outlooks have continued in realtime to present each week. The product package consists of two outlook maps and a text discussion describing the forecast rationale and challenges or issues of the current forecast. The outlooks maps (Figure 1) display the forecast probabilities of the favored category (above or below average) for the two-week period mean temperature and total precipitation. The purpose of the product is to (1) provide an outlook for mean temperature / total precipitation for the current Week 3-4 outlook gap and (2) provide advance notice of potential large-scale pattern changes to assist decision makers.

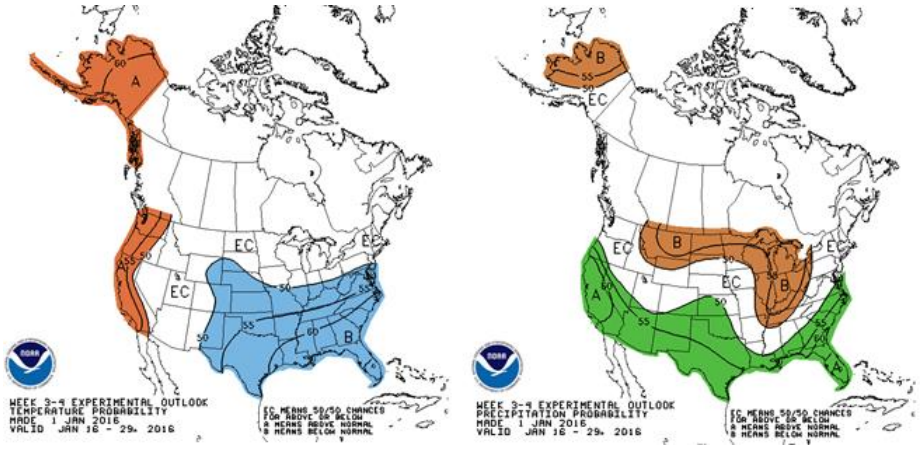

Fig. 1 Forecast maps for the experimental product released on January 1, 2016. The shading depicts the favored category (blue/orange or brown/green for below/above average temperature or precipitation respectively. The contours represent the probabilities of the favored category. The white areas (labeled EC for equal chances) are regions where forecast signals are weak and each forecast category (above or below) are equally likely.

The input that contributes to the outlooks are somewhat diverse and includes utilizing relationships associated the Madden Julian Oscillation (MJO). These include connections between MJO strength and phase and North America temperature and precipitation patterns as well as lead-lag relationships to important higher latitude variability such as the Arctic Oscillation (AO) or North Atlantic Oscillation (NAO). Statistical

Correspondence to: Jon Gottschalck, Climate Prediction Center, NOAA/NWS/NCEP, 5830 University Research Court, College Park, MD; E-mail: Jon.Gottschalck@noaa.gov

guidance used in the forecast process includes (1) a MJO-ENSO phase model (Johnson et al. 2014), (2) a Multiple Linear Regression model that uses daily Nino3.4 index information, MJO indices and linear trends as predictors for Week 3-4 temperature and precipitation (Harnos *et al*. 2016) and (3) constructed analogues based on 200-hPa streamfunction to construct a forecast objectively based on closely matching analogues. The Coupled Linear Inverse Model (C-LIM), developed at the Earth System Research Laboratory (ESRL), tropical forecast is used to serve as a complement to dynamical model tropical forecasts (Newman et al. 2009) as well.

Available dynamical model guidance plays an important role in the outlook. Output from the NCEP Climate Forecast System (CFS), the European Centre for Medium Range Weather Forecasts (ECMWF) and the Japan Meteorological Agency (JMA) modeling systems is available to the forecaster for several variables including 500-hPa and 200-hPa height, temperature and precipitation. The model data is bias corrected based on available reforecasts for systematic errors across all forecast lead times.

Figure 2 shows the verification of the experimental outlooks during the first year of release. For temperature, the forecast skill has nearly been entirely positive throughout the period, although high variability in the scores from week to week do exist at times. The average Heidke Skill Score (HSS) over the period is +55. On average, the precipitation forecasts have demonstrated little forecast skill with an average HSS of +3 over the period, although there have been periods of positive skill during individual weeks.

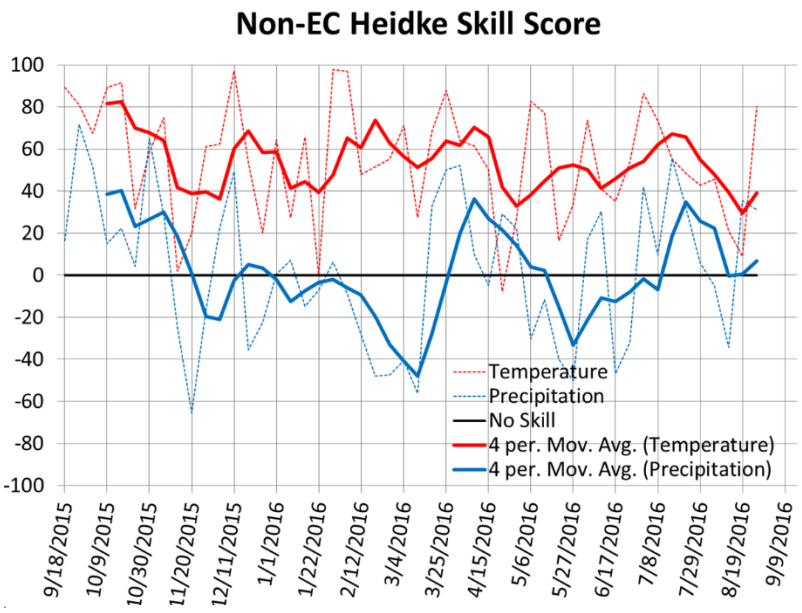

Fig. 2 Time series of Heidke Skill Score (HSS) for the period from September 18, 2015 through August 26, 2016. The red/blue lines represent temperature and precipitation respectively and the solid lines show monthly running means.

The Climate Prediction Center has collected comments on the experimental product package (outlook maps and a text discussion) over the past year. It is the interpretation of CPC from these survey results that the experimental product package has been received positively overall. Survey questions where a quantitative response was requested (ranking from 1 to 10 with 10 being highest) focused on two areas, (1) technical quality of the product/service (e.g. forecast accuracy, timeliness, problems with display) and (2) how easy you found the product/service to interpret or use. The results indicated an average score for both questions of just below 8. In addition, when asked whether the National Weather Service (NWS) should prepare and release this type of product, 95% of the respondents answered yes. See Figure 3.

Work on the project over the next year will include the migration of the current experimental forecast tool suite to operational platforms to ensure reliability. We also plan to obtain, process and include in the forecast tool suite dynamical model output from Environment Canada, apply additional post processing strategies to the dynamical model forecasts as well as explore additional statistical methods for forecast tool development including objective consolidation strategies. CPC also plans to continue to collaboratively interface with partners on other initiatives targeting this time period.

In summary, CPC began issuing experimental Week 3-4 temperature and precipitation outlooks in September 2015. A two-stream approach in tool development is being used with work targeting both

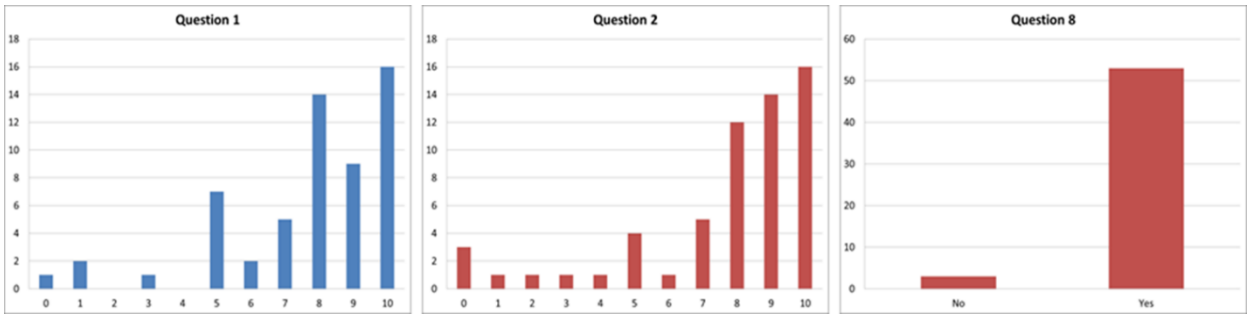

Fig. 3 Survey results to date with the number of respondents on the x-axis and the ranking from 1-10 on the y-axis. The specific questions for each chart are outlined in the text.

dynamical model guidance and statistical forecast tools. Forecasts of opportunity are likely to serve as the backbone of product. On average, skill scores to date for temperature have been positive while no consistent forecast skill has been demonstrated for precipitation. Available stakeholder feedback has generally been positive to date. CPC will continue to leverage other resources from other initiatives where possible to improve our understanding at this forecast time scale as well as to build upon current experimental services.

References

Johnson, N., A.C. Collins, S.B. Feldstein, M.L. L'Heureux, and E.E. Riddle, 2014: Skillful wintertime North American temperature forecasts out to 4 weeks based on the state of ENSO and the MJO. *Wea. Forecasting*, **29**, 23-38.

Harnos, D., N. Johnson, S. Baxter, M. L'Heureux, and A. Allgood, 2016: Combined ENSO, MJO, and trend influences on temperature and precipitation for probabilistic weeks 3 and 4 forecasts. *7th NOAA Testbeds & Proving Grounds Workshop*, College Park, MD, Session II Science Theme Paper 6. [Available online at http://www.testbeds.noaa.gov/events/2016/workshop/agenda.html]

Newman, M., P.D. Sardeshmukh, C. Penland, 2009: How important is air-sea coupling in ENSO and MJO evolution? *J. Climate*, **22**, 2958–2977.

Science and Technology Infusion Climate Bulletin
NOAA's National Weather Service
41st NOAA Annual Climate Diagnostics and Prediction Workshop
Orono, ME, 3-6 October 2016

Assessment of Ensemble Regression to Combine and Weight Seasonal Forecasts from Multiple Models of the NMME

Dan C. Collins
Climate Prediction Center, NOAA/NWS/NCEP, College Park, Maryland

1. Introduction

Ensemble and multi-model ensemble prediction systems have become state-of-art tools for climate forecasts on subseasonal and seasonal timescales. Ensemble prediction systems are meant to identify the forced climate signal, through generation of multiple realizations of the forecast, the differences of which can be attributable to uncertainty in the outcome due to the chaotic nature of the climate system. From ensemble predictions, it is possible to derive the probability of uncertain future events. The use of several models in a multi-model ensemble (MME) is known to improve on the forecasts of a single model ensemble, through the chance cancellation of individual model errors (Becker *et al.*, 2014; Kirtman *et al.*, 2014). The North American Multi-Model Ensemble (NMME) has been used as guidance for real-time seasonal forecasts by the Climate Prediction Center since August of 2011. Hindcasts over multiple years can be used to identify and correct the systematic biases of each model system. However, in addition to model biases, it is possible to discern the skill of each model as a function of region and season. Identifying models and regions of lower and higher skill, and utilizing this information to combine and weight the forecasts, should improve the skill of probabilistic forecasts. We seek to intelligently combine models to extract forced signals from the NMME and eliminate poor forecasts when possible.

2. Methodology and data

In this study, NMME seasonal forecasts for North America are calibrated and consolidated using a regression methodology to improve the reliability of probabilities and weight individual models according to their skill. Calibration entails relating the probabilities determined from an ensemble of forecasts to the skill of the forecast system, such that probabilities assigned are a reliable representation of the expected frequency of an event's occurrence. Reliable probabilities are considered skillful when they also resolve differences between cases with high and low probabilities. The spread of ensemble members should inform the probabilities of events, though models can be unreliable in representing the actual frequency of events.

Regression is widely used for correction of dynamical model forecasts and has been successfully applied at the Climate Prediction Center to dynamical model forecasts of temperature and precipitation for subseasonal lead times from 2 to 4 weeks. In this study, we apply the ensemble regression (EREG) method to NMME seasonal forecasts (Unger *et al.*, 2009). EREG retains the ensemble spread to represent conditional uncertainty of forecasts, to the extent that spread is found to be a reliable indicator of the average mean square error of a model's forecasts. EREG uses the expected value of the mean square error of hindcasts to adjust the model probability density function (PDF) and improve the reliability of probabilistic forecasts – collapsing the spread when either skill is low, or spread is a poor indicator of skill. EREG maintains the resolution of categorical forecasts, when the model spread is a good indicator of skill, while minimizing the mean square error of the ensemble mean.

Initially, each NMME model is calibrated individually using the EREG methodology. To combine the individual EREG-corrected model forecasts, we test two possible methods: 1. Combinations with no further adjustment of the MME PDF such that regressed model anomalies are weighted by their correlation to observations; and 2. Combinations with additional weighting of each individual model probability by its correlation to observations. The ensemble regression technique is compared to forecasts made by estimating the probability from the count of ensemble members (CE) in each category after bias corrections of model means and variances. Forecasts are verified using the Brier skill score (BSS), as well as assessed for reliability.

Correspondence to: Dan C. Collins, Climate Prediction Center, NOAA/NWS/NCEP, 5830 University Research Court, College Park, MD; E-mail: dan.collins@noaa.gov

For this study, we test calibration and weighting using the November 1st initializations from the model hindcasts for predictions of DJF Temperature, *i.e.*, lead-1 winter forecasts. Hindcasts are available from DJF 1982-83 to DJF 2010-11. GHCN and CAMS 2-m temperature observations are used for verification. We consider the skill and calibration of probability forecasts for terciles (above-normal, below-normal and near-normal, defined as the lower-third, mid-third and upper-third, respectively, of the climatological distribution for the 1982-2011 period). Extreme, above-normal and below-normal, seasonal forecasts at the 10th and 90th percentile respectively, consistent with the tercile forecasts, were also derived but are not shown in this study. The regression-calibration EREG methodology follows Unger *et al.*, 2009, "Ensemble regression". All statistics – the climatologies of model and observational seasonal mean and variances, as well as correlations, reliability and BSS – were cross-validated using a leave-1-year-out methodology, such that dependent data used in training the regression were independent of the verification.

3. Results

The baseline methodology that combines individual model counts of ensemble (CE) members to generate probability forecasts, after bias and variance corrections, indicates that models with regions of poor skill deteriorate the skill of the NMME when models are combined. Figure 1 shows the Brier skill scores for the CFS on the left and the combined NMME on the right, using the CE method to indicate probabilities. Note that in parts of the eastern US, skill in the CFS is higher than the combined NMME.

By calibrating probabilities from the individual models of the NMME using ensemble regression (EREG), models with areas of negative or zero skill are effectively removed from the final NMME forecast, improving

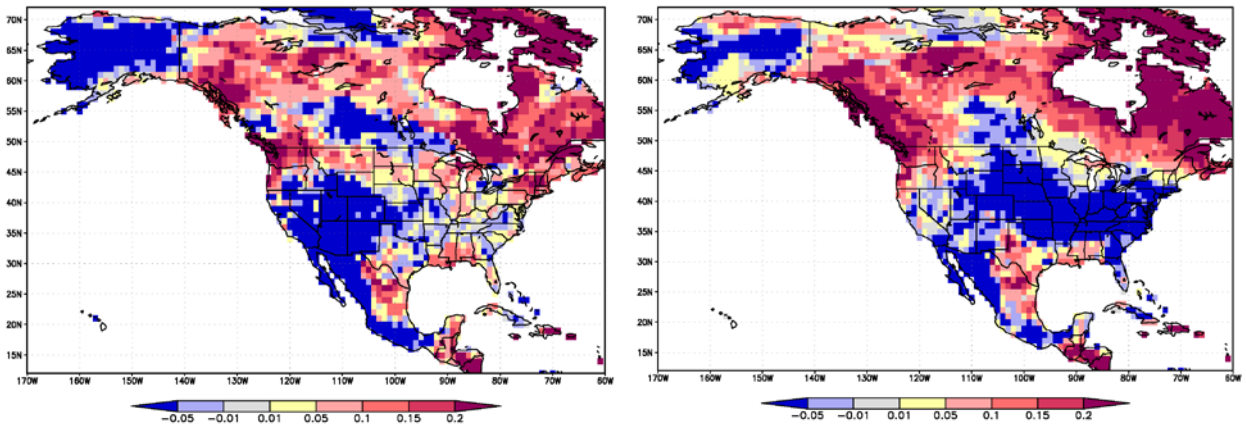

Fig. 1 Cross-validated Brier skill scores at each grid point for the uncalibrated count of ensemble members from the CFS (left) and for the combined NMME (right). Negative skill is depicted in blue.

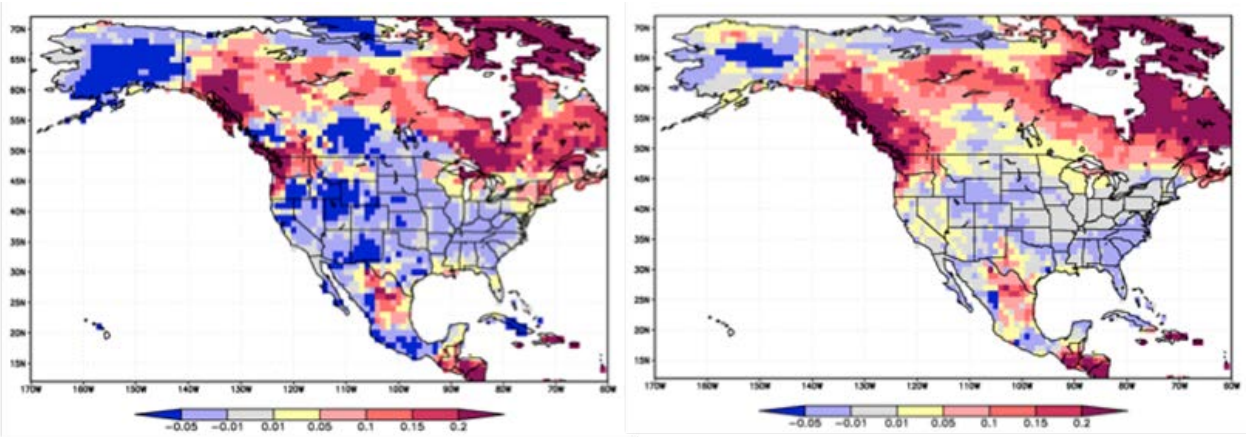

Fig. 2 Cross-validated Brier skill scores at each grid point for the EREG calibrated CFS (left) and for the combined NMME (right). Negative skill is depicted in blue.

the combined skill. Figure 2 shows the Brier skill scores for the CFS and NMME as in Figure 1, but for the EREG-calibrated probabilities. The consolidated NMME forecast improves upon the skill of the CFS alone in nearly all regions.

Using counts of ensemble members, individual models of the NMME are found to be under-dispersive or over-confident, while calibrating probability forecasts using ensemble regression produces more reliable forecast probabilities (Figure 3). It is shown that the calibrated probabilities using EREG are an improvement over CE for almost all individual models (Figure 4). However, the Brier skill score of the combined EREG-calibrated NMME is only a slight improvement over the Brier of the combined CE model probabilities. The combined calibrated forecasts are found to be slightly under-confident (Figure 3). Further work is needed to account for the additional skill obtained from combining multiple models to obtain a calibrated NMME forecast.

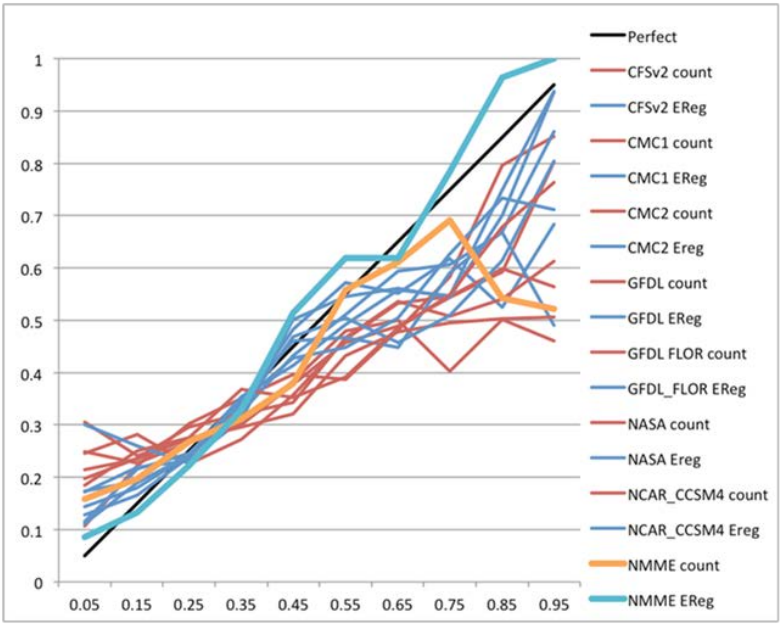

Fig. 3 Reliability diagram showing all models for the count of ensemble members (red) and EREG-calibrated probabilities (blue), reliability of the combined NMME count of ensembles (orange) and NMME EREG probabilities (cyan).

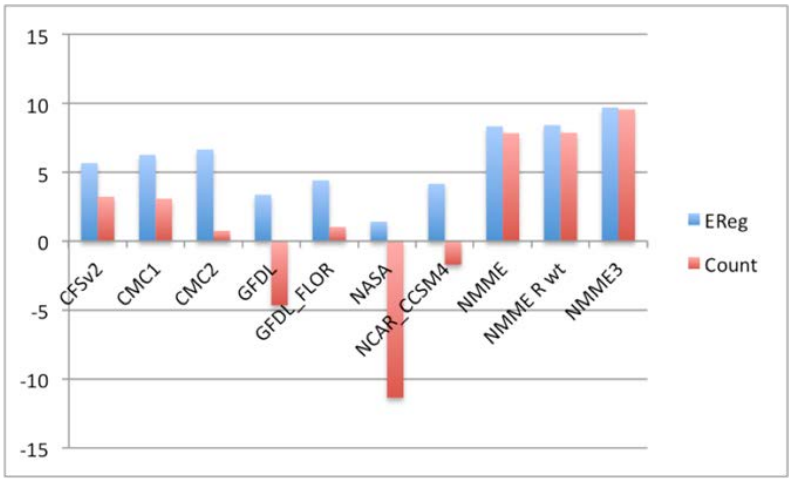

Fig. 4 Average Brier skill scores (in percent) over North America for individual models, the combined NMME, correlation-weighted NMME (NMME R wt), and a 3-model NMME (NMME3), for the count of ensemble members (red) and EREG calibrated probabilities (blue).

4. Summary and conclusions

It is found that ensemble regression (EREG) for individual model forecasts is often an improvement on counts of ensembles (CE) and climatology forecasts. Also, use of EREG to combine and weight models of the NMME virtually removes individual models in areas and seasons with no skill, improving the NMME forecast skill.

In the winter season (DJF) lead-1 temperature forecasts, skill is not significantly changed by weighting models using correlation in the seasonal NMME system beyond initial gains from regression. Skill for correlation-weighted model probabilities in Figure 4 ("NMME R wt") is nearly identical to the combined calibrated model forecasts without additional weighting of probabilities. It is noteworthy that regression effectively weights the anomalies of each model by its correlation to observations, prior to calculation of probabilities. This produces improvements in both the individual model Brier skill scores and the combined NMME skill over counts of ensemble members. Further analyses showed that the results are generally true for other seasons. Selecting and combining the three models with the highest average cross-validated skill (see far right bars of Figure 4), skill of a 3-model MME

is greater than the full NMME. This suggests that evidence-based selection of models might be used to optimize skill.

References

Becker, E., H. van den Dool, and Q. Zhang, 2014: Predictability and forecast skill in NMME. *J. Climate*, **27**, 5891-5906.

Kirtman, B. P., and Coauthors, 2014: The North American multimodel ensemble: phase-1 seasonal-to-interannual prediction; phase-2 toward developing intraseasonal prediction. *Bull. Amer. Meteor. Soc.*, **95**, 585-601.

Unger, D. A., and Coauthors, 2009: Ensemble regression. *Mon. Wea. Rev*. **137**, 2365-2379.

Science and Technology Infusion Climate Bulletin
NOAA's National Weather Service
41st NOAA Annual Climate Diagnostics and Prediction Workshop
Orono, ME, 3-6 October 2016

Evaluation of an NMME-based Hybrid Prediction System for Eastern North Pacific Basin Tropical Cyclones

Christina Finan[1, 2], Hui Wang[1], and Jae-Kyung Schemm[1]
[1]*Climate Prediction Center, NOAA/NWS/NCEP, College Park, Maryland*
[2]*Innovim LLC., Greenbelt, Maryland*

Based on the previously developed model for the prediction of the Atlantic seasonal hurricane activity, the hybrid dynamical-statistical model utilizing the North American Multi-model Ensemble (NMME) has been expanded to predict hurricane activity for eastern North Pacific basin in further support of the NOAA's Hurricane Seasonal Outlook from the Climate Prediction Center (CPC). A hybrid dynamical-statistical model was first developed for the Atlantic using multiple linear regression relationships derived from forecasts and hindcasts with the NCEP Climate Forecast System v. 2 (CFSv2) and observational datasets (Wang *et al.* 2009). This project uses the data available through the NMME experiment, both real-time forecasts and hindcasts, which has shown that an ensemble approach improves skill over the individual CFSv2 system (Kirtman *et al.* 2014).

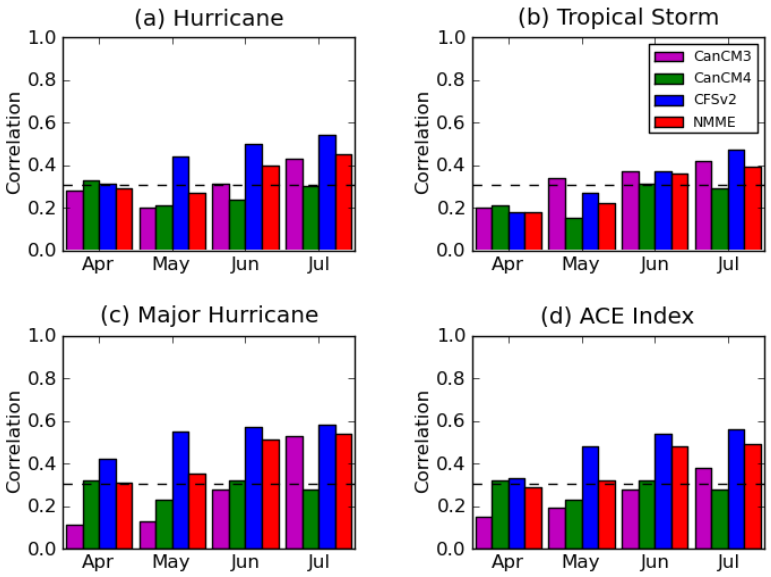

Fig 1 Hindcast prediction correlations for the eastern North Pacific basin for the four predictands: (a) hurricanes, (b) tropical storms, (c) major hurricanes and (d) the ACE index. Each model's (CFSv2, CanCM3/4, CCSM4) hindcast and the NMME hindcast using initialization months April through July were correlated with observed values are averaged over the 1982-2010 period. The dashed line denotes the 95% significance level.

Predictand	CanCM3	CanCM4	CFSv2	NMME
Hurricane	2.80	2.74	2.77	2.66
Tropical Storm	4.03	3.99	4.03	3.92
Major Hurricane	2.36	2.24	2.13	2.15
ACE Index	55.69	52.60	51.86	51.88

Table 1. Hindcast RMSE for April initial conditions averaged over the 1982-2010 period. The NMME and CFSv2 are the two models with the lowest RMSE values.

For the eastern North Pacific tropical cyclone (TC) activity forecasts, the selected predictors are the averaged July – September wind shear forecasts over the central tropical Pacific (10°S-7.5°N, 165°E-135°W) and sea surface temperature forecasts over the central North Pacific (20-36°N, 165°E-135°W) from a suite of four global climate models (GCMs): the CFSv2, Canadian Centre for Climate Modeling and Analysis Climate Model Versions 3 and 4 (CanCM3, CanCM4) and the NCAR Community Climate System Model Version 4 (CCSM4). The anomalous forecasts for shear and SSTs are used in unique regression relationships, fitted for each individual model to produce forecasts for four predictands: anomalous number of tropical storms,

Correspondence to: Christina Finan, Climate Prediction Center, NOAA/NWS/NCEP, 5830 University Research Court, College Park, MD and Innovim LLC, Greenbelt, MD; E-mail: christina.finan@noaa.gov

hurricanes, major hurricanes and accumulated cyclone energy (ACE) index for the full hurricane season, June through November. The anomalies are calculated using each model's 1982-2010 hindcast climatology. The NMME forecasts are an equally weighted average of the four model's forecasts. The forecasts skill was cross-validated over the 1982-2010 period.

The anomaly correlations between hindcast and observed tropical cyclone (TC) activity are shown in Figure 1 for three of the individual models and the averaged NMME suite. The CCSM4 was removed from the NMME mean due to low correlations in the hindcast analysis. The CFSv2 has the highest skill across the suite, followed by the NMME. The NMME however, reduces the RMSE for two of the predictands, tropical storms and hurricanes, when compared to the three individual models (Table 1). For the other two predictands,

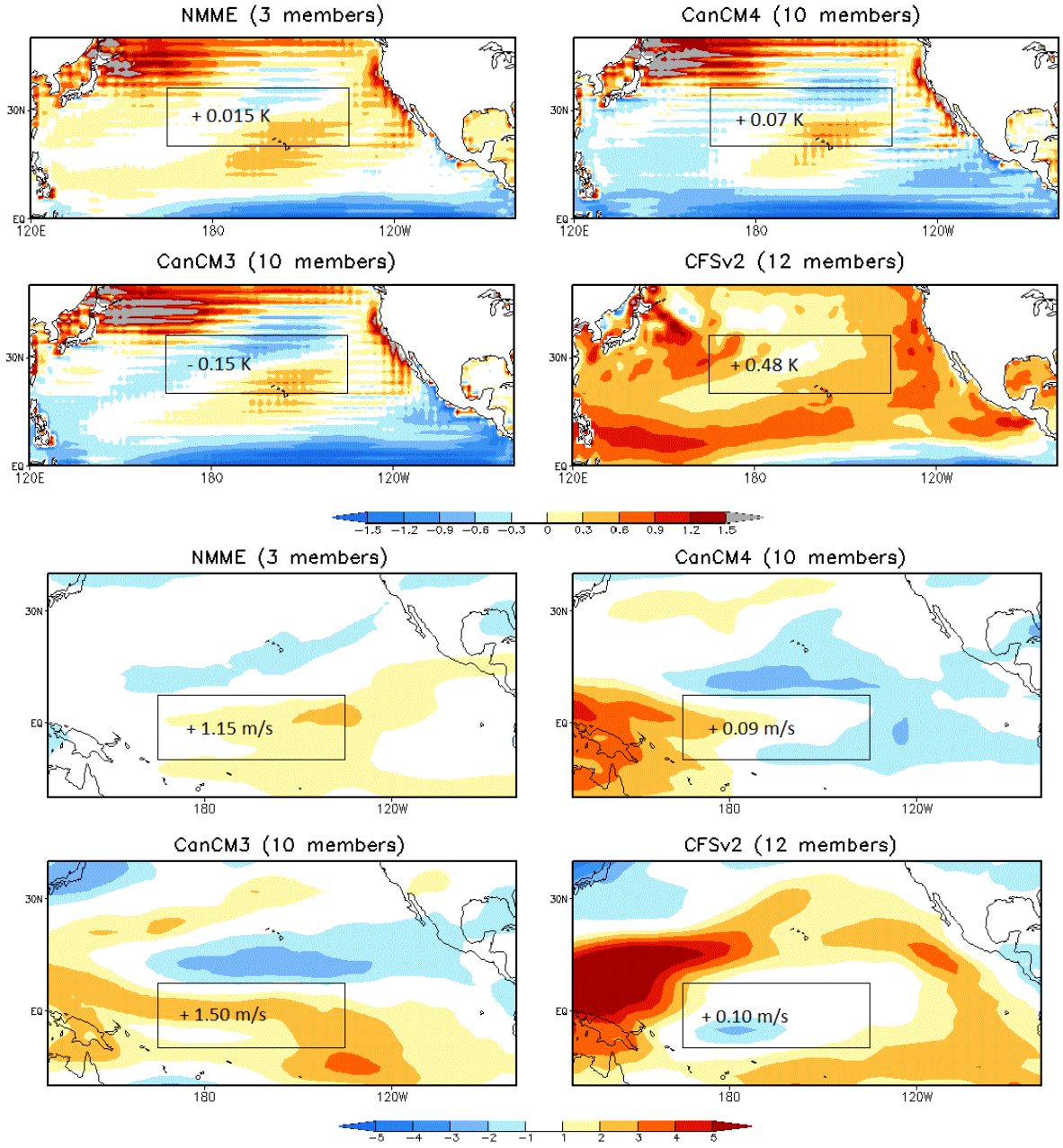

Fig 2. 2016 forecast of anomalous SST (a) and wind shear (b) for the July-September period from forecast runs with April 2016 initial conditions. The area of prediction is outlined and with area-averaged anomaly value displayed. This value was used as a predictor in the forecast, excluding the NMME suite mean. The NMME forecast is an equal-weighted average of each model's individual forecast.

the RMSE between CFSv2 and NMME are comparable. The hybrid model has the highest skill for the major hurricane predictand, followed by the ACE index.

The hybrid dynamical-statiscal model was tested in real-time, using the forecasts with April 2016 initial conditions from the CanCM3, CanCM4 and CFSv2 to predict for the 2016 eastern North Pacific hurriance season. The forecasts from the three individual models were averaged to create the NMME forecast for the 2016 season. The ensemble mean April 2016 forecasts of wind shear and SSTs from July to September are shown in Figure 2 for individual models, as well as for the NMME. The area of prediction used to construct the predictors is outlined in a black box, with the spatial average displayed. Both the CanCM3 and CanCM4 SST fields show warm anomalies in the central North Pacific, with cold anomalies to the north, while the CFSv2 SST field shows an overall warm signal for the North Pacific basin. The CFSv2 and CanCM4 wind shear fields show a slight enhancement, but mostly neutral signal for the central tropical Pacific, while the CanCM3 shows a stronger enhancement. The NMME averages for the SST field shows a near-normal forecast and the wind shear forecast is above-normal.

Table 2 details the forecasts from each individual model and the NMME averages, alongside the observations from the 2016 eastern North Pacific hurricane season. The CanCM3 and CanCM4 forecasted a near-normal season, as well as the NMME averaged forecast. The CFSv2 forecasted a below-normal season. For the eastern North Pacific, the 2016 hurricane season was classified as above-normal. All of the models underforecasted the 2016 season. The CanCM4 model was the closest in forecast, with a near-normal season on the top-end of the prescribed ranges for each predictand. The CFSv2, while performing the best in the hindcast evaluations, had the lowest performance in the real-time prediction. During the summer of 2016, the eastern Pacific was undergoing a shift in the ENSO cycle, after a record-high El Niño in 2015-16. Many of the models forecasted a shift to a La Niña phase duing the summer of 2016 in the Eastern Pacific (also seen in Fig. 2), which remained in a neutral state. The La Niña phase typically brings a near-normal or below-normal hurricane season to the Eastern Pacific, which could explain the underforecasted season by the models.

Variable	CanCM3	CanCM4	CFSv2	NMME	Observations
Hurricanes	7-9 (8)	8-9 (8)	5-7 (6)	6-8 (7)	12
Tropical Storms	13-15 (14)	15-16 (15)	11-14 (13)	13-15 (14)	18
Major Hurricanes	3-4 (3)	3-4 (4)	1-3 (2)	2 – 4 (3)	5
ACE	93-117 (105)	100-124 (112)	45-98 (71)	79 – 113 (96)	144

Table 2. The NMME-based hybrid prediction of the 2016 TC season over the ENP basin. The forecasted ranges are shown, with the average forecast in parentheses. The hybrid system with April ICs predicts a near-normal season. The observed totals of July – September 2016 fall into the above-normal ranges based on the basin climatology.

The hybrid statsical-dynamical model created for the eastern North Pacific basin showed skill over the hindcast period. Even though the CFSv2 showed more skill in the hindcasts than the NMME average, it showed the lowest skill overall in the real-time forecast for the 2016 season. Other models from the NMME project may be explored, as hindcast and variable datasets become available and are analyzed. Including more recent years in the training period for 2016 could also improve the forecasting skill, as three out of the five past years have been above average for TC activity in the eastern North Pacific. The NMME hybrid model is expected to continue to be of use in developing a comphrensive NOAA Hurricane Seasonal Outlook.

References

Kirtman, B. P., and Coauthors, 2014: The North American Multimodel Ensemble: Phase-1 seasonal-to-interannual prediction; Phase-2 toward developing intraseasonal prediction. *Bull. Amer. Meteor. Soc.*, **95**, 585-601.

Wang, H., J.-K. E. Schemm, A. Kumar, W. Wang, L. Long, M. Chelliah, G. D. Bell, and P. Peng, 2009: A statistical forecast model for Atlantic seasonal hurricane activity based on the NCEP dynamical season forecast. *J. Climate*, **22**, 4481-4500.

Science and Technology Infusion Climate Bulletin
NOAA's National Weather Service
41st NOAA Annual Climate Diagnostics and Prediction Workshop
Orono, ME, 3-6 October 2016

Integration of Systems Engineering into Weather-Climate Model Optimization

Jiayu Zhou[1] and David DeWitt[2]

[1]*Office of Science and Technology Integration, NOAA/NWS Headquarters*
[2]*Climate Prediction Center, NOAA/NWS/NCEP*

1. Introduction

In the meteorological model development, tuning is often applied to improve model performance. As tremendous efforts being made to press simulations closer to nature, climate-weather models are getting increasingly sophisticated (more physical, chemical and biological processes, higher horizontal and vertical resolutions, and complex interactions with added degrees of freedom). Because of resource constraints, it is impractical to conduct all tests to find the optimum configuration, causing progresses retarded helplessly. The urgency for model optimization has become another prominent issue in systems engineering since the Earth System Modeling Framework (ESMF) project launched to build a flexible software infrastructure to increase portability, interoperability, and code reuse.

The Orthogonal Array Test (OAT), a systems engineering approach of fractional factorial design, is widely used in industrial and agricultural production and proven to be effective to deal with multiple factors, levels and interactions with reliability and sensitivity analysis. It has been very successful in system configuration, parameter level selection and tolerance design etc. (SSTES 1975, Taguchi 1984)

In this introductory presentation for the meteorological community, the basic principles of OAT design are illustrated, followed by the way of statistical analysis to determine dominant factors, significant interactions and percent contribution by individual component. Its ensemble capability to evaluate inherent variations and noises is also demonstrated. Finally, flexible designs to meet special application needs are briefly explored.

2. Fractional factorial design

The most strateforward optimization strategy is to run a separate experiment for each factor and take on all possible combinations of levels across all factors, while the obvious difficulty would be the prohibitively large number of experiments if the factors are numerous for a sophisticated system. It would be ideal to study more factors in a single experiment. The fractional factorial design emerges as the times require to select a limited number of experiments which produce the most information.

3. Orthogonal Array Testing

The philosophy of the OAT approach is to design the product quality inspection into the production process, not to make it after the product being made. The results of one experiment directs the choice of factors in succeeding experiments. The OAT estimates the effects of control factors on the response mean and variation, making products robust that are insensitive to external environment

Being an orthogonal array, its columns are mutually orthogonal by definition. In a column, each level occurs an equal number of times. The OAT has its advantages to alow non-quantitative factors and enable ensemble practice to measure inherent variations. By analysis of the outcome, it determines the dominant factors and significant interactions, as well as the percent contribution of each factor/interaction to the performance result. The minimum number of experiments would be expected to find the optimium configuration.

3.1 Methodology

Following is a brief illustration of technical procedures via a hypothetical example.

Correspondence to: Jiayu Zhou, Office of Science and Technology Integration, NOAA's National Weather Service Headquarters, 1325 East West Highway, Silver Spring, MD 20910; E-mail: jiayu.zhou@noaa.gov.

3.1.1 Experimental design

The purpose of this experiment is to find the optimum configuration of a GCM in respect of four factors in consideration, *i.e.* A- cloud, B- surface boundary layer, C- model initialization, and D- resolution. Each factor has two levels. For example, A- cloud could have two different parameterization schemes, so does B- surface boundary layer, C- initialization process and D- resolution based on the research focus. The experiment target would be a specific performance measure (y_i), *e.g.* skill score *etc.*

To make a design, the $L_8(2^7)$ table (Table 1, rows 1-8) is used. (Note $L_n(E^f)$, where n (= (E - 1) x f + 1= 8) is the number of experiments, f (= 7) the maximum number of factors that the table can accommodate, and E (=2) the number of levels inspected.) Factors A, B, C and D are assigned to the 1st, 2nd, 3rd and 7th column, respectively. The 3rd column is used for examining the importance of interaction between A and B (AxB) according to the principle of design. Subsequently, eight experiments can be performed taking the level assigned for each factor. The last column records the experiment results.

Table 1 Orthogonal array $L_8(2^7)$ and factors assignment

Factor / Exp.	1 A	2 B	3 AxB	4 C	5	6	7 D	Performance Measure
1	1	1	1	1	1	1	1	y_1
2	1	1	1	2	2	2	2	y_2
3	1	2	2	1	1	2	2	y_3
4	1	2	2	2	2	1	1	y_4
5	2	1	2	1	2	1	2	y_5
6	2	1	2	2	1	2	1	y_6
7	2	2	1	1	2	2	1	y_7
8	2	2	1	2	1	1	2	y_8
I	I_1	I_2	I_3	I_4	I_5	I_6	I_7	Total
II	II_1	II_2	II_3	II_4	II_5	II_6	II_7	$T=\sum_{i=1}^{8} y_i$
I - II	I_1-II_1	I_2-II_2	I_3-II_3	I_4-II_4	I_5-II_5	I_6-II_6	I_7-II_7	
$(I - II)^2$	$(I_1 - II_1)^2$	$(I_2 - II_2)^2$	$(I_3 - II_3)^2$	$(I_4 - II_4)^2$	$(I_5 - II_5)^2$	$(I_6 - II_6)^2$	$(I_7 - II_7)^2$	
$\hat{w}$	$(I_1 - II_1)/8$	$(I_2 - II_2)/8$	$(I_3 - II_3)/8$	$(I_4 - II_4)/8$	$(I_5 - II_5)/8$	$(I_6 - II_6)/8$	$(I_7 - II_7)/8$	
S	$(I_1 - II_1)^2/8$	$(I_2 - II_2)^2/8$	$(I_3 - II_3)^2/8$	$(I_4 - II_4)^2/8$	$(I_5 - II_5)^2/8$	$(I_6 - II_6)^2/8$	$(I_7 - II_7)^2/8$	

3.1.2. Analysis

The rows 9-14 of Table 1 are used for analysis, where I_i and II_i are summation of level 1 and level 2 results in column *i*, respectively. Columns 5 and 6 represent uncertainties. Table 2 performs the analysis of variance (ANOV) to access the importance of each factor and the significance of interaction inspected.

Table 2 Analysis of variance

Factor	S	df	S/df	F	Significance
A	S_1	E_1-1	S_1/df_A	$\frac{S_1/df_A}{S_e/df_e}$	Comparing with $F_\alpha(df_x,df_e)$: * at $\alpha = 0.05$ significance level ** at $\alpha = 0.01$ significance level Blank – Insignificant Note: e – reference of uncertainties; df – degree of freedom; E1 = E2 = E4 = E7 ≡ E; $^{\$}S_e = S_5 + S_6$, when AxB is significant. Otherwise, $S_e = S_3 + S_5 + S_6$
B	S_2	E_2-1	S_2/df_B	$\frac{S_2/df_B}{S_e/df_e}$	
C	S_4	E_4-1	S_4/df_C	$\frac{S_4/df_C}{S_e/df_e}$	
D	S_7	E_7-1	S_7/df_D	$\frac{S_7/df_D}{S_e/df_e}$	
AxB	S_3	$(E_1-1)(E_2-1)$	S_3/df_{AXB}	$\frac{S_3/df_{AxB}}{S_e/df_e}$	
e	$^{\$}S_e$	n-1-(df_A+df_B+ df_C+df_D+df_{AxB})	S_e/df_e	*NA*	

3.1.3 Ensemble capability

It is highly preferable to embrace uncertainty analysis in the optimization process to yield more robust result. This is done by OAT via replication of experiment with perturbed initial conditions/boundary conditions/factor parameters. The analysis follows an expanded ANOV procedure described in text books (Roy 2010).

3.2 Flexible design and applications

The orthogonal array can be constructed to have as many schemes as possible with maximum number of factors with different levels for the smallest number of experimental runs, *e.g.* $L_8(2^7)$, $L_{16}(2^{15})$, $L_9(3^4)$, $L_{32}(4^9)$, $L_{25}(5^6)$ *etc.* (Bolboacă and Jäntschi 2007) The flexible design observes following principles:

a. Use an OAT array that has more rows than df required;
b. Different factors/interactions can't be assigned to a same column;
c. The interaction between two columns of $L_n(E^f)$ occupies E-1 columns described in the interaction table.

There are also many ways to meet various application needs, such as:

a. *Column merging* : Assign factors having different levels in an OA simultaneously;
b. *Dummy levels*: Assign factors having less levels to OA of more levels;
c. *Compounding factors*: Assign factors having more levels to OA of less levels;
d. *Fractional addition*: Make additional tests with a few new levels for a factor found having some kind of trend to influence the performance result;
e. *Dividing zones*: Repeat costly experiments less times than inexpensive ones.

4. Prospects

Orthogonal Array Test technique selects a set of test cases from a universe of tests and makes testing efficient and effective, having advantages of multiformity, parallelity and synthetic comparability. The optimum configuration resulted from OAT is the best combination among not only the test conditions but also all conditions of possible combinations in a given case.

Beside promoting model improvement, OAT has a lot of potential for meteorological applications, such as assessing the dependence of satellite retrieved atmospheric profiles on physical and statistical parameters of the data assimilation system, and transforming model output into sensible climate/weather parameters, for

example. It could also help identify model structural errors when being used for model tuning as explained by Hourdin *et al.* (2016).

In practice, the performance measure criterion for system optimization is not unique. Keeping in mind the model approximate nature and observations uncertainties, it is important to make physical sense and not over-tune the factors. Professional knowledge of the fundamental processes inherent in the system also helps to make experiment design more efficient, *e.g.* knowing some interactions nonexistent could considerably decrease the level of effort.

References

Bolboacă, S. and L. Jäntschi, 2007: Design of experiments: useful orthogonal array for number of experiments from 4 to 16. *entropy*, **9**, 198-232.

Hourdin, F., and Coauthors, 2016: The art and science of climate model tuning. *Bull. Amer. Meteor. Soc.*, in press. doi:http://dx.doi.org/10.1175/BAMS-D-15-00135.1.

Roy, Ranjit K., 2010: *A primer on the Taguchi method* (2nd Edition). Society of Manufacturing Engineers, 304pp.

SSTES, 1975: *Orthogonal Array Test Design – A Multifactor Test Method* (in Chinese). Shanghai People's Press, 229 pp.

Taguchi, G., 1984: Introduction to quality engineering-Taguchi methods. American Supplier Institute, Inc., Romulus, MI.

Science and Technology Infusion Climate Bulletin
NOAA's National Weather Service
41st NOAA Annual Climate Diagnostics and Prediction Workshop
Orono, ME, 3-6 October 2016

Objective, Temporally and Spatially Skill-Weighted Consolidation of Dynamical Model Forecasts for Week-2 Outlooks

Scott Handel, Melissa Ou, Mike Charles, Luke He, Dan Collins, Stephen Baxter, and David Unger
Climate Prediction Center, NOAA/NWS/NCEP, College Park, Maryland

1. Introduction

The Climate Prediction Center (CPC) currently produces automated extended range probabilistic temperature and precipitation outlooks for the contiguous United States and Alaska on a daily basis. These automated outlooks are the primary source of guidance for CPC's official week-2 manually drawn outlooks during the week and form the basis of the official automated outlooks on weekends. The probabilistic information expressed by these outlooks reflects the chances that the mean temperature (total accumulated precipitation) over the period will fall into the most likely of three classes: above, below, or near normal (median).

By definition, this three class system reflects only a limited representation of the forecast probability distribution as probabilities are available only in reference to the 33rd and 67th percentiles of the climatological distribution. Moreover, these probabilities are currently calculated through a subjective weighting of dynamical and statistical forecasts which was predetermined by the collaborative group of CPC forecasters. These subjective weightings do not take temporal and spatial variations of skill into account.

The week-2 Consolidation Project (CON) was designed, in part, to increase the skill of CPC's automated week-2 probabilistic temperature and precipitation outlooks by objectively weighting input forecast tools through analysis of past skill both temporally and spatially. In this way, the CON tool can more effectively utilize the independent information of each of its component input dynamical forecasts.

Additionally, the CON provides information on a wider spectrum of the forecast probability distribution similar to what is currently available for CPC's seasonal outlooks. Thus, users can have access to the mean temperature or accumulated precipitation values corresponding to the median, tails, or most likely range in the forecast distribution.

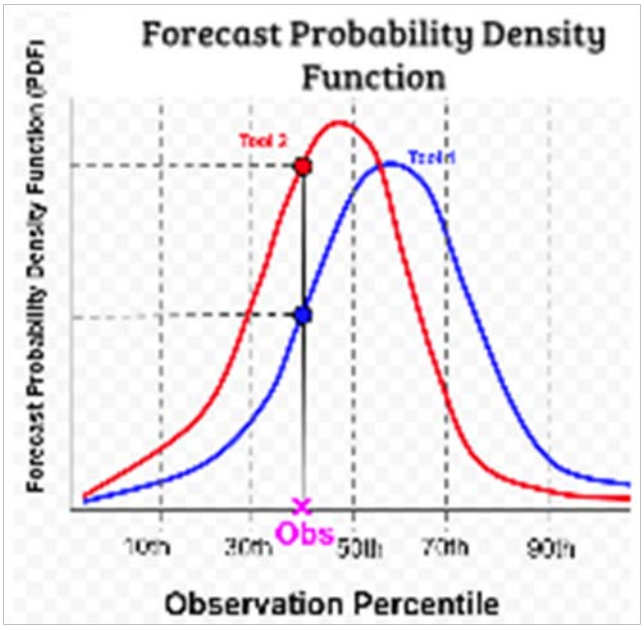

Fig. 1 Example of probability curves for 2 input tools for one day in the evaluation period at a grid point. 'X' marks the percentile that was actually observed that day, and the red and blue circles denotes the estimated probability values at the observation. Tool 2 in this case had the higher "winning" probability, because it was more confident at where the observation verified.

2. Methodology

2.1 Calculation of probability density function values

A probability density estimate is obtained of each of the input forecast tools at the observed percentile for the valid date/location for a range of past dates. These values are compared to determine which tools perform better than others to get weights for the consolidation. Below is a diagram (Fig. 1) showing an example of how two tool probabilities

Correspondence to: Scott Handel, Climate Prediction Center, NOAA/NWS/NCEP, 5830 University Research Court, College Park, MD; E-mail: Scott.Handel@noaa.gov

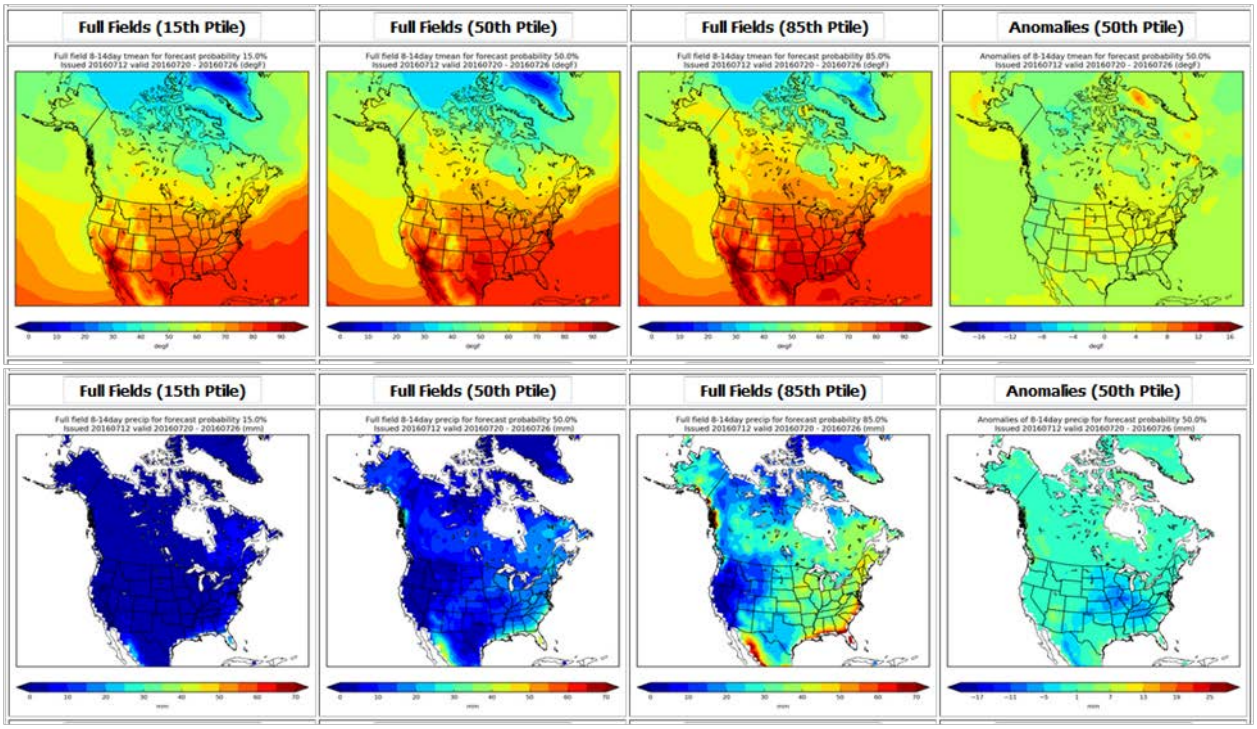

Fig. 2 Temperature (top) and precipitation (bottom) outputs. (See descriptions in Section 3.1 for details.)

would be compared for a specific date/location compared to the observation. This example represents 2 different tools (blue and red curves) of the forecast probabilities in PDF format. The "winning" tool would be Tool 2 in Fig. 1 since the area under the curve surrounding the observed percentile was greater than tool 1. This process is iterated over the entire evaluation period, doing an additive count of how many times each of the tools "win" over the period.

2.2 Weighting procedure

Weights are determined for each 1x1 degree grid point using the accumulated count of which input had the highest PDF value at the observation during the skill evaluation period. The evaluation period contains 135 days in total (90 days from the previous year centered on the forecast center day as well as the last 45 days from the current year). In order to minimize discontinuities, a 9 point smoother is applied to the weights for each grid point. Weights for land (ocean) areas are smoothed with the weights for the surrounding land (ocean) areas.

3. Output

3.1 Full field output

Binary, gridded output files containing full field mean temperature and total precipitation values at 19 probability of exceedance levels are produced on a daily basis. Additionally, maps of the consolidated forecast full field values at the 15th, 50th, and 85th probability of exceedance levels are produced for both mean temperature and accumulated precipitation (first three columns of Fig. 2). Anomaly maps representing the difference between the full field values at the 50th percentile of the forecast distribution and the 50th percentile of the climatological distribution are also provided (last column of Fig. 2).

3.2 Probabilistic output

Binary gridded output files containing the probability of the mean temperature or accumulated precipitation exceeding 19 climatological thresholds are produced on a daily basis. Additionally, graphical maps are produced for forecast tercile probabilities, (top left of Fig. 3), percent weights of each of the input

forecast tools (bottom row of Fig. 3), and climatological percentile values corresponding to the observed mean temperature or total precipitation during the forecast valid period (top right of Fig. 3).

4. Results

Preliminary verification statistics were compiled for the period January 1 - September 1, 2016. For week-2 temperature and precipitation outlooks, the mean Heidke Skill Score (HSS) for the consolidated output surpassed the HSS for all of its inputs. Consolidated temperature (precipitation) HSS was 35.1 (16.0) as compared to input ECMWF Ensemble HSS of 33.3 (13.4) and GEFS HSS of 31.2 (13.8).

5. Conclusions/Next steps

The objective, skill-weighted, week-2 CON tools show promise for providing more skillful first guesses to CPC's manually drawn official weekday forecasts and mostly automated weekend forecasts. In addition, through improvements in skill to CPC's automated guidance, the consolidation tool may increase the skill of the official week two probabilistic outlooks and the efficiency of their production. Moreover, by providing information on a wider spectrum of the forecast probability distributions, the week-2 CON provides information consistent with CPC's current seasonal POE output, which contains similar information. Since the CON POE produces output for a wide spectrum of POE levels, this could aid the forecasters that produce the probabilistic U.S. Hazards Outlook through the identification of the most likely mean temperature and accumulated precipitation ranges as well as the potential for extreme events. The production of weight maps of the input dynamical model forecast tools may also prove useful for the week-2 U.S. Hazards Outlook though the identification of areas of relative skill among the input model forecasts.

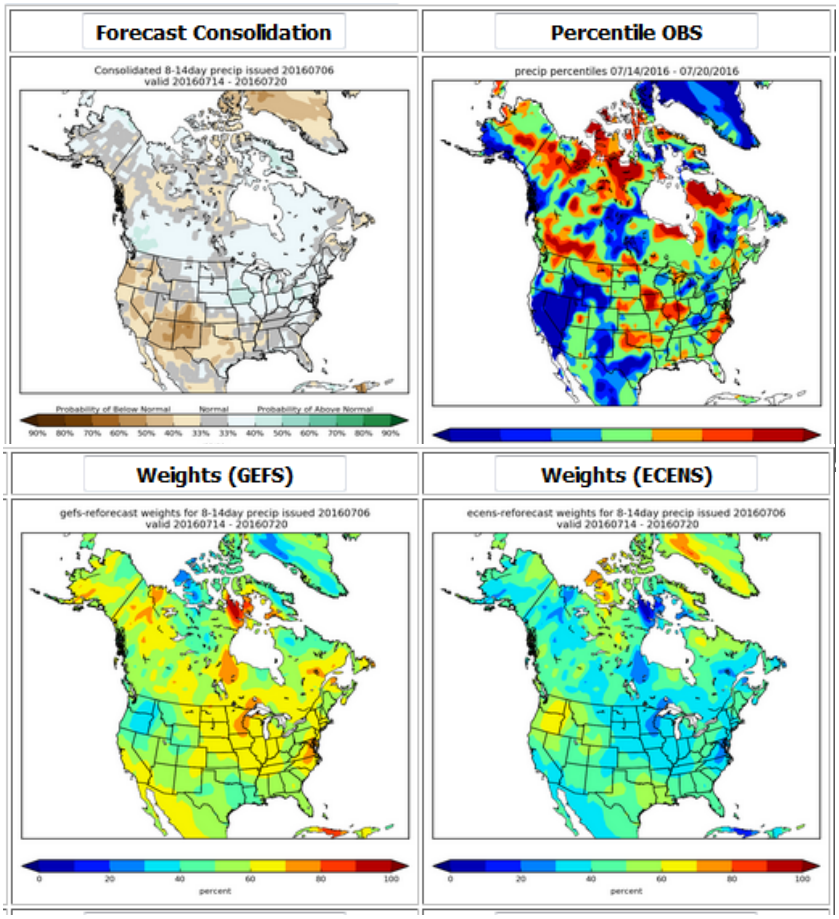

Fig. 3 Tercile Probabilistic Precipitation Output (top left), Percentile Observations (top right), and Weights (bottom row). (See descriptions in Section 3.2 for details.)

Planned future work incorporates inclusion of additional dynamical and statistical tool input as well as a more thorough skill evaluation of the CON output, (including probabilistic measures such as the RPSS and Reliability Diagrams). Future evaluations will also include skill comparisons with additional combination techniques (such as equal weighting).

References

Unger, D.A., H. van ven Dool, E. O'Lenic, D. Collins, 2009: Ensemble regression. *Mon. Wea. Rev.*, **137**, 2365-2379.

Science and Technology Infusion Climate Bulletin
NOAA's National Weather Service
41st NOAA Annual Climate Diagnostics and Prediction Workshop
Orono, ME, 3-6 October 2016

Preliminary Results of Evaluation of Week 3-4 Reforecast Data from Environment Canada

Qin Ginger Zhang, Dan Collins, and Jon Gottschalck
Climate Prediction Center, NOAA/NWS/NCEP, College Park, Maryland

1. Introduction

This study supports the current experimental Climate Prediction Center (CPC) week 3-4 temperature and precipitation outlooks, which are released once per week and focus on mean climate conditions anticipated for a two week forecast period. CPC is preparing to add realtime forecasts of the Global Ensemble Prediction System (GEPS) from the Environment Canada (EC) to its set of week3-4 forecast tools. An assessment of the GEPS reforecast is a first step in this process.

2. Model and Data Procedure

The GEPS reforecast was implemented at the Canadian Meteorological Center (CMC) of Environment Canada operations in December 2013 (see Gagnon *et al.* 2015). The main goal of the reforecast procedure is to generate a historical dataset that is representative of the current operational GEPS forecast. GEPS forecasts are an integral part of the collaboration with the United States National Centers for Environmental Prediction (NCEP) in the North American Ensemble Forecast System (NAEFS) project.

The reforecast dataset used in this study is the extension reforecast initialized once per week on Thursdays (2016 calendar) out to 32-days. There are 4 members (1 control run with 3 perturbation runs) at 1x1 spatial resolution. We evaluate the variables of 2m temperature, surface precipitation, 500 hPa and 200 hPa heights. We estimate model mean bias as well as derive skill information from the ensemble mean over the reforecast period (1995-2014). For comparing with observations, the verification data used are the CPC's unified temperature, CPC land only gauge-satellite merged precipitation data, and CDAS reanalysis for 500 hPa and 200 hPa heights.

3. Results

In order to assess model forecast ability, mean biases for the week 3-4 forecast period were calculated from model climatology (1995-2014) of the ensemble mean (4 member averaged) for each IC to against the observed climatology. For convenient discussion and easily displaying, seasonal model biases of 4 variables were averaged for DJF, MAM, JJA and SON. The difference of the ensemble mean bias with observations averaged over the CONUS for week1-4 for each initial time was also investigated. In general, there is a cold bias over western North America in 4 seasons and a warm bias over the central U.S. in MAM, JJA and SON. For precipitation, a wet bias is over eastern North America in winter, spring and summer, but a dry bias is indicated over the central CONUS in JJA and SON.

Anomaly correlations were calculated to represent the ensemble mean forecast skill for DJF, MAM, JJA and SON of 2m temperature and precipitation from GEPS. The anomalies are uncalibrated but remove the model systematic errors by the reforecast from 1982-2014. The forecast skill of week3-4 temperature is relatively low on average over the U.S. (see Fig. 1). The forecast skill of precipitation is even lower than that of temperature, which is similar to the assessment results of ECMWF and JMA models.

4. Summary

Since September 2015, CPC has prepared and experimentally disseminated Week 3-4 U.S. temperature and precipitation outlooks once per week. In order to apply bias correction methodologies, it is important to obtain process and evaluate reforecast datasets so that dynamical model systems can contribute to this Week

Correspondence to: Qin Ginger Zhang, Climate Prediction Center, NOAA/NWS/NCEP, 5830 University Research Court, College Park, MD; E-mail: Qin.Zhang@noaa.gov

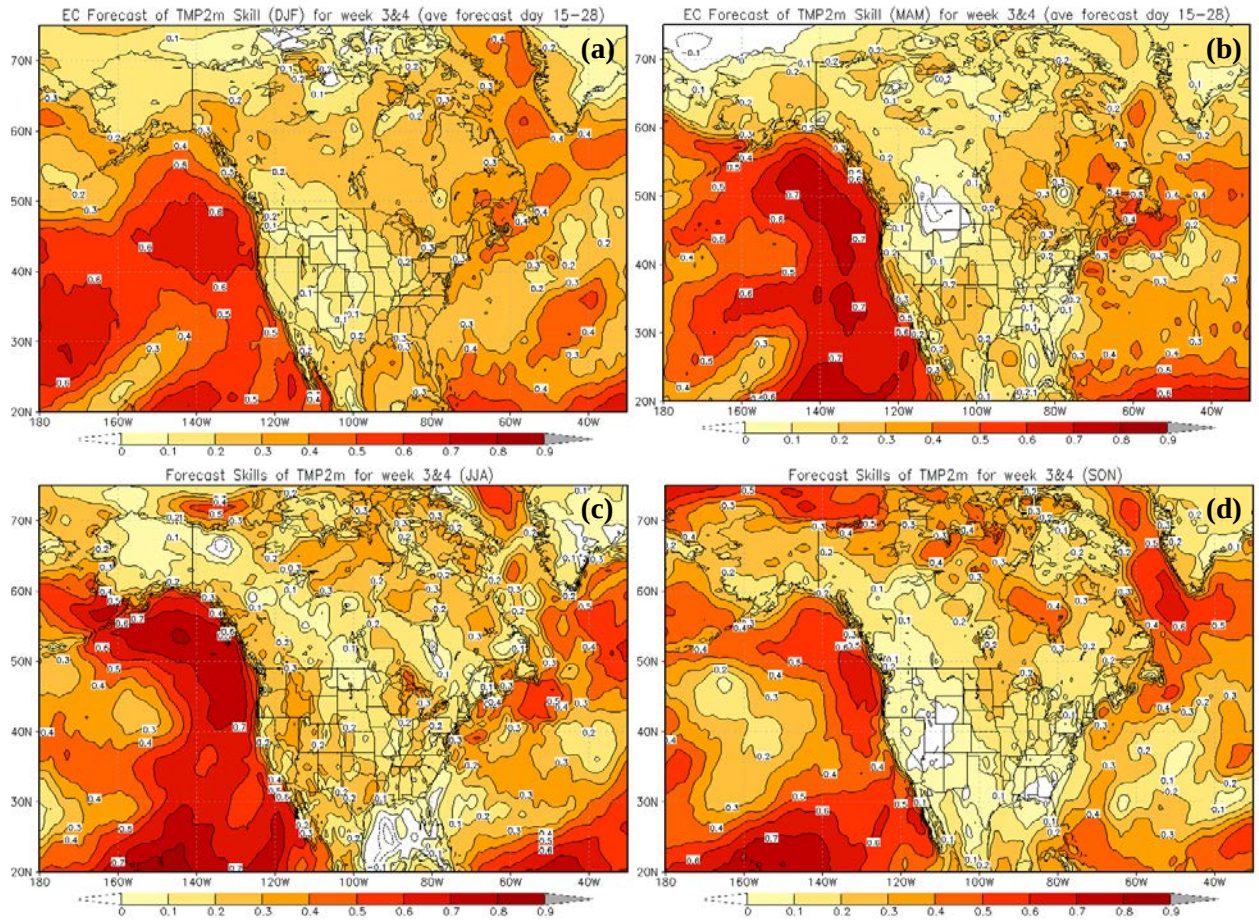

Fig. 1 Week 3-4 forecast skill of 2m temperature for (a) DJF, (b) MAM, (c) JJA and (d) SON seasons.

3-4 effort. We present preliminary results using the Environment Canada (EC) Global Ensemble Prediction System (GEPS) reforecast data that extends to 32 days. These reforecasts are produced once per week, ranging from 1995-2014 and including 4 members. Two meter temperature, precipitation and 500 hPa height were evaluated. Both temporal and spatial verification information is presented. As compared to observations, the GEPS exhibits a cold bias for western North America and a wet bias over eastern North America. The GEPS reforecast skill for Week 3-4 is relatively low, on average, over the U.S. and similar to that of models from other operational centers. Forecast opportunities, however, do exist in some regions and seasons.

Acknowledgements. We thank N. Gagnon for the reforecast data of GEPS from Environment Canada.

References

Gagnon, N., and Co-authors, 2015: Improvement to the Global Ensemble Prediction System (GEPS) reforecast system from version 3.1.0 to version 4.0.0. Canadian Meteorological Centre Technical Note.

Science and Technology Infusion Climate Bulletin
NOAA's National Weather Service
41st NOAA Annual Climate Diagnostics and Prediction Workshop
Orono, ME, 3-6 October 2016

Assessing Performance of Calibrated Multi-model Ensembles in the 3–4 Week Forecast Period

Kyle MacRitchie[1, 2], Dan Collins[2], and Jon Gottschalck[2]
[1]*Innovim LLC., Greenbelt, Maryland*
[2]*Climate Prediction Center, NOAA/NWS/NCEP, College Park, Maryland*

1. Introduction

The NOAA Climate Prediction Center (CPC) began experimental week 3-4 probabilistic forecasts of below and above normal temperature and precipitation in September 2015. These forecasts are issued weekly on Friday afternoon. The CPC uses a number of tools to aid in its forecast creation including three dynamical models: the NCEP Climate Forecast System (CFS), the Japan Meteorological Agency (JMA) model, and the European Centre for Medium-Range Weather Forecasts (ECMWF) model.

Ensemble calibration (Unger *et al*., 2009), trained on the model reforecast data, is helpful to produce reliable real-time forecasts and to generate a full probability distribution from which forecast probabilities can be calculated. We conducted this study to examine the improvements that ensemble calibration yields over raw model forecasts.

2. Data and methodology

The CFS reforecast dataset includes hindcasts initiated daily from 1999–2010. Each run of the CFS includes four ensemble members which we increased to eight by including the previous forecast each day. The ECMWF reforecast dataset spanned 1996–2014 and included five ensemble members run once per week. Our JMA reforecast data included runs of five ensemble members on the 10th, 20th, and final day of each month from 1991–2010. All reforecast data was on a 1° x 1° horizontal grid.

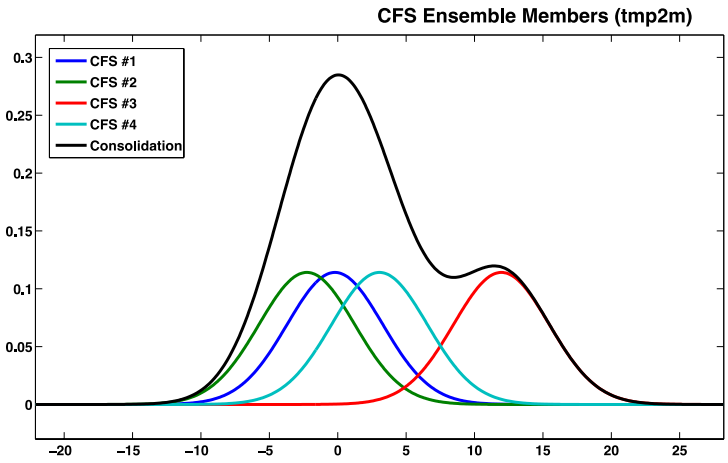

Fig. 1 Schematic showing Ensemble Regression based on Unger *et al*. (2009).

We evaluated the hindcasts using Brier Skill Scores, and reliability diagrams, which are commonly used at CPC.

Brier Skill Scores (BSS) measure the accuracy of probabilistic forecasts. The squared term in the BSS ensures that large errors are penalized more than small errors.

$$BS = \frac{1}{N}\sum_{i=1}^{N} (F_i - O_i)^2 \quad , \qquad BSS = 1 - BS_f / BS_r$$

where N is the total number of forecasts, F is the forecast probability for above normal temperature or precipitation, and O is the observed probability. BS_f is the forecast's Brier score and BS_r is the reference score for predicting climatology which is 0.5 in this case. Values range from -∞ to 1. 1 indicates perfect forecast and 0 no skill when compared to the reference forecast.

Correspondence to: Kyle MacRitchie, Innovim LLC., Greenbelt, MD and Climate Prediction Center, NOAA/NWS/NCEP, 5830 University Research Court, College Park, MD; E-mail: kyle.macritchie@noaa.gov

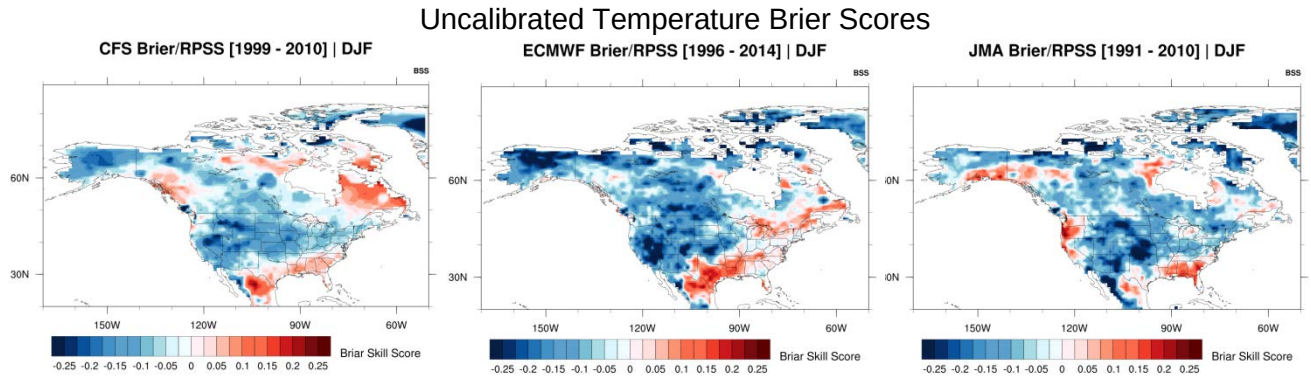

Fig. 2 Comparison between uncalibrated and calibrated Brier Skill scores for temperature.

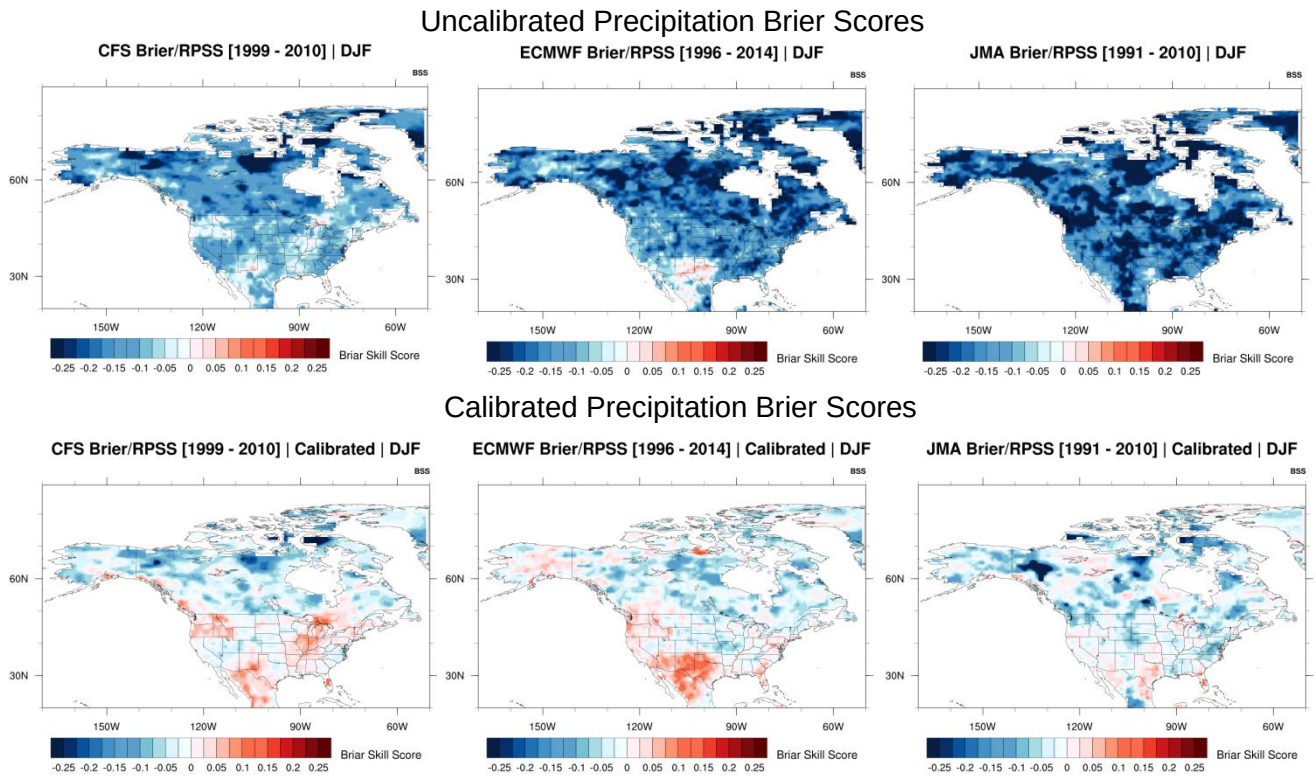

Fig. 3 Comparison between uncalibrated and calibrated Brier Skill scores for precipitation.

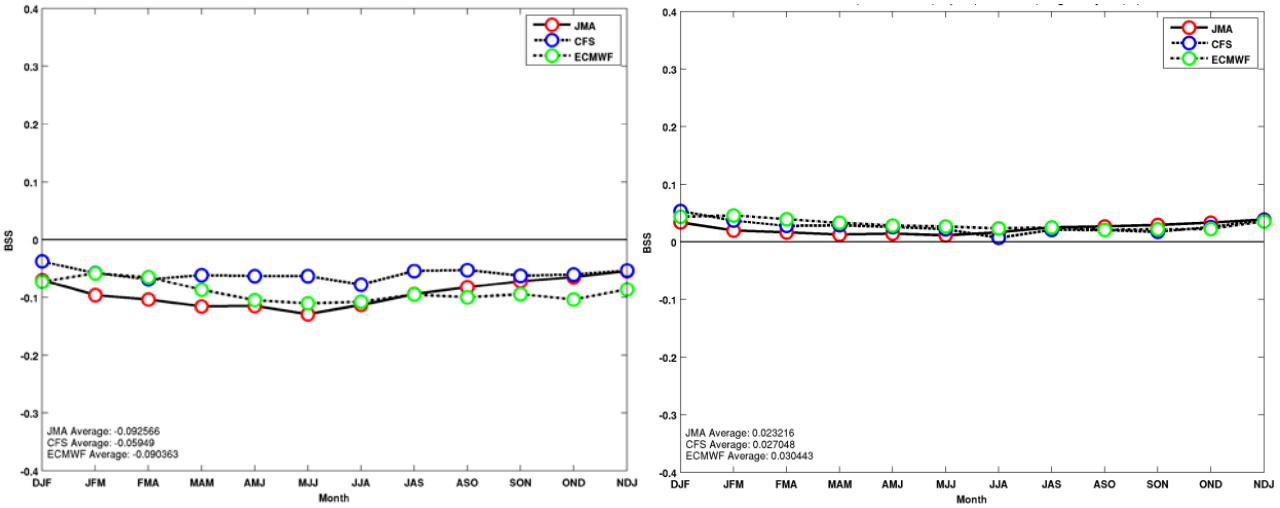

Fig. 4 Brier skill scores averaged over North America for uncalibrated (left) and calibrated (right) week 3+4 2m temperature forecast.

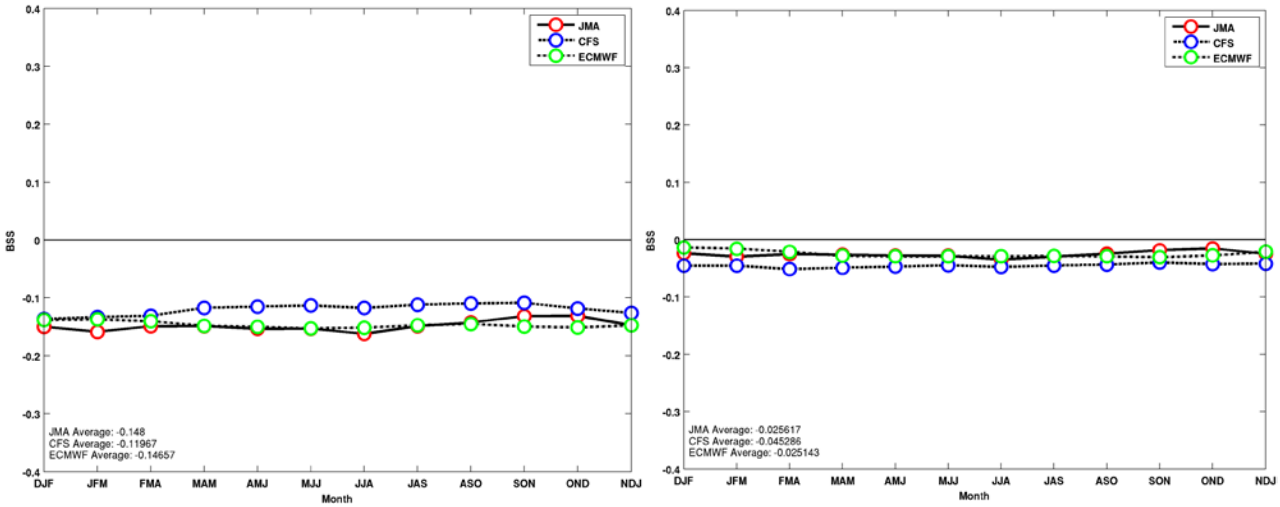

Fig. 5 Same as Fig. 4 but for precipitation.

Ensemble regression (Unger *et al*. 2009) was developed at CPC as a method to fit a calibrated probability density function to each ensemble member based on the model's reforecast performance. In a simplistic sense, ensemble regression weights forecasts based on the correlations between the model's reforecasts and verifications. The calibrated PDFs are assigned to each ensemble member and can then be combined for use in forecasting, as shown in Fig. 1.

3. Results

Our results show that Ensemble Regression improves model temperature and precipitation forecasts throughout the Continental United States (CONUS). Figures 2 and 3 show Brier skill scores over the CONUS for DJF temperature and precipitation forecast, respectively. Each column represents output from a specific model, the top rows show uncalibrated forecasts, and the bottom rows show forecasts after calibration with Ensemble Regression.

Skill increases from calibration are evident nearly everywhere on the map for both temperature and precipitation forecasts, although temperature forecast improvements are uniformly better than precipitation forecast improvements. This is also evident in Figs 4 and 5 which show the Brier skill scores averaged over the CONUS (weighted by the cosine of latitude).

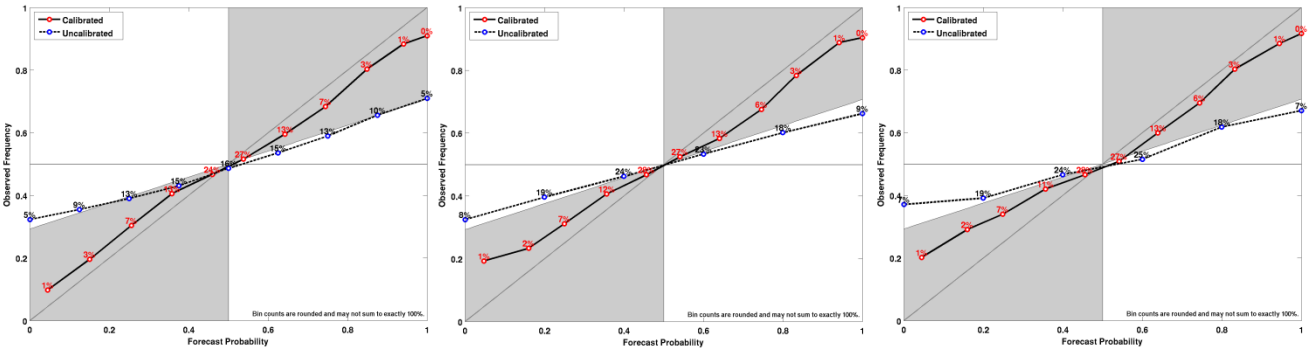

Fig. 6 Reliability diagrams of week 3-4 DJF 2m temperature forecasts over North America for models of CFS (left), ECMWF (middle) and JMA (right). Numbers next to each dot indicate the percentage of events in each bin.

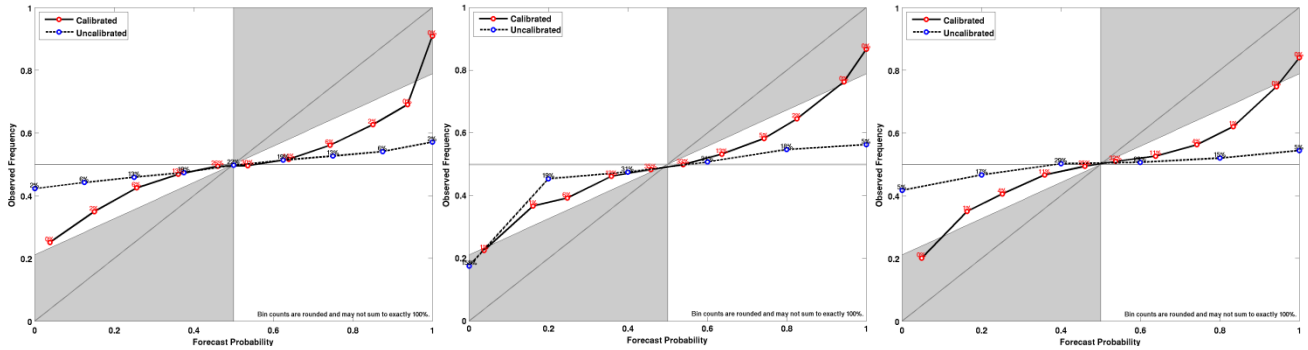

Fig. 7 Same as Fig. 6 but for precipitation.

Each model does noticeably better after calibration, although temperature forecasts are improved more than precipitation forecasts, which are markedly stuck in negative BSS territory.

Figures 6 and 7 show the effects of calibration on model reliability. As expected, calibration increases reliability within each model for both temperature and precipitation forecasts.

4. Summary

Our results show that all three models are more skillful at temperature forecasts than precipitation forecasts with 3-4 week lead times. Calibration using Ensemble Regression yields significant improvements across multiple skill and reliability metrics for both temperature and precipitation. Weeks 3-4 forecasts are inherently difficult and we will continue to improve them with whatever techniques we find.

References

Unger, D. A., H. van den Dool, E. O'Lenic, and D. Collins, 2009: Ensemble regression. *Mon. Wea. Rev.*, **137**, 2365–2379.

Science and Technology Infusion Climate Bulletin
NOAA's National Weather Service
41st NOAA Annual Climate Diagnostics and Prediction Workshop
Orono, ME, 3-6 October 2016

Roles of Remote and Local Forcings in the Variation and Prediction of Regional Maritime Continent Rainfall in Wet and Dry Seasons

Tuantuan Zhang[1], Song Yang[1,2,3], Xingwen Jiang[4], and Bohua Huang[5]

[1]*Department of Atmospheric Sciences, Sun Yat-sen University, Guangzhou, Guangdong, China*

[2] *Institute of Earth Climate and Environment System, Sun Yat-sen University, Guangzhou, Guangdong, China*

[3] *Guangdong Province Key Laboratory for Climate Change and Natural Disaster Studies, Sun Yat-sen University, Guangzhou, Guangdong, China*

[4]*Institute of Plateau Meteorology, China Meteorological Administration, Chengdu, Sichuan, China*

[5]*Department of Atmospheric, Oceanic, and Earth Sciences, George Mason University, Fairfax, Virginia*

ABSTRACT

Seasonal prediction of extratropical climate (*e.g.*, the East Asian climate) is partly dependent upon the prediction skill for rainfall over the Maritime Continent (MC). A previous study by the authors found that the NCEP Climate Forecast System, version 2 (CFSv2), had difference in skill between predicting rainfall over the western MC (WMC) and the eastern MC (EMC), especially in the wet season (Fig. 1). In this study, the potential mechanisms for this phenomenon are examined. It is shown that observationally in the wet season (from boreal winter to early spring) the EMC rainfall is closely linked to both ENSO and local sea surface temperature (SST) anomalies, whereas the WMC rainfall is only moderately correlated with ENSO. The model hindcast unrealistically predicts the relationship of the WMC rainfall with local SST and ENSO (even opposite to the observed feature), which contributes to lower prediction skill for the WMC rainfall. In the dry season (from boreal late summer to fall), the rainfall over the entire MC is significantly influenced by both ENSO and local SST in observations and this feature is well captured by the CFSv2. Therefore, the hindcasts do not show apparently different skill in rainfall prediction for EMC and WMC in the dry season (Fig. 1). The possible roles of atmospheric internal processes are also discussed.

This work has been published in *Journal of Climate* in 2016.

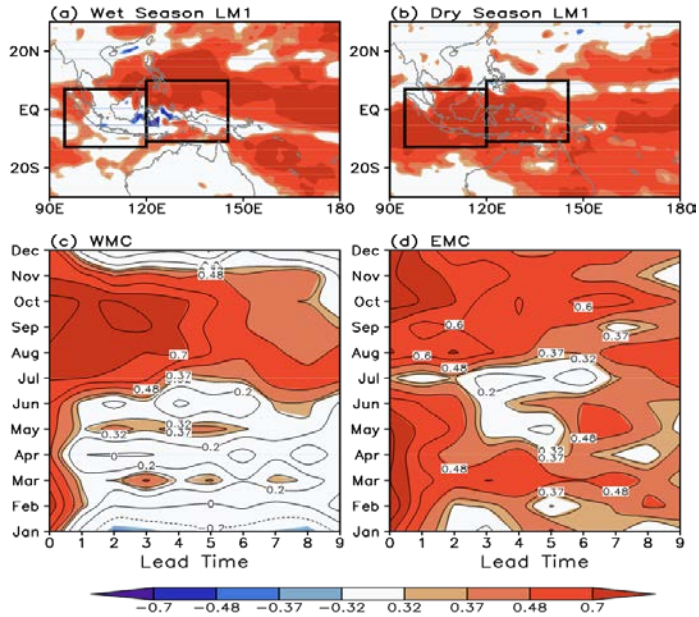

Fig. 1 Correlations of rainfall (mm/day) between observation and CFSv2 in 1-month lead for (a) wet season and (b) dry season, and correlations between observation and CFSv2 predictions for area-averaged rainfall for (c) WMC and (d) EMC. Values exceeding the 90%, 95%, and 99% confidence levels are shaded. The domains used to define WMC (13°S-7°N, 95°E-120°E) and EMC (11°S-10°N, 120°E-145°E) are outlined with black boxes in (a) and (b).

References

Zhang, T., S. Yang, X. Jiang, B. Huang, 2016: Roles of remote and local forcings in the variation and prediction of regional Maritime Continent rainfall in wet and dry Seasons. *J. Climate*, **29**, 8871-8879.

Correspondence to: Tuantuan Zhang, Department of Atmospheric Sciences, Sun Yat-sen University, Guangzhou, Guangdong, China; E-mail: zhtuant@mail2.sysu.edu.cn.

Science and Technology Infusion Climate Bulletin
NOAA's National Weather Service
41st NOAA Annual Climate Diagnostics and Prediction Workshop
Orono, ME, 3-6 October 2016

To Improve Hydrological Prediction: The Value of Medium Range Forecasts

Li Xu[1,2] and Kingtse C. Mo[1]

[1]*Climate Prediction Center, NOAA/NWS/NCEP, College Park, Maryland*
[2]*Innovim LLC., Greenbelt, Maryland*

1. Introduction

In this study, we investigated the contribution of medium range forecasts (MRF) to hydroclimate seasonal CFSv2 forecast skill over the United States. The control experiment is the CFSv2 seasonal forecasts. The testing experiment is the MRF_CFSv2 merged forecasts. In the merged forecasts, the first 14 days of each CFSv2 temperature (T) and precipitation (P) forecasts were replaced by a member of the MRF forecasts. The merged T and P forcings were used to drive the Variable Infiltration Capacity (VIC) land model to obtain soil moisture (SM) and runoff (RO) seasonal forecasts. The MRF-CFSv2 merged forecasts were compared with the CFSv2 forecasts. The improvement is limited to lead-1 month. The merged forecasts show improvement of T. The P forecasts have low skill and only have limited improvement. Overall, the skill of the merged SM and RO forecasts are higher but the differences are not statistically significant for most areas.

2. Motivation

Shukla *et al.* (2012) showed that there is potential improvement of soil moisture and runoff forecasts over the Ensemble Stream Prediction (ESP) at lead-1 month by replacing the first 14 days of the ESP forecast by the MRF forecast. In this study, we assessed the improvement of the CFSv2 seasonal forecasts by the MRF-CFSv2 merged forecasts. For seasonal hydroclimate forecasts, the initial conditions play an important role. The initial conditions are the same for the CFSv2 only and the MRF-CFSv2 merged forecasts. The difference in skill comes from the Median Range weather forecasts.

3. Data & methods

3.1 CFSv2 control experiment

The daily CFSv2 temperature (T) and Precipitation (P) forecasts (Saha *et al.* 2014) were downscaled to 0.5 degrees and were error-corrected by using the BCSD method (Mo *et al.* 2012). The error-corrected T and P forecasts were then used to drive the VIC land surface model to obtain SM and runoff (RO) forecasts. Surface winds data were obtained from climatological CDAS dataset. Total 11 members of CFSv2 forecast were selected to match the MRF ensemble forecast. The initial conditions were taken from a VIC retrospective simulation VIC(SIM) by driving the VIC model with observed T and P. The SM and RO from the VIC(SIM) were then used for verification.

3.2 MRF_CFSv2 merged experiment

MRF temperature and precipitation reforecasts (Hamill *et al.* 2013) were interpolated to the same grid as the CFSv2 control experiment. The ensemble mean of 11 members of T and P forecast were bias corrected by using the previous 45-day training period. The corrections were evenly distributed to each member. The first 14 days of each member of the CFSv2 forecasts were replaced by a member of the error-corrected MRF forecasts. The transition period during day 15-16 is weighted with 2/3 and 1/3 accordingly. After day 16, only CFSv2 forecasts were used.

For each member, the MRF_CFSv2 merged T and P forecasts were used to drive a VIC simulation to obtain SM and Runoff forecasts. The surface winds are the same as the CFSv2 only experiment. We then took equally weighted ensemble average of all members.

Correspondence to: Li Xu, Climate Prediction Center, NOAA/NWS/NCEP, 5830 University Research Court, College Park, MD; E-mail: Li.Xu@noaa.gov

4. Verification

Total 26 year (1985-2010) forecasts at four representative initial dates (Jan 01, Apr 01, Jul 01 and Oct 01) were evaluated. The temperature and precipitation forecasts were verified against the objective analysis based on the gauge observations from the CPC unified dataset. The SM and RO forecasts were verified against the SM and RO from the retrospective simulation VIC(SIM). The runoff at grid points is further aggregated to the USGS 48 hydrological sections. Forecast skill is indicated by the Pearson correlation. The Fisher's Z test was used to assess the statistical significance of the forecast skill improvement.

5. Results

The impact of merging MRF_CFSv2 ensemble forecasts is limited to the forecasts at lead-1 month. The MRF_CFSv2 merged forecasts improve lead-1 month temperature CFSv2 forecasts overall with the largest impact over the western region. The forecast skill for P forecasts is very low for the lead-1 month. There is very little statistically significant improvement in P due to the MRF-CFSv2 merge.

As a result, the merged MRF_CFSv2 forecasts improve the SM and accumulated runoff forecasts, but the differences in skill are overall not statistically significant (Fig.1). There is some statistically improvement for lead-1 month runoff forecasts (Fig.2) due to the slightly improved soil moisture. The enhancements in skill are regional and seasonal dependent. For hydroclimate forecasts at lead-1 month, skill is largely contributed

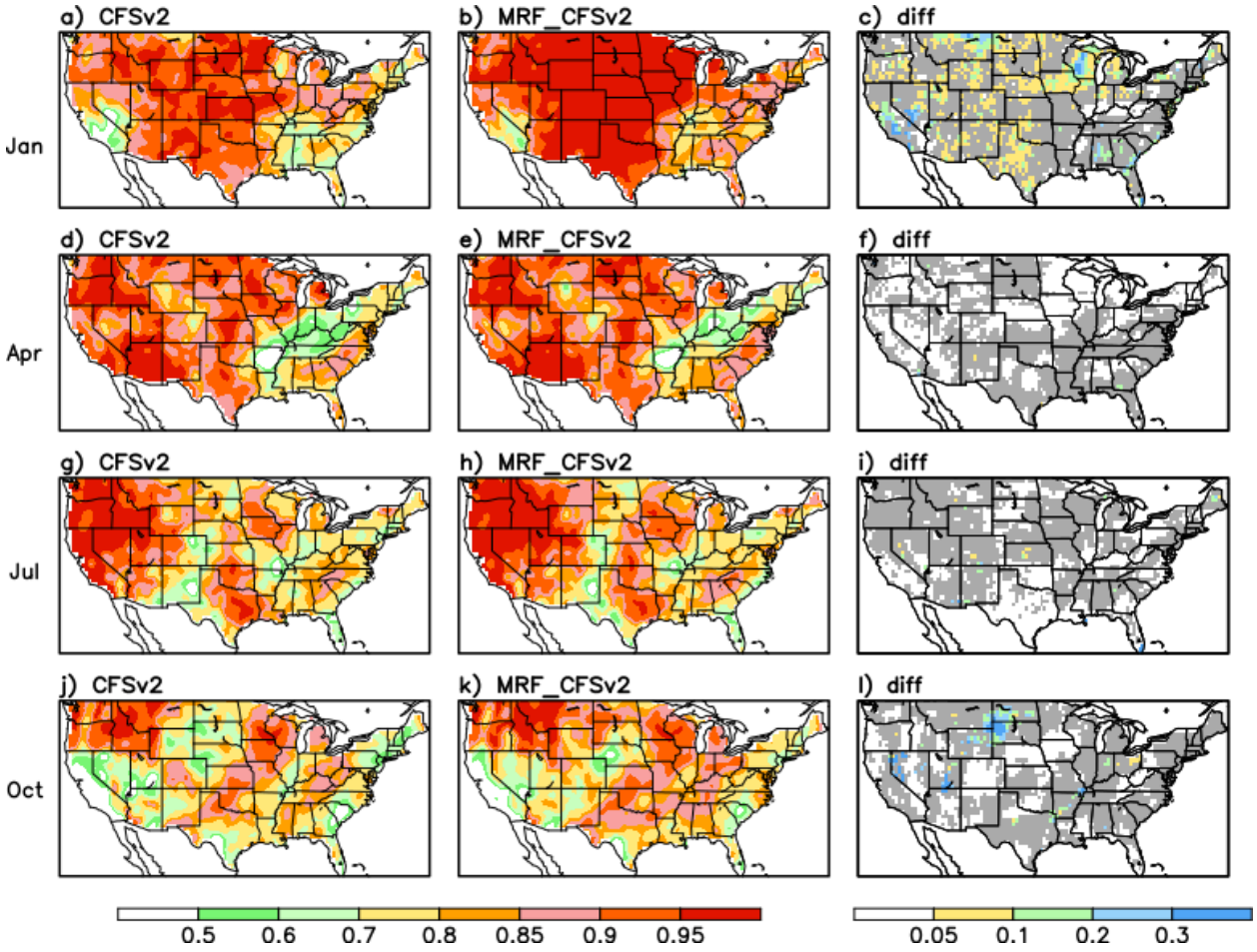

Fig. 1 Forecast skill for January (a) CFSV2 forecasts, (b) MRF_CFSv2 merged forecasts for lead-1 month as measured by the Pearson correlation. Areas where values are significance at the 5% level are sheded. (c) difference between (a) and (b). Grey shading indicated improvement. Areas where difference is statistically significant at the 5% confidence level are colored. (d) - (f), (g) - (i) and (j) - (l) are the same as (a) – (c), but for April, July and October, respectively.

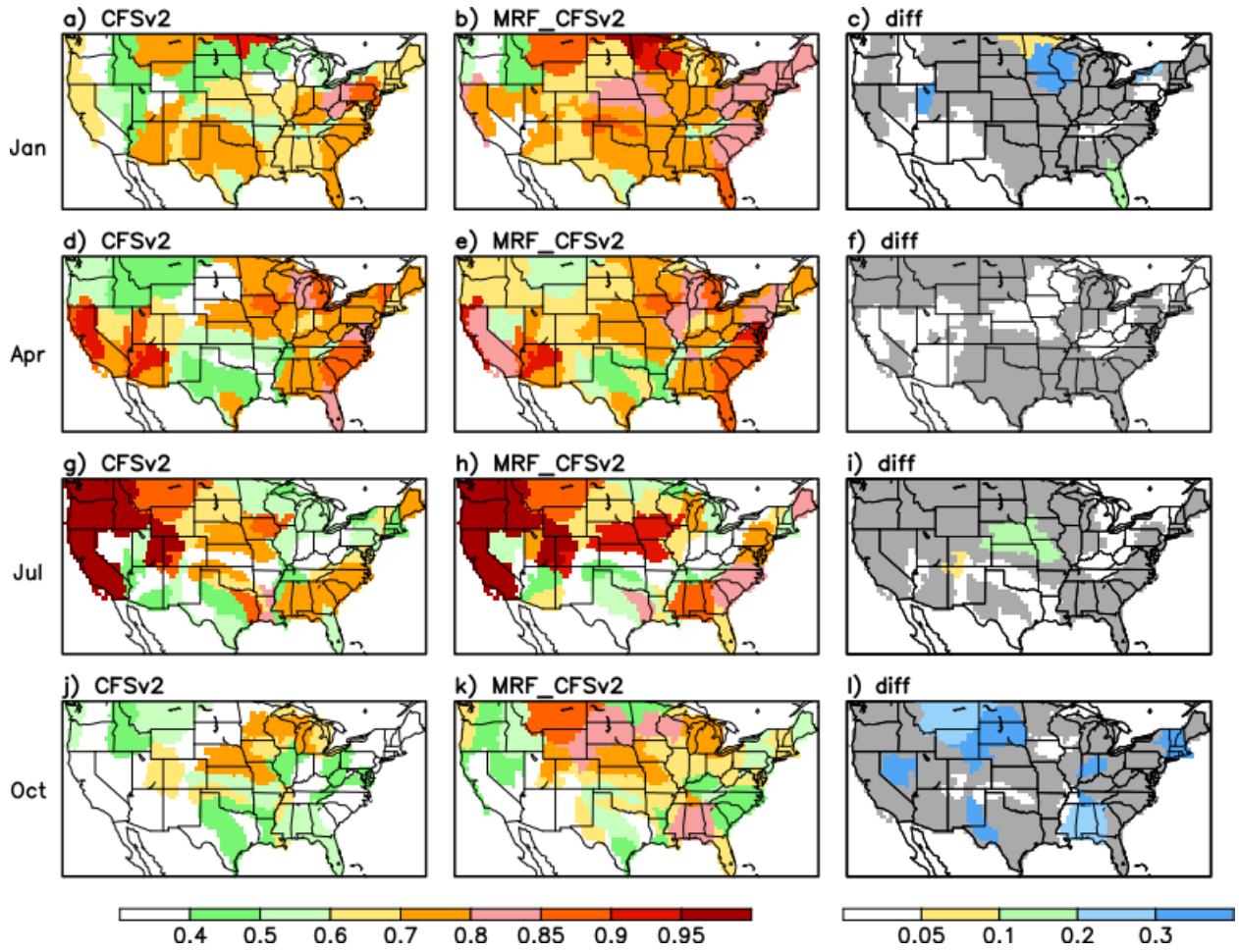

Fig. 2 Same as Fig. 1, but for the forecast skill of accumulated runoff at 48 hydrological sub-sections.

by the initial conditions. At longer leads, climate forcing becomes important, but the skill is too low to make any realistic difference.

Acknowledgements. This project is funded by the CPO MAPP and NIDIS grants.

References

Hamill, T. M., and Coauthors, 2013: NOAA's Second-Generation Global Medium-Range Ensemble Reforecast Dataset. *Bull. Amer. Meteor. Soc.*, **94**, 1553-1565.

Mo, K. C., S. Shukla, D. P. Lettenmaier, and L. C. Chen, 2012: Do Climate Forecast System (CFSv2) forecasts improve seasonal soil moisture prediction? *Geophys. Res. Lett.*, **39**, L23703, doi:10.1029/2012GL053598.

Saha, S., and Coauthors, 2014: The NCEP climate forecast system version 2. *J. Climate*, **27**, 2185-2208.

Shukla, S., N. Voisin, and D. Lettenmaier, 2012: Value of medium range weather forecasts in the improvement of seasonal hydrologic prediction skill. *Hydrol. Earth Syst. Sci.*, **16**, 2825-2838.

Science and Technology Infusion Climate Bulletin
NOAA's National Weather Service
41st NOAA Annual Climate Diagnostics and Prediction Workshop
Orono, ME, 3-6 October 2016

Observed Tropical Climate Variability and Long-term Trend Influences on U.S. Temperature and Precipitation Forecasts for Weeks 3 and 4

Daniel S. Harnos[1], Nathaniel C. Johnson[2,3], Stephen R. Baxter[1],
Michelle L. L'Heureux[1], and Adam D. Allgood[1]

[1]*Climate Prediction Center, NOAA/NWS/NCEP, College Park, Maryland*
[2]*Geophysical Fluid Dynamics Laboratory, NOAA, Princeton, NJ*
[3]*Department of Atmospheric and Oceanic Sciences, Princeton University, Princeton, NJ*

1. Introduction

The Climate Prediction Center (CPC) began issuing probabilistic, two-class forecasts of 2-meter temperature (T_{2m}) and precipitation (P) for the combined weeks 3-4 period (days 15-28) in September 2015. This product serves to bridge the gap between traditional extended range forecasts (days 8-14) and monthly forecasts. The week 3-4 period has been typically thought to be one of low forecast skill, due to insufficient time for boundary conditions to take hold on a forecast, while dynamical guidance suffers from substantial growth of initialization errors.

While dynamical model guidance will always play a substantial role in forecasting, statistical methods can potentially exploit signals from the initial climatic state that can uniquely inform subseasonal forecasters. For example, Riddle *et al.* (2013) and Baxter *et al.* (2014) revealed impacts of the Madden-Julian Oscillation (MJO) through subseasonal timescales on the circulation and T_{2m} of North America. Johnson *et al.* (2014) used a compositing method (detailed in next section) to support that non-linear combined influences of MJO, long-term trend, and the El Niño-Southern Oscillation (ENSO) could often produce skillful week 3-4 wintertime U.S. T_{2m} forecasts. This work seeks to extend Johnson *et al.* (2014) to all seasons while incorporating P forecasts, and also to explore the impacts of ENSO/MJO linearity/non-linearity on week 3-4 forecasts.

2. Data and methodology

Training and cross-validation data for T_{2m} (Janowiak *et al.* 1999) and P (Xie *et al.* 2010) are taken over running 3-month periods between 1982-2013 to evaluate days 15-28, with these same datasets utilized for verification purposes. ENSO information is utilized in the form of the Oceanic Niño Index (3-month running mean Niño 3.4 region SST anomaly) and the daily Real-time Multivariate MJO (RMM; Wheeler and Hendon 2004) index to characterize the MJO.

The first methodology to investigate Week 3-4 predictability of T_{2m} and P is the so-called "phase model" (PM) of Johnson *et al.* (2014), which closely follows traditional compositing methods. In short, mean and variance shifts are quantified based upon the historical 15-28 day distributions of T_{2m} and P for subsets of ENSO (three states - El Niño, Neutral, or La Niña following typical conventions), and the MJO (nine states – one for each conventional phase and another when the amplitude is < 1), with an additional mean shift associated with linear long-term trend. A Gaussian probability density function (PDF) is assumed for the forecast distribution, with a fourth root transform utilized to increase normality for P, where the summed means (ENSO, MJO, and trend) and variances (ENSO and MJO) build the forecast PDF. This PDF can then be compared to the climatological median values, to evaluate what proportion of the forecast distribution are above- and below-normal.

While the former method yields differences in the forecast state based on ENSO, MJO, and trend it can often have abrupt forecast discontinuities when transitioning between climatic states (*e.g.* MJO phases 4, 5, or a weak MJO) while the solutions also fail to scale for potential impacts sourced from the amplitude of the

Correspondence to: Daniel S. Harnos, Climate Prediction Center, NOAA/NWS/NCEP, 5830 University Research Court, College Park, MD; E-mail: daniel.harnos@noaa.gov

background climate state. These shortcomings can be addressed through a multiple linear regression (MLR) framework, with predictands of T_{2m} and P and standardized predictors of: RMM1 and RMM2 for MJO, the 2-week mean Nino 3.4 anomaly from OISSTv2 (Reynolds et al. 2007) for ENSO, and a daily index for linear long-term trend. The regression relationship is used to determine the mean shifts in the day 15-28 T_{2m} and P distributions based on the initial climatic state, while the climatological variance is used in conjunction with a skill correction then used to build a Gaussian forecast PDF. This PDF is then evaluated with respect to climatological values, as with the PM.

All skill evaluations utilize the Heidke Skill Score (HSS), which is the difference of the number of correct forecasts and number of forecasts to be expected to be randomly correct (50% in a two-class forecast), divided by the difference of the total number of forecasts and number of forecasts expected to be randomly correct. The HSS can range over ±100, with a score of 0 indicating no improvement relative to random chance while positive values indicate added value. Cross-validation is performed using a leave-one-year out methodology.

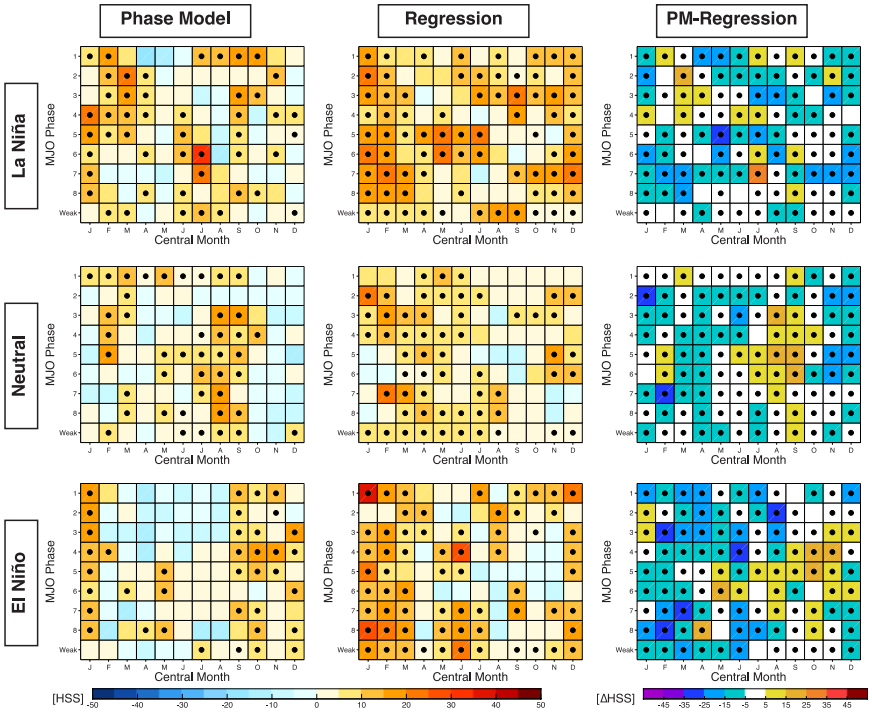

Fig. 1 Hindcast T_{2m} HSS spatially averaged for all U.S. grid cells via the PM (left column), MLR (center column) and difference between the two (right column) across MJO/ENSO base states and running 3-month period. Dots indicate statistical significance ≥ 95% via Monte Carlo Simulation.

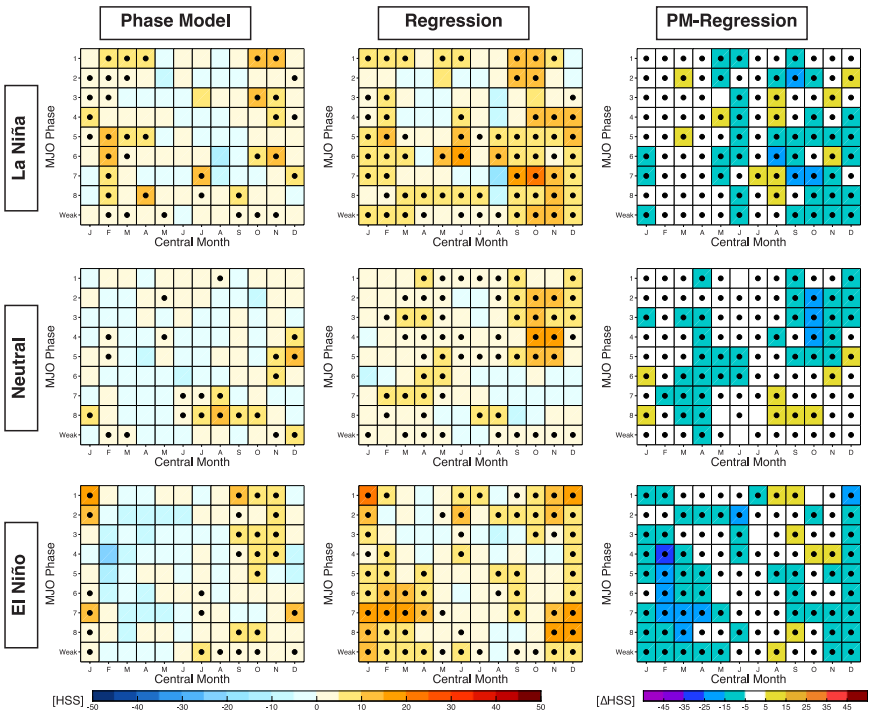

Fig. 2 As in Figure 1, but for P.

3. Cross-validation performance

Cross-validation reveals both the PM and MLR on average across the U.S. are largely, and often significantly, skillful across a breadth of many initial ENSO and MJO states in multiple seasons for both T_{2m} (Fig. 1) and P (Fig. 2). For each predictand, embedded periods of enhanced predictability, evidenced by marked increases in HSS, or "forecasts of opportunity" exist (*e.g.* MJO phases 2-5 with a background La Niña during FMA). Also notable is that skill

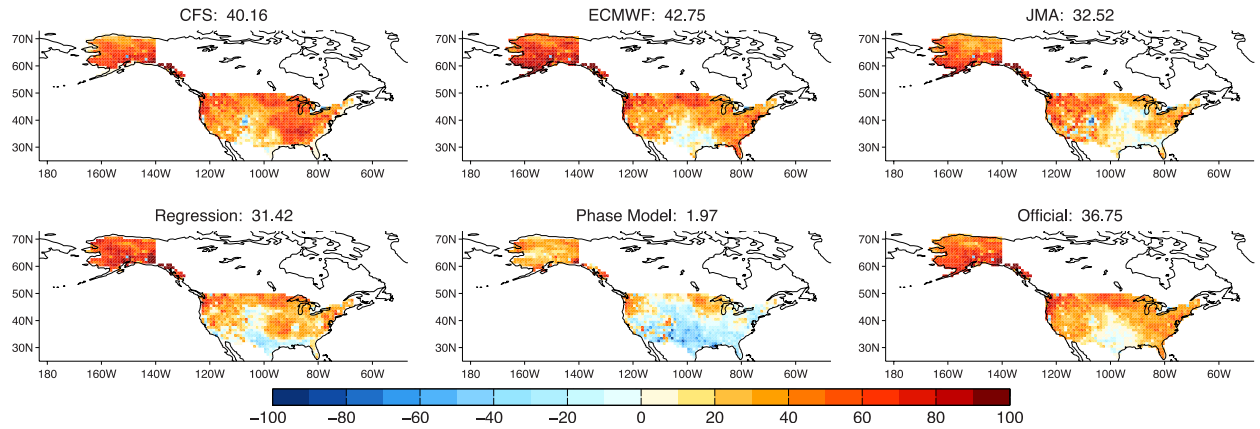

Fig. 3 T_{2m} HSS values for the listed dynamical and statistical guidance and official CPC outlooks. U.S. average values shown in panel titles.

often exists in the absence of an active MJO and non-neutral ENSO state, including for *P*, where trends are assumed to hold a lesser impact.

Comparisons can also be made between the relative performance of the PM and MLR, relating to the underlying assumptions used in building each statistical model (rightmost column of Figs. 1 and 2). In general, the MLR (cooler colors) outperforms the PM (warmer colors) with the exception of late (early) boreal summer (autumn). These differences between the two methodologies are generally statistically significant in both T_{2m} and *P*. This implies that the magnitude of large-scale teleconnections generally holds importance, and the linear assumption is reasonably well founded as utilized in the regression forecast. This also suggests that the importance of predictand mean shifts in the forecast PDFs dwarfs that of variance shifts within MJO and ENSO states, as there is no variance adjustment relative to climatology in the MLR, whereas the PM does account for variance differentiation dependent upon the initial state. Given the typically superior performance of the MLR relative to the PM and the similar drivers of each statistical method, it is reasonable to question about the necessity of the PM. While rooted in similar information, the differing methodologies of the MLR and PM can often yield differing probabilistic forecasts for geographic regions, while one method is skillful and the other lacks skill (not shown) where the tool with greater HSS can be emphasized.

4. Real-time performance

Results are presented here for the statistical guidance along with bias-corrected dynamical model ensemble guidance from several sources (CFSv2, ECMWF, and JMA) and official CPC outlooks for the "real-time" period since CPC began issuing Week 3-4 outlooks (18 September, 2015 - 8 July, 2016). HSS values are reported for all grid points (*i.e.* equal chances in the official CPC outlooks have 50% taken as hits and misses to create a consistent point of comparison with guidance products the encompass all points).

Figures 3 and 4 show the HSS values at the grid point level for T_{2m} and *P* respectively over the real-time period for the five guidance sources and official CPC outlooks. For T_{2m}, HSS values are shown to be largely skillful, with domain average values typically in the 30-40 range, indicative of 65-70% of forecasts being in the correct category relative to normal. For *P*, HSS values are lower with domain averages typically in the ±5 range, values that are likely not robust given limited sample for the real-time period. The worst performing forecast over the real-time period in both T_{2m} and *P* comes from the PM, likely due to the lack of canonical El Niño impacts observed during 2015-2016. Interestingly, the MLR seems to not suffer from the lack of typically observed ENSO impacts and performs closely to, or sometimes better than, dynamical model guidance and the official CPC outlooks.

In evaluating Figures 3 and 4 one notes the consistent regions of high HSS (for T_{2m} it is widespread outside the Southern Plains, for *P* it is focused in Alaska and the Northern/Central Plains) and low HSS (for T_{2m} the Southern Plains, for *P* the Southwest) for all forecasts with the exception of the PM. It is worth exploring whether there are possible co-dependent relationships between the dynamical and statistical

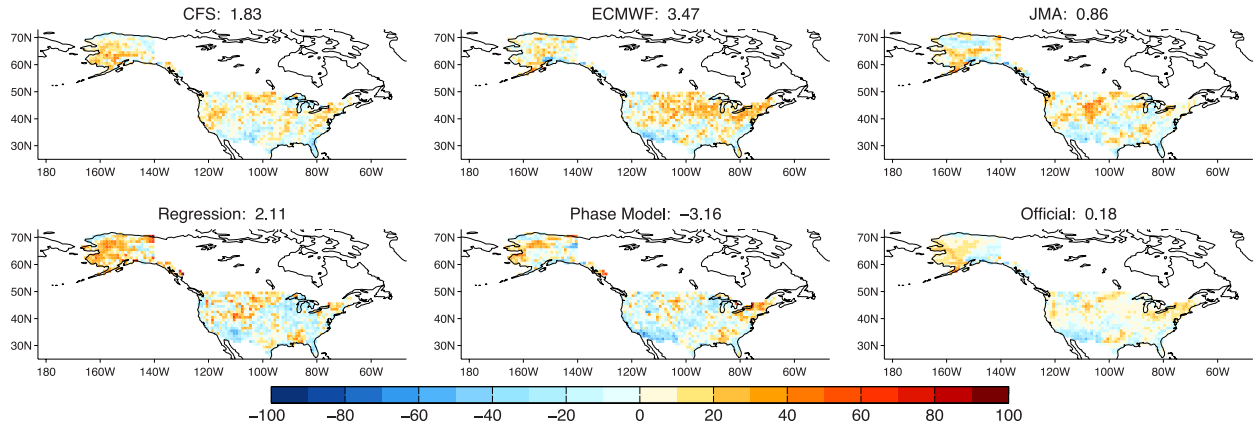

Fig. 4 As in Figure 3 but for *P*.

guidance, with the official outlooks having a clear dependency given that they are based on the aforementioned guidance. Figure 5 shows the time series of HSS spatially averaged across the U.S. for each of the forecast products over the real-time period. With the exception of the PM for T_{2m} it is apparent that dynamical and statistical guidance tends to cluster closely together on a weekly basis. Combined with Figures 3 and 4, these analyses suggest limited novel information between the dynamical models and ENSO/MJO/trend-based statistical guidance for the Week 3-4 timeframe. An analysis of the correlation coefficient at the grid-scale level of the forecast probabilities for T_{2m} and P of the weekly dynamical model forecasts with the MLR for the real-time period reveals several broad regions with values $\geqq 0.6$ (not shown). For T_{2m} these regions vary, and appear closely tied to dynamical model representation of long-term trend, while for P the highly correlated regions are focused in the west and south, regions where ENSO has a substantial footprint. Altogether, such analyses suggest limited novel information being provided from dynamical model guidance relative to the ability of the ENSO/MJO/trend baseline to characterize variance, and instead the model forecasts appear to be largely derived upon the model's representation of impacts from the latter modes of variability. Future work should seek to explore the utility of dynamical model guidance across climate timescales relative to background climate states, such as the three modes explored here at subseasonal periods, or ENSO and trend for the seasonal timeframe.

Acknowledgements. This project was funded by the NOAA/CPO MAPP program. We appreciate the respective forecast centers for supplying their dynamical model ensemble guidance. Augustin Vintzileos and Dan Collins respectively post-processed the CFS and JMA.

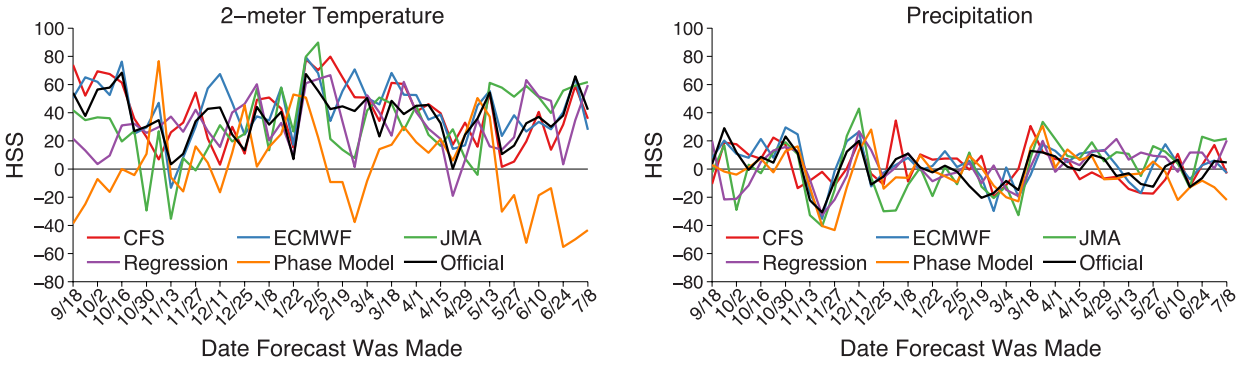

Fig. 5 Time series of U.S. averaged HSS for T_{2m} (left) and P (right).

References

Baxter, S., S. Weaver, J. Gottschalck, and Y. Xue, 2014: Pentad evolution of wintertime impacts of the Madden-Julian Oscillation over the Contiguous United States. *J. Climate*, **27,** 7356-7367.

Janowiak, J., G. Bell, and M. Chelliah, 1999: A gridded database of daily temperature maxima and minima for the conterminous US: 1948-1993. *NCEP/CPC Atlas 6*, Natl. Cent. For Environ. Predict., Camp Springs, MD.

Johnson, N. C., D. C. Collins, S. B. Feldstein, M. L. L'Heureux, and E. E. Riddle, 2014: Skillful wintertime North American temperature forecasts out to 4 weeks based on the state of ENSO and the MJO. *Wea. Forecasting*, **29,** 23-38.

Reynolds, R. W., T. M. Smith, C. Liu, D. B. Chelton, K. S. Casey, and M. G. Schlax, 2007: Daily high-resolution-blended analyses for sea surface temperature. *J. Climate*, **20,** 5473-5496.

Riddle, E. E., M. B. Stoner, N. C. Johnson, M. L. L'Heureux, D. C. Collins, and S. B. Feldstein, 2013: The impact of the MJO on clusters of wintertime circulation anomalies over the North American region. *Clim. Dyn.*, **40,** 1749-1766.

Wheeler, M. C. and H. H. Hendon, 2004: An all-season real-time multivariate MJO index: Development of an index for monitoring and prediction. *Mon. Wea. Rev.*, **132,** 1917-1932.

Xie, P., M. Chen, and W. Shi, 2010: CPC unified gauge-based analysis of global daily precipitation. Preprints, *24th Conf. on Hydrology*, Atlanta, GA, Amer. Meteor. Soc., 2.3A. (Available online at http://ams.confex.com/ams/90annual/techprogram/paper_163676.htm.)

Science and Technology Infusion Climate Bulletin
NOAA's National Weather Service
41st NOAA Annual Climate Diagnostics and Prediction Workshop
Orono, ME, 3-6 October 2016

Evaluating CPC's Operational Seasonal Temperature Forecasts: Why Aren't We Beating a Categorically Warm Forecast?

Stephen Baxter
Climate Prediction Center, NOAA/NWS/NCEP, College Park, Maryland

1. Introduction

The U.S. NOAA Climate Prediction Center (CPC) issues operational seasonal outlooks each month for the next 13 overlapping three-month seasons. The current process was implemented in 1995, and is three category in nature (above-, below-, or near-normal). There is also an equal chances (EC) category, in which there is no tilt away from climatological probabilities. Beginning in 2006, the forecast was informed by an objective consolidation of forecast tools detailed in O'Lenic *et al.* (2008). This work was initiated to see whether or not CPC's operational outlooks have adequately incorporated the consolidation forecast in the decade following its implementation.

CPC's seasonal forecast process is informed by various dynamical and statistical tools, including the Climate Forecast System (CFS), the National Multi-Model Ensemble (NMME), canonical correlation analysis, screening multiple linear regression, and constructed analog forecasts. A number of these are evaluated by an objective consolidation process that outputs probabilistic temperature and precipitation forecasts. Even following the implementation of the objective consolidation, the 0.5 month lead seasonal forecast skill has been slow to improve (Peng *et al.* 2012) for both temperature and precipitation. It is known that long term trends provide most of the forecast skill in temperature, with Peng *et al.* (2012) showing that a simple 10-year Optimal Climate Normals (OCN, average anomaly of the most recent 10 years) outperforms CPC's 0.5-month lead seasonal forecast. Only non-EC forecasts are considered in that calculation.

	1995-2005	2006-Present
Non-EC Forecast	21.83	26.93
All Forecasts	10.15	***15.91***
Coverage (%)	47.46	***58.54***

Table 1 Comparison of forecast skill and coverage before and after the implementation of the objective consolidation. Bold figures in the recent period suggest that the difference between the two periods is significant at or beyond the 98% level according to a two-sample *t*-test.

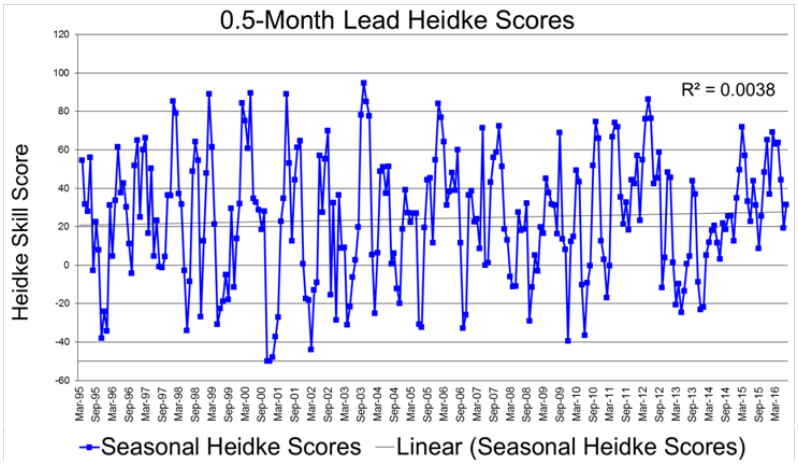

Fig. 1 Time series of official forecast skill for non-EC forecasts from 1995-present. No statistically significant trend is observed. The average over all forecasts is 24.36.

The goal of this study is two-fold:

- Evaluate the performance of CPC's official seasonal temperature forecasts in the decade following implementation of the objective consolidation.
- Consider as a benchmark a categorically warm forecast. This is the simplest assumption given a non-stationary climate.

Correspondence to: Stephen Baxter, Climate Prediction Center, NOAA/NWS/NCEP, 5830 University Research Court, College Park, MD; E-mail: Stephen.Baxter@noaa.gov

2. Methods

CPC's three category (above-, near-, and below-normal) 0.5-month lead seasonal temperature forecasts are evaluated over the CONUS on a 2°x2° grid from 1995-2016 over all seasons, with comparisons made for pre- and post-consolidation time periods. The verifying dataset results from a CPC analysis of Global Telecommunication System (GTS) data. The forecast and verification categories are the terciles derived from the appropriate climatology (*i.e.* the 1961-1990 climatology for forecasts issued in the 1990s).

Since CPC's official Government Performance and Results Act (GPRA) measure is the 48-month running Heidke skill score for non-EC areas of the 0.5-month lead seasonal temperature forecast, skill is assessed here using the Heidke skill score (HSS):

$$HSS = 100 * \frac{H-E}{T-E}$$

where H is the total number of hits, E is the number expected by chance, and T is the total number of forecasts. For a three category system, E=T/3. Heidke scores are also calculated for a categorically warm forecast ('warm dot') for comparison to the official forecast. Linear trends are calculated for the various time series, and statistical significance is assessed using a Student's *t*-test.

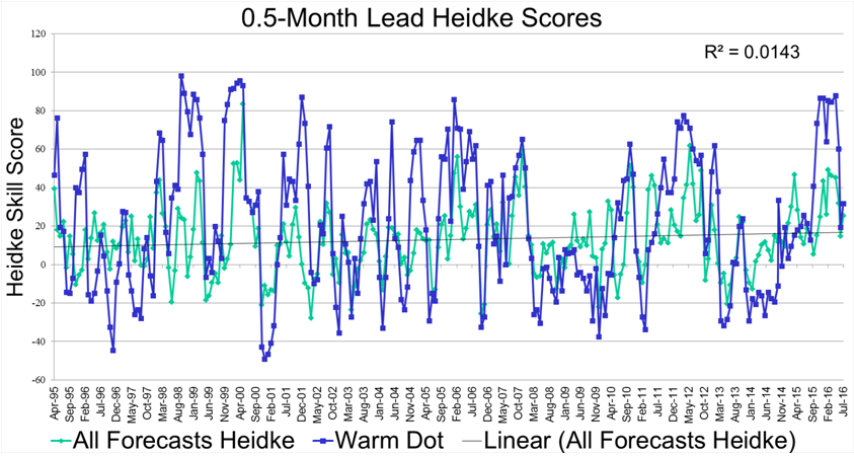

Fig. 2 Time series of official forecast skill from the official forecasts using all grid points (including EC). The time series of skill from a categorically warm forecast is also plotted. There is no signfiicant trend in either. The two time series are correlated at 0.61. The average of all official forecasts is 13.01; the average of a categorically warm forecast is 21.33.

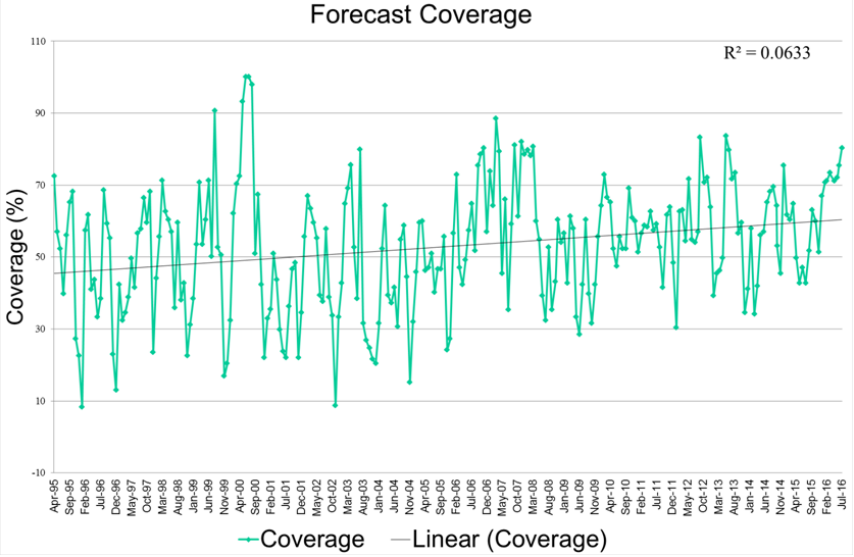

Fig. 3 Time series of forecast coverage from 1995-2016. This is the percentage of non-EC forecasts. There is a significant trend in this time series, owing mostly to a step evident when the consolidation became operational.

3. Results

The time series of official forecast skill (non-EC) from 1995 through summer 2016 is plotted in Figure 1. There is little trend in overall seasonal forecast skill since the implementation of the current forecast process in 1995. However, the implementation of the consolidation in 2006 did lead to a significant increase in forecast coverage and, as a result, all-forecasts skill (Figures 2 and 3). Since the linear trends may conceal differences in forecast skill between the pre- and post-consolidation periods, Table 1 summarizes the epochal differences in forecast skill, showing that there is indeed a statistically significant increase in 'all forecasts' skill and coverage of non-EC forecasts. Note that the non-EC forecast skill and 'all forecasts' skill are perfectly related by coverage, since EC forecasts are by definition correct one-third of the time, contributing a HSS value of 0.

While the consolidation has made a positive impact on the official forecast, a categorically warm forecast performs substantially better than the 0.5-month lead official forecast (Figure 4), and this difference grows with longer leads (not shown). The official forecast appears to add value to a categorically warm forecast over parts of the Northwest and extreme southern portions of the CONUS. This is likely due to skill afforded by the El Niño-Southern Oscillation phenomenon. Analyzing the time series of the difference in forecast skill between the official and categorically warm forecasts suggests that the categorically warm forecast is only outperformed when observations are cold (not shown).

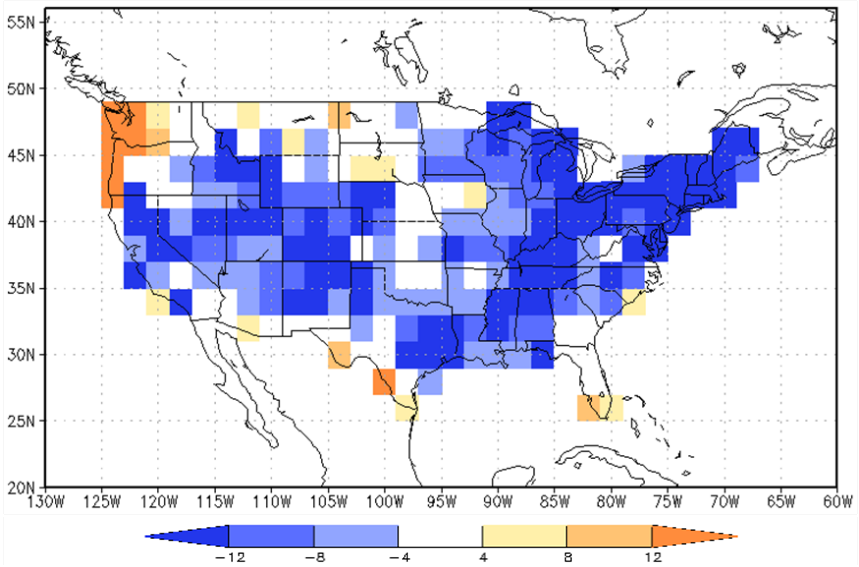

Fig. 4 Spatial distribution of the difference in HSS between the official forecast (all forecasts) over all seasons, and HSS of a categorically warm forecast. Blue colors show where a categorically warm forecast outperforms the official forecast.

4. Conclusions

While a statistically significant linear trend in the 0.5-month lead temperature forecast scores is not found, there is a significant difference in coverage and all-forecast (including the EC category) scores between the early (1995-2005) and late (2006-2016) periods. However, it is found that a categorically warm forecast is substantially better than CPC's seasonal forecasts, at least in a deterministic sense. The spatial distribution of forecast skill suggests that CPC's forecast skill derives almost entirely from trend, with some enhancement from ENSO over the Northwest, especially during spring (not shown).

Because CPC's official 0.5-month lead seasonal temperature forecasts do not adequately capture the long-term trends related to a non-stationary climatology, they can add little value to stakeholders. There are concrete steps that we can take to quickly improve our all-forecast skill scores and improve the value of our seasonal forecast products:

- Eliminate the 'Equal Chances' category from the seasonal temperature outlooks.
- Implement a new consolidation process that more transparently decomposes the seasonal forecast into components related to trends, decadal variability, and interannual variability.
- Explore issuing forecasts relative to a current climatology to isolate potentially predictable patterns of decadal and interannual variability; the available skill may currently be masked by mishandling of long-term trends.

References

O'Lenic, E. A., 2008: Developments in operational long-range climate prediction at CPC. *Wea. Forecasting*, **23**, 496–515.

Peng, P., A. Kumar, M. S. Halpert, and A. Barnston, 2012: An analysis of CPC's operational 0.5 month lead seasonal outlooks. *Wea. Forecasting*, **27**, 898–917, doi:10.1175/WAF-D-11-00143.1.

3. ENSO & Recent Climate Anomalies

41th NOAA Annual Climate Diagnostics and Prediction Workshop

3-6 October 2016, Orono, Maine

Science and Technology Infusion Climate Bulletin
NOAA's National Weather Service
41st NOAA Annual Climate Diagnostics and Prediction Workshop
Orono, ME, 3-6 October 2016

Remarkable Increase in Global Sea Surface Temperature in 2014 and 2015: How Was It Related to El Niño and Decadal Variability?

Yusuke Urabe[1], Tamaki Yasuda[1], Hitomi Saitou[1], Kazuto Takemura[1], Yoshinori Oikawa[1], and Shuhei Maeda[2]

[1]*Climate Prediction Division, Japan Meteorological Agency*

[2]*Meteorological Research Institute, Japan Meteorological Agency*

1. Introduction

The globally averaged sea surface temperature (GASST) exhibits centennial warming trend, well-known as global warming, with decadal time scale fluctuations (Fig. 1a). While the annual mean GASST for the 2000-2013 period has stayed below the previous highest record of 1997/98, the recent GASST shows the rapid warming after 2013 and continuously breaks the highest record in 2014/15 and 2015/16. The increase is accompanied by a strong El Niño event, presenting, at least qualitatively, consistent condition with those indicated by previous studies such as Trenberth *et al.* (2002). However, the recent increase of GASST and observed anomalies are rather insistent and it is worth examining how much the El Niño event attributed the recent warming of GASST and investigating other contributing factors.

2. Data and methods

SST and subsurface temperature distributions are obtained via objective analysis (COBE-SST; Ishii *et al.* 2005) and ocean data assimilation (MOVE-G2; Toyoda *et al.* 2013) operated by the Japan Meteorological Agency (JMA). The Japanese 55-year Reanalysis (JRA-55) dataset (Kobayashi *et al.* 2015) is used to investigate atmospheric circulation patterns. Climatology is defined as average for the period from 1981 to 2010. The SST anomaly averaged in the NINO-3 region (5°S–5°N, 150° –90°W) is referred to as "NINO-3 SST", and its anomaly is used as an indicator of the El Niño-Southern Oscillation (ENSO). Considering typical ENSO lifecycles, annual mean values are defined as average from July to June. Average from July 2014 to June 2015 is termed annual mean value for 2014/15, for example.

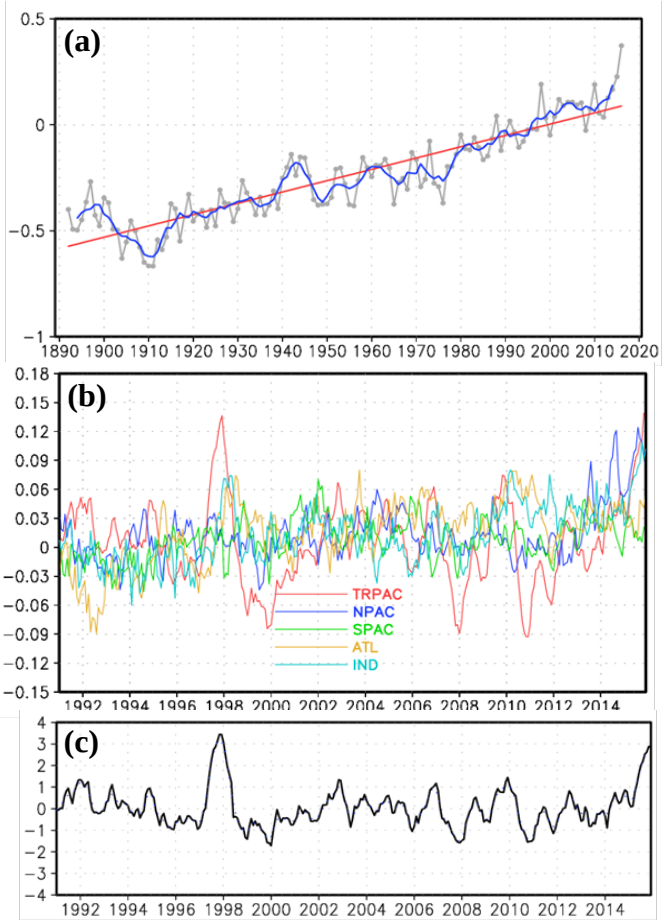

Fig. 1 (a) Time series of global averaged sea surface temperature (GASST) anomalies (°C). The gray, blue, and red lines represent annual mean GASST anomalies, their five-year running mean, and the long-term linear trend, respectively. (b) Monthly time series of contributions to a GASST anomaly in the tropical Pacific (10°S–10°N) (red line), North Pacific (dark blue line), South Pacific (green line), Atlantic (yellow line), and Indian Ocean (light blue line). (c) Monthly time series of anomaly of NINO-3 SST.

Correspondence to: Yusuke Urabe, Climate Prediction Division, Japan Meteorological Agency, 1-3-4 Otemachi Chiyoda-Ku, Tokyo, Japan; y_urabe@met.kishou.go.jp

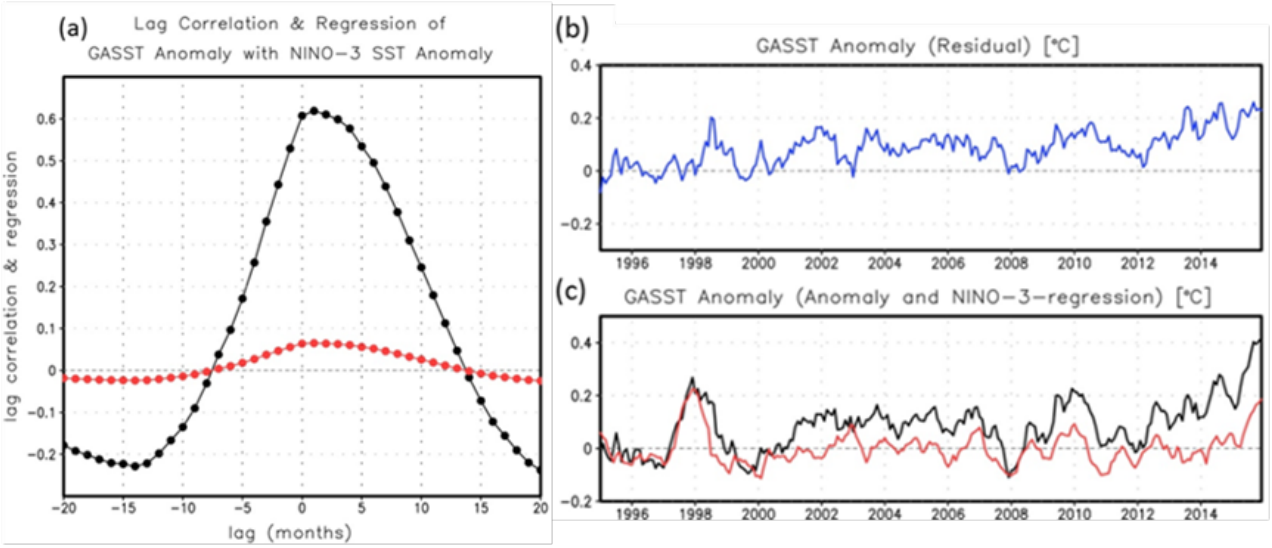

Fig. 2 (a) Lag correlation (black line) and regression (red line) coefficients between anomalies of GASST and NINO-3 SST. Positive lag means NINO-3 SST leads GASST. (b, c) Time series of GASST anomalies (black line) separated into the component calculated from the one month lag regression to NINO-3 SST anomalies (red line) and the residual component (blue line).

3. Time series and contributing factors

Figure 1b shows the time series of contributions of SST anomalies integrated in the each basin to GASST. These contributions are determined from the area-integrated SST anomaly in each basin divided by the area of the global ocean domain.

Historically, the tropical Pacific (red line) has the greatest contribution, and interannual variabilities in the tropical Pacific and Indian Ocean (light blue line) associated with ENSO are evident, which are consistent with previous studies (*e.g.* Klein *et al.* 1999). Indeed, the previous highest record was marked in 1997/98 when a strong El Niño event occurred and increases in GASST and NINO-3 SST are comparable to those observed in recent years. On the other hand, the North Pacific (dark blue line), which started to get warmer around 2013, stands out in recent years compared with 1997/98.

Trenberth *et al.* (2002) show that the global surface temperature increases accompanying El Niño events with a lag of several months. According to the lag correlation and regression coefficients shown in Fig. 2a, the GASST exhibits a similar response with rather small lag and a maximum regression of +0.08°C per 1°C anomaly of NINO-3 SST with one-month lag. Then, the GASST anomalies separated into a component calculated from the one-month-lag regression to NINO-3 SST anomalies (NINO-3-regression) and the residual component (Figs. 2b, c). NINO-3-regression compensates for much of GASST increase from 2014/15 to 2015/16, indicating that the remarkable increase in this period is mainly attributed to the development of a strong El Niño event (Fig. 2c). The residual component increased in around 2013 and 2014 and positive values persisted since then, which is supposed to correspond to the positive anomalies in the North Pacific and contribute to the extremely large GASST anomaly drastically exceeding that of 1997/98. The remarkably large positive anomaly observed in the North Pacific in 2013 is referred to as “blob” and attributed to atmospheric forcing including advection and entrainment in addition to surface heat flux in the recent study by Bond *et al.* (2015). However, detailed mechanism that induced the anomalous atmospheric forcing is still unclear and further investigation is necessary.

4. Variability in horizontal and vertical temperature distribution

In spatial distribution of anomaly of SST and vertically averaged temperature (VAT) from the surface to 300-m depth, La Niña-like condition, which is indicated to have persisted since around 2000 to 2013 (Urabe and Maeda, 2014; and references therein) is observed in 2013/14 (Fig. 3a, d). In 2014/15 (Fig. 3b, e), positive anomalies propagated from the western part to the central and eastern part, and the amplitude of which is

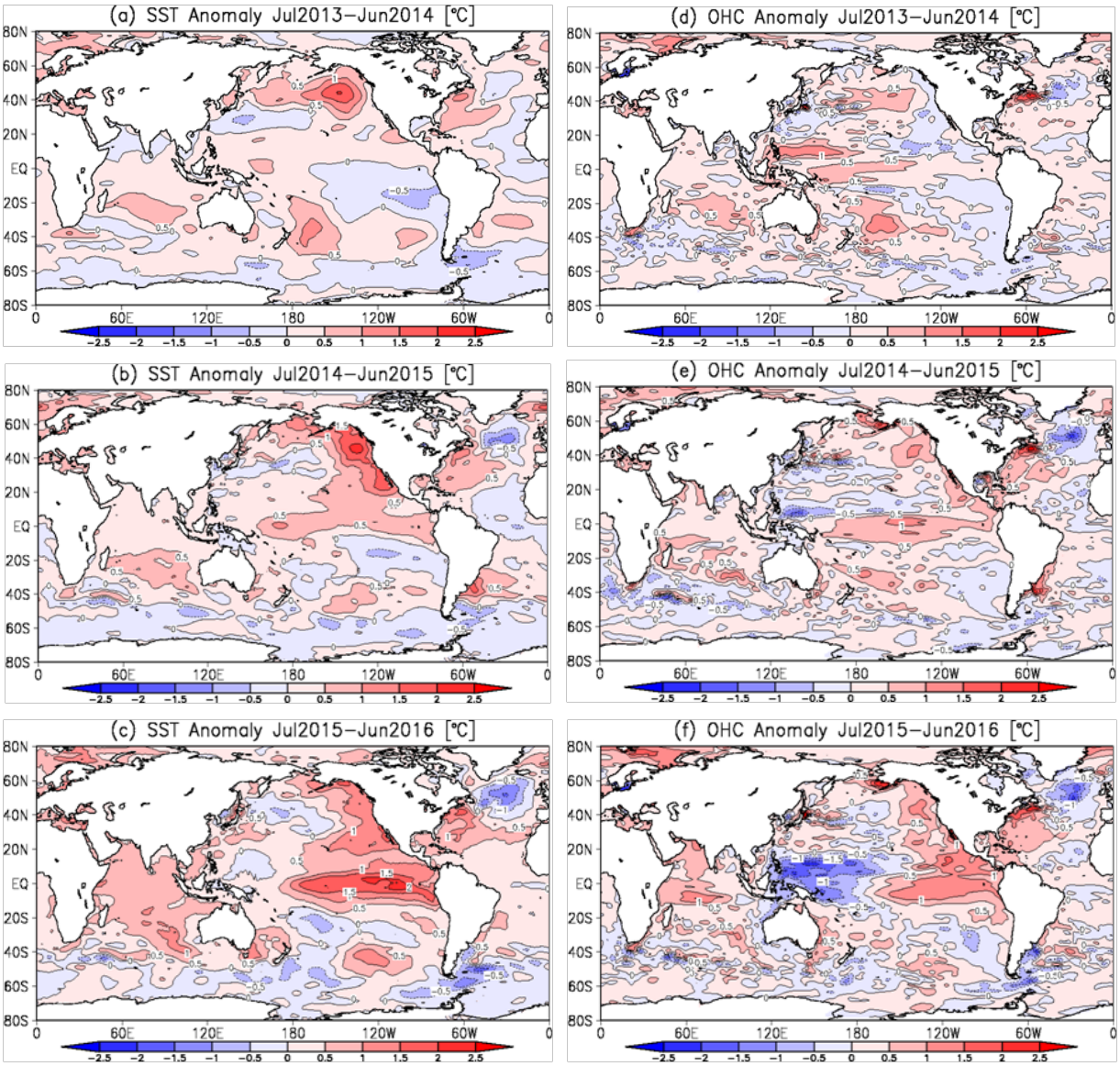

Fig. 3 Annual mean anomalies of SST in (a) 2013/14, (b) 2014/15, and (c) 2015/16. (d–f) Same as (a–c) for vertically averaged temperature (VAT) from sea surface to 300-m depth. Units are °C.

significantly enhanced in the eastern part in 2015/16 (Fig. 3c, f). Significant warming in SST is also recognized in the North Pacific around the west coast of North America (Figs. 3a-c). These spatial patterns of warming are quite consistent with the area-integrated anomalies presented in Fig. 1b. These variabilities indicate that drastic changes have occurred not only at the sea surface but also in the ocean subsurface associated with the development of El Niño.

Along with the changes in horizontal patterns, distinct changes in vertical temperature profile also proceeded in 2014/15/16. In a time–depth diagram of the area-averaged temperature in the tropical Pacific, positive anomalies had been observed at a 100–300-m depth, with no clear anomalies detected near the sea surface until the beginning of 2014 (Fig. 4a). Subsequently, the positive anomalies were replaced to a 30–100-m depth in around spring 2014, which indicates vertical temperature profile in the subsurface remarkably changed along with the surface warming and subsurface cooling, which can be consistently understood as weakening of thermocline gradient which is well known as the typical variability associated with El Niño, despite the El Niño event not being evident in the SST field (Fig. 3b). Finally, the positive anomalies

expanded into the sea surface and intensified in 2015 along with the development of a strong El Niño event and negative anomalies appeared around 100–300-m depth.

The warming near the surface was observed in 1997/98 (Fig. 4b) as in 2015/16. However, significant positive temperature anomalies in subsurface region (deeper than 100m) before an occurrence of El Niño event, which had been continuously observed until 2013 in Fig.4a, were not recognized before the early 1997. In the recent years, the subsurface positive anomalies persisted during surface warming in 2014, which could contribute to further surface warming in 2015/16. As a result, significant positive anomalies near the surface continued for more than two years. In contrast, for 1997/98, vertical reversal of temperature anomalies between surface and subsurface started around the beginning of 1997 from temporal and weak La Niña condition and after that positive anomaly near the surface continued only for a little more than one year. The results shown here suggest that the background oceanic condition, i.e., subsurface positive temperature anomaly in tropical Pacific, is one of key factors that generate difference between 1997/98 and 2014/15/16. Those subsurface temperature anomalies correspond to positive VAT anomalies in the western tropical Pacific observed before 2013 (Figs. 3d, 4a).

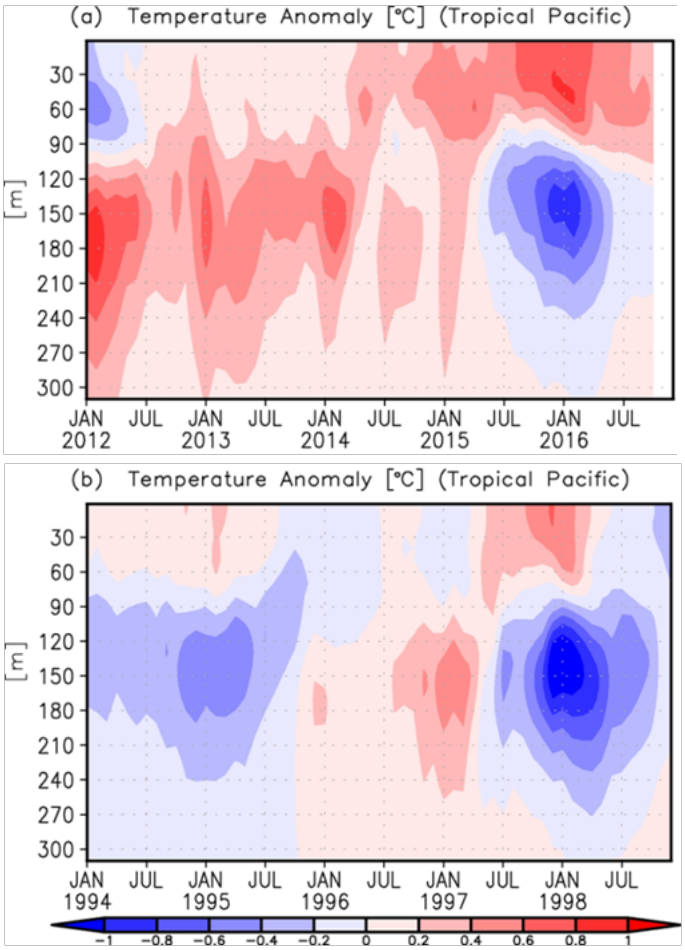

Fig. 4 (a) Time–depth diagram of temperature averaged in tropical Pacific [20° S–20° N, 100° E–100° W] for (a) 2012-2016 and (b) 1994-1998.

5. Summary and discussion

The remarkable increase in the GASST in 2014 and 2015 is generally attributed to the emergence and development of an El Niño event, and warming in the North Pacific also contributed to extreme anomaly observed in 2015/16, substantially larger than that in 1997/98 when the previous highest record was marked associated with a strong El Niño. In the tropical Pacific, positive subsurface temperature anomalies accumulated in the west, which was redistributed to the sea surface, stretching from the central to eastern part in conjunction with the development of the El Niño event. The warmed ocean surface in the tropical Pacific persisted from early 2014 to early 2016, much longer than that observed from early 1997 to mid-1998.

Recent studies indicate that La Niña-like conditions associated with decadal climate variability trigger ocean heat uptake into Pacific subsurface and play important role in weakened increase of the global surface temperature (the so-called “hiatus”; Easterling and Wehner, 2009) in the last decade (England *et al.* 2014; Liu *et al.* 2016). Urabe and Maeda (2014) indicate that positive subsurface temperature anomaly in the western tropical Pacific, especially off-equator from near Philippines to the date line (Fig. 3d), had been continuously accumulating along with the recent La Niña-like condition in decadal timescale. The temperature anomaly redistribution between subsurface and surface observed in recent years are in stark contrast with the conditions continued during the hiatus, in other words, the recent warming event is possibly accompanied by a rebound from the hiatus. Although it is difficult to show whether global warming hiatus ended around 2014/15/16, we should continue to monitor the climate system carefully in order to assess the subsequent status of global warming.

References

Bond, N. A., M. F. Cronin, H. Freeland and N. Mantua, 2015: Causes and impacts of the 2014 warm anomaly in the NE Pacific. *Geophys. Res. Rett.*, **42**, 3414-3420, doi: 10.1002/2015GL063306.

Easterling, D. R. and M. F. Wehner, 2009: Is the climate warming or cooling? *Geophys. Res. Rett.*, **36**, L08706, doi:10.1029/2009GL037810.

England, M. H., S. McGregor, P. Spence, G. A. Meehl, A. Timmermann, W. Cai, A. S. Gupta, M. J. McPhaden, A. Purich and A. Santoso, 2014: Recent intensification of wind-driven circulation in the Pacific and the ongoing warming hiatus. *Nat. Climate Change*, **4**, 222–227, doi:10.1038/NCLIMATE2106.

IPCC, 2013: Climate change 2013: the physical science basis. Working group I contribution to the fifth assessment report of the intergovernmental panel on climate change. Cambridge University Press, Cambridge, UK and New York, USA.

Ishii, M., A. Shouji, S. Sugimoto and T. Matsumoto, 2005: Objective analyses of sea-surface temperature and marine meteorological variables for the 20th century using ICOADS and the Kobe Collection. *Intl. J. Climatol.*, **25**, 865–879.

Klein, S., B. J. Soden and N.-C. Lau, 1999: Remote sea surface temperature variations during ENSO: Evidence for a tropical atmospheric bridge. *J. Climate*, **12**, 917–932.

Kobayashi, S., Y. Ota, Y. Harada, A. Ebita, M. Moriya, H. Onoda, K. Onogi, H. Kamahori, C. Kobayashi, H. Endo, K. Miyaoka and K. Takahashi, 2015: The JRA-55 reanalysis: General specifications and basic characteristics. *J. Meteor. Soc. Japan*, **93**, 5-48, doi:10.2151/jmsj.2015-001.

Liu, W., S. P. Xie and J. Lu, 2016: Tracking ocean heat uptake during the surface warming hiatus. *Nature commun.* **7**:10926 doi:10.1038/ncomms10926.

Toyoda, T., Y. Fujii, T. Yasuda, N. Usui, T. Iwao, T. Kuragano and M. Kamachi, 2013: Improved analysis of seasonal-interannual fields using a global ocean data assimilation system. *Theor. Appl. Mech. Jpn.*, **61**, 31–48.

Trenberth K. E., J. M. Caron, D. P. Stepaniak and S. Worley, 2002: Evolution of El Niño-Southern Oscillation and global atmospheric surface temperatures. *J. Geophys. Res.*, **107**, AAC 5-1 – AAC 5-17, doi:10.1029/2000JD000298

Urabe, Y. and S. Maeda, 2014: The relationship between Japan's recent temperature and decadal variability. *SOLA*, **10**, 176-179, doi:10.2151/sola.2014-037.

Science and Technology Infusion Climate Bulletin
NOAA's National Weather Service
41st NOAA Annual Climate Diagnostics and Prediction Workshop
Orono, ME, 3-6 October 2016

Atmospheric Secular Mode and Its Possible Impact to Recent El Niño Teleconnection

Peitao Peng and Arun Kumar
Climate Prediction Center, NOAA/NWS/NCEP, College Park, Maryland

1. Atmospheric secular mode

Secular changes of the atmospheric circulation are usually illustrated with linear trend. Drawbacks of this linear approximation are obvious, for example, it can't catch decadal and inter-decadal variability. An attempt to resolve this issue is by using empirical orthogonal function (EOF) analysis. The outcome, however, is not quite promising, because the trend tends to be mixed with several other modes, among which is the ENSO teleconnection mode. The mixing of the trend with ENSO teleconnection may not be physically meaningful, since the Nino 3.4 SST index itself shows little long-term trend. Inspired by the successful separation of ENSO teleconnection mode from other modes in Peng *et al.* (2014), we developed a new method to retrieve atmospheric secular mode. The procedure is to remove ENSO teleconnection pattern linearly from the data (*e.g.* 200hPa height) first, and then apply EOF analysis to the residual. With this

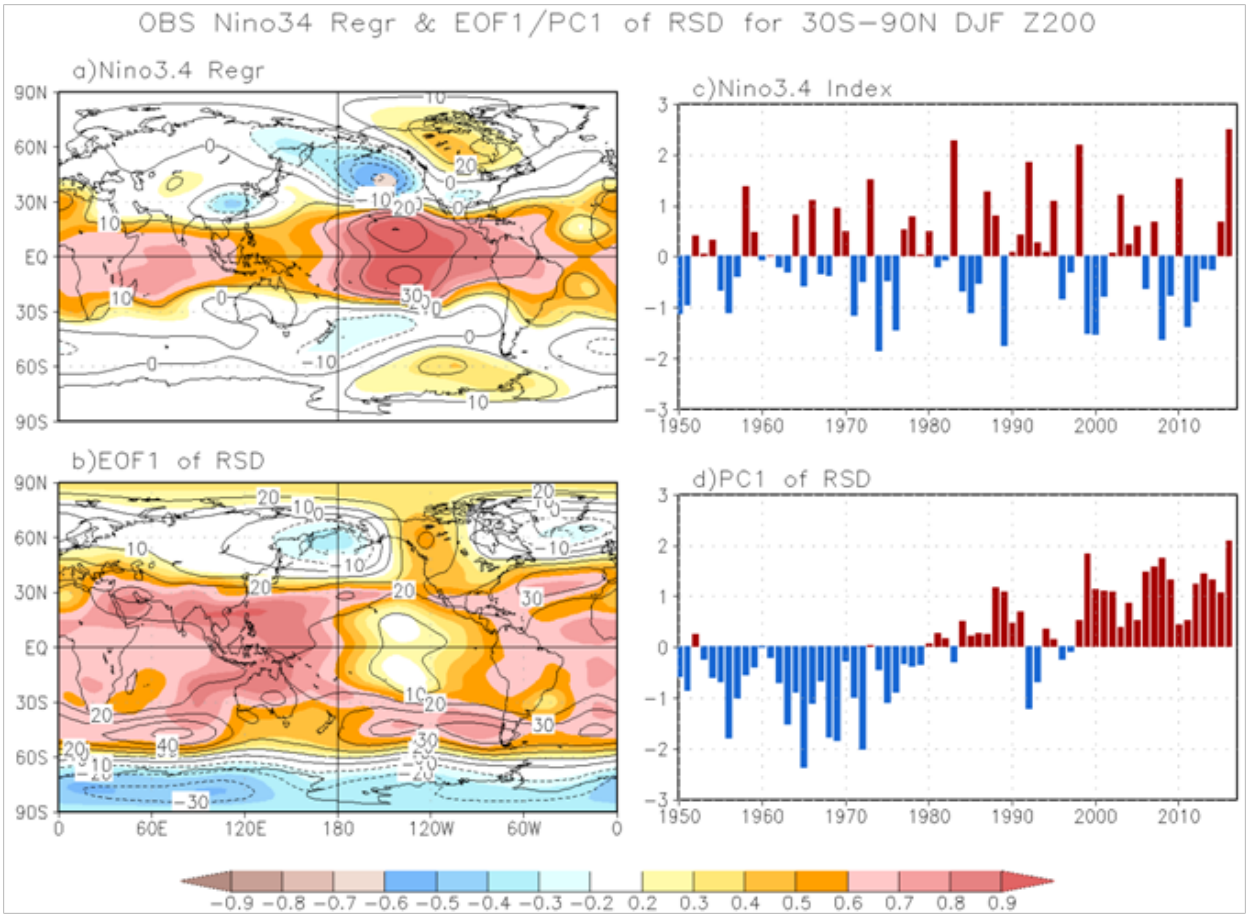

Fig. 1 ENSO teleconnection mode of DJF Z200 (upper) and the EOF1/PC1 of the DJF Z200 residual with ENSO mode linearly removed (lower). The spatial patterns are drawn with the regression (contours) and correlations (shadings) of the Z200 field to their corresponding time series (right panels).

Correspondence to: Peitao Peng, Climate Prediction Center, NOAA/NWS/NCEP, 5830 University Research Court, College Park, MD; E-mail: peitao.peng@noaa.gov

procedure, it is found that the first EOF mode can represent both long-term trend and inter-decadal variability. Further analysis indicates that the secular mode is related to the variation of sea surface temperatures (SSTs) in tropical Pacific warm pool and the Indian Ocean. This mode is potentially useful in climate diagnostics and short-term climate prediction.

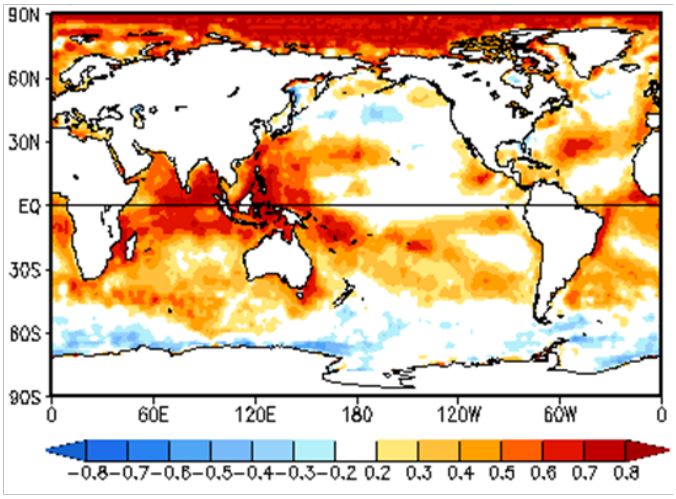

Fig. 2 Correlations of the PC1 of the DJF Z200 residual (Fig. 1a) to the DJF SSTs over 1949-2016 period.

Fig. 1 shows the ENSO teleconnection mode and the secular mode of DJF Z200. The ENSO teleconnection mode is well known, and a notable feature worth to be emphasized here is its biggest amplitude in the 2015/16 winter. For the secular mode, the spatial pattern exhibits mostly positive in the tropics, and wavy in extra-tropics. A notable feature in the northern hemisphere (NH) is a ridge centered over the west coast of North America. The time series is dominated by a warming trend, and superimposed to the trend is inter-decadal and inter-annual fluctuations. Note the magnitude of the time series at 2015/16 is the highest in the data period.

Fig. 2 gives the correlations of SST to the time series of the secular mode. Obviously, the higher correlations are in the tropical Pacific warm pool and the Indian Ocean, suggesting the secular mode is likely forced by the air-sea interactions in those regions.

2. Possible impact on 2015/16 El Nino teleconnection

An immediate application of the secular mode is to interpret the abnormal El Nino teleconnection pattern in 2015/16 winter. It is well known that the 2015/16 El Nino is among the strongest in record, the North American climate in the winter, however, was quite different from the canonic patterns corresponding to strong El Nino. The significant different features include the precipitation deficit in southern California and

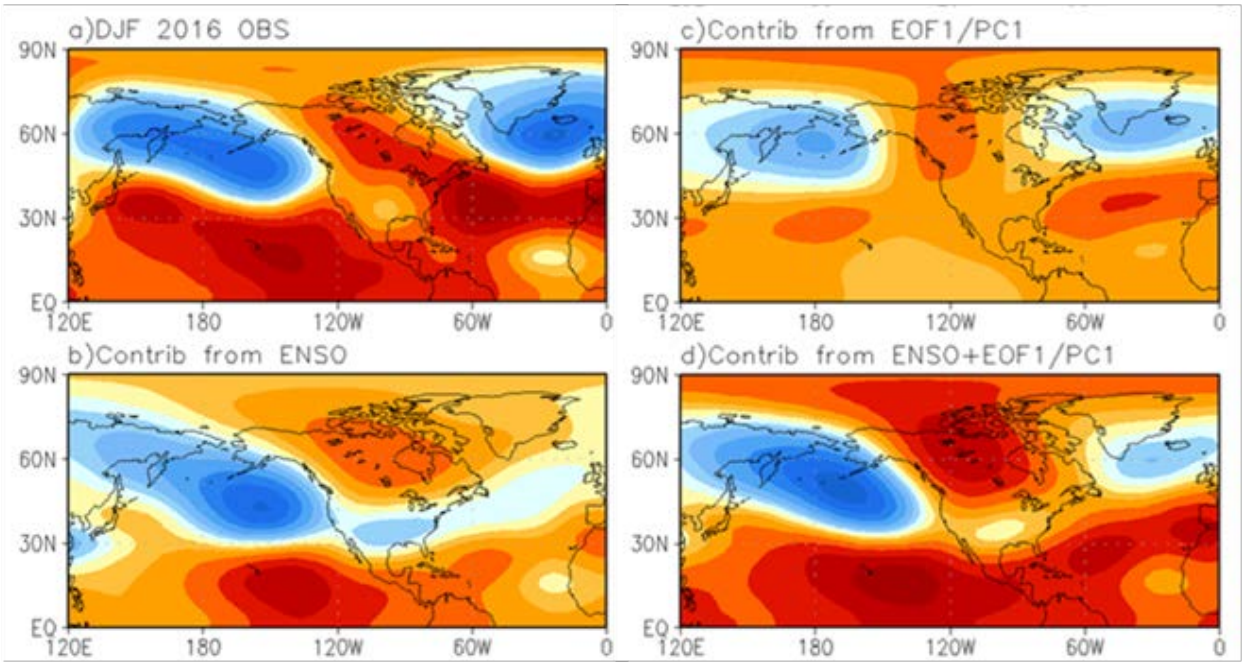

Fig. 3 DJF Z200 anomalies observed in 2015/16 (a), reconstructed with ENSO mode (b), with the secular mode (c) and with the both modes (d).

the moderate warming in the southern part of the United States, whereas in past strong El Nino winters, whole California had abundant rainfall and the southern states were mostly colder. In order to understand the unusual climate, we applied the analysis procedure describe above to the DJF 200hPa height (Z200) field since 1949. It is found that the secular mode, with its biggest amplitude ever since 1950, brought a strong ridge in the western coast of the continent, thus hindered storms to reach southern California. This mode also had contribution to the warming in the southern states for that winter.

Fig. 3 shows the Z200 anomalies observed in 2015/16 winter (panel a), and reconstructed with ENSO mode alone (panel b), with secular mode alone (panel c) and with the both modes (panel d). Panel b gives the canonic ENSO teleconnection pattern, where the low extending to west coast and southern states of US would bring excessive rainfall and lower temperature there. Panel c tells the impact of the secular mode, that is, building up a ridge over the west coast and pushing the jet northward over the ocean. As a result, the secular mode would cause less rainfall and warmer temperature in California and southern states, opposite to the ENSO effect. Panel d, being a combination of panel b and c, well resembles panel a, thus demonstrates that the secular mode is likely an important cause of the non-canonic El Nino teleconnection pattern in the winter.

References

Peng, P., A. Kumar, and B. Jha, 2014: Climate mean, variability and dominant patterns of the Northern Hemisphere wintertime mean atmospheric circulation in the NCEP CFSv2. *Clim. Dyn.*, **42**, 2783-2799.

Science and Technology Infusion Climate Bulletin
NOAA's National Weather Service
41st NOAA Annual Climate Diagnostics and Prediction Workshop
Orono, ME, 3-6 October 2016

Interaction Between the Indian Ocean Dipole and ENSO Associated with Ocean Subsurface Variability

Hui Wang[1], Arun Kumar[1], and Raghu Murtugudde[2]
[1]*Climate Prediction Center, NOAA/NWS/NCEP, College Park, Maryland*
[2]*ESSIC, University of Maryland, College Park, MD*

1. Introduction

The Indian Ocean dipole (IOD) is an intrinsic coupled mode of variability in the tropical Indian Ocean. It has broad impacts on regional climate. An IOD index is defined as the difference between sea surface temperature (SST) anomalies averaged over the western Indian Ocean (WIO, 50°–70°E, 10°S–10°N) and eastern Indian Ocean (EIO, 90°–110°E, 10°S–Eq.). An important issue in the studies of IOD is the relationship between IOD and the El Niño-Southern Oscillation (ENSO) and the potential feedbacks from each other. Previous studies have shown that the development of IOD can be independent of ENSO, but ENSO may exert significant influence. In recent years, it has also been found that IOD can affect ENSO. Clearly, there exists an intimate interaction between IOD and ENSO but the detailed phenology of their mutual evolution has not been reported thus far.

Although a positive (negative) IOD tends to co-occur with El Niño (La Niña), the spatial-temporal covariations of these two major climate modes have not been well documented. Our earlier modeling study (Wang *et al.* 2016) documented the time evolution of IOD and the associated ocean subsurface variability in the absence of ENSO. The current study is aimed at examining the time evolution of IOD in the presence of ENSO and characterizing the interaction between IOD and ENSO. The present work complements our previous analysis by looking at the spatial-temporal covariations between IOD and ENSO, identifying any lead-lag relationships between them, and quantifying the influence of ENSO on IOD. This is done by analyzing a 500-year long fully coupled model simulation, which retains the ENSO variability (referred to as ENSO run hereafter), and comparing the results with a parallel 500-year simulation with the ENSO variability suppressed

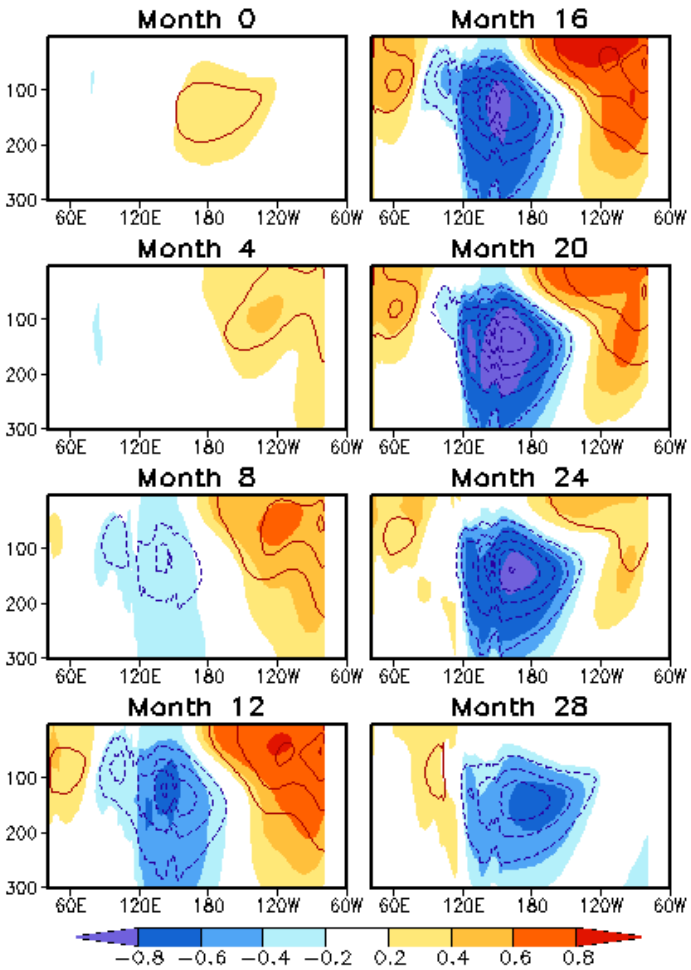

Fig. 1 Correlation (shading) and regression (contour) coefficients of monthly mean ocean temperature averaged over 10°S–5°N against the PC time series of the first EEOF from month 0 to month 28. Month 28 denotes ocean temperature lagging PC1 by 28 months. Contour interval is 0.25 K with negative values dashed and zero contours omitted.

Correspondence to: Hui Wang, Climate Prediction Center, NOAA/NWS/NCEP, 5830 University Research Court, College Park, MD; E-mail: hui.wang@noaa.gov

(daily SST nudged to its climatology in the tropical Pacific; referred to as no-ENSO run hereafter). The latter was analyzed in Wang *et al.* (2016) to characterize the spatial-temporal evolution of IOD in the absence of ENSO. The differences in the characteristics of IOD between the two simulations will indicate the impact of ENSO on IOD. Both simulations were conducted with the NCEP CFS version 1 coupled model.

2. Covariations between IOD and ENSO

The spatial-temporal covariations between IOD and ENSO are examined by using the extended empirical orthogonal function (EEOF) method. The EEOF analysis is based on the spatial-temporal covariance matrix of monthly mean ocean temperature from the last 480-year ENSO run averaged between 10°S and 5°N with a temporal window of 18 months. The longitude–depth domain for the EEOF analysis is from 50°E to 180° over the tropical Indian Ocean and western Pacific and from the 5-m depth to the 225-m depth below the sea surface.

Figure 1 shows the first EEOF mode in the form of correlation and regression maps for ocean temperature averaged between 10°S and 5°N. They are obtained by correlating and regressing the ocean temperature anomalies against the principal component (PC) time series of EEOF1 for ocean temperature lagging PC1 by 0 month to 28 months. This mode accounts for 31% of surface and subsurface temperature variance in the tropical Indian Ocean and western Pacific.

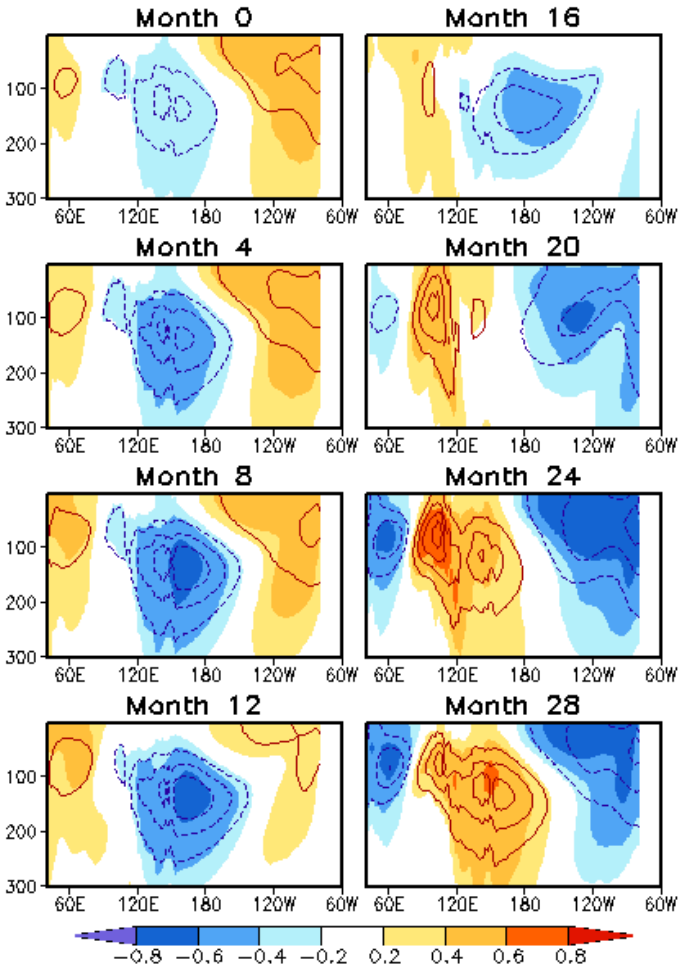

Fig. 2 Same as Fig. 1 but for the second EEOF.

The time evolution of EEOF1 begins with warm subsurface temperature anomalies in the tropical western Pacific (Fig. 1, month 0). From month 0 to 4, they propagate eastward along the thermocline and generate warm SST anomalies in the eastern and central Pacific, which leads to Bjerknes feedback and an El Niño. In the following months (months 8-16), the El Niño continues to grow with increases in SST and subsurface temperature anomalies. In the meantime, cold temperature anomalies develop in the tropical western Pacific, as well as in EIO while warm anomalies develop in WIO. The latter two form a positive IOD. During the decay phase of the El Niño (months 16-24), warm temperature anomalies in WIO move eastward and replace cold anomalies in EIO, nearly synergistically with the eastward propagating cold anomalies in the subsurface tropical Pacific. As a consequence, a basin-wide warming takes place in both the surface and subsurface tropical Indian Ocean, consistent with the processes of the tropical Indian Ocean surface and subsurface responses to El Niño found in previous studies. Figure 1 illustrates that the development of a positive IOD and its transition to a basin-wide warming in the tropical Indian Ocean are embedded in the evolution of an El Niño and thus lag the El Niño. EEOF1 reflects the IOD response to ENSO.

The second EEOF is shown in Fig. 2, which accounts for 16% of the surface and subsurface temperature variance. In month 0, there is an El Niño in the tropical Pacific and a positive IOD in the tropical Indian Ocean. Similar to EEOF1 (Fig. 1, months 16-24), the decay of the El Niño in EEOF2 is associated with the thermocline variability in the tropical Pacific and eastward propagating temperature anomalies in the tropical Indian Ocean, leading to a basin-wide mode (Fig. 2, months 8-16). In month 20, the tropical Pacific is characterized by a La Niña, whereas EIO is dominated by warm anomalies. In the following months, cold

anomalies develop in WIO, leading to a negative IOD. Additionally, there are weak warm anomalies in the western Pacific in month 20 following the development of warm anomalies in EIO. These warm anomalies continue to intensify during months 20-28, shift eastward, and continue to prepare the deep tropical Pacific for the next El Niño. The warm anomalies in the surface and subsurface of the western Pacific come after the warm anomalies in EIO originating from WIO. This suggests that both the IOD and the following basin-wide mode lead the forthcoming El Niño.

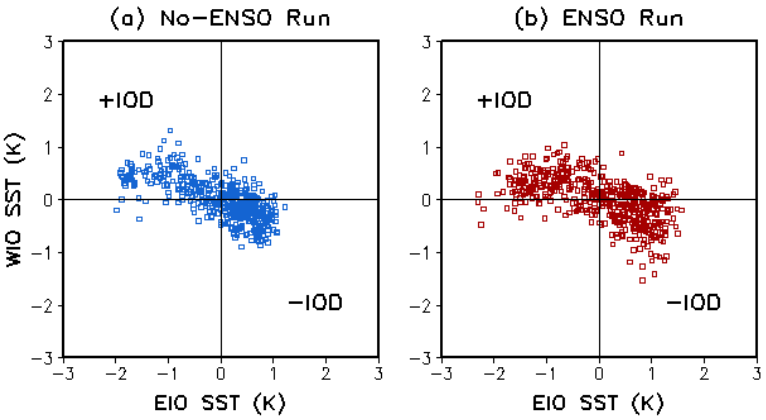

Fig. 3 Scatter plot of 480-year EIO SST versus WIO SST in SON for (a) the no-ENSO run and (b) the ENSO run.

The two leading EEOF modes capture the covariations between IOD and ENSO that are associated with tropical ocean subsurface variability. In both modes, there are strong links between surface and subsurface temperature anomalies. In the first mode, a positive IOD lags an El Niño. In the second mode, a positive IOD and a basin-wide mode lead the development of warm ocean temperature anomalies in the western Pacific and the occurrence of El Niño. The results suggest that the IOD and the basin-wide warming in the tropical Indian Ocean may be a response to El Niño, which in turn may help the development of El Niño. Their two-way interaction is further examined in the following two sections.

3. Impact of ENSO on IOD

A comparison of the power spectra of the IOD index between the ENSO run and no-ENSO run (not shown) suggests that ENSO significantly enhances the variability of IOD at interannual time scale. ENSO can also affect the intensity of IOD. Figure 3 shows the scatter plot of EIO SST anomaly versus WIO SST anomaly in September-November (SON), the peak season of IOD, for both the ENSO run and no-ENSO run. It is evident that the amplitudes of these SST anomalies are larger in Fig. 3b than in Fig. 3a, especially in the right lower quadrant during the negative IOD phase. Compared to the no-ENSO run, the SST variance in the ENSO run is enhanced by 42% and 25%, respectively, in the eastern and western poles of IOD. The variance of the IOD index is increased by 30%. The corresponding increases are 14% (eastern pole), 2% (western pole), and 6% (dipole) when IOD is in a positive phase. In contrast, they are 55%, 50%, and 52% when IOD is in a negative phase. Therefore, the ENSO impact on the IOD intensity is larger for the eastern pole than for the western pole, and is stronger during a negative IOD event than during a positive event. The results reveal an asymmetry of the ENSO influence between the positive and negative IOD phases.

4. Influence of IOD on ENSO prediction

The impact of IOD on ENSO should be manifest in its influence on the skill of ENSO prediction. Figure 2 demonstrates that the evolution of EEOF2 involves eastward propagation of warm temperature anomalies from WIO, followed by the development of warm subsurface temperature anomalies in the western tropical Pacific which in turn leads to an El Niño. The processes provide a physical basis for using SST anomaly in WIO as a predictor for ENSO prediction. To demonstrate the feasibility of this claim, a linear regression model is employed to statistically forecast winter seasonal mean (December-February, DJF) Niño 3.4 SST. The forecasts are cross-validated and compared with statistical forecasts using warm water volume (WWV) as a predictor, defined as the volume of water warmer than 20°C in the tropical Pacific (120°E-80°W, 5°S-5°N) derived from TAO moorings, as well as the CFSv2 dynamical seasonal forecasts.

Figure 4 shows the forecast skills assessed by anomaly correlations between the predicted and observed Niño 3.4 SST over 1983-2010, the CFSv2 hindcast period. Both predictors, namely, WIO SST and WWV, are derived from preseason observations. To predict DJF Niño 3.4 SST, WIO SST and WWV of each month from the January of previous year to the November of current year are used as an input for the linear-

regression forecast model, corresponding to lead times from 22 months to 0 month (Fig. 4, x-axis labels). The CFSv2 only provides 9-month lead forecasts, resulting in the DJF Niño 3.4 SST forecasts with lead times from 6 months (initialized in May) to 0 month (initialized in November).

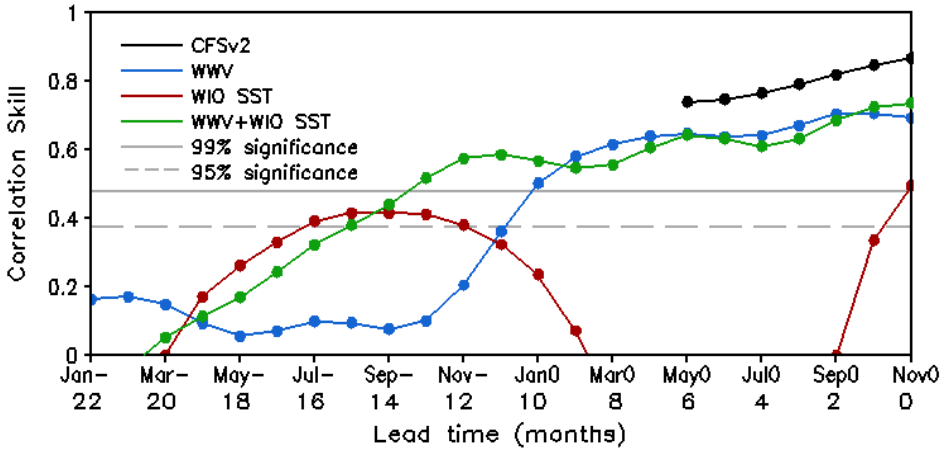

Fig. 4 Anomaly correlation skills of CFSv2 dynamical forecast (black) and statistical forecasts using one predictor (blue for WWV; red for WIO SST) and two predictors (WWV + WIO SST, green) for DJF Niño 3.4 SST with lead times from 22 months to 0 month, corresponding to forecasts made from January of previous year to November of current year (Jan– to Nov0 with – and 0 for previous year and current year, respectively). Solid (dash) gray line denotes the threshold of the anomaly correlation at the 99% (95%) significance level.

The CFSv2 has the highest forecast skill at all available lead times (Fig. 4, black line). The skill of the statistical forecasts based on WWV (blue line) is lower than the dynamical forecasts, but the anomaly correlations are above the 99% significance level (0.48, solid gray line) at 0- to 10-month leads. There is a sharp decrease in the anomaly correlation at the 12-month lead, beyond which no skillful forecasts are found. The maximum lead of 12 months is likely determined by the time needed for subsurface temperature anomalies from the tropical western Pacific to cross the Pacific basin and reach the sea surface in the tropical eastern Pacific. When using the WIO SST as a predictor (red line), skillful forecasts are found at either a short lead time of 0 month (above the 99% significance level) or longer leads of 12–16 months (above the 95% significance level). The former is associated with the co-occurrence of IOD and ENSO, whereas the latter is attributed to the signal of warm WIO SST anomalies appearing well ahead (> 1 year) of El Niño (Fig. 2). The skill of the WIO SST-based forecasts is lower than those of the CFSv2 and the WWV-based forecasts, but the lead time of skillful forecasts with the WIO SST is longer than the other two.

When using both WIO SST and WWV as predictors, the forecast skill (Fig. 4, green line) is comparable to that based solely on WWV (blue line) at lead times from 0 to 10 months, but is significantly improved at longer leads. Figure 4 suggests that for the ENSO prediction, the statistical forecast based on WWV can extend the limit of lead time of the dynamical forecast from 6 months to 10 months. Using the WIO SST as an additional predictor can further extend the lead times of skillful forecasts up to 13 (15) months at the 99% (95%) significance level.

5. Conclusions

The interaction between IOD and ENSO is examined using coupled global climate model simulations. The covariability of IOD and ENSO is analyzed by applying the EEOF method to the surface and subsurface ocean temperatures in the tropical Indian Ocean and western Pacific. The first EEOF mode shows the evolution of IOD that lags ENSO, whereas the second mode exhibits the transition from a dipole mode to a basin-wide mode in the tropical Indian Ocean that leads ENSO. Both modes have high loadings in the tropical ocean subsurface. The lead-lag relationships between IOD and ENSO suggest a two-way interaction between them. A comparison between two 500-year model simulations with and without ENSO suggests that ENSO can enhance the variability of IOD at interannual time scale. The influence of ENSO on the IOD intensity is larger for the eastern pole than for the western pole, and is stronger in a negative IOD phase than in a positive phase. The influence of IOD on ENSO is demonstrated by the improvement of ENSO prediction with a linear regression forecast model when considering SST in the western pole as an ENSO precursor. The improvement of the ENSO forecast skill is found not only at a short lead time (0 month) but also at long leads

(10-15 months). The eastward propagation of surface and subsurface temperature signals from WIO that precede the development of heat content anomaly in the tropical western Pacific is the key for extending the lead time for ENSO prediction. Our results are consistent with previously reported findings but add finer points to the mechanisms of ENSO-IOD interactions and improve the predictive understanding of the monsoon-IOD-ENSO system. Forecast experiments with CFS are underway to quantify the impact in the full coupled framework so that the details of the oceanic tunnel and the atmospheric bridge of this active partnership between IOD and ENSO can be fully exploited.

References

Wang H., R. Murtugudde, and A. Kumar, 2016: Evolution of Indian Ocean dipole and its forcing mechanisms in the absence of ENSO. *Clim. Dyn.*, **47,** 2481–2500.

Science and Technology Infusion Climate Bulletin
NOAA's National Weather Service
41st NOAA Annual Climate Diagnostics and Prediction Workshop
Orono, ME, 3-6 October 2016

What Is the Variability in US West Coast Winter Precipitation during Strong El Niño Events?

Arun Kumar and Mingyue Chen
Climate Prediction Center, NOAA/NWS/NCEP, College Park, Maryland

1. Introduction

The equatorial Pacific Ocean was in a strong El Niño state after late 2015. The amplitude of warm sea surface temperatures (SSTs) over the region associated with El Niño-Southern Oscillation (ENSO) was similar to previous El Niño events in 1982-83 and 1997-98, which were the strongest El Niño events in the past 60 years.

The climate in the United States (US) is significantly influenced by El Niño events. The anticipated influence on the US winter precipitation that includes above normal precipitation conditions across the southern US and below normal conditions over the northern part of US, however, was not observed. In contrast to expected El Niño response, the observed precipitation anomalies in the 2015/16 winter were above normal over Pacific Northwest and were below normal over the entire California. A question that is addressed in this analysis is: How different could be the west coast winter precipitation on an event-to-event basis from the typical El Niño composite mean (or the El Niño response) pattern?

In this analysis, we utilize data from large set of hindcasts and real time forecasts from National Centers for Environmental (NCEP) Climate Forecast System version (CFSv2). A sample size that exceeds 8000 seasonal mean outcomes for differing forecast SST conditions is used to address the question of event-to-event El Niño variability in California seasonal mean rainfall.

2. Data

The model forecast data used in this study includes 3-month seasonal means (OND, NDJ, and DJF) of winter precipitation and SST. The hindcast data is 30 years (1982-2011) and is combined with 4 years (2012-2015) real-time forecasts from the NCEP's CFSv2 (http://cfs.ncep.noaa.gov; Saha *et al*., 2014). For hindcasts, there are four forecasts of nine months every 5th day starting at January 1st each year. In real-time configuration, CFSv2 has four forecasts of nine months every day. By collecting forecasts from all lead times for a specific target season (Chen and Kumar, 2015), there is a sample of 5040 in hindcasts (30 years hindcasts * 7 different month leads * 6 initial dates per month * 4 members per start date) and approximately a sample of 3360 in real-time forecasts (4 years forecasts * 7 different month leads * 30 initial dates per month * 4 members per start date).

Based on an ensemble 8400 members for each target season, the variability of winter precipitation over the US west coast during strong El Niño events was examined. In the model forecasts if one defines strong El Niño as forecast members with the 3-month-mean Niño3.4 SST anomalies at least two times of their standard deviation then out of 8400 members there are 592, 498, and 316 strong El Niño events for OND, NDF, and DJF, respectively.

3. Results

To quantify the dependency in the west coast precipitation response to ENSO, we binned the area averaged precipitation over the regions of California and the Pacific Northwest (PNW) according to the predicted amplitude of the Niño3.4 SST index. This analysis uses the entire forecast sample of 8400. For each SST bin, shown in Fig. 1 are mean precipitation anomaly (the red bars) and the spread (the blue whiskers) in precipitation for forecast samples in each bin. The figure is arranged from strong negative to strong positive

Correspondence to: Arun Kumar, Climate Prediction Center, NOAA/NWS/NCEP, 5830 University Research Court, College Park, MD; E-mail: arun.kumar@noaa.gov.

values of Niño3.4 SST index for OND, NDJ, and DJF. Figures 1a-c are for the California precipitation and Figs. 1d-f are for the PNW precipitation. The sample size for each bin is shown in the bottom panels of Fig. 1. The magnitude of spread is the standard deviation of individual members in the bin with respect to the ensemble mean of samples in the bin.

For the precipitation over the region of California, the mean precipitation signal increases from negative anomaly for cold phase of ENSO to positive anomaly for warm episodes with larger amplitudes during warm SSTs. The amplitude of precipitation anomalies, *i.e.*, the strength of the precipitation response to ENSO signal increases from OND to DJF. An important point to note is that the magnitude of spread is generally greater than that of signal even in DJF when the signal is the strongest. This implies that the outcome of precipitation for one specific season can be very different from the mean response.

In general, the amplitude of the mean signal increases quasi-linearly with increasing amplitude of SSTs, and the wet signal shows larger amplitude than that of dry signal. It is interesting to note that the spread for individual outcomes does not change from neutral to strong ENSO conditions. These results have been noted in earlier studies, for example, Hoerling and Kumar (1997), Chen and Kumar (2015) for the quasi-linearity of the signal, and Kumar *et al.* (2000), Peng and Kumar (2005) for the constancy of noise.

For the PNW precipitation, the anomaly changes from positive in cold phase of ENSO to negative in

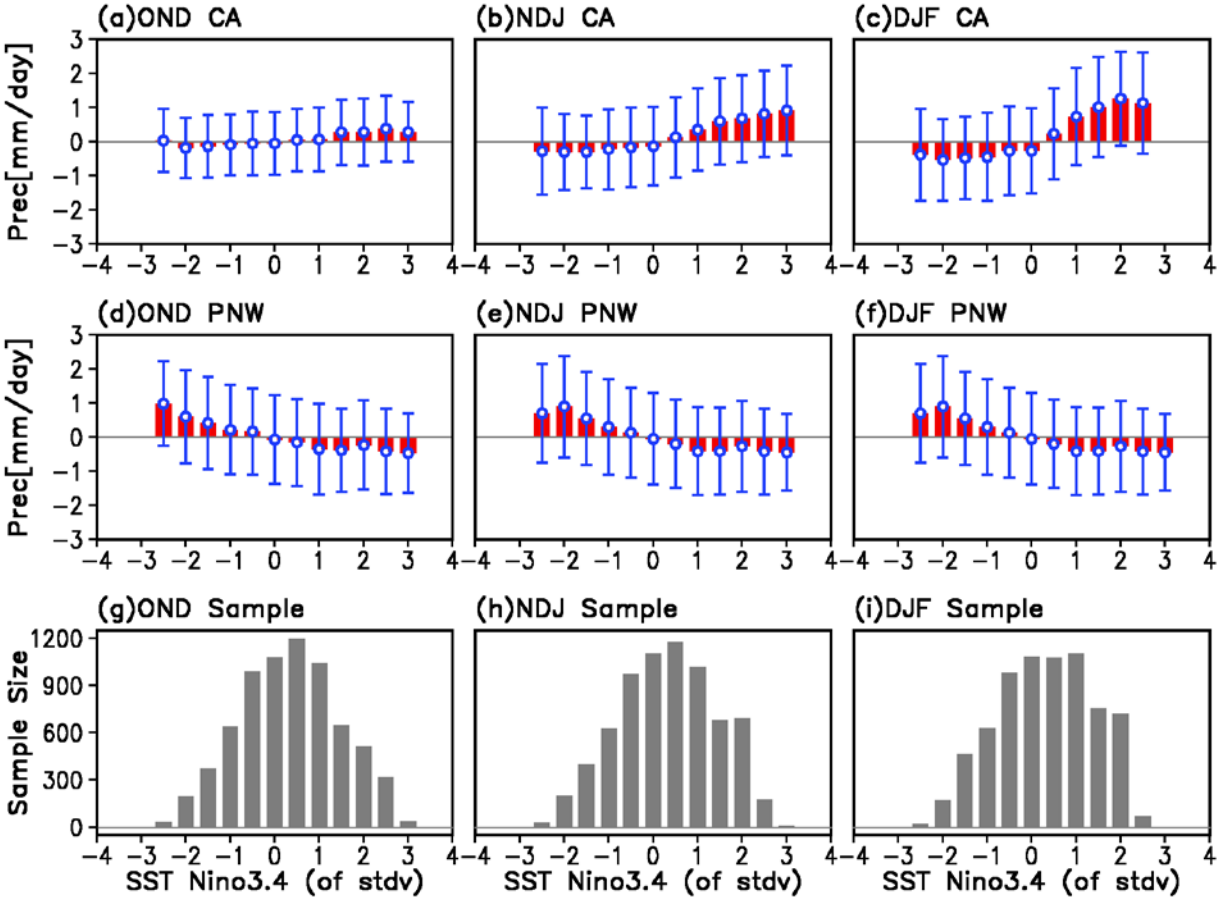

Fig. 1 The areal-mean precipitation ensemble mean anomaly averaged in each bin of Niño3.4 SST index (the red bars) and the spread of individual members from the ensemble mean in the same bin (the blue whiskers). The bin width of the Niño3.4 SST index is 0.5 of its standard deviation and the red bars are shown in the middle of the bin. Panels a, b, and c are for the region of California during OND, NDJ, and DJF, respectively. Panels d, e, and f are for the region of Pacific Northwest (PNW; 118—126°W, 43—50°N). The gray bars in the panels of g, h, and i are the corresponding sample size for each SST bins during each season.

warm phase of ENSO, which is in opposite sign to the California precipitation. The PNW precipitation also shows less seasonality in the ENSO signal and smaller magnitude of the ratio of the signal to noise.

To further illustrate the behavior in mean response and spread from event-to-event, the PDF of seasonal mean precipitation for strong El Niño events is compared with its climatological PDF. The results are shown in Figs. 2a, c, and e for the California precipitation and Figs. 8b, d, and f for the PNW precipitation.

In response to strong SST anomalies in El Niño events, the California precipitation probability density function (PDF) moves towards the right of its climatological PDF and the probability for extreme wet event are increased. Consistent with Fig. 1, the largest separation between the PDFs is for the DJF.

As the spread during El Niño does not change much across different PDFs, an increase in probability for positive precipitation anomalies over CA is mainly due to the PDF shift. However, we note that the spread among ensemble members during extreme El Niño events is still appreciably large, and implies that even during strong El Niño events, although the probability of positive precipitation anomalies over California is enhanced, there is still a considerable probability to have negative anomalies. This variability in the seasonal mean outcomes for individual seasons is a limiting factor on the level of predictability.

The PNW ENSO precipitation PDF shifts to the left of its climatology PDF. However, the magnitude of the shift is much smaller compared with that over the California, so that, the precipitation predictability over the PNW is much less than that over the California.

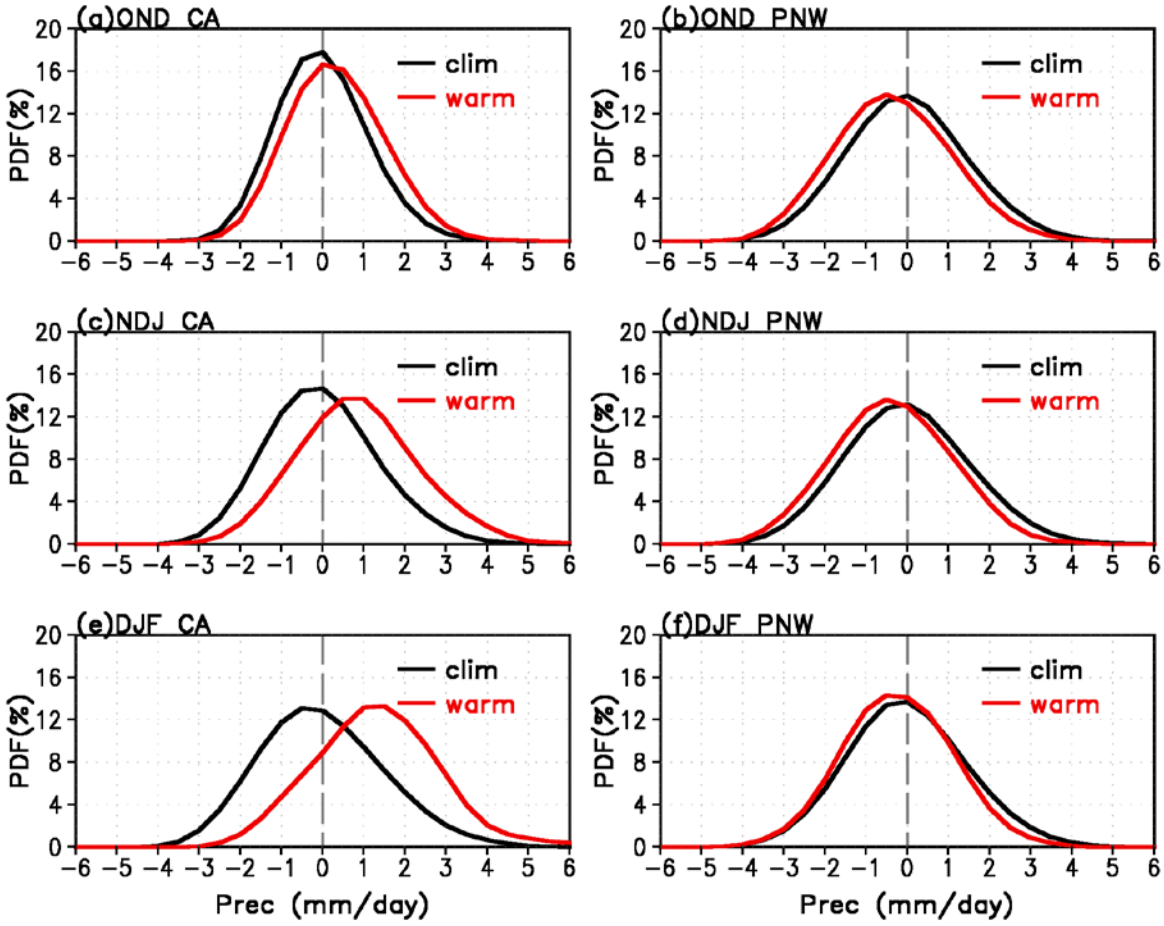

Fig. 2 The PDF of precipitation anomalies for strong El Niño events (red) and its climatological PDF based on all members (black) during seasons of OND, NDJ, and DJF. Panels a, c, and e are for the region of California, and b, d, and f are for the region of PNW (118—126^{o}W, 43—50^{o}N).

4. Summary

The analysis based on a large sample of seasonal means demonstrated that the seasonal mean precipitation signal over the west coast of US during strong El Niño events, although was consistent with the documented signal with negative anomalies over the northern Pacific Northwest and positive anomalies over the southern region that include California, it was within the range of possible seasonal mean outcomes. This is because for individual forecasts the variability in seasonal mean precipitation is very large. As a consequence, there will be an appreciable probability for seasonal mean precipitation anomaly to have its sign opposite to the mean response to El Niño. This interplay between the precipitation response to El Niño, and event-to-event variability, even during strong El Niño events, can account for the fact that seasonal mean precipitation along the west coast of US during the strong El Niño event of 2015/16 was opposite to the expected ENSO response.

References

Chen, M., and A. Kumar, 2015: Influence of ENSO SSTs on the spread of the probability density function for precipitation and land surface temperature. *Clim. Dyn.,* **45**, 965-974. doi:10.1007/s00382-014-2336-9

Hoerling, M. P., and A. Kumar, 1997: Origins of extreme climate states during the 1982-83 ENSO winter. *J. Climate*, **7**, 745-766.

Kumar, A., A. G. Barnston, P. Peng, M. P. Hoerling, and L. Goddard, 2000: Changes in the spread of the variability of the seasonal atmospheric states associated with ENSO. *J. Climate*, **13**, 3139-3151.

Kumar, A., and M. Chen, 2017: What is the variability in US west coast winter precipitation during strong El Niño events? *Clim. Dyn.*, to appear.

Peng, P., and A. Kumar, 2005: A large ensemble analysis of the influence of tropical SSTs on seasonal atmospheric variability. *J. Climate*, **18**, 1068-1085.

Saha, S., and Coauthors, 2014: The NCEP climate forecast system version 2. J. Climate, **27**, 2185-2208. doi:10.1175/JCLI-D-12-00823.1

Science and Technology Infusion Climate Bulletin
NOAA's National Weather Service
41st NOAA Annual Climate Diagnostics and Prediction Workshop
Orono, ME, 3-6 October 2016

A staged communication approach to advising Australian industry on the risk of El Niño or La Niña developing

Robyn Duell, Felicity Gamble, Andrew Watkins, and David Jones
Australian Bureau of Meteorology

Communicating the development of El Niño and La Niña is often challenging due to the general misconception that transition to an event can happen rapidly, and that impacts will suddenly appear - just like flicking a switch. Additionally, the association of El Niño with drought in Australia and La Niña with floods can often complicate the message, meaning that probabilistic information is often treated as deterministic.

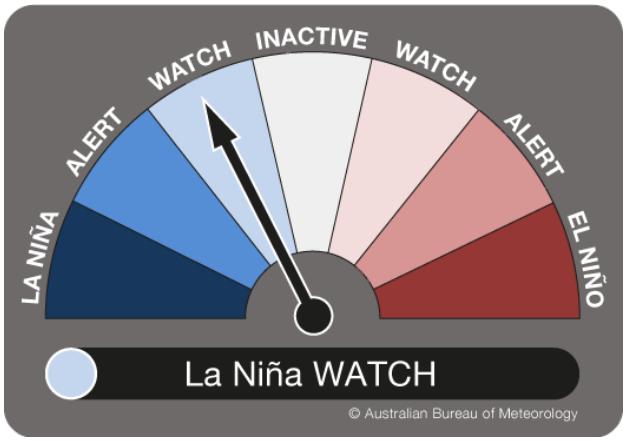

Fig. 1 A staged approach to communication of the ENSO Outlook.

In Australia, the Bureau of Meteorology (the Bureau) is responsible for issuing updates on the current status and outlook of the El Niño-Southern Oscillation (ENSO), including declaring the onset and end of an event. To assist in the communication of ENSO as events develop, the Bureau has developed an online climate watch tool, the ENSO Outlook. This tool advises stakeholders of the potential for El Niño or La Niña development over the coming months using a staged approach (*i.e.* watch, alert, and declaration of an event as shown in Fig. 1) and includes the likelihood (percentage chance) of an event occurring.

The development and success of the tool was presented, including selection of criteria, assessment of hit and miss rate (Table 1), objectivity of the tool, and user feedback.

Visit the Bureau's ENSO Outlook service on the web: http://www.bom.gov.au/climate/enso/outlook/

Hit Rate	El Niño	La Niña
WATCH	50%	56%
ALERT	71%	73%
EVENT	91%	70%

Miss Rate	El Niño	La Niña
WATCH	0%	11%
ALERT	0%	0%
EVENT	0%	4%

Table 1 Hit and miss rate of ENSO Outlook based on historical analysis from January 1980 to December 2015.

References

Gamble, F., A. Watkins, D. Jones, V. Webb and A. Evans, 2016: Tracking the El Niño-Southern Oscillation in real-time: A staged communication approach to event onset. *Journal of Southern Hemisphere Earth Systems Science*, submitted.

Correspondence to: Robyn Duell, Australian Bureau of Meteorology, Melbourne, Australia;
E-mail: robyn.duell@bom.gov.au

4. PREDICTION, ATTRIBUTION & ANALYSIS OF HIGH IMPACT EXTREMES CLIMATE EVENTS

41th NOAA Annual Climate Diagnostics and Prediction Workshop

3-6 October 2016, Orono, Maine

Science and Technology Infusion Climate Bulletin
NOAA's National Weather Service
41st NOAA Annual Climate Diagnostics and Prediction Workshop
Orono, ME, 3-6 October 2016

Enhancing Resilience to Heat Extremes: Forecasting Excessive Heat Events at Subseasonal Lead Times (Week-2 to 4)

Augustin Vintzileos[1], Jon Gottschalck[2], Mike Halpert[2], and Adam Allgood[2]
[1]*University of Maryland – ESSIC/CICS-MD*
[2]*Climate Prediction Center, NOAA/NWS/NCEP, College Park, Maryland*

1. Introduction

Heatwaves are among the most dangerous, yet invisible, of natural hazards. According to NOAA, the distribution of 30-year based annual mean fatalities from natural hazards in the U.S. ranks as follows; those from heat (130), floods (81), tornadoes (70), lightning (48) and hurricanes (46). Resilience to excessive heat events will be augmented by using multi-scale prognostic systems.

A scalable system for forecasting excessive heat events at lead times beyond Week-1 was developed at the University of Maryland and the NOAA Climate Prediction Center. This Subseasonal Excessive Heat Outlook System (SEHOS) consists of (a) a monitoring/verification component and (b) a forecasting component which in its baseline version uses NOAA's Global Ensemble Forecast System (GEFS) predictions of temperature and humidity from Day-8 to Day-14. In this presentation, we discuss the definition of heat events, sources of predictability and present the forecast skill of SEHOS for the GEFS reforecast period. Finally we argue on the importance of using multi-model approaches in SEHOS systems especially when targeting forecast leads beyond Week-2.

2. Definition of heat events

The first target was to develop a definition of heat waves which would include both the effects of heat on the human body and the restrictions of probabilistic subseasonal forecasting. The factors we considered in the development of the heatwave definition are:

(1) Impacts of heat grow non-linearly as temperature and humidity increase:

As a consequence the definition must be based on indices representing the thermal discomfort. In this work we use *NOAA's Heat Index.*

(2) Impacts of heat increase as a function of their duration:

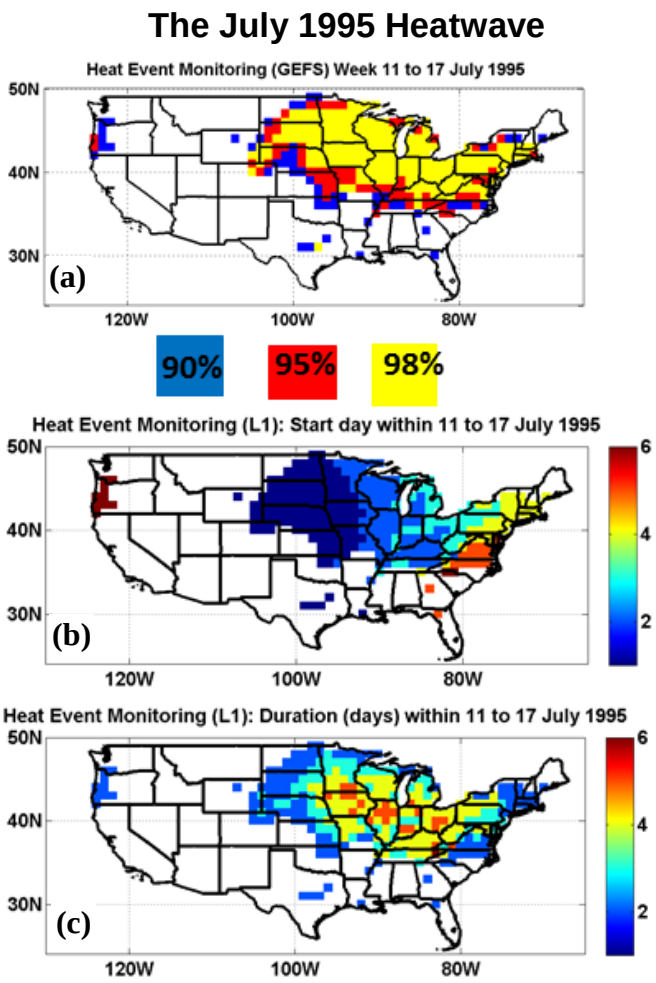

Fig. 1 (a) Grid cells with at least one EHE for the week 11-17 July 1995 for events defined at 90% (blue), 95% (red) and 98% (yellow), (b) the first day of the EHE within the given week for 90% events and (c) the duration (in days) of the EHE.

Correspondence to: Augustin Vintzileos, University of Maryland – ESSIC/CICS-MD;
E-mail: augustin.vintzileos@noaa.gov

The heat load increases as a function of the duration of the heat wave. Therefore, it is necessary to include information about the number of consecutive days under heat stress.

(3) *Impacts of heat depend on geographical location:*

A heat event of the same intensity has graver impacts in locations in more northern latitudes.

(4) *High apparent temperatures are felt differently as a function of time within the warm season:*

Due to acclimatization to heat the impact of a heat wave during the beginning of the warm season will be graver.

Based on these considerations we define:

- An Excessive Heat Day as a day with Maximum Heat Index exceeding a given percentile **α** of the Cumulative Distribution Function computed from the historical record for the geographical location and time-frame within the warm season.

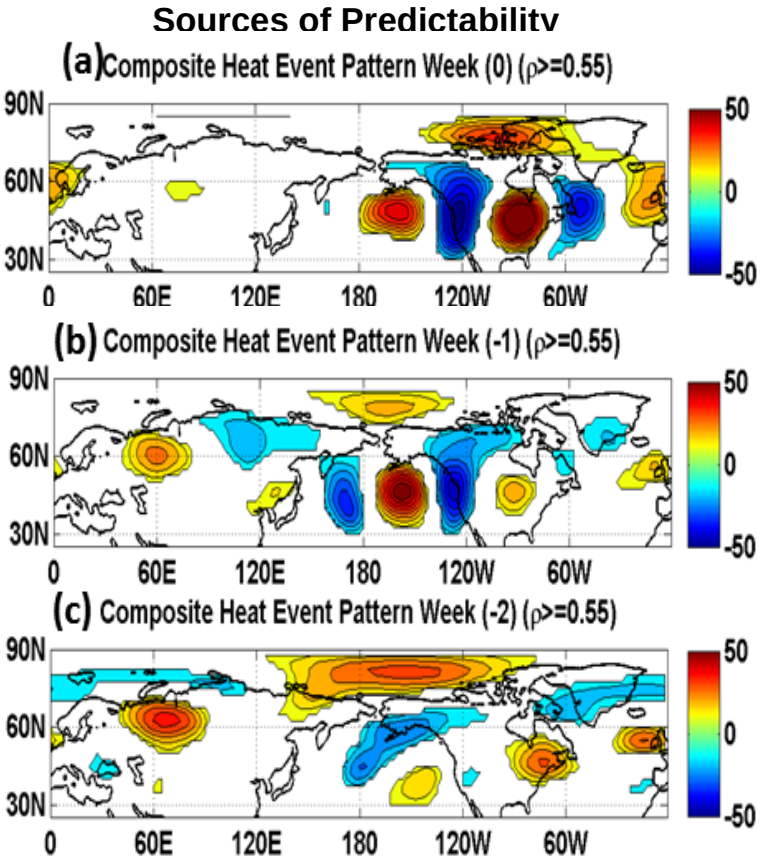

Fig. 2 Weekly mean anomalies of geopotential at 500hPa (in meters) composited for 42 EHE resembling the EHE of July 1995 for (a) during the week of the EHE, (b) the week prior to the EHE and (c) three weeks prior to the EHE.

- An Excessive Heat Event (EHE) as a succession of at least two heat days. We define Heat Events at Level-1 (α=90%), Level-2 (α=95%), and Level-3 (α=98%).

As an example of the utility of this index Figure 1 shows the spatial structure and evolution of the excessive heat event that affected the Chicago area in July 1995 resulting to abnormal mortality that exceeded 700 cases. Meteorological data of temperature and relative humidity derived from surface pressure and specific humidity at 2 meters are from the NCEP/NCAR Reanalysis.

During the week between 11-17 July, 1995 we observe the occurrence of a very intense EHE with large geographical coverage (yellow color in Figure 1a). The EHE was initially detected at the center of the country (blue colors in Figure 1b) and then propagated eastward reaching the mid-Atlantic area 5 days later. The duration of the EHE (for level 90%) exceeded 4 days for the area around Chicago (red color in Figure 1c).

3. Sources of predictability of EHE

Sources of predictability at subseasonal lead times can be investigated based on the above definition of EHE. Figure 2 shows the composite weekly mean anomalies of geopotential at the level of 500hPa. The composite is based on 42 EHE similar to the EHE of July 1995. During the week of the composite EHE (Figure 2a) we note strong positive departures of height over the Midwest which are associated with the EHE. A similar large scale structure is seen for the week prior to the EHE. Therefore one source of predictability for such EHE at Week-2 is a large scale stationary Rossby wave. Figure 2c shows the composite weekly geopotential anomaly pattern during three weeks before the event. We are currently examining whether the pattern of Figure 2c can be considered as the 'seed' of the stationary Rossby wave.

4. Forecasting excessive heat events

The baseline system for this research is the Global Ensemble Forecast System and the associated 1985-2014 reforecast conducted by NOAA/ESRL. The forecast methodology is the following. We first compute the historical distribution of the Heat Index at each grid point, during a 7-day window around the forecast day under consideration. In order to account for systematic biases this distribution is a function of forecast lead time from the reforecast. Then we compare the realtime forecast to this distribution and define the given forecast day as an Excessive Heat Day or not depending on the value of α (see section 1). Finally we compute whether a EHE occurs during forecast week-2 and its start day and duration. This algorithm is repeated for each forecast ensemble member and the statistics computed, *i.e.*, probability of occurrence, mean first day and mean duration of the forecast.

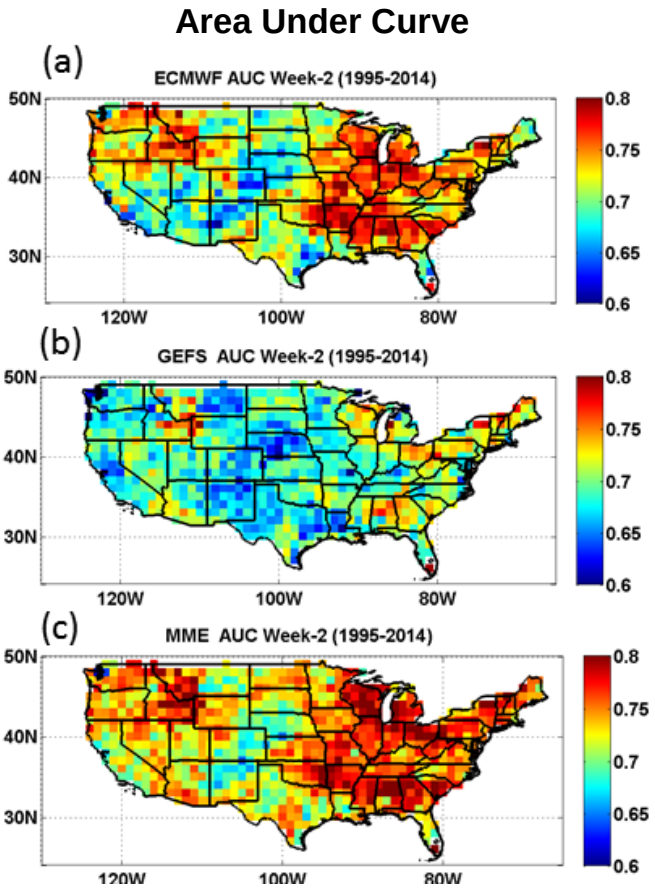

Fig. 3 Area under the ROC Curve (AUC) for (a) ECMWF, (b) GEFS and (c) GEFS and ECMWF combination. Values of AUC close to one (red) indicate a good forecast system to contrast values close to 0.5 (blue).

Verification of the baseline system is based on the reforecasts initialized daily from 13 May to 15 September from 1985-2014. For the sake of comparison with the ECMWF model we also evaluate the forecast skill for reforecasts that are initialized twice per day from 1995-2014, *i.e.*, following the initialization strategy of ECMWF. The verification technique is the Receiver Operating Characteristics (ROC) and the Area Under Curve (AUC) which we compute for each grid point. Figure 3 compares the AUC of the (a) ECMWF, (b) GEFS and, (c) GEFS+ECMWF super-ensemble. We must underline that the GEFS reforecasts are done with an older version of the model and are initialized using the CFS-Reforecasts and not its own analysis. This means that Figure 3 cannot be used for direct comparison of the models but rather as an indication of the possibility to forecast EHE at subseasonal lead times (starting from forecast Week-2).

Comparison of Figures 3a and 3b shows that the most difficult areas for forecasting EHE is in the center parts of the CONUS. The ECMWF shows an overall better forecast quality for the reasons explained in the previous paragraph. It is important to note that by combining the GEFS and ECMWF models the forecast quality is superior to each model separately.

5. Conclusions

We introduced a definition of excessive heat events that is compatible with both requirements of accounting for the physiological effects of heat to the human body and the constraints of probabilistic subseasonal forecasting. We show that there is skill in forecasting EHE at forecast Week-2. We also computed the AUC for forecast Week-3 (not shown) finding a large decrease in forecast skill over most of the locations. However, multi-model approaches again show some promising results when used for forecast Week-3.

Acknowledgements. This study is supported by NOAA grants: NA15OAR4310081, NA14NES4320003, and NA16OAR4310147

Science and Technology Infusion Climate Bulletin
NOAA's National Weather Service
41st NOAA Annual Climate Diagnostics and Prediction Workshop
Orono, ME, 3-6 October 2016

Assessing Temperature Extreme Trends in Western ME and NH

Chris Kimble
National Weather Service – Gray, Maine

1. Motivation

One of the more visible aspects of National Weather Service (NWS) management of climate observing sites is the reporting of daily record highs and lows. It is these daily records which help place an extreme event in a historical context. Saying it has never been hotter or colder before is both dramatic and meaningful. These historical extremes help place brackets around our expectations of what weather is possible on any given day. It can be expected that there may be a change in frequency of setting record highs and lows as the climate at any location changes. In fact, several active social media followers of NWS Gray have taken note of an apparent trend in these records, mostly at Portland, Maine. It seems apparent to several followers that Portland rarely sets new record lows anymore, while record highs continue to fall. This project attempts to discover whether an observable trend exists, and point to some local factors which are likely to influence any trends observed. In an attempt to provide some context, the project was expanded beyond Portland, Maine to include the other two climate reporting locations in the NWS Gray forecast area for which records are routinely reported: Concord, New Hampshire and Augusta, Maine.

2. Methodology

For this project the database of record highs and lows was accessed for Portland, Concord, and Augusta. For each daily record high and low (through the end of 2015), the year in which the record occurred was recorded. Because some records occur in multiple years (ties), each year in which the record occurred was recorded in order to avoid favoring more recent records. This resulted in greater than the 366 record highs and 366 record lows for each location that would otherwise be reported. For each location, the number of times each year appeared in the record books was recorded.

In order to determine the change in frequency of record high and low temperatures with time, we must first understand a basic premise. That is that if all years were equal, then each year would occupy an approximately equal number of slots in the record books. That is to say there would not be a preference toward records set earlier in the period of record or a

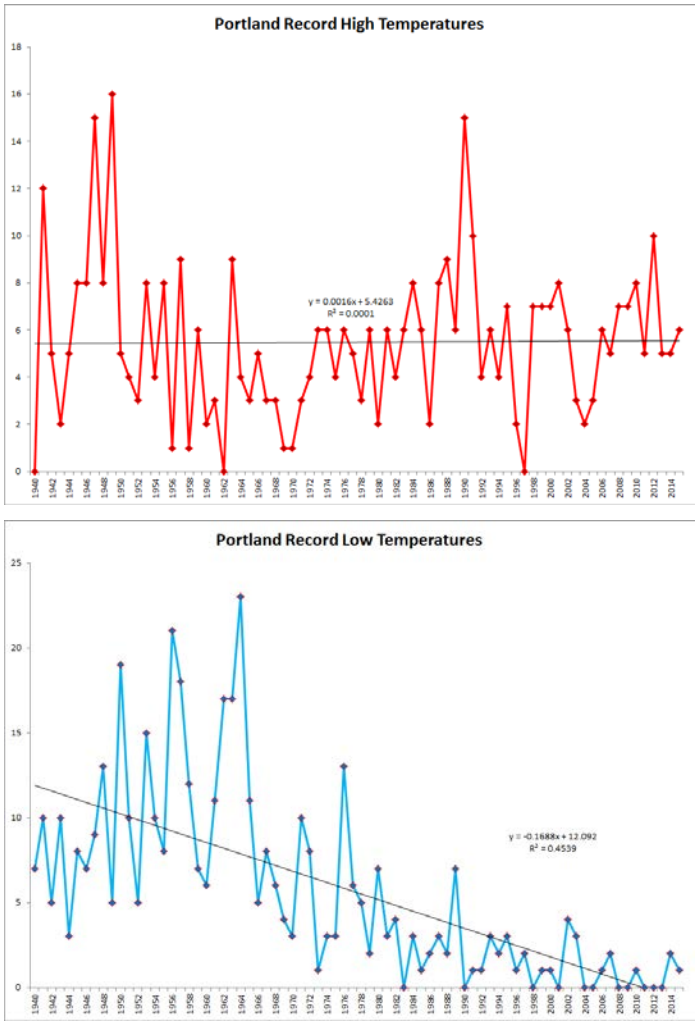

Fig. 1 (a) Record High Temperatures at Portland, ME show very little long term trend and a low correlation. (b) Record Low Temperatures at Portland, ME show a sharp downward trend and a strong correlation.

Correspondence to: Chris Kimble, National Weather Service – Gray, Maine; E-mail:

preference toward more recent records. Breaking a record which was set last year would be just as likely as breaking one set at the beginning of the period of record. The number of records set each year would be approximately equal to the total number of records divided by the total number of years in the period of record. The degree to which these assumptions break down will illustrate the variability from one year to the next and across several decades of a changing climate. Years which experience greater frequency in record highs or record lows would be seen as periods of more extreme warmth or cold, respectively.

3. Results

3.1 Portland, Maine (1940 – present)

Temperature records taken from the Portland International Jetport from November 1940 through December 2015 were used for this study. While earlier records exist from locations "downtown," long-standing NWS policy excludes these records from current reports due to the strong differences observed between the two locations during a period of overlapping records. Since November 1940, temperature records were taken exclusively at the Portland International Jetport which has seen significant airport expansion and suburbanization of the surrounding area from the 1960s to present.

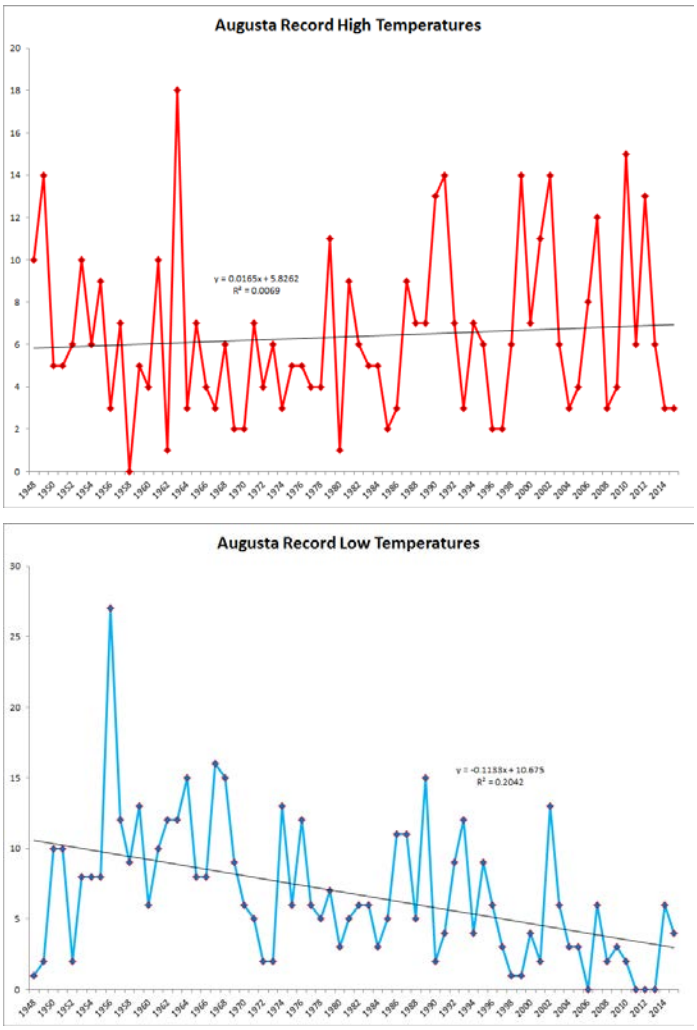

Fig. 2 (a) Record High Temperatures at Augusta, ME show very little long term trend and a low correlation. (b) Record Low Temperatures at Augusta, ME show a moderate downward trend and a moderate correlation.

Over the course of the 75-years of records, there were a total of 417 instances of record highs set or tied, yielding an average of 5.6 record highs set or tied per year. The most set in any one year was 16 in 1949. There were two full years which did not set or tie any record highs (1962 and 1997). Figure 1a charts the number of record highs in each year. There was no observable trend in record highs over the course of the period of record, as the slope of the regression line was near zero with very little of the variation explained by this regression line. There were a few years which stood out including several in the 1940s (1941, 1947, 1949), 1990, and 2012.

An analysis of the record lows showed a different story. There were 425 instances of record lows set or tied, yielding an average of 5.7 record lows set or tied per year. The most set in any one year was 23 in 1964. There were 11 years which did not set or tie any record lows, all of which were 1983 or later (most recently in 2013). Figure 1b charts the number of record lows in each year. There was a distinct downward trend in the frequency of record lows set over the course of the period of record. The slope of the regression line was sharply negative with a substantial amount of the variance explained by this regression line. During the first 30 years of records, it is common to see more than 10 record lows set or tied per year, while during the last 20 years it is common to see few or none. The most recent year to surpass the long term average of 5.7 record lows set or tied per year was 1989 when 7 such records occurred. There were a few years which stood out including 1948, 1950, 1953, 1956, 1957, 1958, 1962, 1963, 1964, and 1976.

3.2 Augusta, Maine (1948 – present)

This study used the temperature records available from the Augusta State Airport over the period June 1948 through December 2015. Since June 1948, temperature records were taken exclusively at the Augusta State Airport.

Over the course of the 69-years of records, there were a total of 435 instances of record highs set or tied, yielding an average of 6.4 record highs set or tied per year. The most set in any one year was 18 in 1963. There were no record highs set or tied in 1958. Figure 2a charts the number of record highs in each year. Although a slight upward trend is noted over the period of record, the slope of the regression line was very small with very little of the variation explained by that regression line. There were a handful of years which stood out including 1949, 1963, 1990, 1991, 1999, 2010, and 2012.

There were 460 instances of record lows set or tied, yielding an average of 6.8 record lows set or tied per year. The most in any one year was 27 in 1956. There were no record lows set or tied in four years (2006, 2011, 2012, and 2013). Figure 2b charts the number of record lows in each year. There was a downward trend in frequency of record lows set over the course of the period of record indicated by the negative slope of the regression line. A significant amount of the variance is explained by the regression line, though this correlation is about half as strong as is seen at Portland. The years that stood out included 1956, 1959, 1964, 1967, 1968, 1974, 1989, and 2002.

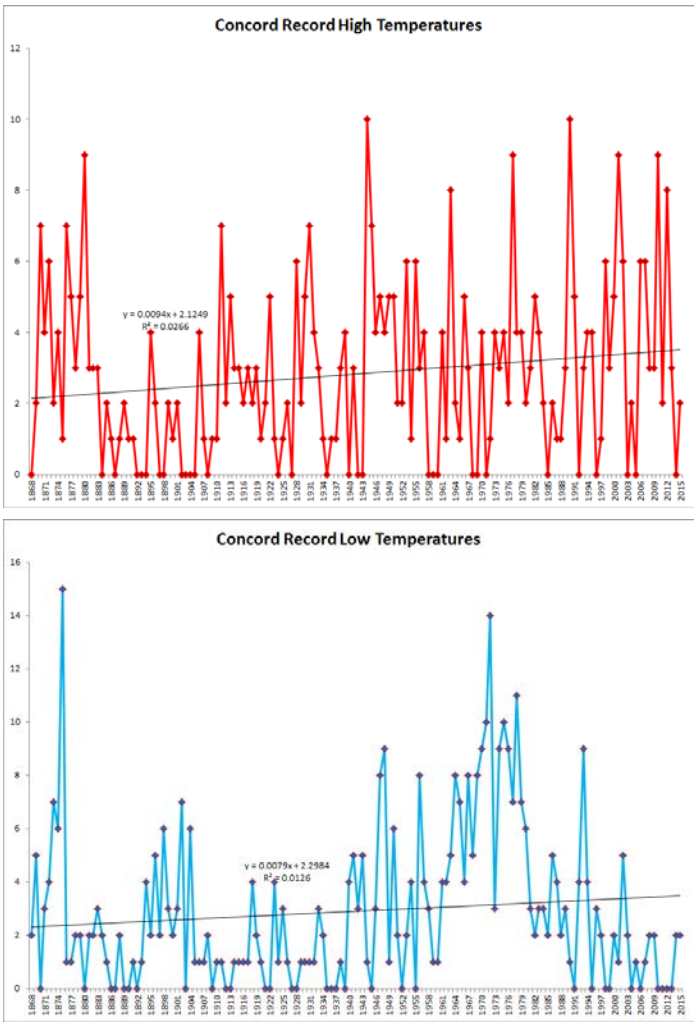

Fig. 3 (a) Record High Temperatures at Concord, NH show very little long term trend and a low correlation. (b) Record Low Temperatures at Concord, NH show very little long term trend and a low correlation. There is a notable drop from the 1970s to present.

3.3 Concord, New Hampshire (1868 – present)

Temperature records at Concord come from a variety of locations near Concord from 1868 to present. From 1868 to 1941, most of the observations came from locations in the downtown core of Concord. From 1941 until the present, observations were taken at the nearby Concord Municipal Airport.

Over the course of the 148-years of records at Concord, there were a total of 418 instances of record highs set or tied, yielding an average of 2.8 records set or tied per year. The most set in any one year was 10 in 1990 and 1944. There were 31 individual years which do not have a record high set or tied. Figure 3a charts the number of record highs in each year. Although a slight upward trend is noted over the period of record, the slope of the regression line was small explaining very little of the variation. A handful of years stood out including 1880, 1944, 1963, 1977, 1990, 2001, 2010, and 2012.

There were 427 record lows set or tied, yielding an average of 2.9 set or tied per year. The most in any one year was 15 in 1875. There were 32 years which do not have a record low set or tied. Figure 3b charts the number of record lows in each year. Although there is a slight upward trend in the linear regression line, the slope is very small with very little of the variation explained by this line. There was a period of numerous record lows set in the 1960s and especially the 1970s, which being in the last half of the 148-year record

cause the linear regression line to tilt upward. The years which stood out as having set or tied many record lows include 1875, 1948, 1970, 1971, 1972, 1975, 1976, 1978, and 1993.

4. Conclusions

A look at the trends in record temperatures at these three locations reveals no substantial trend in the frequency of record high temperatures. Record highs are still being set at about the same rate as earlier years in the record database.

There is a general downward trend in the frequency of record low temperatures. The most frequent record lows were observed in the third quarter of the 20th century with a sharp downward trend continuing into the present. This downward trend is most obvious at Portland and Augusta where a shorter period of record prevents a broader view. A longer period of record available at Concord reveals periods of extreme cold in the more distant past along with periods which set few record lows. Suburbanization and airport expansion likely affect Portland's modern records, leading to fewer extreme cold temperature records.

Acknowledgements. This analysis could not have been completed without the assistance of Ryan Colantonio of the Ohio State University who spent hours performing quality checks on the record databases. Other staff members at NWS Gray also contributed including Justin Arnott, John Jensenius, and Nikki Becker.

Science and Technology Infusion Climate Bulletin
NOAA's National Weather Service
41st NOAA Annual Climate Diagnostics and Prediction Workshop
Orono, ME, 3-6 October 2016

A New Dataset to Analyze Extreme Events in New England

Muge Komurcu[1,2] and Matthew Huber[3,2]

[1]*Department of Earth, Atmospheric and Planetary Sciences, Massachusetts Institute of Technology, Cambridge, MA*

[2]*Earth Systems Research Center, University of New Hampshire, Durham, NH*

[3]*Department of Earth, Atmospheric and Planetary Sciences, Purdue University, West Lafayette IN*

1. Introduction

In recent years, New England has been experiencing changes in regional climatology such as more frequent land falling tropical cyclones, Nor'easters and heat waves. Cost of the damages caused by these changes has been alarming for the regional economy and stakeholders. To prepare for these impacts in city and state levels, it is essential to be able to simulate future changes in regional climatology and extreme events. Global model projections have been too coarse to assess changes in regional scales and the impacts assessment models such as economic tools and hydrological, forest and ecosystem models require much higher resolution data that is capable of simulating, in detail, changes in extreme events. Hence, downscaling methodologies have been proposed to produce the high-resolution climate variables needed to assess climate change impacts at regional scales. Statistical downscaling, where historical statistical relations are obtained between observed and modeled variables, is commonly used due to its smaller computational cost. However, the downside of the method is that it assumes statistical relations between variables remain the same in to the future. Dynamical downscaling, on the other hand, uses regional climate models to downscale global model projections meaning that variables are calculated based on physically based parameterizations produced from theory, observations and retrievals through years of research.

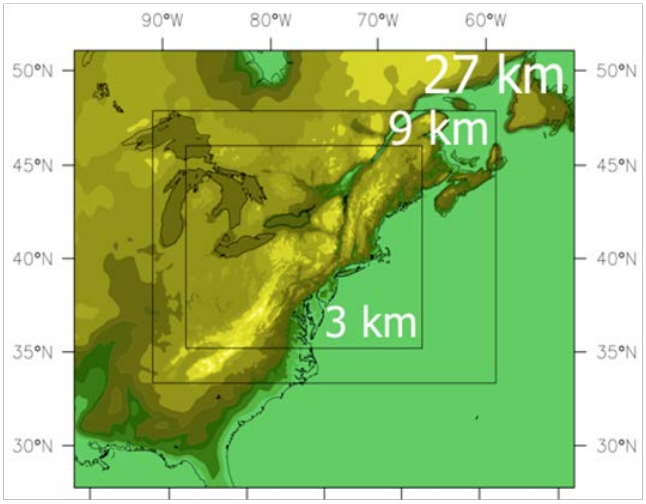

Fig. 1 Simulation domain used in our WRF simulations.

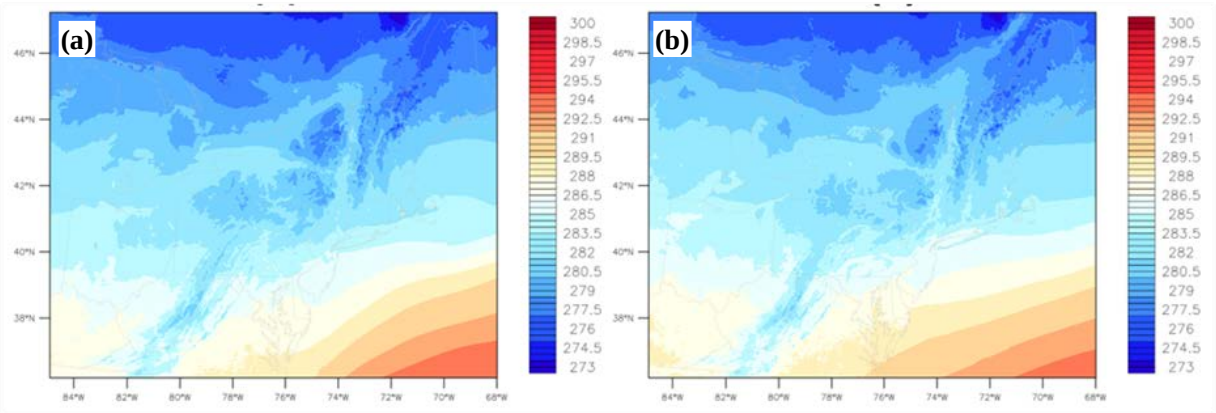

Fig. 2 Annual mean 2m air temperature (K) for **(a)** ERA-Interim driven WRF simulations **(b)** CESM driven WRF simulations for 2006-2015.

Correspondence to: Muge Komurcu, Department of Earth, Atmospheric and Planetary Sciences, Massachusetts Institute of Technology, Cambridge, MA; E-mail: muge@mit.edu

Our study is part of the efforts through a National Science Foundation Experimental Program to Stimulate Competitive Research (NSF EPSCoR) funded inter-disciplinary project (New Hampshire EPSCoR Ecosystems and Society) aiming to assess climate change impacts on regional hydrology, ecosystems and economy in New Hampshire in order to support sustainable management of natural resources and regional economy. Because these changes are highly sensitive to changes in extremes, we choose to use dynamical downscaling.

2. Methodology

We dynamically downscale bias corrected CESM projections (Bruyere *et al.*, 2014 and 2015) under a high impacts emissions scenario (representative concentration pathway (RCP) 8.5) using the Weather Research and Forecasting (WRF) model (Skamarock *et al.*, 2008) version 3.6.1 for three time slices representative of Present Day (PD) (2006-2020), Mid Future (MF) (2041-2060) and Far Future (FF) (2081-2100) time periods. In our WRF simulations, we use three nested domains with 27, 9 and 3 km horizontal resolutions (Figure 1) and two-way nesting. We use ~ 45-day simulations to simulate each month (15+30; 15+31; 15+28) within the time slices omitting first 15-days for initialization. In all our CESM driven WRF simulations, greenhouse gas concentrations for RCP 8.5 are implemented to interact with the WRF radiation scheme (RRTMG). Convection is resolved in the innermost domain. To evaluate our model performance, we also perform reanalysis driven (ERA-Interim) historical simulations (2006-2015) using the same model setup.

3. Data availability

The aim of this NSF funded study is to produce this high-resolution future climate dataset to be used in further impacts assessment models and to enable further downscaling studies. For this reason, all input, boundary, restart and output files are available for public use. Eventually the data will be available through the Data Distribution Center at University of New Hampshire. Until then, we ask that interested parties contact the authors of this report directly to obtain the subset of their interest. Please note that there is a usage policy in effect. To obtain a full list of all available output variables and for all other questions regarding the details of the simulations, please contact the first author (muge@mit.edu).

4. Analysis & discussion

For this short report, we will focus on temperatures and temperature extremes. In Figure 2, we present historical (2006-2015) annual mean 2 m air temperature for domain 3 (the innermost domain with 3 km horizontal resolution) from (a) ERA-Interim driven and (b) CESM driven WRF simulations. Our WRF model setup is capable of producing both the magnitude and structure of mean state temperature at 2 meters exceptionally well (Figure 2).

We provide a preview of extreme temperatures simulated into the future with comparison to PD time periods using percentile exceedances at 95 % (Figure 3).

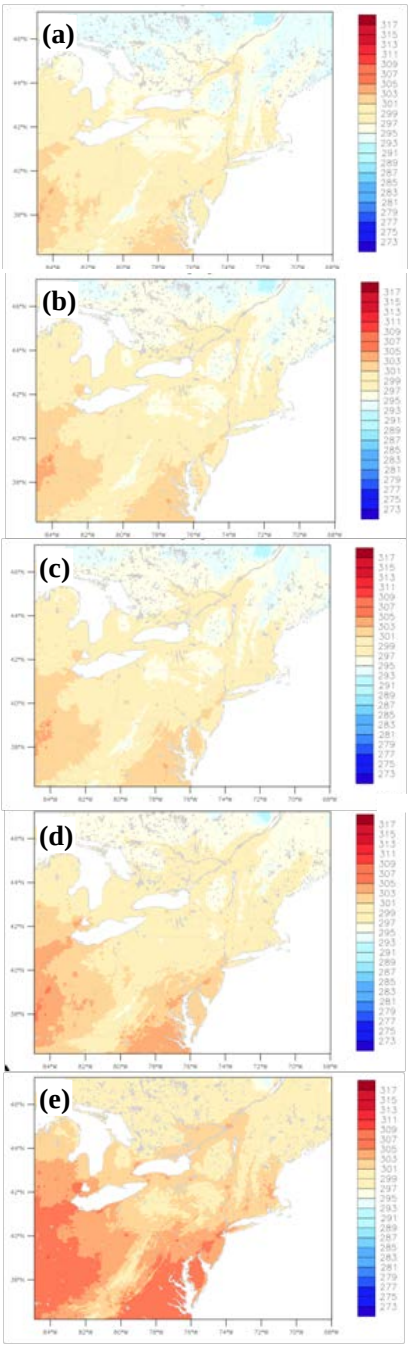

Fig. 3 95th percentiles of 2m air temperature for **(a)** ERA-Interim driven WRF simulations (2006-2015), **(b)** CESM driven WRF historical simulations (2006-2015), **(c)** CESM driven WRF present day simulations (2006-2020), **(d)** CESM driven WRF mid future simulations (2041-2060), **(e)** CESM driven WRF far future simulations (2081-2100).

While mean characteristics are well represented in Historical CESM driven WRF simulations compared to ERA-Interim driven WRF simulations, the former has overall slightly higher temperatures in extreme (Figure 3). As seen in Figure 3, extreme temperature events become more severe into the future. The average number of days per year where 2m air temperatures exceed 303K averaged over domain 3 is 1.6 days for PD and 12.4 days for FF time periods.

Several journal articles detailing our simulations and analyzing our output are currently in preparation.

Acknowledgements. Support for this project was provided through NSF EPSCoR grant 1101245. We would like to acknowledge our 12 million core hour NCAR Yellowstone CISL allocation (CNHA001), David L. Hart and all staff at NCAR CISL help for their support throughout the project. M. Komurcu would like to thank Cindy Bruyere, Jimmy Dudhia and Hugh Morrison of NCAR for treasured discussions during the initial stages of this study.

References

Bruyère, C. L., A. J. Monaghan, D. F. Steinhoff, and D. Yates, 2015: Bias-corrected CMIP5 CESM data in WRF/MPAS intermediate file format. TN-515+STR, NCAR, 27 pp., DOI: 10.5065/D6445JJ7.

Bruyère C. L., J. M. Done, G. J. Holland, and S. Fredrick, 2014: Bias corrections of global models for regional climate simulations of high-impact weather. *Clim. Dyn.*, **43**, 1847-1856, DOI: 10.1007/s00382-013-2011-6.

Skamarock, W. C., J. B. Klemp, J. Dudhia, D. O. Gill, D. M. Barker, M. Duda, X.-Y. Huang, W. Wang and J. G. Powers, 2008: A description of the advanced research WRF version 3, NCAR Technical Note.

Science and Technology Infusion Climate Bulletin
NOAA's National Weather Service
41st NOAA Annual Climate Diagnostics and Prediction Workshop
Orono, ME, 3-6 October 2016

February 2015: A Month to Remember in New England for Record Cold

Corey A. Bogel and Victor J. Nouhan
NOAA's National Weather Service, Caribou, Maine

1. Introduction

An extreme cold air outbreak affected all of the Northeast U.S. during February 2015 (NWS ER 2015). In some locations it was the all-time coldest month ever observed. The extreme cold led to ice buildup on waterways and made navigation difficult, slowed commerce, and forced ferry services to be suspended. Boat traffic was restricted as far south as parts of the upper Chesapeake Bay for about a week due to icy conditions, and the start of maple season was delayed by up to three weeks in New England, New York, and Ohio because the extreme cold kept sap from flowing.

The possible causes of the record cold were discussed, and a review of the official forecast from the Climate Prediction Center (CPC), along with the forecasts from two climate models were presented.

2. Data

This study utilized data from the NCEP/NCAR Reanalysis (Kalnay *et al.* 1996) from NOAA's Earth System Research Laboratory. The official forecasts from the CPC were examined as well as the CFSv2 (Saha *et al.* 2014) and NMME (Kirtman *et al.* 2014) forecasts. The ENSO and MJO discussions from the CPC were used as well as the ENSO indices for each region. Prior research that investigated the cold outbreak of January 1977 (Namias 1978), which was the only month in the Northeast U.S. to be more severe than the February 2015 cold outbreak since 1948 was also examined (Walsh *et al.* 2001). Global SST anomalies and Pacific-North America (PNA) and East Pacific (EP-NP) teleconnection patterns were examined.

3. Summary of results

During February 2015 there were persistently low 500 hPa heights across central Siberia, northern Canada, and into the Great Lakes and Northeast U.S. Examining the 500 hPa composite anomalies from

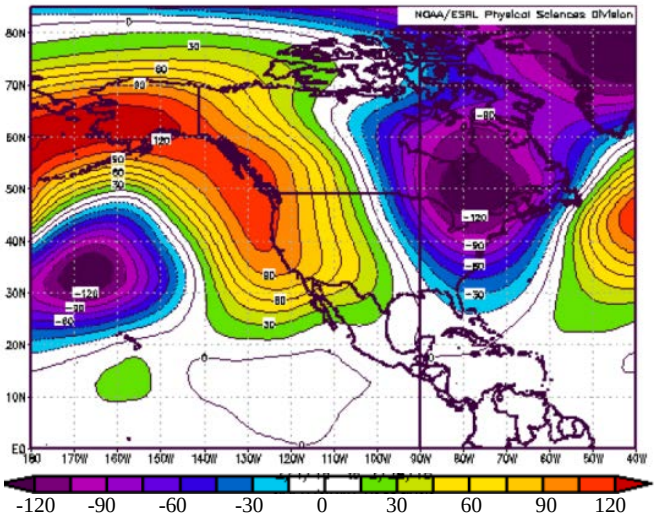

Fig. 1 500 hPa geopotential height composite anomaly (m), from the 1981-2010 climatology, during February 2015. Figure *from NOAA's Earth System Research Laboratory*

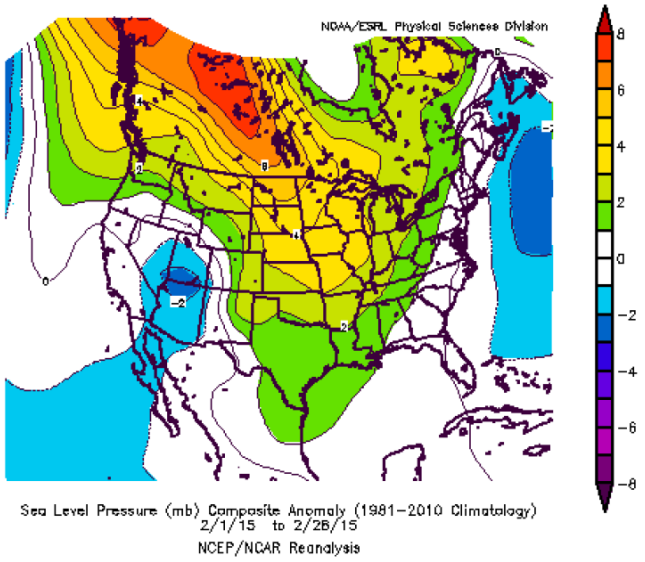

Fig. 2 Sea level pressure composite anomaly (mb), from the 1981-2010 climatology, during February 2015. Figure *from NOAA's Earth System Research Laboratory.*

Correspondence to: Corey A. Bogel, NOAA's National Weather Service, Caribou, Maine; E-mail: corey.bogel@noaa.gov.

1981-2010 climatology (Fig. 1), significant negative anomalies were noted across the greater Northeast U.S. including all of New England. The persistence of the upper air pattern led to well below normal temperatures at the surface, which corresponded well with the upper air anomalies (Nouhan 1999). The sea level pressure composite anomaly (Fig. 2) showed that surface pressures were lower than the climatological mean just off the Northeast U.S. coast. This was due to a series of surface lows that moved toward the Northeast U.S. coast from the west and intensified across the Canadian Maritimes. The persistence of this pattern led to favorable conditions for pulling cold Canadian air into the Northeast U.S. on the back side of the surface lows. Above average sea surface temperatures (SSTs) were observed across the western and central equatorial Pacific as well as along the west coast of North America and across parts of the north Atlantic Basin. The positive SST anomalies along the west coast of North America potentially helped to amplify the mean long wave ridge over the western North America coast, and were likely a significant factor in the long wave pattern at mid and upper latitudes. The positive SST anomalies in the north Atlantic may have been an additional source of latent heat for enhanced east coast cyclogenesis for the New England coast. Additional reinforcing shots of cold air followed the passage of the cyclones and also likely aided in keeping the cold air in place throughout the month. The Madden-Julian Oscillation (MJO) was weak with no coherent MJO pattern observed during the month of February. The fact that the MJO was not coherent and did not disrupt the quasi-stationary position of anomalous convection across the western equatorial Pacific may have been a driver in the persistence of the upper air pattern. It is proposed that the more western displaced Pacific equatorial positive SST anomalies and associated enhanced convection observed during February 2015 and January 1977 potentially resulted in a more regional (rather than basin wide) enhancement of the Hadley Cell circulation over the west central and central tropical north Pacific.

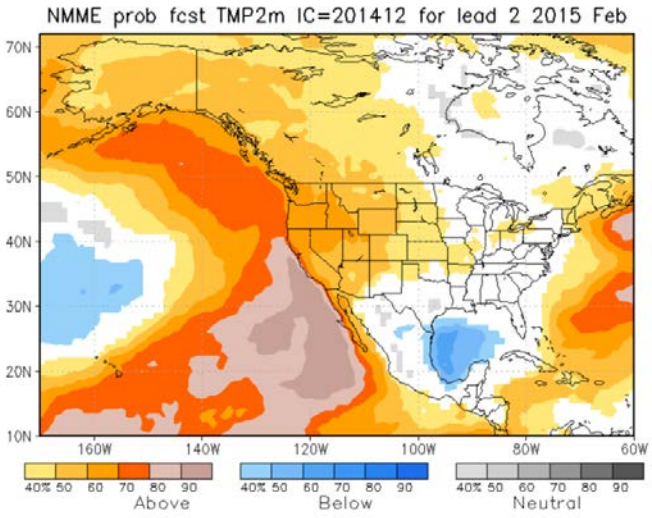

Fig. 3 NMME forecast issued December 9, 2014, valid for February 2015. 2-m temperature tercile probabilities.

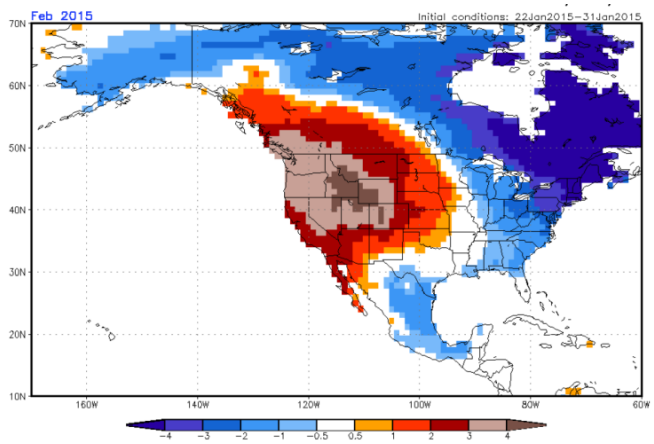

Fig. 4 CFSv2 2-m temperature anomalies (K) forecast for February 2015 based on initial conditions from January 22-31, 2015.

The NMME did not have a signal pointing toward an unusually cold February, and in fact the lead 2 outlook in December indicated an increased likelihood of above normal temperatures (Fig. 3). The CFSv2, which is one of the component members of the NMME, did have an increasing cold signal during the month of January (Fig. 4). The official forecast from the CPC issued on 15 January 2015 had no skill compared to a random forecast; however, the CPC forecast issued on 31 January 2015 (Fig. 5), accurately forecasted an increased likelihood of below normal temperatures in February. The climate models gave little lead time for such a significant event, and were unable to provide any guidance to the forecaster as to whether the anomalies would be record breaking. There are still a significant amount of unknowns that affect monthly climate forecasts and more work is needed to better predict these events.

4. Discussion

February 2015 was one of the coldest Februaries on record across the Northeast U.S., and in some locations the all-time coldest month on record. An upper air analysis showed that there was a very persistent pattern during the month with a strong ridge along the west coast of North America, and a strong downstream trough that extended from the Canadian Archipelago into the Northeast U.S. The pattern retrograded during the month, but only very slowly. This kept a fresh supply of cold arctic air across the Northeast U.S. all month. The lack of a well defined MJO, enhanced convection across the tropical west Pacific, and positive SST anomalies along the west coast of North America may have all played a role in the persistence of the upper air pattern. Surface cyclogenesis along and off the Northeast U.S. coast also likely played a role in keeping the cold air in place across the region.

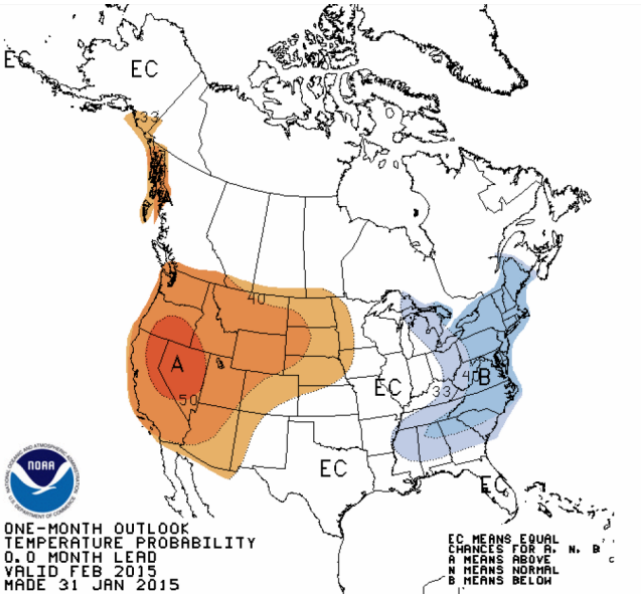

Fig. 5 The final official National Weather Service's Climate Prediction Center temperature forecast for February 2015 from the CPC that was issued January 31, 2015.

Prior extreme cold months did not have a similar distribution to February 2015 in the 500 hPa geopotential height composite anomalies across North America (Konrad 1989). There is therefore not one common composite anomaly pattern in the 500 hPa geopotential heights that forecasters can look for when attempting to determine whether a month has the potential for being record cold, but rather different distributions in the 500 hPa geopotential heights may lead to such extreme outcomes. The mean 500 hPa patterns did, however, show a mean trough in all cases across the Northeast U.S. Further evaluation of the composite anomalies associated with extreme cold months would be a worthy endeavor. Rapid surface cyclogenesis along and off the Northeast U.S. coast does appear to play an important role in reinforcing the cold air.

References

Kalnay, E., and Coauthors, 1996: The NCEP/NCAR 40-year reanalysis project. *Bull. Amer. Meteor. Soc.*, **77**, 437-471.

Kirtman B, and Coauthors, 2014: The North American Multi-Model Ensemble (NMME): Phase-1 seasonal to interannual prediction; Phase-2 toward developing intra-seasonal prediction. *Bull. Amer. Meteor. Soc.*, **95**, 585-601, DOI 10.1175/BAMS-D-12-00050.1

Konrad, C.E., and S.J. Colucci, 1989: An examination of extreme cold air outbreaks over Eastern North America. *Mon Wea. Rev.*, **117**, 2687-2700.

Namias, J., 1978: Multiple causes of the North American abnormal winter 1976-77. *Mon. Wea. Rev.*, **106**, 279-295.

National Weather Service Eastern Region (NWS ER) Quarterly Climate Impacts and Outlooks, March 2015. [Available online at http://www1.ncdc.noaa.gov/pub/data/papers/RCSD/NIDIS-pdf/ER-Winter-2014-15-Quarterly-updated-v2.pdf]

Nouhan, V., 1999: The use of 500 mb Non-Teleconnection area indicies over North America in determining arctic air mass potential east of the Rockies. *NWS Central Region Applied Research Paper*, **20**, NOAA's National Weather Service, Kansas City, MO.

Saha, S., and Coauthors, 2014: The NCEP Climate Forecast System version 2. *J. Climate*, **27**, 2185–2208.

Walsh, J. E., A.S. Phillips, D.H. Portis and W.L. Chapman, 2001: Extreme cold outbreaks in the United States and Europe, 1948-99. *J. Climate*, **14**, 2642-2658.

Science and Technology Infusion Climate Bulletin
NOAA's National Weather Service
41st NOAA Annual Climate Diagnostics and Prediction Workshop
Orono, ME, 3-6 October 2016

Causes of Extreme Ridges that Induce California Droughts

Haiyan Teng and Grant Branstator
National Center for Atmospheric Research, Boulder, CO

ABSTRACT

California droughts are often caused by high-amplitude and persistent ridges near and off the west coast without apparent connections with ENSO. Here with a hierarchy of climate models, we demonstrate that extreme ridges in this region are associated with a continuum of zonal wavenumber-5 circumglobal teleconnection patterns that originate from midlatitude atmospheric internal dynamics. Although tropical diabatic heating anomalies are not essential to the formation and maintenance of these wave patterns, certain persistent heating anomalies may double the probability of ridges with amplitudes in the 90th percentile occurring on interannual time scales. Those heating anomalies can be caused by either natural variability or possibly by climate change and they do not necessarily depend on ENSO. The extreme ridges that occurred during the 2013/2014 and 2014/2015 winters (Fig. 1) could be examples of ridges produced by heating anomalies that are not associated with ENSO. This mechanism could provide a source of subseasonal-to-interannual predictability, beyond the predictability provided by ENSO.

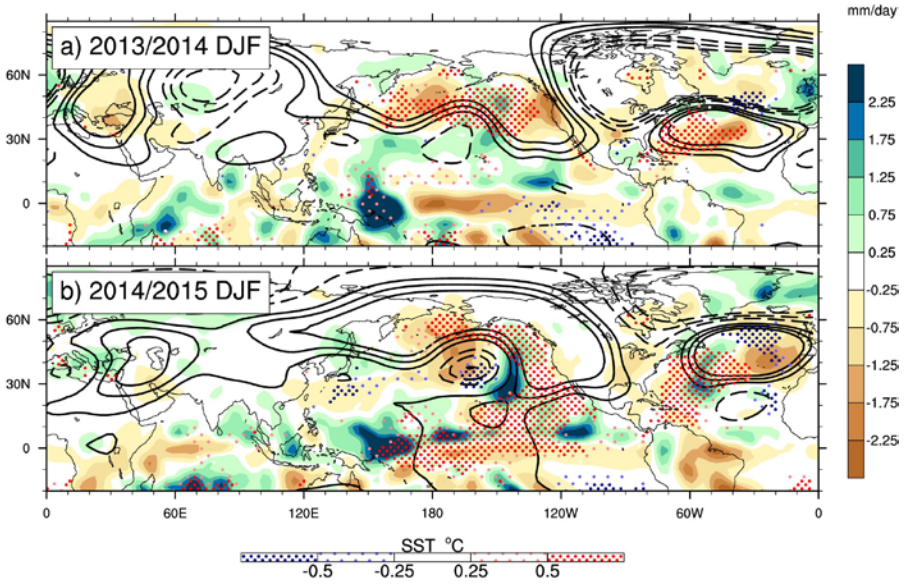

Fig.1 Seasonal mean 200 hPa geopotential height (z200, contours, at ±20,40,60m), precipitation (shading, mm/day), and sea surface temperature (SST, dots, °C) anomalies in DJF of a) 2013/2014 and b) 2014/2015 relative to the 1979-2015 climatology.

This work is in press in Journal of Climate in 2017.

References

Teng, H. and G. Branstator, 2017: Causes of extreme ridges that induce California droughts, *J. Climate*, in press.

Correspondence to: Haiyan Teng, National Center for Atmospheric Research, Boulder, CO;
E-mail: hteng@ucar.edu

Science and Technology Infusion Climate Bulletin
NOAA's National Weather Service
41st NOAA Annual Climate Diagnostics and Prediction Workshop
Orono, ME, 3-6 October 2016

Attribution and Prediction of China Droughts Across Scales

Xing Yuan, Linying Wang, Shanshan Wang, Peng Ji, and Miao Zhang
CAS Key Laboratory of Regional Climate-Environment for Temperate East Asia (RCE-TEA), Institute of Atmospheric Physics, Chinese Academy of Sciences, Beijing, China

1. Introduction

Droughts are driven by naturally occurring climate variations. However, climate change and human activities may have altered the characteristics of droughts, and increased society's vulnerability to them. Droughts have a variety of spatiotemporal scales from flash droughts at local scales that are usually concurrent with heat extremes, to seasonal/decadal droughts at regional to continental scales that are associated with large-scale climate anomalies and certain atmospheric circulation patterns. Droughts also have quite different implications across a number of sectors, depending on whether they manifests as a meteorological, agricultural or hydrological drought, where the latter type of droughts could be affected by human activities directly. This raises many challenges to attributing changes, understanding predictability and to investigating the impacts of droughts across spatial and temporal scales in a changing environment. This article will show a few progresses on the attribution and prediction of China droughts across scale, which also has implications for drought research over other regions of the world.

2. Increasing flash droughts over China during past 30 years

In recent years, the frequent occurrence of flash droughts across the world has raised much attention. Flash drought is triggered by heatwave accompanied with low soil moisture (SM) and high evapotranspiration (ET). Due to its rapid onset and unusual intensity, the impact of flash drought can be devastating in some cases. Here we assessed the long-term trend and variability of flash droughts over China during 1979-2010 based on pentad-mean temperature from over two thousand meteorological stations and SM and ET from three global reanalysis products (Wang *et al.* 2016). Overall, all three reanalysis data show that there is an increasing trend

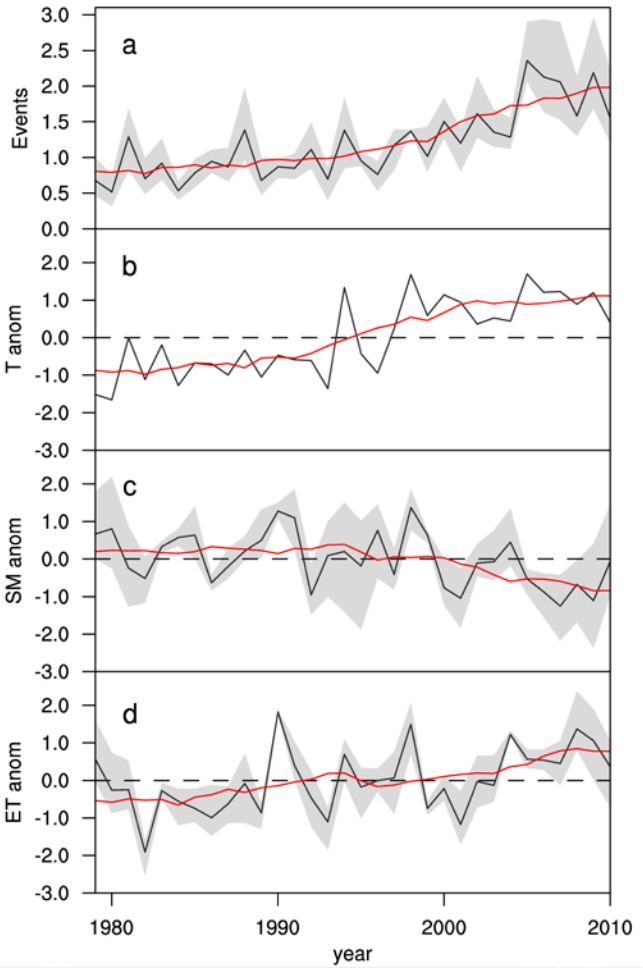

Fig. 1 Changes of ensemble mean flash drought event and its component variables averaged over China. (a) The number of flash drought events per year, (**b**) surface air temperature (T) anomaly, (**c**) soil moisture (SM) anomaly, (**d**) ET anomaly (black curves). The red curves are the 10-year running means and the grey shadows are the ranges of results from different reanalysis products. (Wang *et al.*, 2016)

Correspondence to: Xing Yuan, CAS Key Laboratory of Regional Climate-Environment for Temperate East Asia (RCE-TEA), Institute of Atmospheric Physics, Chinese Academy of Sciences, Beijing, 100029, China;
E-mail: yuanxing@tea.ac.cn

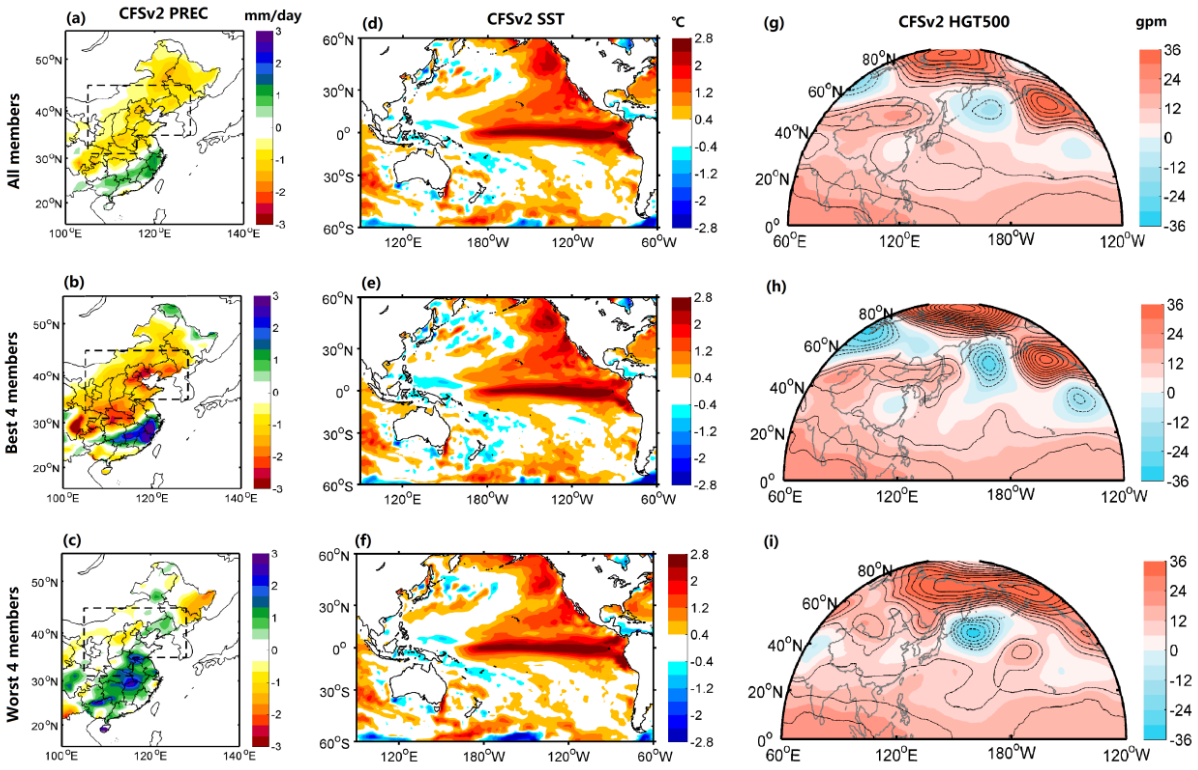

Fig. 2 Spatial distributions of CFSv2 predicted anomalies of precipitation, SST and 500-hPa geopotential height in the summer of 2015. The left panels are the composite of (a) all ensemble members, (b) four best and (c) four worst members for 0.5-month lead seasonal forecasts of precipitation anomaly(mm/day). The middle (d–f) and right panels (g–i) are the same as the left, but for the anomalies of SST (°C) and 500-hPa geopotential height (gpm). (Wang *et al.*, 2017)

for flash droughts in recent 30 years though there is some difference in amplitudes (Fig. 1). The increase in flash droughts is associated with changes of annual mean surface air temperature, SM and ET. The warming amplitude is 0.36°C per decade ($p < 0.01$) over China for the period 1979-2010. The long-term variability of SM and ET are less significant, despite a drying trend for SM ($p < 0.05$) and an increasing trend for ET ($p < 0.05$). Thus the ensemble mean of flash droughts increases by 109% over the whole period and the increase is mainly associated with the long-term warming trend. The increasing trends in flash droughts even tripled despite the warming hiatus since 1998. Further analyses indicate that the interannual variability of flash droughts is influenced by variation in SM and ET and the effect of the decreased temperature is compensated by decreased SM and increased ET (Wang *et al.* 2016).

3. Seasonal forecasting of the 2015 severe summer drought over North China

With a good prediction of the 2015/16 big El Niño, NCEP's Climate Forecast System version 2 (CFSv2) roughly captured the 2015 extreme summer drought over North China (Fig. 2, top panels). This raises a question of whether the 2015/16 monster El Niño help the forecasting of the 2015 extreme summer drought. Here, we show that a strong El Niño does not necessarily result in an extreme drought, but it depends on whether the El Niño evolves synergistically with Eurasian spring snow cover reduction to trigger a positive summer Eurasian teleconnection (EU) pattern that favors anomalous northerly and air sinking over North China. As seen from Fig. 2g, CFSv2 generally captured the positive EU circulation pattern across Eurasia, which led to a well-captured drought pattern over North China but with an underestimation of intensity. Meanwhile, comparing the performances of predicted sea surface temperature (SST) between four best and four worst cases, little difference were found for the predicted SST anomalies, which both agreed with the observed SST anomaly well, suggests that a strong El Niño signals can be predicted by the dynamical climate forecast model quite well (Figs. 2e, f). However, it does not necessarily mean that it will increase the

predictability of the extreme summer drought in North China. In fact, the composite of the four best members was more skillful than the full ensemble mean in terms of the prediction of the positive EU pattern (Fig. 2h), while the four worst composite totally failed to capture such circulation pattern (Fig. 2i) and thus missed the drought (Fig. 2c). Indeed, our results showed that a dynamical-statistical forecasting approach that combines both the low- and high-latitudes precursors is more skillful than the dynamical forecasting at long lead (Wang *et al.* 2017).

4. The role of human interventions on hydrological drought forecasting

We also assessed the effects of human interventions on the drought propagation based on five decades (1961-2010) of naturalized and observed streamflow datasets over a heavily managed river basin, the Yellow River basin in northern China. After calibrating the Variable Infiltration Capacity (VIC) land surface hydrological model grid by grid, the impact of human intervention on the hydrological drought predictability is being explored within the ESP/VIC and NMME/VIC forecasting framework that has been established over the Yellow River basin (Yuan 2016; Yuan *et al.* 2016). Overall, the nonlinear response of hydrological drought to meteorological drought has been increased by human activities, and the response time also increases especially during the summer seasons. We use the Brier Score (BS) to evaluate the probabilistic forecast skill for the ensemble hydrological droughts within a set of 29-year (1982-2010) hindcasts (Fig. 3). In natural conditions, BS values increases along with the increase in lead times. And the NMME/VIC outperforms the ESP/VIC by decreasing BS 11%-26% in the first month and by 3%-14% in the second and third months. While in anthropocene, both ESP/VIC and NMME/VIC perform better than the natural cases, and the forecast skill does not decrease over lead times. This indicates that besides climate predictability, taking account of human interventions is of great importance for hydrological drought forecasting (Yuan *et al.* 2017).

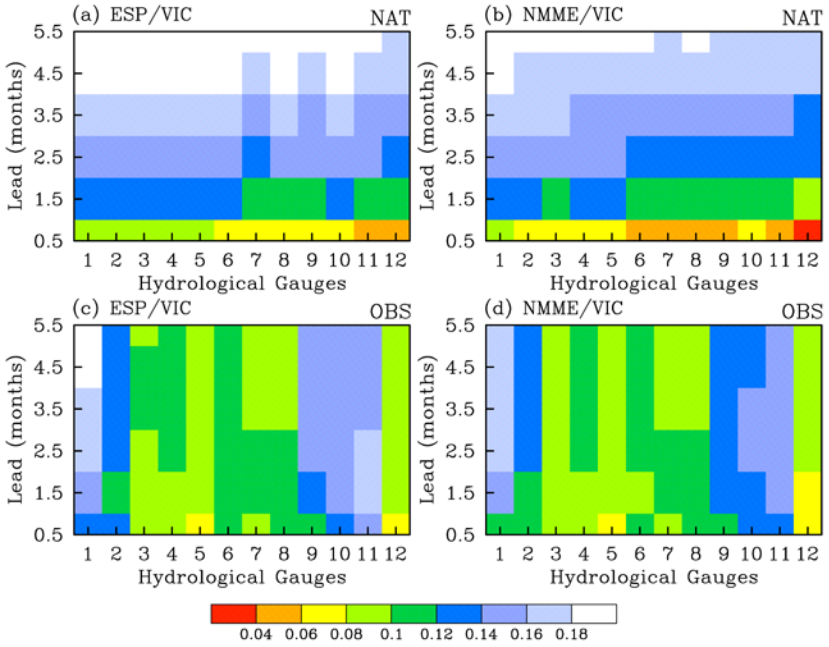

Fig. 3 Brier score (BS) for ensemble hydrological drought forecasts from a climatology method (ESP/VIC) and the climate-model-based approach (NMME/VIC) against VIC offline simulated (a, b) and observed (c, d) streamflow at different leads over the Yellow River basin during 1982-2010. For the verification against observed streamflow, the forecasts have been post-processed. (Yuan *et al.*, 2017)

5. Summary

As the climate becomes warmer and the human interventions become more intensive, both the risk for flash drought and the severity of hydrological drought are increasing, which call for more attention for combining traditional multi-scale drought predictability studies (*e.g.*, exploring canonical oceanic and land precursors) with a decision maker-oriented research. Therefore, effectively linking the advances in hydro-climatological predictability with drought mitigation and adaptation is a grand challenging in a foreseeable future.

Acknowledgements. This work was supported by the National Natural Science Foundation of China (No. 91547103), National Key Research and Development Program (2016YFA0600403), China Special Fund for

Meteorological Research in the Public Interest (Major projects) (GYHY201506001), CAS Key Research Program of Frontier Sciences (QYZDY-SSW-DQC012), and the Thousand Talents Program for Distinguished Young Scholars.

References

Wang, L., X. Yuan, Z. Xie, P. Wu, Y. Li, 2016: Increasing flash droughts over China during the recent global warming hiatus. *Scientific Reports*, **6**, Article number: 30571, doi: 10.1038/srep30571.

Wang, S., X. Yuan, and Y. Li, 2017: Does a strong El Niño imply a higher predictability of extreme drought? *Scientific Reports*, **7**, Article number: 40741; doi: 10.1038/srep40741.

Yuan, X., F. Ma, L. Wang, Z. Zheng, Z. Ma, A. Ye, and S. Peng, 2016: An experimental seasonal hydrological forecasting system over the Yellow River basin-Part 1: Understanding the role of initial hydrological conditions. *Hydrol. Earth Syst. Sci.*, **20**, 2437–2451, doi:10.5194/hess-20-2437-2016.

Yuan, X., 2016: An experimental seasonal hydrological forecasting system over the Yellow River basin-Part 2: The added value from climate forecast models. *Hydrol. Earth Syst. Sci.*, **20**, 2453–2466, doi:10.5194/hess-20-2453-2016.

Yuan, X., M. Zhang, and L. Wang, 2017: Understanding and seasonal forecasting of hydrological drought in the anthropocene. *Hydrol. Earth Syst. Sci.*, revised.

Science and Technology Infusion Climate Bulletin
NOAA's National Weather Service
41st NOAA Annual Climate Diagnostics and Prediction Workshop
Orono, ME, 3-6 October 2016

The Quantification of Rainfall Needed to Overcome Drought: A Study in North Texas

Jasmine Montgomery[1] and D. Nelun Fernando[2]
[1]*University of Oklahoma, Norman, Oklahoma*
[2]*Texas Water Development Board, Austin, Texas*

1. Introduction: 2010–2015 drought over Texas

Texas is no stranger to dry, hot weather. The state has a reputation of being one large desert. That is not the case; but, in 2011, the perception of a desert seemed to become a reality. Texas had been through plenty of dry and wet spells and 2011 appeared to be just another dry spell, at first. When the heat did not let up and with a lack of rainfall, the state had entered a very serious drought.

With excessive heat and little rainfall, the year of 2011 became the driest year on record for the state of Texas (Richter 2012). The 2010–2015 drought was the second worst drought on record in the state. Days of heavy rainfall in May 2015 helped reverse the cumulative soil moisture deficit in the state. It was only in July 2015 that Texas was finally drought free (Fig. 1).

2. Study area and problem statement

The study focused on the drought that affected North-Central Texas, within the coordinates of 31.35°N-34.11°N and 95.41°W-98.56°W.

Starting in 2011, the drought caused lakes and rivers in North Texas to dry out. For example, a streamflow gauge on the East Fork Trinity River recorded a discharge of 0.0003 ft^3/s in September 2014. During the drought many lakes in North Texas fell to more than ten feet below full capacity (Fig. 2).

There was measurable rain over the study area in the winter of 2011/2012 and in the fall of 2013. However, the rainfall was not sufficient to raise water levels in lakes in the region. The research question this study seeks to address is: How much rainfall is needed to overcome a drought-induced soil moisture deficit so that runoff occurs?

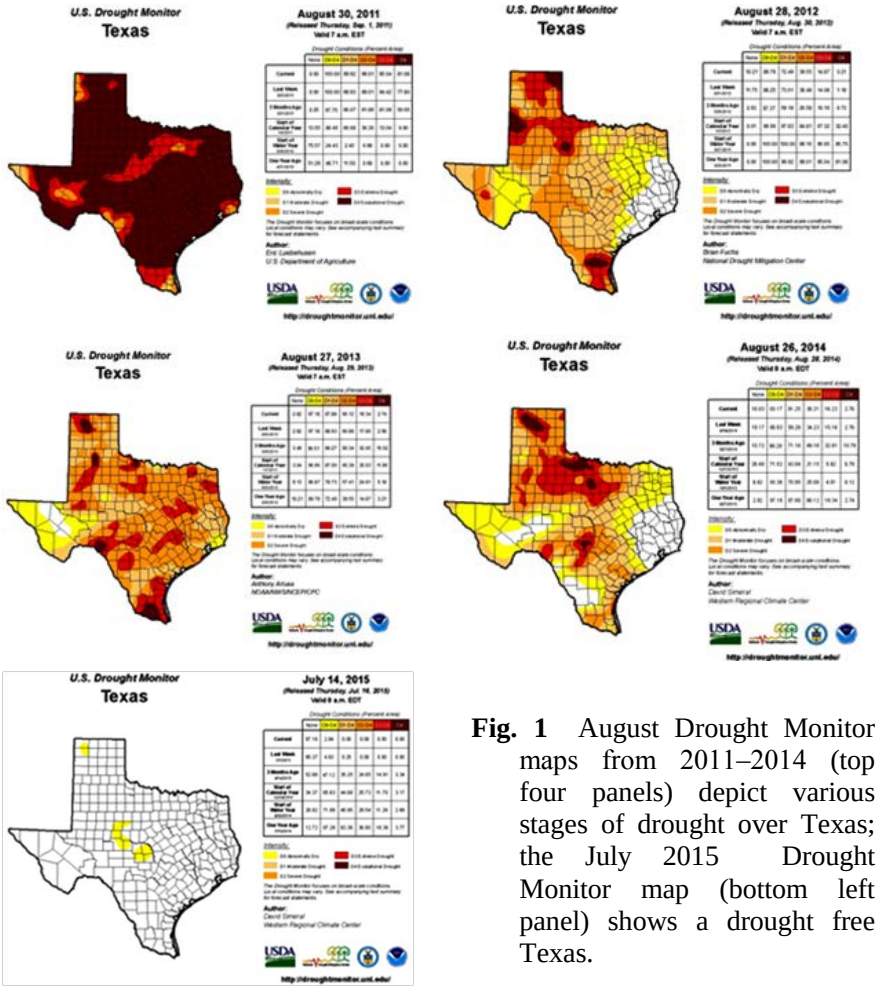

Fig. 1 August Drought Monitor maps from 2011–2014 (top four panels) depict various stages of drought over Texas; the July 2015 Drought Monitor map (bottom left panel) shows a drought free Texas.

Correspondence to: D. Nelun Fernando, Texas Water Development Board, Austin, Texas;
E-mail: Nelun.Fernando@twdb.texas.gov

3. Methodology and datasets used

The study focused on understanding the evolution of soil moisture anomalies and associated rainfall accumulations and reservoir levels. Area-averaged monthly soil moisture anomalies within the study domain were compared with area-averaged monthly rainfall accumulations, as well as with reservoir levels and streamflow to determine when the soil moisture deficit eased and runoff occurred.

Datasets used include:

- Precipitation Reconstruction over Land (PREC/L) rainfall dataset from the Climate Prediction Center (Chen *et al.*, 2002)
- Simulated soil moisture from the MOSAIC model output of the North American Land Data Assimilation System (NLDAS, Xia *et al.*, 2012)
- Reservoir levels for lakes in North Texas from http://waterdatafortexas.org/reservoirs/statewide
- Streamflow data for gauges upstream of the reservoirs from the U.S. Geological Survey (http://waterwatch.usgs.gov)

4. Results

During the 2010–2015 drought, the soil moisture anomalies in North Texas were negative for most of the time. That would be expected of a drought, but there were moments that the anomalies became positive. If the soil moisture anomalies are positive (Fig. 3), that may show relief in the region; but it does not always mean the drought is ending. The soil moisture anomalies during the 2010–2015 drought ranged from [negative] 0.03807 to [positive] 0.027442. From the worst of the drought to the end of the drought, there is a difference of 0.065. The lowest anomaly, - 0.03807, occurred in December 2012; but the lowest soil moisture value occurred in August 2011 with a value of 0.048 m^3/m^3. A reason as to why the dates do not match up is because August is the driest month of the year. So, a low value for soil moisture is not too far away from the norm; of which, the anomaly for August 2011 was - 0.022. When the lowest anomaly occurred by December 2012, North Texas had been in an intense drought for over a year. When the heavy rains came to North Texas in 2015, the moisture content rose and the anomalies became positive. December and May of 2015, respectively, had the highest and second highest amounts of soil moisture.

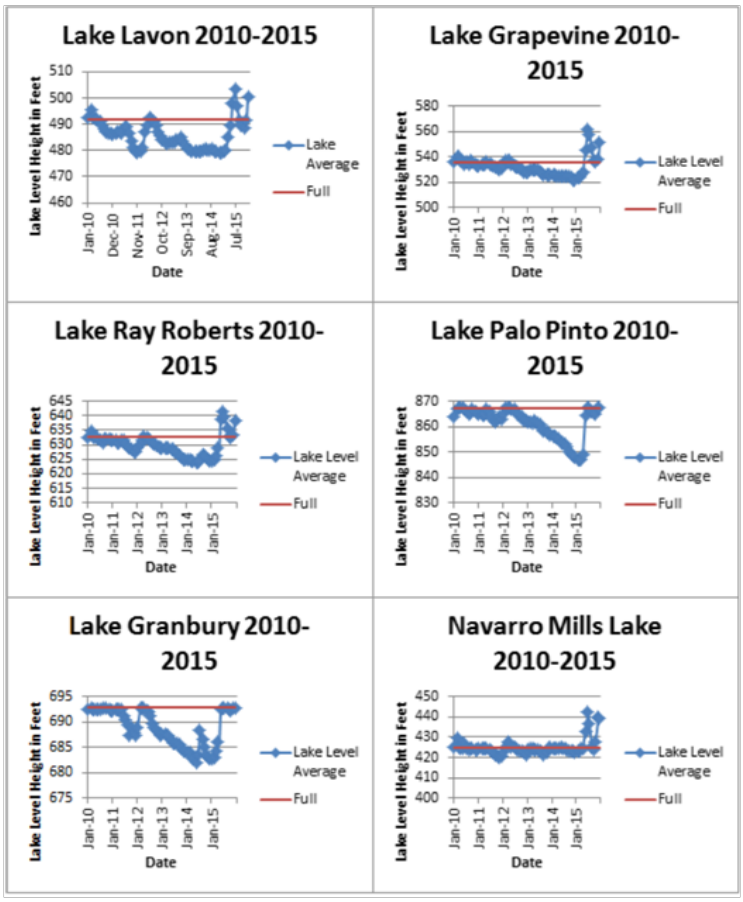

Fig. 2 Lake levels for six reservoirs in North Texas from 2010 to 2015. The blue line shows the lake level and the red line shows conservation storage capacity (data source: http://waterdatafortexas.org/reservoirs/statewide).

The calculated monthly rainfall average was about 3.15 inches from the PREC/L 1979-2015 dataset. This allows an answer to be reached for the original question of how much rainfall is needed to overcome a drought. The rainfall and soil moisture datasets were compared graphically (Fig. 4) to assess how much rainfall it took to end a drought, specifically the 2010–2015 drought. We assumed that three consecutive months of positive soil moisture anomalies could be a possible indicator of the

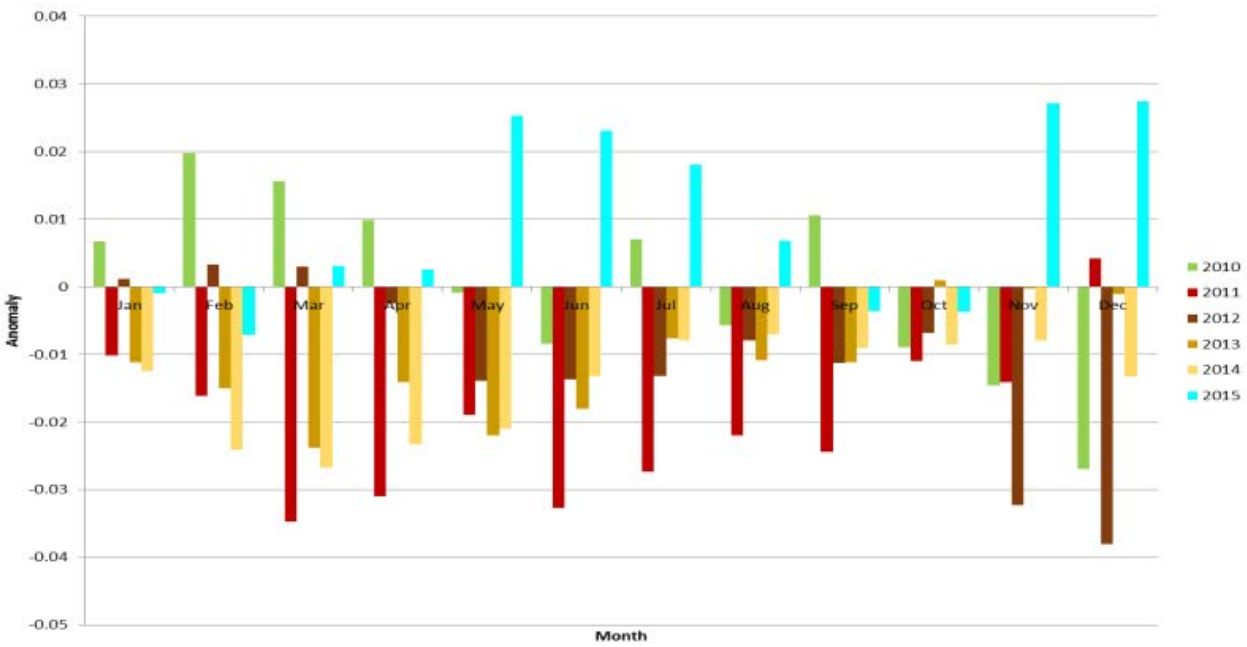

Fig. 3 Monthly soil moisture anomalies from 2010–2015.

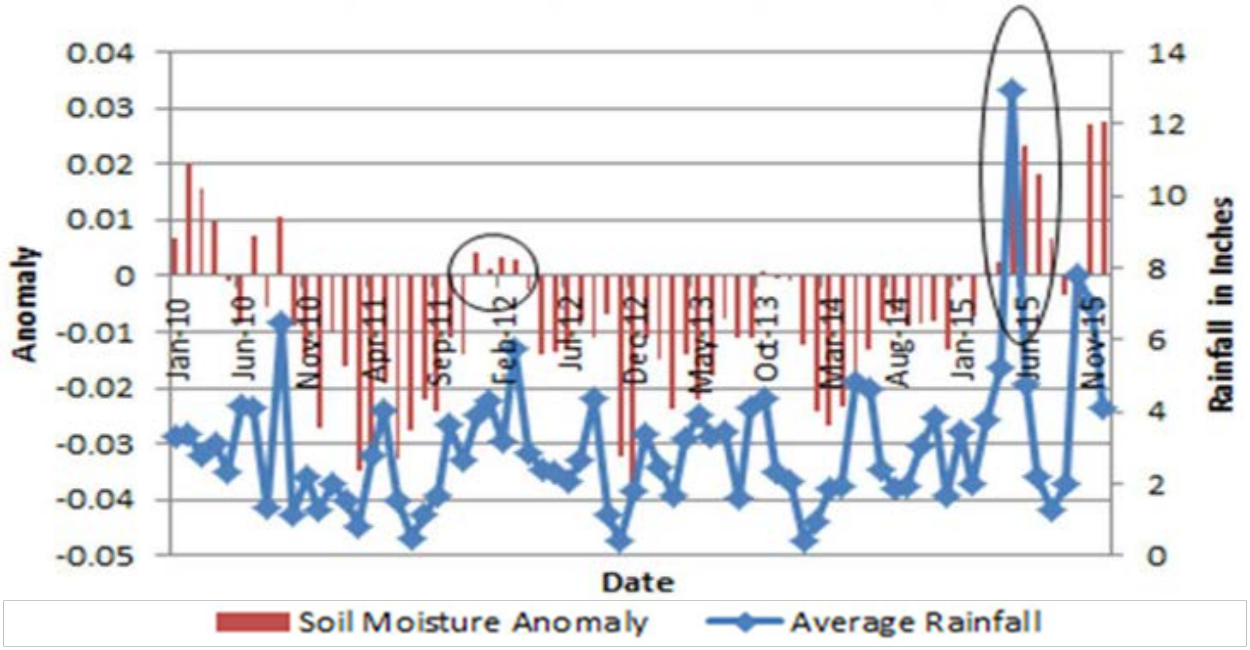

Fig. 4 Soil moisture anomalies and the average monthly rainfall from 2010–2015.

drought ending. The occurrence of three months of positive anomalies happened twice during the period of 2010–2015.

December 2011 through March 2012 is four months of positive anomalies, but the anomaly for these months was less than 0.01. The second continuous spell of positive monthly soil moisture anomalies commenced in March 2015 and remained positive through August. There were positive anomalies in rainfall during the first and second occurrences of consecutive months with positive soil moisture anomalies. The last positive rainfall anomaly before October 2013 was in March 2012 with 5.78 inches of rainfall. The rain that fell in May 2015 made that month the wettest month on record (Chuck 2015) with an average of 12.97 inches falling over the area of study.

5. Conclusions

The 2010–2015 drought was incredibly harsh on the state of Texas. As the drought lengthened, the amount of rainfall required to overcome it increased. A comparison of rainfall and soil moisture anomalies indicated that three consecutive months of positive soil moisture anomalies could be a possible indicator of drought termination. We found that it takes about 10–15 inches of rainfall within a thirty day period is needed to overcome a soil moisture deficit of the same severity as the 2010–2015 drought in North Texas. The methods applied in this study could be applied to different drought scenarios (*e.g*. short-term or multi-year under varied geographical settings) to quantify the rainfall needed to overcome prevailing soil moisture deficits.

References

Chen, M., P. P. Xie, J. E. Janowiak, and P. A. Arkin, 2002: Global land precipitation: A 50-yr monthly analysis based on gauge observations: *J. Hydrometeor.*, **3**, 249-266. doi: 10.1175/1525-7541(2002)003 <0249:GLPAYM>2.0.CO;2.

Chuck, E., 2015: Texas flooding: Here's a look at the state's rainfall by the numbers. *NBC News, 29 May 2015*. http://www.nbcnews.com/news/weather/35-trillion-gallons-water-texas-record-rain-numbers-n366541.

Richter, M., 2012: 2011 was the driest year on record in Texas. *Reuters*. http://www.reuters.com/article/us-weather-record-texas-idustre80700920120108.

Xia, Y., K. Mitchell, M. Ek, J. Sheffield, B. Cosgrove, E. Wood, L. Luo, C. Alonge, H. Wei, J. Meng, B. Livneh, D. Lettenmaier, V. Koren, Q. Duan, K. Mo, Y. Fan, and D. Mocko, 2012: Continental-scale water and energy flux analysis and validation for the North American Land Data Assimilation System project phase 2 (NLDAS-2): 1. Intercomparison and application of model products, *J. Geophys. Res.*, **117**, D03109, doi:10.1029/2011JD016048.

Science and Technology Infusion Climate Bulletin
NOAA's National Weather Service
41st NOAA Annual Climate Diagnostics and Prediction Workshop
Orono, ME, 3-6 October 2016

An Operational Drought Monitoring System for the Caribbean and Central America

Miliaritiana Robjhon[1,2] and Wassila Thiaw[1]

[1]*Climate Prediction Center, NOAA/NWS/NCEP, College Park, Maryland*
[2]*Innovim LLC., Greenbelt, Maryland*

1. Introduction

The recent 2015 El Nino drought devastated the economy of many Small Island Developing States of the Caribbean and Central America. Reports indicated several nations suffered a production loss of up to 50 percent. The Caribbean was impacted by a comparable drought in 2009-2010, which prompted regional meteorological organizations and institutions to establish a drought and precipitation monitoring network. However, effective monitoring and early warning information systems still remain a challenge due to the smallness of the scale of the Caribbean land relative to surrounding waters and ensuing limited availability of useful data.

To enhance capabilities of regional meteorological and hydrological services in drought monitoring and provide decision support tools to policymakers in the region, the Climate Prediction Center's International Desk has expanded its monitoring areas to the Caribbean and is developing tools to help detect and classify drought and track near real-time rainfall season characteristics, a critical determinant of drought development.

2. Tools

Using a consolidation of evidence-approach, similar to that used in the United States Drought Monitor, Standardized Precipitation Index (SPI) and soil moisture percentile rankings at multiple time scales are used. Additionally, rainfall season characteristics, including onset, evolution, and demise of the season are also tracked to provide an assessment of near real-time seasonal performance.

2.1 Rainfall season characteristics

Information on rainfall season characteristics is highly important for monitoring applications. The onset, mid-season dry spells, and early cessation of the season are all determinants of drought development. Figure 1a exhibits a bimodal distribution of rainfall, with the first rainfall season from May-August and second rainfall season from August-November over the "Dry Corridor" of Central America, delimited by 92°W-83°W, 10°N-16°N. The two seasons are divided by a period of reduced rainfall, also referred to as "Mid-Summer Drought". The onset and demise of the first and second rainfall seasons are determined using anomalous rainfall accumulation as in Coelho *et al.* (2015). First, daily rainfall anomaly is computed. Cumulative rainfall anomaly is then calculated from a few months earlier than the typical start of the rainfall season. The onset is defined as the relative minimum of the smoothed, 21-day centered moving averaged accumulated rainfall anomaly. Conversely, the demise is defined as the relative maximum of the smoothed curve.

The 2015 first rainfall season began in early June and the season was very short, while the second season started in early October and was relatively long (Fig. 1b). The onset of the 2015 first rainfall season occurred in early June and was late by two weeks relative to the climatological onset in early to mid-May (Fig. 1c). The 2015 second rainfall season started in early to mid- October and was delayed by six weeks relative to the climatological onset in early September (Fig. 1d). The demise of the 2015 first rainfall season occurred in late June and was ahead of the climatology, which is in mid to late August, by nine weeks (Fig. 1e). The demise of the 2015 second rainfall season took place in early December and was prolonged by two weeks compared to the climatology in mid to late November (Fig. 1f).

Correspondence to: Miliaritiana Robjhon, Climate Prediction Center, NOAA/NWS/NCEP, 5830 University Research Court, College Park, MD 20740; E-mail: miliaritiana.robjhon@noaa.gov

2.2 Drought monitor

Drought monitoring, specifically tailored for the Caribbean requires high to medium-resolution data. SPI at 1, 3, 6, and 12 month time scales is computed using the 0.25^0 x 0.25^0 near real-time Tropical Measuring Mission Multi-Satellite Precipitation Analysis (Huffman *et al.* 2007). Soil moisture percentile rankings are calculated from the 0.5^0x 0.5^0 soil moisture output of the Climate Prediction Center's Leaky Bucket Model (Fan and van den Dool 2004).

Figure 2a shows SPI over portions of northeastern Tropical Pacific, Caribbean Sea, to western Atlantic during March-May 2015. Drought conditions were detected in May 2015 as indicated by large negative values of SPI along the Gulf of Fonseca of Central America, Hispaniola, Puerto Rico, and the northern portions of the Lesser Antilles. Abnormal dryness is observed across the southern parts of the Lesser Antilles. While wet soil is observed over Central America, neutral to dry soil is depicted over the Caribbean (Fig. 2b). Time series of SPI shows long-term drought developed over Roseau, Dominica as early as early spring 2015 (Fig. 2c). However, soil moisture did not dry out until late spring to early summer 2015 (Fig. 2d).

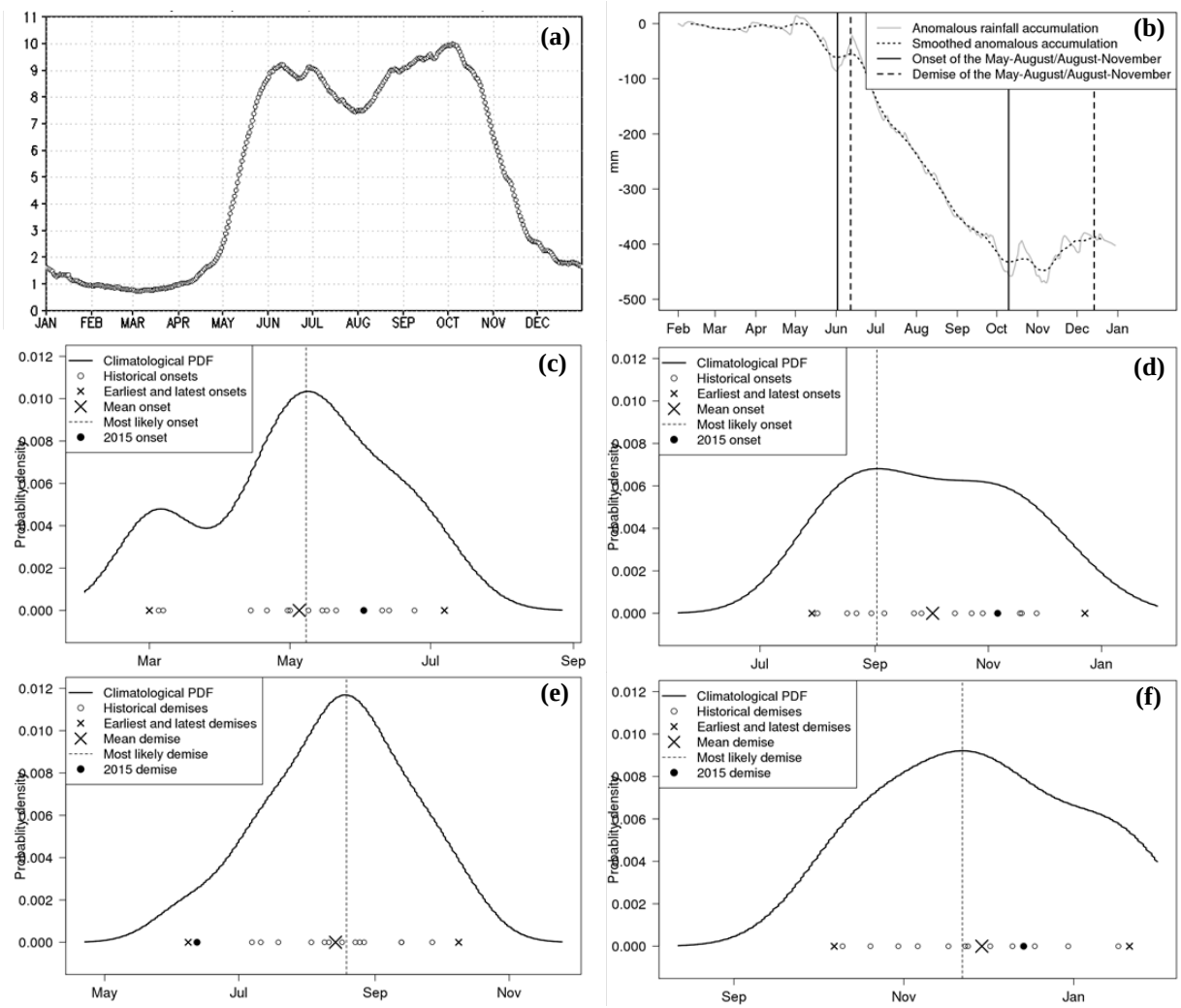

Fig. 1 Daily rainfall climatology over the "Dry Corridor" of Central America, delimited by 92°-83°W; 10°-16°N (a); anomalous rainfall accumulation and onset and demise of the 2015 first and second rainfall seasons (b); probability distribution function for the onset of the first (c) and second (d) rainfall season; probability distribution function for the demise of the first (e) and second (f) rainfall season.

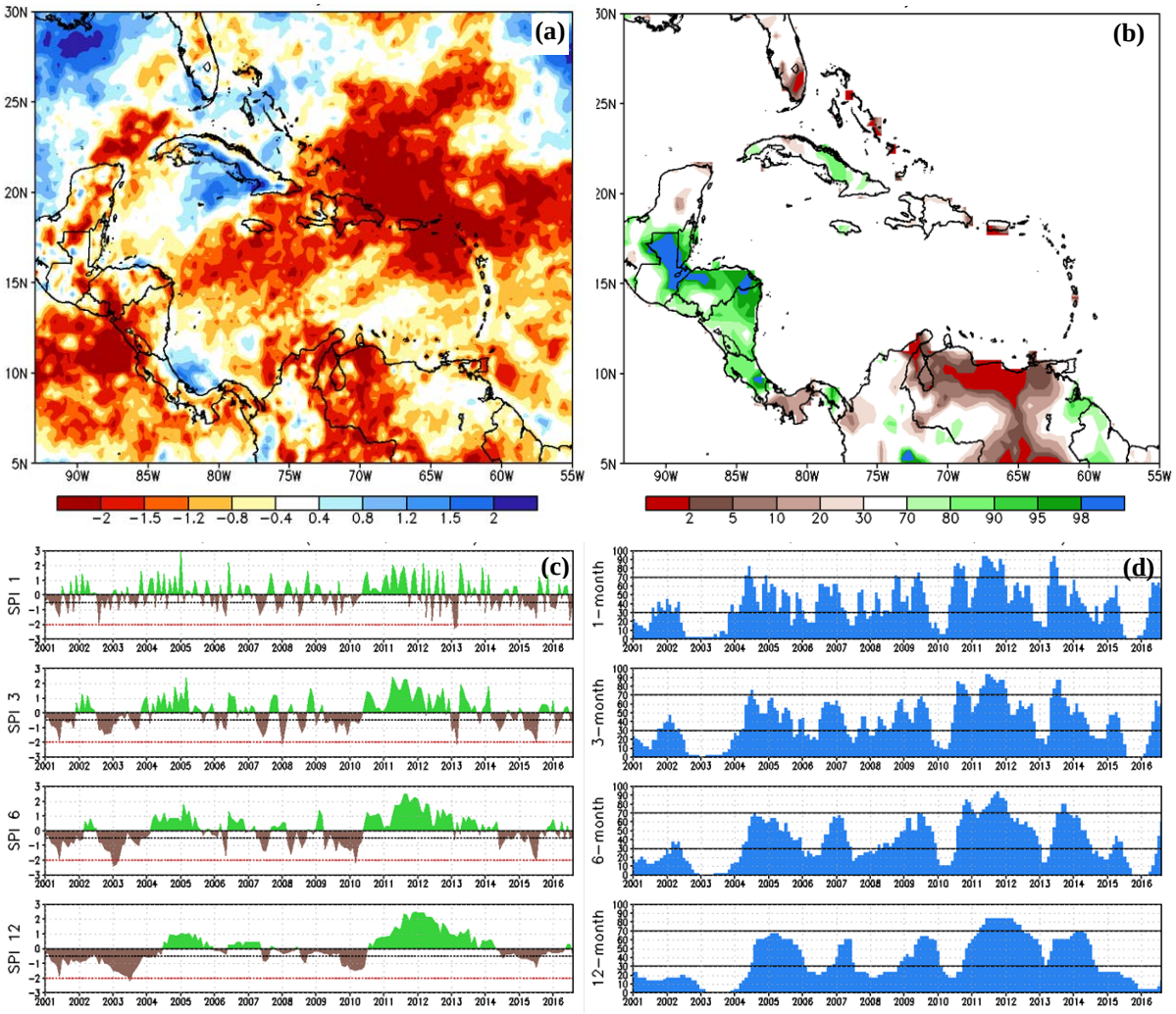

Fig. 2 Basin-wide Standardized Precipitation Index at 3-month time scale, ending in May 2015 (a); soil moisture percentile during March-May 2015 (b); time series of Standardized Precipitation Index at 1, 3, 6, and 12-month time scale over the nearest grid point (15.309°N, 61.379°W) to Roseau, Dominica (c); same as (c) but for soil moisture percentile (d).

3. Summary and future works

Near real-time monitoring of drought indices enabled the timely detection of short and long-term drought over the Caribbean and Central America in 2015. Basin-wide and grid point Standardized Precipitation Index and soil moisture percentile at 1, 3, 6, and 12-month time scales showed developing drought over Roseau, Dominica as early as spring 2015. However, the soil did not dry out until late spring to early summer 2015. Over the "Dry Corridor" of Central America, both the first and second rainfall seasons were delayed relative to the climatological onset. However, the first rainfall season was very short due to a precocious cessation of rainfall, while the second season was relatively long, with a slightly delayed demise of the season.

Future work include development of drought indices using the Climate Prediction Center Morphing technique precipitation data, implementation of rainfall characteristics analysis over grid points or sub-regions, and exploration of potentials toward drought outlook using the National Multi-Model Ensemble prediction.

References

Coelho, C.A.S., D.H.F. Cardoso, and M.A.F. Firpo, 2016: Precipitation diagnostics of an exceptionally dry event in Sao Paulo, Brazil. *Theor. Appl. Climatol.*, **25**: 769. doi:10.1007/s00704-015-1540-9.

Fan, Y., and H. van den Dool, 2004: Climate Prediction Center global monthly soil moisture data set at 0.5° resolution for 1948 to present. *J. Geophys. Res.*, **109**, D10102, doi:10.1029/2003JD004345.

Huffman, G.J., R.F. Adler, D.T. Bolvin, G. Gu, E.J. Nelkin, K.P. Bowman, Y. Hong, E.F. Stocker, and D.B. Wolff, 2007: The TRMM Multi-Satellite Precipitation Analysis: Quasi-global, multi-year, combined-sensor precipitation estimates at fine scale. *J. Hydrometeor.*, **8**(1), 38-55.

5. CLIMATE SERVICES

41th NOAA Annual Climate Diagnostics and Prediction Workshop

3-6 October 2016, Orono, Maine

Science and Technology Infusion Climate Bulletin
NOAA's National Weather Service
41st NOAA Annual Climate Diagnostics and Prediction Workshop
Orono, ME, 3-6 October 2016

Consultation with Industry to Improve Australia's Climate Prediction Services

Robyn Duell, Alison Cook, Jeff Sabburg, Helen Bloustein, Andrew Watkins, and David Jones
Australian Bureau of Meteorology

Engaging with climate sensitive industries and understanding user needs is central to the development of climate services at the Australian Bureau of Meteorology (the Bureau). The Bureau has recently upgraded its climate prediction service with further substantial improvements underway. Comprehensive consultation has been undertaken at each phase of service development to not only determine user needs, but also measure levels of comprehension and satisfaction. Key findings were that comprehension of probabilistic climate outlooks is low and that comprehension is directly related to user satisfaction i.e. those that answered comprehension questions correctly were four more times likely to be satisfied with the Bureau's service than those that answered one or more of these questions incorrectly.

Economic analysis indicates that the potential value of improved climate prediction services for Australian agriculture is of the order of AUD 958 million to AUD 1,930 million per year (Centre of International Economics, 2014). Significant value is also estimated for other climate sensitive industries including construction, energy, mining, retail, water, emergency services, tourism, finance, and insurance. Determining user needs and tailoring services to sectors, increasing uptake of services and improving comprehension of probabilistic outlooks are key steps in unlocking the potential value of climate services.

The results from the comprehensive engagement with industry undertaken in both 2010-11 and 2015-16 were presented. This included the method of engagement, recommendations from consultation and the service improvements that resulted. Improvements made to the service as a result of the 2010-11 consultation are shown in Fig.1. The 2015-16 consultation was undertaken to inform significant improvements that will be implemented in the coming years (Fig 2). It is unlikely the Bureau would have secured funding for recent and planned service improvements without the formal quantitative and qualitative feedback collected through these

Fig 1. A comprehensive review of the Bureau's climate outlook service in 2011 showed that about a quarter of users were potentially misinterpreting Bureau climate outlooks, and that users wanted more tailored information for their location. In response, in 2014 the Bureau released a re-built climate outlook service web portal which made information more understandable and accessible. The new website has more functions, such as the ability to tailor outlooks to a specific location and is mobile friendly. Bureau climate outlooks information is now also provided through social media. To improve comprehension, educational videos and an online interactive training course (in partnership with UCAR COMET) are now provided.

Correspondence to: Robyn Duell, Australian Bureau of Meteorology, Melbourne, Australia;
E-mail: robyn.duell@bom.gov.au

consultations.

Links and references:

Visit the Bureau's climate outlook service on the web: www.bom.gov.au/climate/ahead

Read the 2014 Centre of International Economics reports, Analysis of the benefits of improved seasonal climate forecasting for agriculture and Analysis of the benefits of improved seasonal climate forecasting: For sectors outside agriculture, on the web:

http://managingclimate.gov.au/research/current-projects/climate-forecasting-research-2/improved-seasonal-climate-forecasts-the-benefits-for-agriculture/

Key findings from the 2010-11 stakeholder engagement were published in 2012. (Boulton, E., A. Watkins and D. Perry, 2012: A user-centred design approach to the seasonal climate outlook. *Climate Exchange*, World Meteorological Organization, F. Lúcio and T. Avellán, Eds., Tudor Rose, 232-235.)

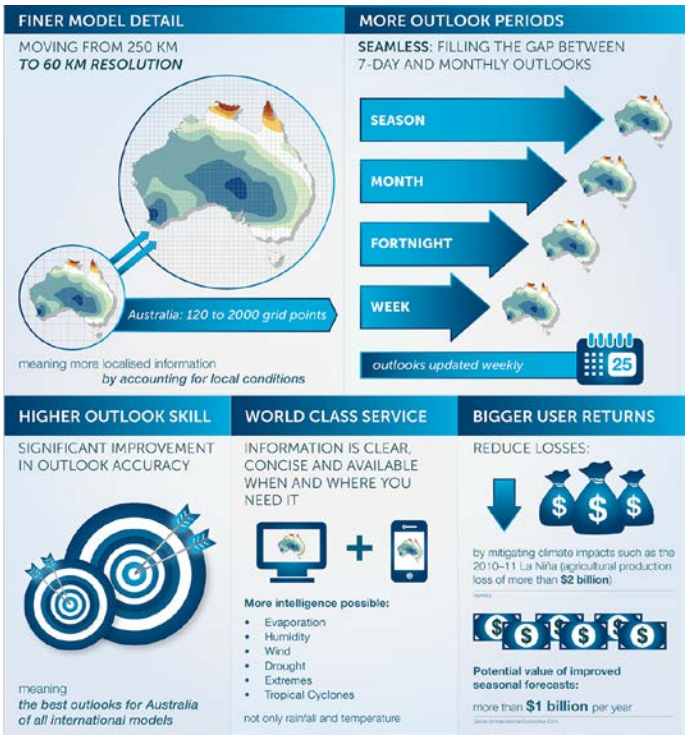

Fig. 2 Planned service improvements.

Science and Technology Infusion Climate Bulletin
NOAA's National Weather Service
41st NOAA Annual Climate Diagnostics and Prediction Workshop
Orono, ME, 3-6 October 2016

Application of Seasonal Rainfall Forecasts to Inform the Implementation of Drought Contingency Triggers in Selected Water Supply Reservoirs in Texas

John Zhu[1], Nelun Fernando[1], Yujuin Yang[1], Chris Higgins[2], and Aaron Abel[2]
[1]*Texas Water Development Board, Austin, Texas*
[2]*Brazos River Authority, Waco, Texas*

1. Introduction

In response to the exceptional drought of 2011, the Texas Water Development Board (TWDB) adopted new rules for its water planning process in 2012. The new rules require all regional water planning groups to include a chapter on drought management in their respective 5-year water plans with the aim of implementing short-term water demand reductions in the face of impending or existing drought conditions. Each water user group in a water planning region is required to develop drought contingency plans and drought action triggers for their respective water supply sources. Water user groups need to consult existing information on impending or current drought conditions before making a decision on whether to implement drought contingency triggers, which set in place voluntary or mandatory water use restrictions.

Reliable forecasts of summer (May, June and July; MJJ) reservoir storage issued at the end of April is vitally important for reservoir operators in Texas because such forecasts could help reservoir operators decide on whether the implementation of drought contingency triggers is warranted for the upcoming summer season.

In this study we report on how we applied improved forecasts of MJJ rainfall, issued at the end of April in a given year, for seasonal storage forecasts at three reservoirs managed by the Brazos River Authority (BRA) on the Brazos river basin in Texas. The objective of the study was to develop a framework by which the BRA could use seasonal rainfall forecasts to inform the implementation of drought contingency triggers on their reservoirs.

2. Improved May-July seasonal rainfall forecasts and the TWDB drought forecast tool

The MJJ season is the critical rainfall season over much of Texas. Failure of this rainfall season tends to result in intense summer drought over Texas (Fernando *et al.*, 2016). Seasonal rainfall forecasts from dynamic climate models are unable to provide more skill than that provided by the autocorrelation of rainfall anomalies, particularly during the summer over the U.S. Great Plains (Quan *et al.*, 2012).

We developed a process-based statistical forecast tool to generate improved forecasts of May-July (MJJ) rainfall over Texas and the South Central U.S. based on our understanding of key processes that drive the failure of late-spring/early-summer rainfall over the region (Fernando *et al.*, 2015). The key processes active in the spring (April) that drive summer rainfall deficits over the South Central U.S. are: mid-tropospheric high pressure, enhanced convective inhibition energy, and low soil moisture. We used geopotential height at 500 hPa, the difference in temperature between 700 hPa and surface dewpoint (as a proxy for convective inhibition), and soil moisture in April as the predictor variables and MJJ rainfall as the predictand in the empirical forecast tool. We find that the skill of rainfall forecasts from the statistical forecast tool exceeds skill due to persistence (*i.e.* autocorrelation) over most of Texas and Oklahoma (Fernando *et al.*, 2015). Given that the failure of the MJJ rainfall season tends to result in intense summer drought over Texas, seasonal forecasts of MJJ rainfall are, in effect, early warnings of impending summer drought.

The TWDB launched a 'Drought Forecast Tool' in May 2016 at http://waterdatafortexas.org/drought/drought-forecast to provide automated probabilistic forecasts of MJJ rainfall for each county in Texas. These forecasts provide information on the likelihood that rainfall in the MJJ season will be above-, near-, or below-normal in a given county.

Correspondence to: John Zhu, Texas Water Development Board, Austin, Texas; E-mail: john.zhu@twdb.texas.gov

3. Water availability modeling in Texas

The Water Right Analysis Package (WRAP) from Texas A&M University is the official water availability modeling (WAM) tool adopted within Texas for the simulation of water use in Texas, where water rights are governed by the Prior Appropriations Doctrine. A conventional WRAP simulation run extends over the entire hydrological record in a single (aka, long-term) simulation. Conditional Reliability Modeling (CRM) is another feature (or mode) that was implemented in the WRAP modeling system to support drought management and operation planning activities. CRM provides the capability to truncate long-term simulations into many short periods by specifying starting month, length of simulation and initial reservoir storage. The CRM output can be used in conjunction with seasonal rainfall forecasts to derive climate-informed reservoir forecasts. In this study we adopt the CRM feature to generate experimental reservoir forecasts for three reservoirs on the Brazos river basin.

3.1 Brazos River Basin and Brazos Water Availability Model

The Brazos River Basin, located in the middle of Texas and runs southeasterly, has a total area of 44,620 square miles. The climate, hydrology, and geography of the basin vary greatly as it extends across Texas from New Mexico to the Gulf of Mexico. Mean annual precipitation varies from 19 inches in the upper basin that lies in the High Plains to 45 inches in the lower basin in the Gulf Coast region. The extreme upper end of the basin in and near New Mexico is an arid flat area that rarely contributes to stream flow.

The Texas Commission on Environmental Quality (TCEQ) maintains water availability models for every river basin in Texas. The TCEQ Brazos WAM Run 8 (current use scenario at monthly time step) is updated and employed in this study. The Brazos WAM model is one of the largest models maintained by the TCEQ. The Brazos WAM RUN 8 has 3,834 control points (77 primary control points with naturalized flow and 66 control points with reservoir net evaporation), 711 reservoirs, 1,725 water rights, and 144 instream flow water rights. The current use scenario consists of diversions being made based on maximum annual amount used in a ten year period (approximately 1991–2000), return flow coefficients and reservoir storage capacities reflecting sedimentation conditions for the year 2000.

The official Brazos WAM model covers a hydrologic period of analysis from January 1940 to December 1997. The extended hydrologic (naturalized flow and reservoir net evaporation) input (1900-1939 and 1998-2014) for the Brazos WAM, produced by Prof. Ralph Wurbs (Texas A&M), is combined with the existing hydrologic input (1940-1997, Wurbs and Kim, 2008; Wurbs, 2015) for the CRM simulation used in this study. We used the full hydrology, extending from 1900–2014, because frequency (or percentile) estimates are improved as sample size increases.

3.2 Reservoirs selected for this study

The United State Army Corps of Engineers, BRA or local municipalities, operate most large reservoirs in the Brazos River Basin. As stated in previous section, reservoir storage is mainly related to inflow and diversion. If diversion varies greatly from year to year, it is difficult to predict reservoir storage even though the inflow is predicted with a higher degree of accuracy. Water usage information from BRA indicates that some large reservoirs have irregular industrial usage that is less predictive. Therefore, this study focuses on three small reservoirs — *i.e.* Lake Limestone, Aquilla Lake, and Proctor Lake (Figure 1).

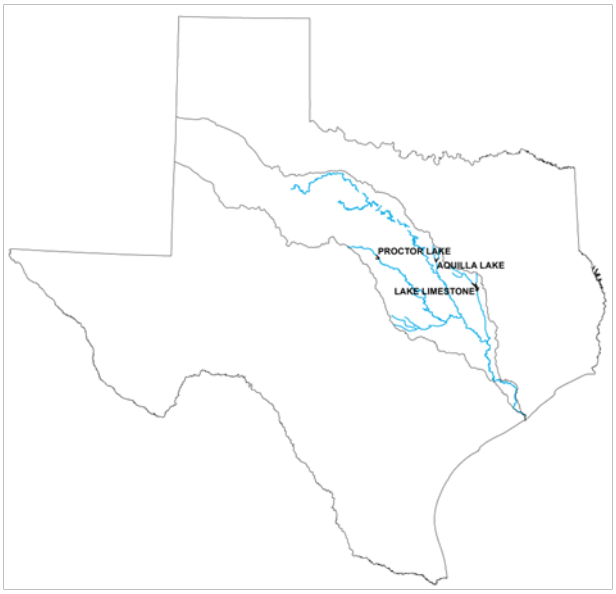

Fig. 1 Brazos River Basin and selected reservoirs in this study.

In this study, CRM simulation starts from May 1 and last for 3 months for 115 (1900-2014) years. Initial reservoir storage for monitored major reservoirs is set

to the actual storage condition on April 30, 2016. For unmonitored reservoirs, they are divided into upper and lower sub-basin and are assigned the percent full to be equal to the overall percent full of all monitored reservoirs in the sub-basin on the same date. Reservoir capacity and area-volume rating curves are updated using the latest available hydrographic surveys. The diversion from reservoirs is updated to reflect 2016 projected conditions.

4. Methodology for applying rainfall forecasts for reservoir storage forecasts

Many factors affect reservoir storage. Among these factors, inflow and diversion generally play important roles in reservoir storage. If diversion can be projected with some degree of certainty, reservoir storage would largely depend on inflow. Inflow or natural river flow in turn is generated by precipitation. Thus, skillful rainfall forecasts could be useful for the generation of skillful reservoir storage forecasts.

We employ two methods to derive reservoir storage forecasts based on information from the seasonal rainfall forecast.

a) Conceptual method

The sequential output from Conditional Reliability Modeling (CRM) reflects all possible situations for storage under assumed water use scenarios. With a sufficiently long period of analysis, simulated storages reflect all possible storage situations related to all historical rainfall situations. In other words, the maximum storage is a reflection of the highest rainfall, while the minimum storage is a reflection of the lowest rainfall. Therefore, the basis of this method is to forecast summer reservoir storage by ranking (percentile) the sequential storage output from the CRM simulation, and by selecting storage at a certain percentile to match the summer rainfall forecast. Given that the probabilistic forecasts of MJJ rainfall cannot directly be applied in the selection of a storage percentile, we use the exceedance probability curve for the rainfall forecast to guide the selection of the storage percentile. We obtain the exceedance probability curve for the grid point in which each reservoir falls. If the probabilistic forecast shows higher probabilities of below normal rainfall, for example as in the hindcast for 2011, we would consult the exceedance probability curve for the selected grid point to obtain the probability for rainfall being less than 50% of normal (Figure 2). The correlation between historical rainfall and simulated storage over the summer demonstrates this relationship and concept (Figure 3).

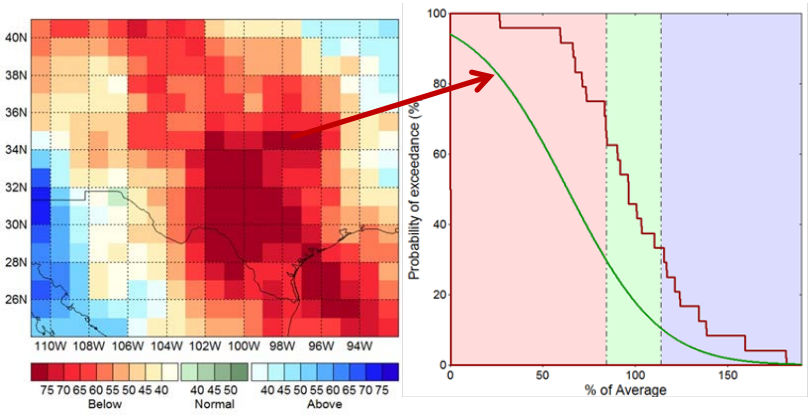

Fig. 2 Probabilistic forecast of 2011 MJJ rainfall (left) and the forecast exceedance probability curve (green) versus the climatological exceedance probability (red) for the grid point over Lake Limestone.

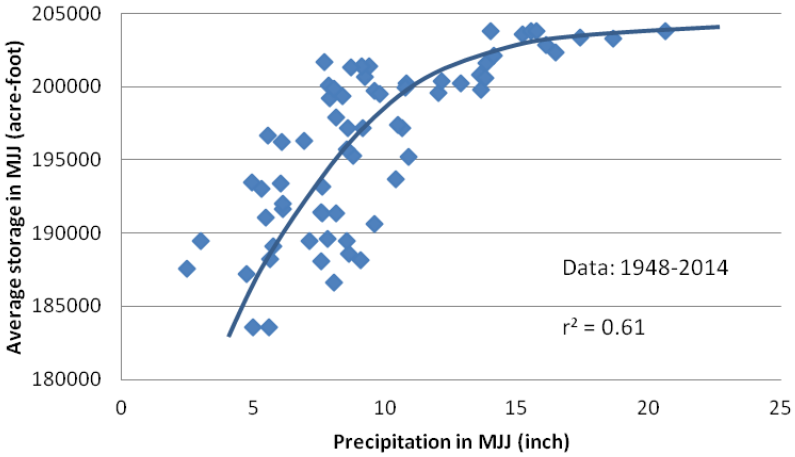

Fig. 3 Correlation between average simulated storage in Lake Limestone and precipitation in its watershed during summer period (assuming full storage in the end of April).

b) Selective method

The Selective method for forecasting reservoir storage requires the identification and use of years in which rainfall is similar to that predicted using the Texas Water Development Board's May–July rainfall forecast tool. By word "similar" we actually mean that the rainfall amount for a given month is within a certain predetermined range (such as from 85% to 115% of forecasted rainfall). The philosophy of this method is based on the assumption that the reservoir storage in a particular month (such as May) should be similar if rainfall in that month is similar. Therefore, using storages of selected historical years should provide a reasonably good prediction of storage for a coming year if the rainfall is similar.

5. Forecast results for 2016

For the Conceptual Method, reservoir storages at typical (1, 10, 20… 100) percentiles are computed for each simulation sequence. The reservoir storage for the summer months (end of MJJ) at the 90th percentile is selected as the forecast storage for each reservoir. The selection of the 90th percentile was informed based on the exceedance probability for 2016 MJJ rainfall being above 100% of normal and the categorical forecast indicating high probabilities (above 95%) for above normal rainfall (Figure 4). Forecast reservoir storage curves for end of May, June and July show no change from May to June and decrease slightly in July for Lakes Limestone (Figure 5) and Proctor (not shown). Forecast reservoir storage at Lake Aquilla was at full capacity for May, June and July (not shown). Observed storage in all three reservoirs were way above any of the drought contingency trigger levels, indicating that there was no necessity to adopt drought management strategies in the summer of 2016.

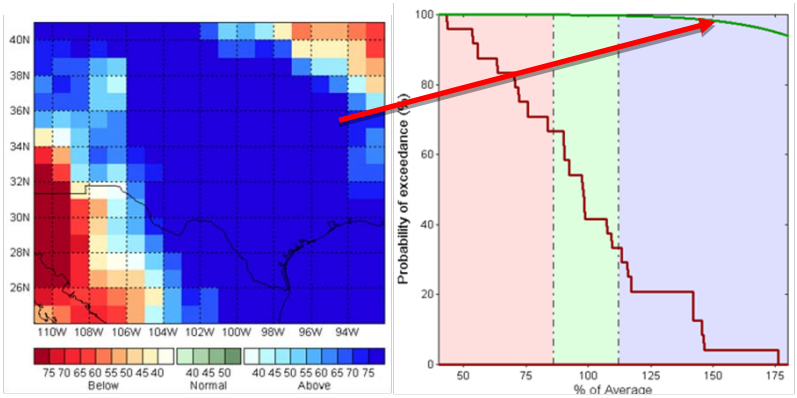

Fig. 4 Probabilistic forecast of 2016 MJJ rainfall (left) and exceedance probability curve for grid point over Lake Limestone.

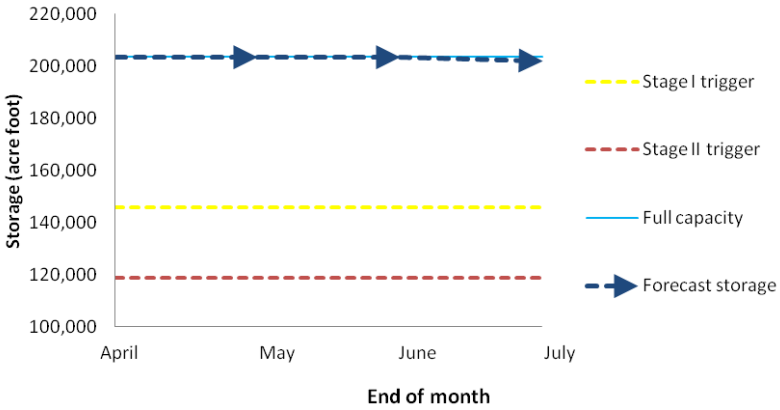

Fig. 5 2016 Storage forecast for Lake Limestone by Conceptual method.

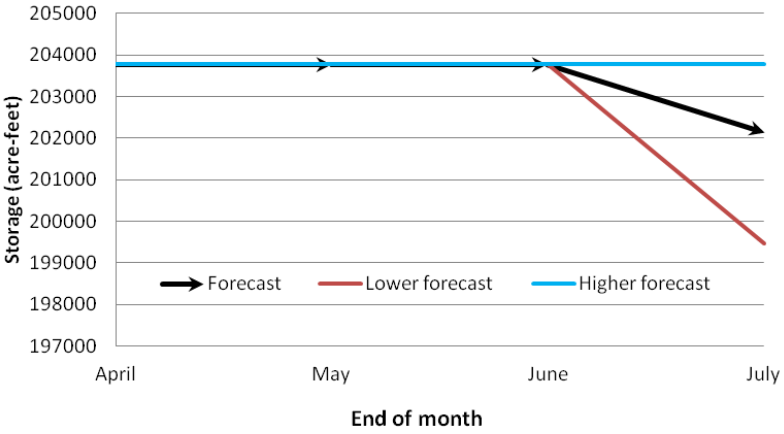

Fig. 6 2016 Storage forecast for Lake Limestone by Selective method.

For the Selective method, several years are selected for each month of May, June and July for each reservoir based on similarity of historical rainfall to the forecast rainfall. The criterion for selection of years is that rainfall of selected years must fall within the range of 0.85 to 1.15 times of forecast rainfall. Simulated

storages of those selected years are picked from the CRM sequential output and their average is denoted as the "storage forecast". The minimum and maximum historical storage values selected by this method indicate the uncertainty range of this forecast (see Figure 6 for results for Lake Limestone; results for Lakes Aquilla and Proctor are not shown).

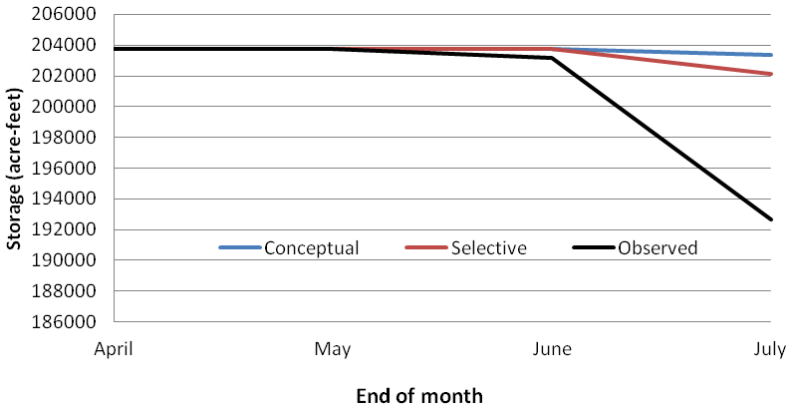

Fig. 7 Comparison of forecasted and observed storages for Lake Limestone.

For Lake Limestone, both Conceptual and Selective methods forecast no change or little change to full storage in the end of June and July, while observed storage was slightly lower than the forecast in June and July. The maximum error of this forecast for July was 5.6% higher than observed (Figure 7). For Lake Aquilla, the Conceptual method forecasts full storage for May, June, and July, which happens to be the same as was observed in those three months (not shown). The forecast from the Selective method for Aquilla is very close to observed values and is only one percent less than observed storage for July (not shown). For Proctor Lake, both the Conceptual and Selective methods forecast no change or little change to full storage at the end of June and July, while actual observed storage went down slightly in July. The maximum error in July was only 1% higher than observed (not shown). Overall, both methods give a good accuracy of forecast.

6. Conclusion and discussion

We operated Conditional Reliability Modeling (CRM) capabilities of the Water Rights Analysis Package (WRAP) and applied 2016 May–July rainfall forecasts to derive storage forecast using the Conceptual method and the Selective method. The storage forecasts for Lake Limestone, Aquilla Lake, and Proctor Lake in the Brazos river basin for the 2016 summer (MJJ) were derived using the 90th percentile curves for these three reservoirs. The wet conditions forecast for MJJ 2016 from the Texas Water Development Board's (TWDB's) rainfall forecasting tool (http://waterdatafortexas.org/drought/drought-forecast) provided input to the selection of the percentile curves. Forecasted reservoir storage curves for end of May, June, and July exhibit no change from May to June and slight decreases in July, indicating low drought management trigger probability. The comparison of the forecast storage with observed storage at the end of July indicates our forecast has good accuracy.

The Selective method may not provide adequate room for risk management given that the uncertainty in the forecast is limited by the number of "similar" cases available for selection from the historical record. More work is needed on the Conceptual method to ascertain the exact relationship between rainfall and reservoir storage. Furthermore, the current model only simulates storage up to the conservation pool and does not account for water stored in the flood pool. Therefore, extending our simulation into the flood pool in a wet year (such as in 2016) is needed for improved reservoir forecasts. Further investigation is also needed to assess the impact of antecedent rainfall in April on storage in May to better understand the role of hydrological persistence in reservoir storage.

Acknowledgements. This study is a component of the TWDB's Drought Early Warning Tool Project funded by the U.S. Bureau of Reclamation WaterSMART Drought Resiliency funding to the TWDB (Grant: R15AP00184; Financial Year: 2015). The Brazos River Authority provided assistance with historical water use data and valuable suggestion for the simulation. Prof. Ralph Wurbs (Texas A&M University) provided extended hydrologic input datasets and guidance in this research.

References

Fernando, D.N., K.C. Mo, R. Fu, B. Pu, A. Bowerman, B.R. Scanlon, R.S. Solis, L. Yin, R.E. Mace, J.R. Mioduszewski, and T. Ren, 2016: What caused the spring intensification and winter demise of the 2011 drought over Texas? *Clim. Dyn.*, **47**, 3077-3090. doi:10.1007/s00382-016-3014-x.

Fernando, D.N., R. Fu, R.S. Solis, R.E. Mace, Y. Sun, B. Yang, and B. Pu, 2015: Early warning of summer drought over Texas and the south central United States: spring conditions as a harbinger of summer drought. Texas Water Development Board. 41 pp, (http://www.twdb.texas.gov/publications/reports/technical_notes/doc/TechnicalNote15-02.pdf).

Quan, X.-W., M. P. Hoerling, B. Lyon, A. Kumar, M. A. Bell, M. K. Tippett and H. Wang, 2012: Prospects for dynamical prediction of meteorological drought, *J. Appl. Meteor. Climatol.*, **51**, 1238-1252.

Wurbs, R. A. and T.J. Kim, 2008: Extending and condensing the Brazos River Basin Water Availability Model, Technical Report 340, Texas Water Resources Institute, December 2008.

Wurbs, R. A., 2015, Water Rights Analysis Package (WRAP) Modeling System reference manual, Technical Report 255, Texas Water Resources Institute, 11th Edition, August 2015.

6. ARCTIC CLIMATE & LINKAGES TO LOWER LATITUDES

41th NOAA Annual Climate Diagnostics and Prediction Workshop

3-6 October 2016, Orono, Maine

Science and Technology Infusion Climate Bulletin
NOAA's National Weather Service
41st NOAA Annual Climate Diagnostics and Prediction Workshop
Orono, ME, 3-6 October 2016

Verification of Experimental Sea Ice Forecasts at the NCEP Climate Prediction Center

Thomas W. Collow[1,2], Wanqiu Wang[2], and Arun Kumar[2]
[1]*Innovim LLC., Greenbelt, Maryland*
[2]*Climate Prediction Center, NOAA/NWS/NCEP, College Park, Maryland*

1. Background

In March 2015 the National Centers for Environmental Prediction (NCEP) Climate Prediction Center began issuing experimental sea ice outlooks to the National Weather Service (NWS) Alaska Region. These outlooks have been received favorably and continued through 2016. The motivation behind these outlooks was to improve the sea ice prediction in the Climate Forecast System Model Version 2 (CFSv2) (Saha *et al.*, 2014), which has too high of a predicted sea ice extent. By using a more observationally consistent dataset of initial sea ice thickness, namely from the Pan-Arctic Ice Ocean Modeling and Assimilation System (PIOMAS) (Zhang *et al.*, 2003) produced by the University of Washington, a more accurate sea ice prediction compared to the operational model output was achieved.

2. Work flow

For each month, March through October, a 10 year hindcast was generated using 5 ensemble integrations for the 2005-2014 period. Each model simulation was initialized from the 8th through the 12th of the month at 00 UTC and integrated through 9 target months. This yielded a total of 50 model integrations per initial hindcast month. Next, model simulated means were taken for each target month and compared to observations from the National Aeronautics and Space Administration (NASA) Team dataset (Cavalieri *et al.* 1996; available at ftp://sidads.colorado.edu/DATASETS) to determine model biases. These biases were then removed from the real time forecasts, which were also initialized from the 8th through 12th of each initial month March through October, with four ensembles per day for a total of 20 realizations for each initial forecast month. The biases are calculated and removed for each individual variable discussed in the next section and the final bias corrected forecast is sent to the NWS Alaska Region.

3. Forecast parameters

3.1 Sea ice concentration

Sea ice concentration is directly output from CFSv2 and represents the percentage of a grid cell covered by sea ice. 100% represents full ice coverage and 0% denotes open ocean. Sea ice concentration yields information on a local scale and is important for planning shipping routes in addition to other operations of Arctic interest.

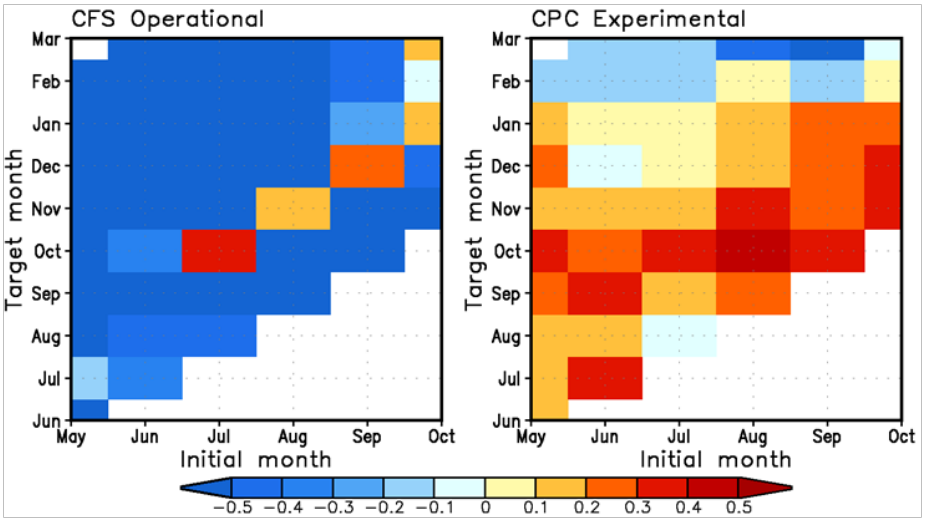

Fig. 1 Sea ice concentration Heidke skill scores for the 2015 forecasts. The x-axis denotes the initial month or the month that the model integration is started, and the y-axis denotes the target month or the month that is being forecasted.

Correspondence to: Li Xu, Climate Prediction Center, NOAA/NWS/NCEP, 5830 University Research Court, College Park, MD; E-mail: Li.Xu@noaa.gov

3.2 Sea ice extent

Sea ice extent is the areal coverage of sea ice across the Arctic. It is a cumulative value and does not yield information on a local scale. Sea ice extent is calculated by taking the sum of grid cells which have a sea ice concentration of 15% or greater in accordance with the definition published in the last IPCC assessment report (Vaughn *et al.*, 2013). Sea ice extent reaches its minimum in September before increasing during Arctic winter. The September sea ice extent value is of particular interest to many given its large downward trend since the 1980s, reaching a record low in 2012.

3.3 Sea ice probability

Sea ice probability is the percentage of ensemble members that have a sea ice concentration value greater than 15% in a particular grid cell, thus making it part of the calculated sea ice extent. Therefore if 10 out of 20 ensemble members have a sea ice concentration greater than 15%, then the sea ice probability value would be 50%.

3.4 First ice melt and ice freeze day

The final parameter in our experimental forecast package is the first calendar day of sea ice melt (IMD) and freeze (IFD), also termed retreat and advance. A summary of these variables and their importance can be found in Collow *et al.* (2016). IMD is defined as the first day in which a grid cell's sea ice concentration drops below 15% and IFD is defined as the first calendar day in which a grid cell's sea ice concentration increases above 15% during the following freeze season. Questions remain in terms of the method to define IMD and IFD, such as the proper melt/freeze threshold (15% is used here) or how long the state change should remain and how to accommodate marginal ice zones. IMD and IFD take sea ice concentration data a step further and can yield information locally on when a particular location will become free of ice (IMD) or become ice covered (IFD). While studying daily maps of sea ice concentration can deliver this information, it is much less time consuming to analyze a single map. Arctic stakeholders benefit greatly from knowing how long a particular location will remain ice free.

4. Verification

Experimental forecasts were verified for 2015 and 2016 using data from NSIDC. The NSIDC sea ice index is used to verify sea ice extent while the NASA Team real time sea ice concentration is used to verify sea ice concentration and sea ice retreat/advance days. For sea ice concentration, the experimental forecasts have skill much higher than the operational product, as shown by the Heidke skill scores in Figure 1. The experimental CFSv2 shows generally positive skill scores versus negative scores for the operational model.

Sea ice extent is also shown to have greater skill in the experimental model versus the operational model (see Collow *et al.*, 2015 for an extensive analysis of hindcasts). For the 2015 forecasts, the root mean square error was about 0.3 * 10^6 km^2 for all target months in the experimental forecasts but varied greatly for the

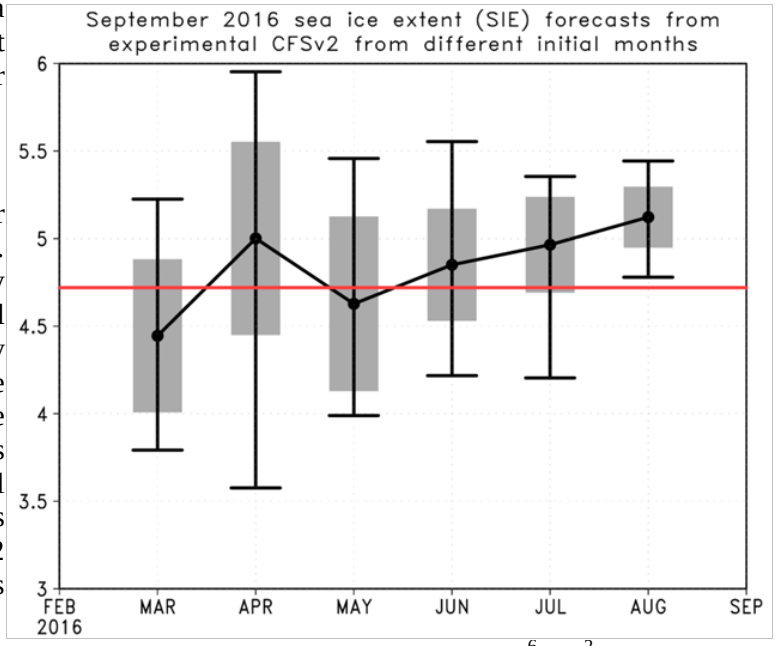

Fig. 2 September 2016 sea ice extent (10^6 km^2) forecast and verification for initial months beginning in March 2016. The x-axis denotes the initial month and the y-axis the sea ice extent. The black dot for each initial month represents the 20 member ensemble mean, the gray shading shows +/- 1 standard deviation from the mean, and the black error bars show the max and min out of all ensemble members. The horizontal red line denotes the observed September sea ice extent from NSIDC (4.72 * 10^6 km^2).

operational model with values as high as 1.2 *10^6 km^2. Figure 2 shows the prediction of September 2016 sea ice extent for initial months starting in March. Although ensemble uncertainty is much higher in March-May, less uncertainty exists starting in June that the 2016 sea ice extent would not be a record low. Sea ice extent achieved record low values in early 2016 which led many research groups to predict that the September minimum would set a new record (https://www.arcus.org/sipn). However, a reversal of atmospheric conditions to cool and stormy during the summer slowed the rate of sea ice melt and as a result the September minimum was much higher than the 2012 record low and closer to our experimental forecasts. This illustrates an important point regarding atmospheric variability, which is impossible to predict several months ahead of time and that enough ensemble members are necessary to provide a range of all possible outcomes, especially for longer time spans.

Finally, first IMD verification for March 2016 initialized forecasts for the 2016 melt season is shown in Figure 3. Generally the experimental forecast provided a good prediction of IMD over most regions, although there is some noise due to atmospheric uncertainty as previously discussed. For example, the Beaufort Sea had exceptionally early melt in 2016, which was not predicted by the model. However, standard deviation values were higher in this region than in the Bering Strait indicating there was more predicted uncertainty in the Beaufort Sea. The mean absolute error over the plotted domain in the bottom right panel (145° -185°W, 50° -75°N) is 15 days, with a large number of points with an absolute error of less than 10 days in the Bering Strait. Not shown here, IFD prediction for the 2015-2016 freeze season based on September 2015 initialized forecasts had a mean absolute difference of 18 days over the same region. Most of the errors were in the southern part of the Bering Strait. Most regions in the Bering Strait and northward had generally lower biases and better prediction (using a region from 65° -75°N, yielded a mean absolute error of only 10 days).

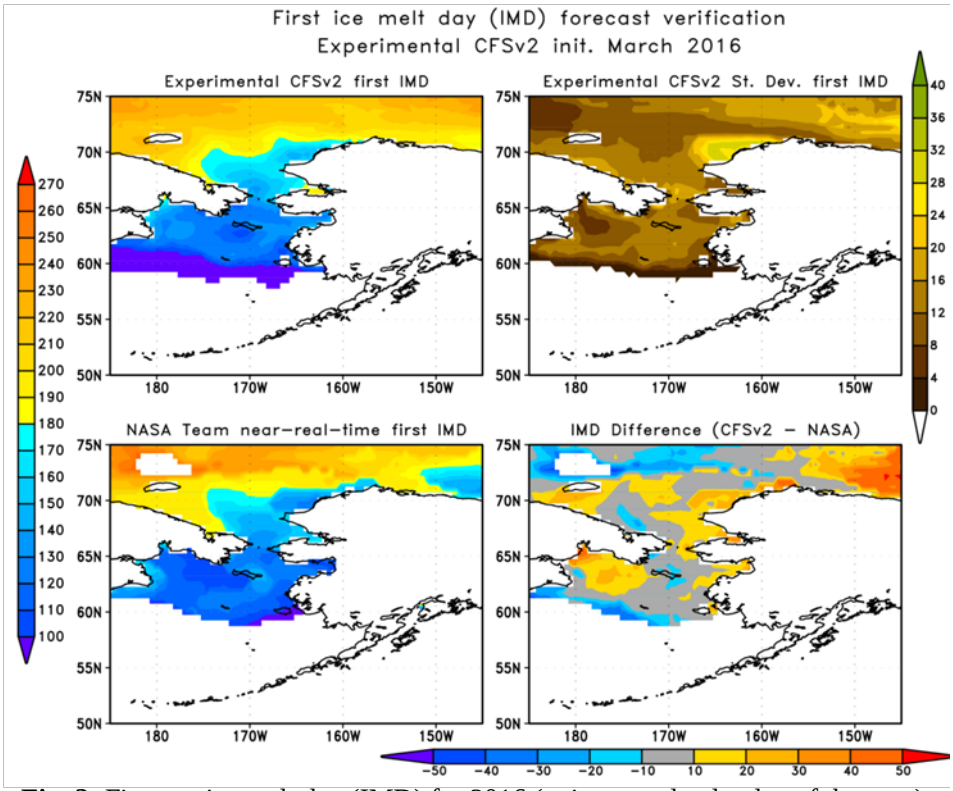

Fig. 3 First sea ice melt day (IMD) for 2016 (units are calendar day of the year), top left: experimental CFSv2 ensemble mean first IMD, top right: experimental CFSv2 first IMD standard deviation of all ensemble members, bottom left: observed first IMD from NASA Team, bottom right: difference between the experimental CFSv2 prediction and NASA Team.

5. Conclusion

As demonstrated experimental sea ice forecasts issued at the Climate Prediction Center are providing beneficial data to stakeholders in the Arctic and have verified better than the operational counterpart. The plan is to continue with experimental products in 2017, while also preparing to provide forecasts of week 3-4 sea ice. Also ongoing is the testing of new oceanic vertical resolutions and the development of a new in-house sea ice thickness dataset which will be used to initialize the CFSv2 model at a later time.

References

Cavalieri, D.J., C.L. Parkinson, P. Gloersen, and H. J. Zwally, 1996, updated yearly: Sea ice concentrations from Nimbus-7 SMMR and DMSP SSM/I-SSMIS passive microwave data [2005-2016]. Boulder, Colorado USA: NASA DAAC at the National Snow and Ice Data Center.

Collow, T. W., W. Wang, A. Kumar, and J. Zhang, 2015: Improving Arctic sea ice prediction using PIOMAS initial sea ice thickness in a coupled ocean-atmosphere model, *Mon. Wea. Rev.*, **143**, 4618-4630, doi:10.1175/MWR-D-15-0097.1.

Collow, T. W., W. Wang, A. Kumar, and J. Zhang, 2016: How well can the observed Arctic sea ice summer retreat and winter advance be represented in the NCEP Climate Forecast System version 2?, *Clim. Dyn.*, in press, doi:10.1175/MWR-D-15-0097.1.

Saha, S., and Coauthors, 2014: The NCEP Climate Forecast System Version 2, *J. Climate*, **27**, 2185-2208, doi: 10.1175/JCLI-D-12-00823.1.

Vaughan, D. G., and Co-authors, 2013: Observations: Cryosphere. In *Climate Change 2013*: *The Physical Science Basis. Contribution of Working Group I to the Fifth Assessment Report of the Intergovernmental Panel on Climate Change*, Cambridge University Press, Cambridge, United Kingdom and New York, NY, USA, 317-382, doi:10.1017/CBO9781107415324.012.

Zhang, J.L. and D. A. Rothrock, 2003: Modeling global sea ice with a thickness and enthalpy distribution model in generalized curvilinear coordinates. *Mon. Wea. Rev.*, **131**, 845-861.

Science and Technology Infusion Climate Bulletin
NOAA's National Weather Service
41st NOAA Annual Climate Diagnostics and Prediction Workshop
Orono, ME, 3-6 October 2016

Recommendations on Categorizing Arctic Air Mass Intensity/Coverage and Improving the Monitoring of Arctic Source Regions Across the Northern Hemisphere

Victor J. Nouhan
NOAA's National Weather Service, Caribou Caribou Maine

1. Introduction

During the last few decades, the science of meteorology/climatology regarding the discovery, categorizing, monitoring, and prediction of teleconnection patterns influencing atmospheric circulation across the northern hemisphere, originating from both the mid-latitudes and tropics, has been established (Wallace and Gutzler 1981, Barnston and Livezey 1987). The science of categorizing, monitoring, and predicting of cold season arctic air masses over the continental source regions of the northern hemisphere and their advection into lower latitudes, unfortunately, has lagged behind knowledge gained by exploring teleconnections during the corresponding period (Namias 1978, Yarnal 1987).

In an effort to activate research in this mostly unexplored topic, this presentation provided recommendations/proposals regarding: 1) defining arctic air masses by intensity and geographic coverage across northern hemispheric continents, 2) better utilizing the few existing established teleconnections that better correlate to arctic air mass formation and advection, especially over North America, and 3) new arctic (non-teleconnection) indices to better help forecast/monitor the development of arctic air masses over all known northern hemispheric source regions and the potential for advection of these air masses into adjacent lower latitudes. The ultimate future goal is monthly monitoring of arctic air mass frequency, coverage, and intensity similar to what the Climate Prediction Center (CPC) has for ENSO and mid/high latitude teleconnections (Climate Diagnostics Bulletin 2016). Please refer to the power point presentation for details on each of the following recommendations.

2. Recommendations on defining arctic air masses and Northern Hemispheric source regions

Air masses become arctic in character once temperatures at the top of the surface inversion reach -10 degree C or less, since colder surface dew points (or frost points) no longer represent a barrier (via latent heat release) to limit falling surface temps during long clear, cold season arctic/sub-arctic nights under positive (dry) hydro-lapse rate environments and light/calm winds.

Recommendation 1): Standardize monitoring arctic air (-10 degree C and colder) using a standard height of 1 KM above ground level (AGL). One KM AGL temperatures would better depict arctic air masses infiltrating complex high terrain especially where average station pressures are less than 900 hPa. The height of 1 KM AGL surface also corresponds to about halfway between 925 hPa and 850 hPa pressure surfaces meteorologists/ climatologists most frequently use temperature to assess the presence of arctic air over near sea level locations.

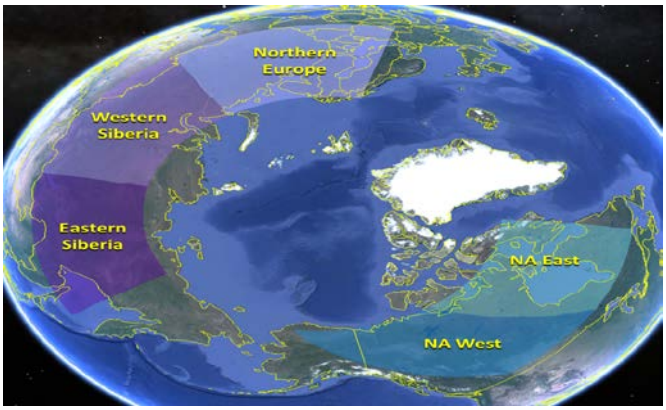

Fig. 1 Recommended Northern Hemispheric Arctic source regions.

Recommendation 2): Define seasonal continental arctic source regions. For the purpose of this

Correspondence to: Victor J. Nouhan, NOAA's National Weather Service, Caribou Caribou Maine;
E-mail: Li.Xu@noaa.gov

presentation, we identify five potential source regions: two across North America (NA) and three across Eurasia (EA) based on frequency differences of loading, residence of arctic air masses, and topography - limited to no greater than 45 degrees longitude wide generally from 50 to 70 degrees N latitude (see Fig. 1).

3. Recommendations regarding rating arctic air mass intensity/coverage

The following recommendations are for rating arctic air mass intensity and coverage.

Recommendation 3): Have descriptive arctic air mass intensities based on NA source region return frequencies per winter(s).

Recommendation 4): Define a numerical arctic air mass intensity index for public awareness and historical ranking purposes.

Recommendation 5): Have arctic area indices that measure the area coverage of arctic and deep arctic air across North America.

Recommendation 6): Define a total arctic index combining recommendations 4 and 5 to provide historical comparison of arctic air masses encompassing large continental areas.

Recommendation 7): Measure arctic air mass transport efficiency by comparing the maximum intensity achieved by an air mass in the source region to the later intensity of the air mass reaching the 50, 45, and 40 degree N latitude bands.

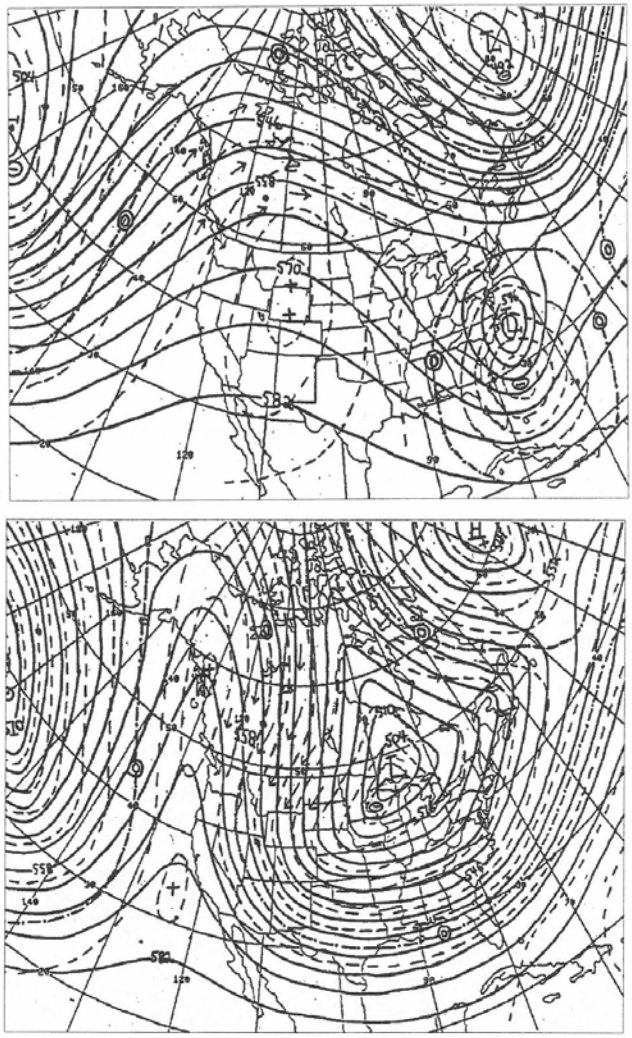

Fig. 2 Examples of 500 hPa North American Pattern with (**a**) positive PNA value and low arctic air mass potential (PNA ++, EP-NP -, TNH-- : NAT--), and (b) positive PNA value and high arctic air mass potential (PNA ++, EP-NP++, TNH++ : NAT++).

4. Northern Hemisphere teleconnection patterns that most reliably correlate to arctic air mass production over northern North America

The following recommendation highlights the use of a new non-teleconnection mid tropospheric pattern by utilizing existing teleconnection patterns that better anticipate the formation and trends of arctic air masses over North America.

Recommendation 8): Combine the EP-NP and TNH teleconnection patterns to produce a single North American Arctic Transition (NAT) Index:

$$NAT = \frac{x(EP\text{-}NP) + y(TNH)}{x + y}$$

where x and y are constants that may differ from 1. The reason for the selection of these two patterns for this proposed index is that both are associated with the greatest strength and fetch length of anomalous North to Northeast component mid-tropospheric flow over the NA arctic source region pointing toward the Canadian Rockies Divide. This resultant confluent flow and deep layer cold advection aloft results in rapid formation of deep arctic air masses with strong surface base inversions, since strong and rapid surface anti-cyclogenesis is favored in the lee of the Canadian Rockies when combined with low level barrier blocking (Nouhan 1999). PNA, NAO, and AO are not as consistently reliable indices for arctic air mass formation for various reasons

(see Fig. 2, also refer to example winter months in the power point presentation). Lastly, it should be noted that the proposed NAT index and the indices mentioned in the following section do not constitute new teleconnection indices, but rather, indices specific to the potential of loading and advection of arctic air across North America and other Northern Hemispheric source regions.

5. Other proposed mid tropospheric circulation indices to monitor potential of Arctic air masses across all Northern Hemisphere source regions

The following recommendations are for other new circulation indices to better anticipate the formation and trends of arctic air masses over all of the Northern Hemisphere.

Recommendation 9): Sectorize Arctic Oscillation (AO) so that the effects of the ocean domain portions of AO can be minimized by applying the following equation to each corresponding source region from figure 1:

$$\text{AOm} = \frac{\text{500 hPa(40°-65°N)S} - \text{500 hPa(65°-90°N)S}}{2}$$

where within the modified Arctic Oscillation (AOm), 500 hPa latitudinal band standardized height anomaly (S) comparisons are reduced to 65°-90°N and 40°-65°N rather than poleward from 20 degrees N (CPC Website) latitude. This contraction of the latitude band comparisons in addition to mostly eliminating ocean domain allows for better correlation to the production of arctic air for each source region. Similar to what is implied by AO, increasing arctic potential is indicated by negative values. In addition to correlating each index to surface temperature anomalies for each source region, indices from neighboring source regions across Eurasia and North America can then be combined or contrasted. Lastly, secular pattern trends can potentially be determined for each source region using re-analysis data.

Recommendation 10): Using the modified sectorized arctic oscillation indices produced from the prior recommendation for the two North America arctic source regions, one can combine centers of action from nearby teleconnection patterns that play a major role in arctic air formation due to topographical impacts on arctic air formation from the Rocky Mountains to improve the potential forecast performance of the indices. For example, one can produce an eastern U.S. version of the NAT index from combining anomalies corresponding to the northwest Canadian Coastline center of action from the EP-NP teleconnection and a western U.S. version of the NAT index by combining anomalies corresponding to the northeast Pacific center of action from the TNH teleconnection pattern. The resultant NATe and NATw indices, which can be used in conjunction with the NAT index would give a better idea of where arctic air is forming and advecting southward over North America without having to compare the corresponding phase of the PNA teleconnection index. Eurasian sectorized arctic oscillations may also benefit from additional modification with nearby teleconnection indices that highlight impacts on arctic air mass potential from adjacent geographical features.

6. Discussion and summary

The proposals/recommendations in the prior sections were given to: 1) provide a common basis as to what qualifies and quantifies as arctic air masses by meteorologists/climatologists, 2) define source regions, and 3) develop specific forecast indices to better anticipate formation and trends of arctic air over each source region. Prior work in this area is limited with a recent work related to monitoring trends of arctic air mass coverage and intensity across North America and Eurasia by Martin 2015 as part of a larger study of monitoring recent trends of both extreme cold and heat by using re-analysis data. Two defining characteristics overlapping with this proposal are: 1) the base definition of arctic air being defined at -10 degrees C, and 2) incorporating intensity by using trends of coverage of the -20 and -30 degree isotherms in addition to the -10 degree isotherm.

This presentation goes further by also proposing new mid tropospheric circulation indices dedicated to the forecasting and monitoring of arctic air masses over each of the Northern Hemispheric source regions. It's important to reiterate that although these new arctic indices were derived from prior existing teleconnection patterns, they no longer constitute what defines teleconnection indices since the arctic indices only gage arctic potential for corresponding limited domain source regions and do not measure explained variance of different

mid tropospheric circulation modes defined under Rotated Principle Component Analysis (Barnston and Livezey 1987). In order to maximize predictability, it is recommended that that pressure level that these new indices are calculated on remains close to the level of non-divergence in order to be not so far above from important topographical features that play a role over each source region, with vertical propagation of Rossby waves from the tropics not likely playing a significant factor as in traditional teleconnection patterns such as the PNA (Baxter 2016).

In summary, if these or similar proposals were instituted, seasonal arctic air mass formation and trends would be able to be monitored in a similar format to how CPC monitors tropical (ENSO) and extra-tropical trends in the Climate Diagnostics Bulletin.

References

Barnston and Livezey 1987: *Mon. Wea. Rev.*, **115**, 1083-1126.

Baxter S. 2016: Rediscovering the MJO Extratropical Response: Streamfunction as a Preferred Variable for Subseasonal Teleconnection Analysis. 2016 Climate Diagnosis and Prediction Workshop.

Martin 2015: An examination of trends in both cold and warm pools over the Northern Hemisphere and North America. [Available on line at: http://www.nwas.org/meetings/nwas16/abstracts_html/Other/abstract_2790.html]

NOAA/NWS/NCEP/CPC Climate Diagnostic Bulletin accessed October 2016. [Available on line at http://www.cpc.ncep.noaa.gov/products/CDB/]

Namias J. 1978: Multiple Causes of the North America Abnormal Winter of 1976/77. *Mon. Wea. Rev.*, **106**, 279-295.

Nouhan V. 1999: The Use of 500mb Non-Teleconnection Indices Over North America in Determining Arctic Air Mass Potential East of the Rockies. NWS Central Region Applied Research Papers, **20**, NOAA's National Weather Service, Kansas City, MO.

Wallace J. and Gutzler D. 1981: Teleconnections in the Geopotential Height Field during the Northern Hemispheric Winter. *Mon. Wea. Rev.*, **109**, 784-811.

Yarnal B. 1987: Teleconnections and Pennsylvania Winter Temperatures. *Earth and Mineral Sciences*, 56, 17-21.

Science and Technology Infusion Climate Bulletin
NOAA's National Weather Service
41st NOAA Annual Climate Diagnostics and Prediction Workshop
Orono, ME, 3-6 October 2016

Prediction of Seasonal Arctic Sea Ice Extent Using the NMME

Kirstin J. Harnos[1,2], Michelle L'Heureux[1], and Qin Zhang[1]
[1]*Climate Prediction Center, NOAA/NWS/NCEP, College Park, Maryland*
[2]*Innovim LLC., Greenbelt, Maryland*

1. Introduction

Arctic sea ice decline is a well-documented topic with many studies outlining the September minimum as decreasing by more than 10% per decade since satellite observations began in 1979. Within the past few decades, the rate of decline has been shown to be increasing significantly due to both thinning ice and longer melt seasons. When it comes to prediction of the Arctic sea ice extent (SIE), there is potential for skillful predictions mainly attributed to individual modeling system's ability to predict the long-term trend (Sigmond *et al.* 2013, Wang *et al.* 2013, Chevallier *et al.* 2013, Holland *et al.* 2011, *etc.*).

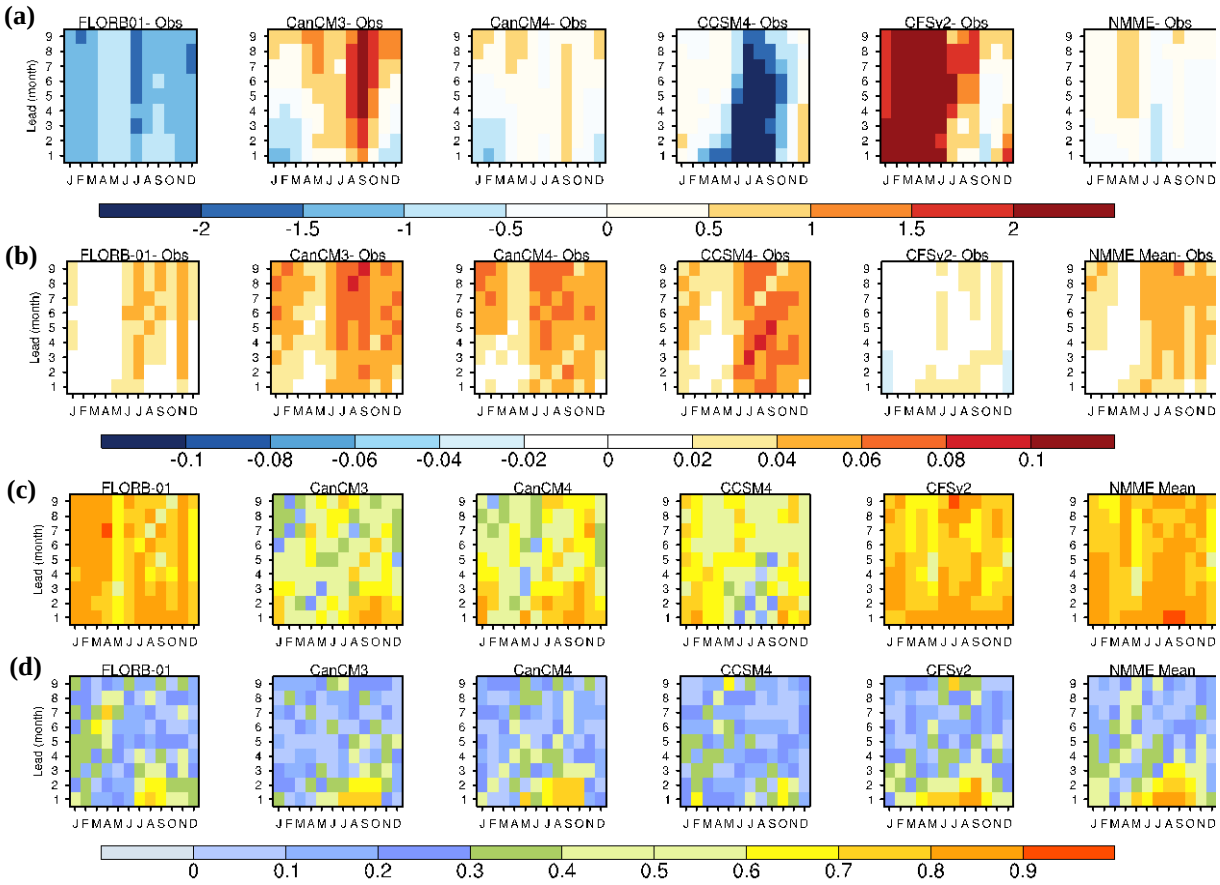

Fig. 1 Model bias (model minus observations) including the NMME for (a) Total SIE [10^6 km^2] and (b) the Y2Y SIE [10^6 km^2]. (c) and (d) are ACC for total SIE and Y2Y, respectively.

SIE prediction skill has been assessed by a variety of dynamical, statistical, and heuristic models. For other variables, it has been shown that predictions using the ensemble means from different models tend to outperform any individual system [Merryfield *et al.* 2013; Stroeve *et al.* 2014]. The North American Multi-Model Ensemble (NMME) takes advantage of the multi-model approach by utilizing a multi-agency team to

Correspondence to: Kirstin J. Harnos, Climate Prediction Center, NOAA/NWS/NCEP, 5830 University Research Court, College Park, MD and Innovim, LLC, Greenbelt, MD; E-mail: kirstin.harnos@noaa.gov

collect and organize global model data on a somewhat uniform spatial and temporal scale. This study seeks to expand on previous multi-platform studies by utilizing output from five NMME models to determine the skill in predicting Arctic SIE based on the long term trend and year-to-year (Y2Y) variability.

2. Data

There are 5 models that currently provide sea ice predictions to the NMME archive. Each hindcast simulation is initialized and allowed to run for either 12 months (CanCM3, CanCM4, FLORB-01, and CCSM4) or 9 months (CFSv2). To maintain consistency for all models and in creating an NMME average, all of the models are evaluated during the 1982-2011 time period, which represents the time when all 5 models have results and for a 9 month forecast extent. Observations derived from NASA Bootstrap version of the National Snow Ice Data Center NASA GSFC sea ice concentration are utilized in order to calculate the skill metrics.

3. Summary of results

Figure 1 shows the model bias for (a) total SIE and (b) Y2Y SIE. Overall, the NMME predictions of total SIE have less error than the individual predictions. In contrast, the Y2Y difference evaluates SIE prediction irrespective of the long-term trend. For all individual models and the NMME, the Y2Y differences show a generally positive bias, meaning that from one year to the next, the models tend to predict more SIE than observed. While the Y2Y values are not providing information on the long-term trend, this result implies the models are not capturing the magnitude of the loss of SIE from one year to the next. The NMME Y2Y bias shows improvement over CanCM3, CanCM4, and CCSM4, with CFSv2 and FLORB-01 having overall the best Y2Y prediction.

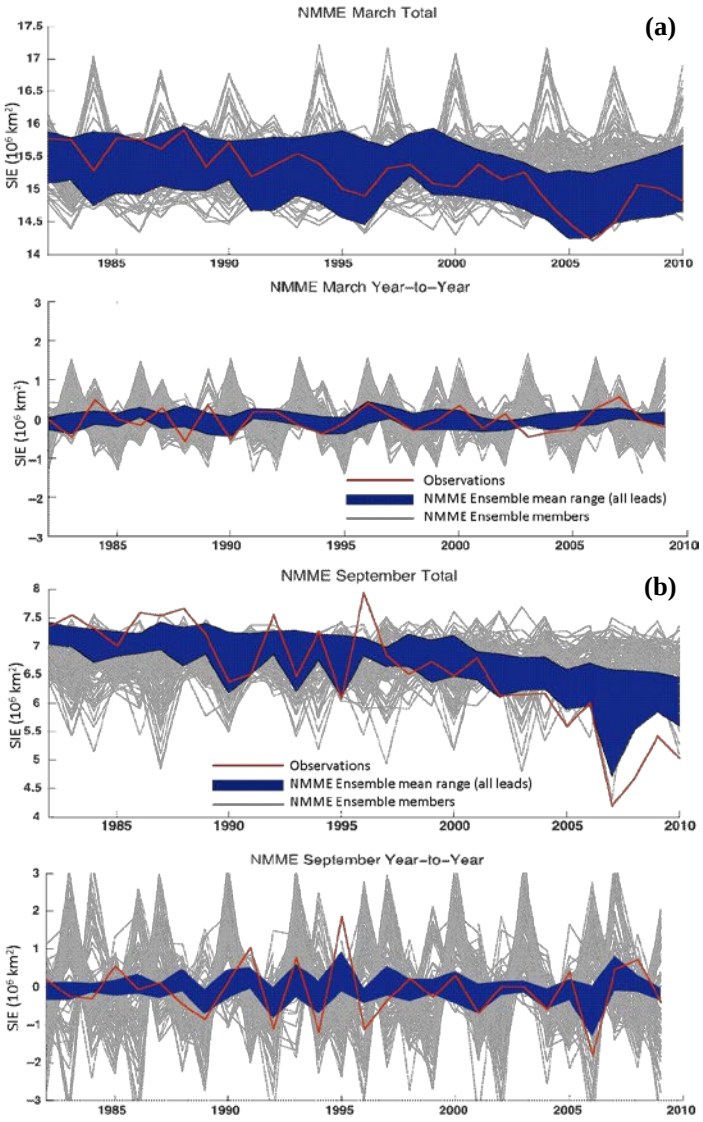

Fig. 2 Time series for NMME SIE in March (a) and September (b) for total (top) and Y2Y (bottom) SIE with observations (red line), the range of ensemble means at all lead times (blue shading), and individual ensemble members (grey lines).

To further quantify prediction skill, Figure 1 also shows the ACC values for the (c) total SIE and (d) Y2Y SIE. One primary feature across all models is the smaller ACC in Y2Y variability compared to the prediction of total SIE. For both total and Y2Y SIE, the NMME predictions result in generally higher ACC compared to the individual. The higher ACC with NMME is evident for predictions of Y2Y variability, especially for lead times greater than 3 months. The NMME also noticeably improves upon CanCM3, CanCM4, and CCSM4 for predictions of total SIE. Overall, relative to the skill of individual models, the NMME offers the most bias reduction for predictions of total SIE, and the correlations are highest for the prediction of Y2Y SIE.

Figure 2 compares the total and Y2Y SIE observational data (red) to the range of ensemble means (blue) and all members (grey) from NMME for 1982-2010. All forecast lead times are shown leading up to the March or September target month. The biases seen in Figure 1 are also reflected within this analysis, except

now it is easier to view the evolution of the model forecasts as the SIE changes over time. For predictions of March total SIE, the observations largely fall within the spread of the NMME. The observations also largely lie within the spread of predictions for March Y2Y SIE. However, for the Y2Y SIE predictions, the variance of the individual members is clearly larger than the observed variability across the NMME.

In contrast to March, predictions for September total SIE show that there are periods of time when the observations clearly lie outside of the spread of the model predictions. This is particularly true in the years following the large sea ice melt in 2007, when the NMME underestimated the degree of sea ice loss. Only during the recent period did the spread of forecasts from these models contain the observed September SIE. As for the March total SIE, the NMME predictions of September SIE appears to encompass the observed variability more often than any individual model. For the September Y2Y SIE, the observations largely lie within the spread of the model forecasts with the exception of the more extreme Y2Y years. But even in those instances, it appears the variance of the Y2Y individual members largely captures the variance of the observational data.

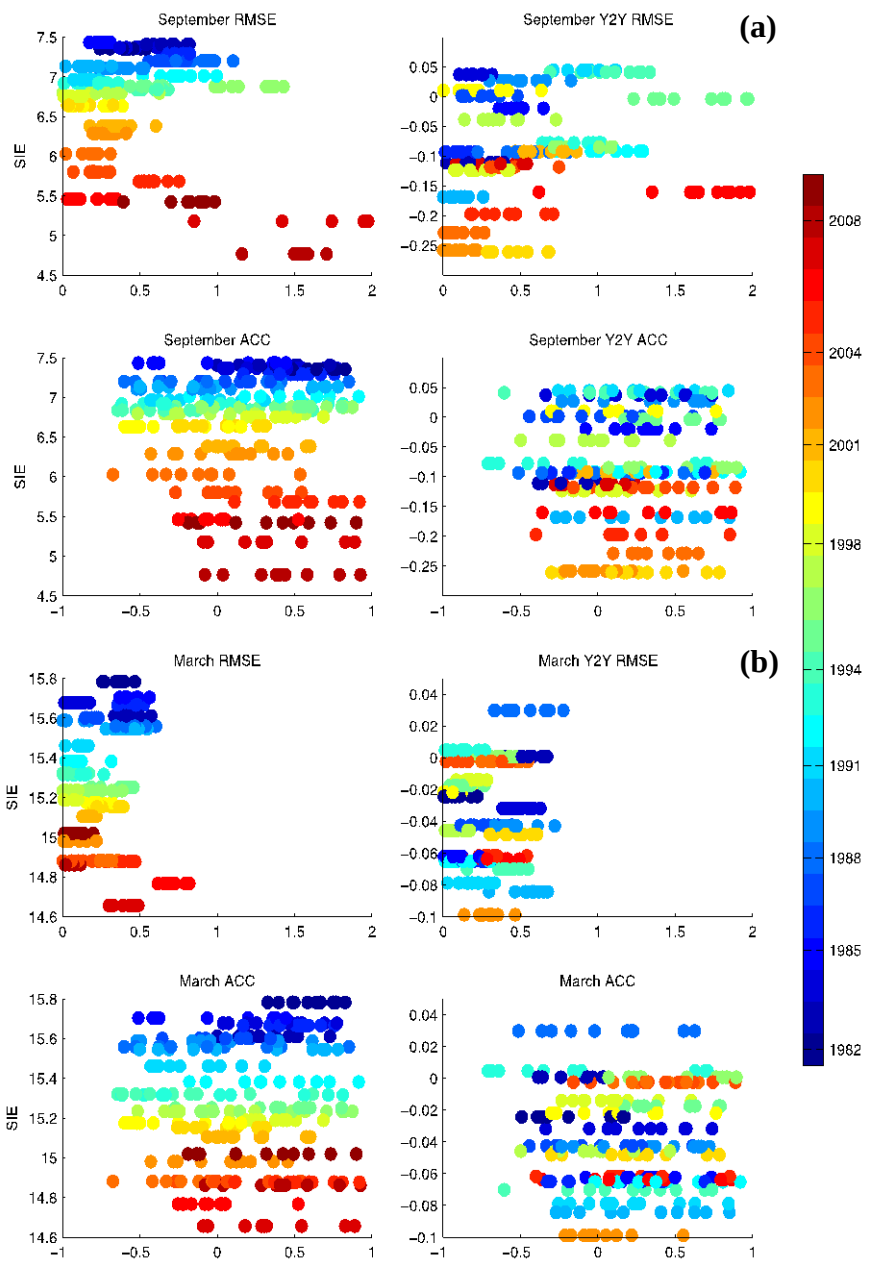

Fig. 3 September (a) and March (b) root-mean-square error (RMSE; top) and ACC (bottom) versus total SIE (left) and Y2Y (right) with year indicated by the colors.

Both the total and Y2Y time series in Figure 2 are smoothed using a 10-year running mean and presented versus model ACC and RMSE values. These scatterplots (Figure 3) show the skill for the 9 forecast lead times with respect to the total or Y2Y SIE. The associated 10-year period is indicated by the color shading, with reds (blues) indicating later (earlier) periods. Over these running 10-year periods, the ACC values in both September and March do not show any clear tendency over time. The RMSE tells a different story especially during September when the RMSE values are considerably larger during the more recent decades than the ones prior. The RMSE for Y2Y SIE does not show the same temporal trend, with the larger errors inclusive of decades with the largest Y2Y departures shown in Figure 2. Because Y2Y changes are independent of the longer-term trends, this suggests that errors in the prediction of the total SIE are increasing

over time because the NMME is not adequately capturing the trend or variability in recent years. In contrast, March does not show the same clear trend over time, and in general, the amplitude of RMSE for both total and Y2Y SIE is smaller in March compared to September, likely due to smaller trends and year-to-year variability during a month when the SIE is typically maximized.

4. Discussion

The NMME approach provides the most gain over individual models through decreased bias for predictions of total SIE and increased correlations of Y2Y SIE variability. There is a tendency for all models and the NMME to over-predict Y2Y SIE from one year to the next. The struggle of the models to predict the following year SIE change, along with the increasingly larger errors for September SIE predictions in recent decades, suggest that prediction of the trend remains a fundamental challenge for most coupled modeling systems. Regardless, it is clear that the average of multiple models generally exceeds the skill of any one modeling system, so the NMME demonstrates value for the prediction of Arctic SIE.

References

Chevallier, M., D. Salas-Melia, A. Voldoire, and M. Deque, 2013: Seasonal forecasts of the Pan-Arctic sea ice extent using a GCM-based seasonal prediction system, *J. Climate*, **26**, 6092-6104, doi:10.1175/JCLI-D-12-00612.1.

Holland, M. M., D. A. Bailey, and S. Vavrus, 2011: Inherent sea ice predictability in the rapidly changing Arctic environment of the Community Climate System Model, version 3. *Clim. Dyn.*, **36**, 1239-1253, doi:10.1007/s00382-010-0792-4.

Merryfield, J. W., W.-S. Lee, G. J. Boer, V. V. Kharin, J. F. Scinocca, G. M. Flato, R. S. Ajayamohan, and J. C. Fyfe, 2013: The Canadian Seasonal to Interannual Prediction System. Part I: Models and Initialization. *Mon. Wea. Rev.*, **141**, 2910-2945. doi: http://dx.doi.org/10.1175/MWR-D-12-00216.1

Sigmond, M., J. C. Fyfe, G. M. Flato, V. V. Kharin, and W. J. Merryfield, 2013: Seasonal forecast skill of Arctic sea ice area in dynamical forecast system. *Geophys. Res. Lett.*, **40**, 529-534, doi:10.1002/grl.50129.

Stroeve, J., L. C. Hamilton, C. M. Bitz, and E. Blanchard-Wrigglesworth, 2014: Predicting september sea ice: Ensemble skill of the SEARCH sea ice outlook 2008–2013. *Geophys. Res. Lett.*, **41**, 2411–2418, doi:10.1002/2014GL059388

Wang, W., M. Chen, and A. Kumar (2013), Seasonal Prediction of Arctic Sea Ice Extent from a Coupled Dynamical Forecast System. *Mon. Wea. Rev.*, **141**, 1375-1394, doi:10.1175/MWR-D-12-00051.1

Science and Technology Infusion Climate Bulletin
NOAA's National Weather Service
41st NOAA Annual Climate Diagnostics and Prediction Workshop
Orono, ME, 3-6 October 2016

The Rapid Arctic Warming of January 2016: Impacts, Processes, and Predictability

S.-Y. Simon Wang[1,2], Yen-Heng Lin[1] and Ming-Ying Lee[3]

[1]*Department of Plants, Soils and Climate, Utah State University, Logan, UT, USA*
[2]*Utah Climate Center, Utah State University, Logan, UT, USA*
[3]*Central Weather Bureau, Taipei, Taiwan*

ABSTRACT

In early January 2016, the Arctic troposphere underwent a substantial warming accompanying a rapid transition in the Arctic Oscillation (AO) into the negative phase (Fig. 1a). The tropospheric polar vortex broke down quickly causing a massive blocking in Siberia with a prolonged accumulation of cold airmass. The supercharged Siberian high then collapsed causing a record cold surge throughout East Asia, e.g. unprecedented snowfall in Taiwan, severe snowstorms in Korea, and even hyperthermia deaths in northern Thailand. The subseasonal property of this rapid AO transition was investigated and compared against the more widely known sudden stratospheric warming (SSW) events, one of which occurred in March 2016 with only mild consequences (Fig. 1b). Diagnostic analysis from the similar tropospheric and stratospheric warming cases indicates that Arctic warming is distinct from the SSW in that tropical sources of teleconnection are discernible (Fig. 2), associated with traceable poleward propagations of EP-flux in the upper troposphere (Figs 3,4). Results indicate a recent and accelerated increase in the tropospheric warming type versus a flat trend in stratospheric warming type (Fig. 5). Moreover, An ECHAM5 model was run to attribute the event and the result suggests that low Arctic sea ice in the 2015-16 winter did enhance the Arctic warming (not shown). Given that the AO transition associated with the tropospheric warming type occurs much more quickly than that with the stratospheric warming type, the noted increase in the former implies intensification in the boreal-winter midlatitude weather extremes.

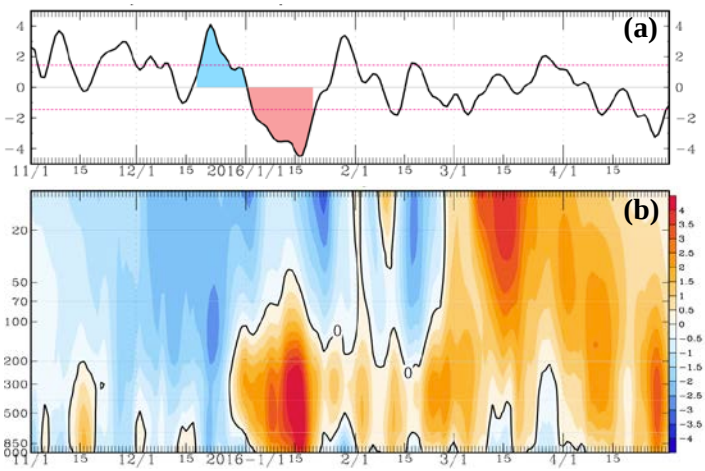

Fig. 1 Time series form November 2015 to April 2016 of (a) Arctic Oscillation index. (b) Standardized geopotential height anomaly over Arctic regions (65°N~90°N).

References

Cohen, J., J.A. Screen, J.C. Furtado, M. Barlow, D. Whittleston, D. Coumou, J. Francis, K. Dethloff, D. Entekhabi, J. Overland, and J. Jones, 2014: Recent Arctic amplification and extreme mid-latitude weather. *Nat. Geosci.*, **7**, 627–637.

L'Heureux, M. L., and R. W. Higgins, 2008: Boreal winter links between the Madden–Julian oscillation and the Arctic Oscillation. *J. Climate*, **21**, 3040–3050.

Riddle, E. E., M. B. Stoner, N. C. Johnson, M. L. L'Heureux, D. C. Collins, and S. B. Feldstein, 2013: The impact of the MJO on clusters of wintertime circulation anomalies over the North American region. *Clim. Dyn.*, **40**, 1749–1766, doi:10.1007/ s00382-012-1493-y.

Correspondence to: Yen-Heng Lin, Department of Plants, Soils and Climate, Utah State University, Logan, UT, USA; E-mail: yheng@pie.com.tw

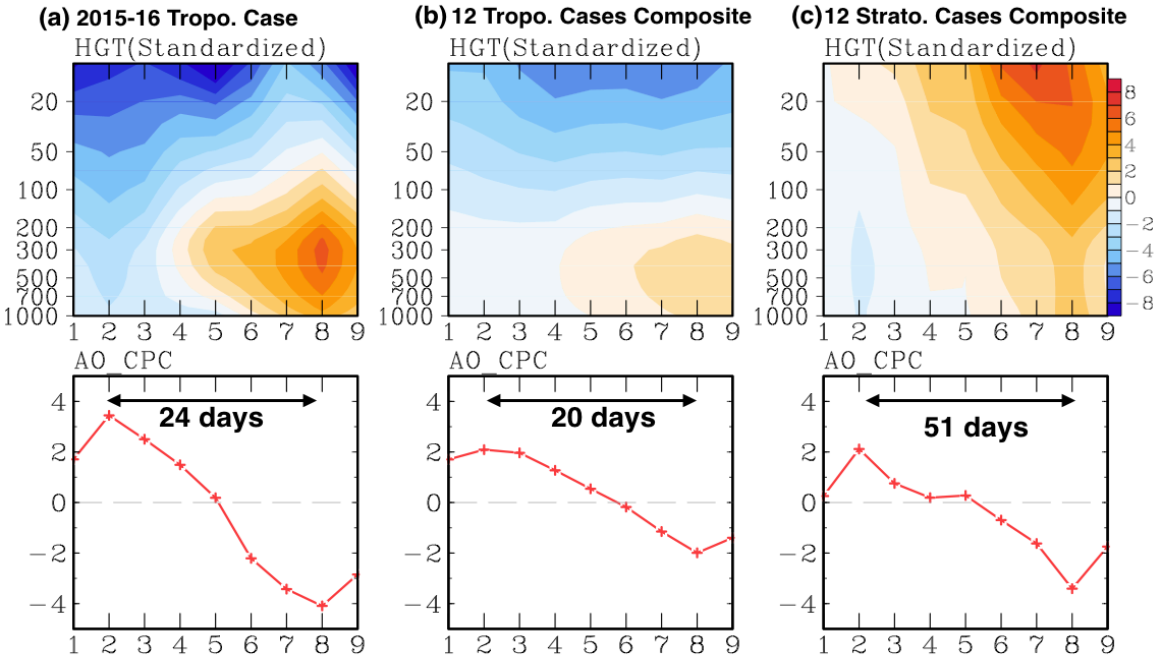

Fig. 2 Nine phases of Standarized Geopotential height over 65°N~90°N and AO index for (a) January 2016 case, (b) 12 AO phase change cases with tropospheric warming, and (c) 12 AO phase change cases with stratospheric warming. The selected composite cases are depended on the AO index with phase change from +1.2 to -1.2 standard deviation.

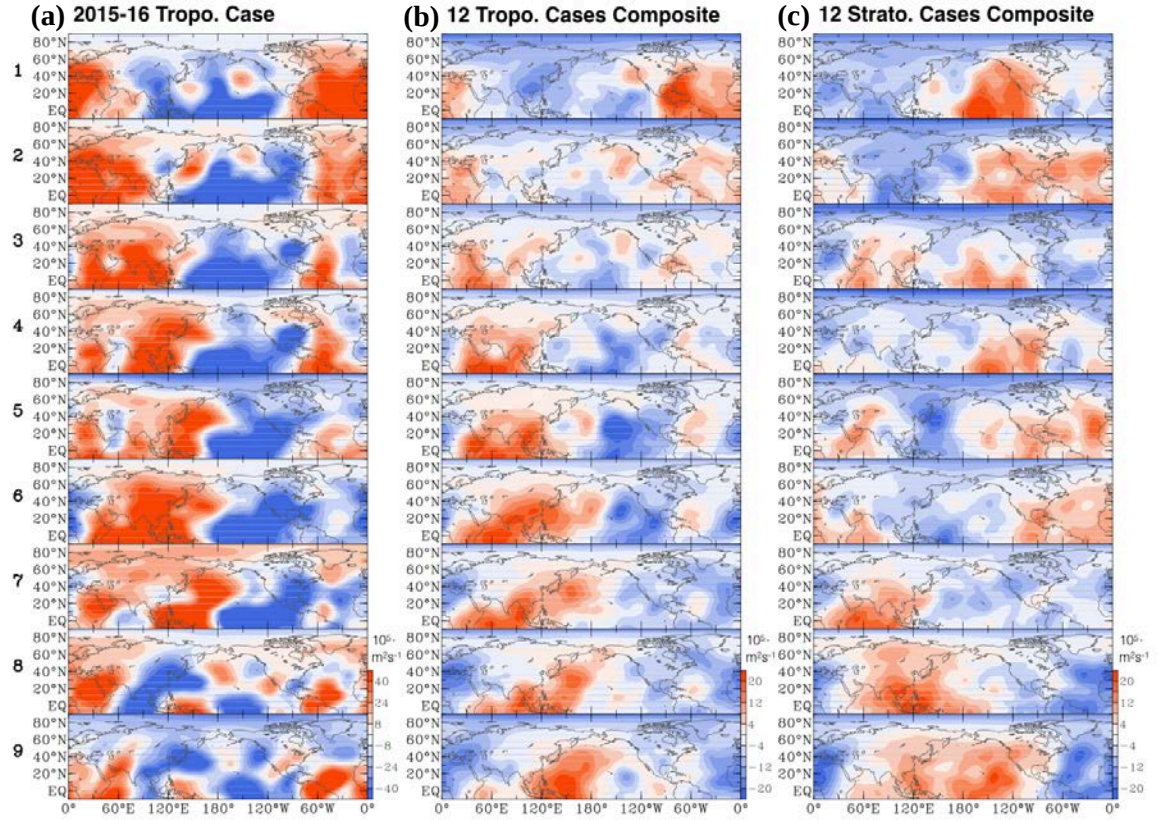

Fig. 3 Nine phases of 250mb velocity potential (VP) for (a) January 2016 case, (b) 12 AO phase change cases with tropospheric warming, and (c) 12 AO phase change cases with stratospheric warming.

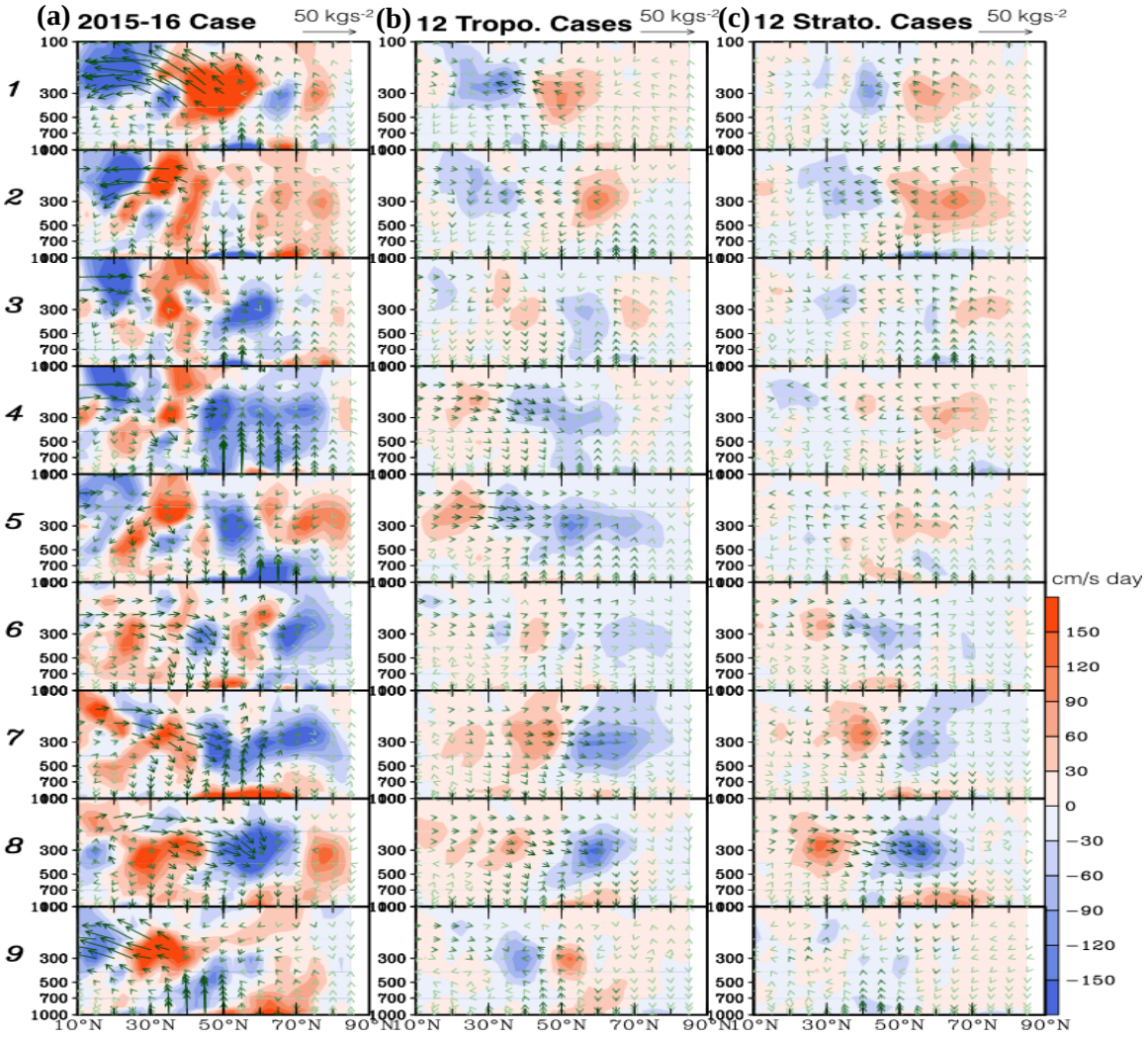

Fig. 4 The same as Fig.3, but for EP-Flux over troposphere.

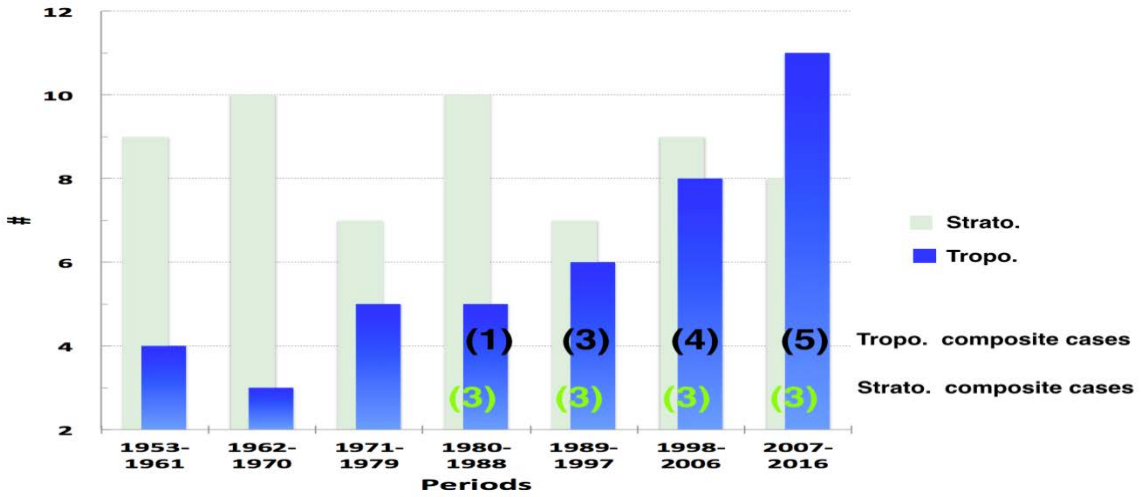

Fig. 5 The total cases of tropospheric and stratospheric warming with 9-years interval (cases are based on standardized geopotential height anomaly only, and the number shows the cases using in composite analysis).

7. GENERAL SESSION: CLIMATE DIAGNOSTICS, PREDICTION, ANALYSES AND REANALYSES

41th NOAA Annual Climate Diagnostics and Prediction Workshop

3-6 October 2016, Orono, Maine

Science and Technology Infusion Climate Bulletin
NOAA's National Weather Service
41st NOAA Annual Climate Diagnostics and Prediction Workshop
Orono, ME, 3-6 October 2016

Rediscovering the MJO Extratropical Response: Streamfunction as a Preferred Variable for Subseasonal Teleconnection Analysis

Stephen Baxter[1] and Sumant Nigam[2]
[1]*Climate Prediction Center, NOAA/NWS/NCEP, College Park, Maryland*
[2]*University of Maryland, College Park, MD*

1. Introduction

Teleconnection analysis serves as a basis for understanding low-frequency (*i.e.* super-synoptic to seasonal) atmospheric variability, and teleconnection patterns serve as building blocks with which one can reconstruct observed atmospheric climate anomalies. While teleconnection analysis has traditionally been conducted to explore recurrent patterns of variability confined to the extratropics (*e.g.* Wallace and Gutzler, 1981; Barnston and Livezy, 1987), there are two clear examples of teleconnection patterns rooted in the subtropics, namely, the atmospheric responses (ranging from the subtropics to the extratropics) to the Madden-Julian Oscillation (MJO) and the El Niño-Southern Oscillation (ENSO). The former is more dominant on subseasonal time scales, while the latter is perhaps the most well-known mode of interannual variability.

The MJO extratropical response can be identified using composite analysis utilizing two different metrics of MJO activity: the popular Wheeler and Hendon (2004) index and a simple velocity potential index derived and monitored by the Climate Prediction Center (CPC). Baxter *et al.* (2014), for example, shows that the MJO can be a useful predictor of subseasonal hydroclimate variability over the contiguous United States, a powerful result given the growing interest in climate prediction that spans the gap between Week-2 forecasts and monthly/seasonal forecasts. That analysis reveals a pattern consistent with various studies highlighting a relationship between the MJO and the Pacific-North America (PNA) pattern as well as the North Atlantic Oscillation (NAO). However, the correlation between the PNA and the MJO (as assessed by either the RMM or CPC index) is modest, on the order of 0.3 or less, as is the correlation between the NAO and MJO. Linear removal of the MJO from the data prior to analysis has little effect on the PNA and NAO patterns. Additionally, a visual inspection of the MJO response pattern and the loading patterns of either the PNA or NAO reveals that there are important differences, and thus the PNA and NAO cannot simply be thought of as an MJO response.

This dilemma is similar to that faced when comparing the PNA and the extratropical response to ENSO. While traditional teleconnection analysis often links PNA and ENSO, an alternative, more physically appropriate analysis reveals that they are quite different. Using 200-hPa geopotential height in a rotated empirical orthogonal function (EOF) analysis yields a PNA pattern as separate from the canonical ENSO response (Nigam, 2003; Nigam and Baxter, 2014). This separation does not readily occur when using 500-hPa geopotential height, as that variable exhibits less tropical and subtropical variance. In that framework then, extratropical variability that is associated with the ENSO response is aliased into the other extratropical patterns of variability, including the PNA. Applying a similar approach to subseasonal teleconnection analysis, however, does not yield an MJO response distinct from teleconnection patterns internal to the extratropical atmosphere. This is likely because the 200-hPa geopotential height variability on subseasonal time scales is much larger at higher latitudes, which are therefore emphasized in an EOF analysis which utilizes the covariance matrix.

The remedy pursued here is to utilize 200-hPa streamfunction, which places the subtropics and the middle and high latitudes on a more equal footing. This is preferred to using the correlation matrix in the EOF analysis since it allows for longitudes that exhibit more variability to be emphasized. The goal of this analysis is to find the MJO extratropical response in the rich spectrum of tropical-extratropical variability.

Correspondence to: Stephen Baxter, Climate Prediction Center, NOAA/NWS/NCEP, 5830 University Research Court, College Park, MD; E-mail: Stephen.Baxter@noaa.gov

Additionally, this analysis is targeted toward looking at any tropical footprints of the other known teleconnection patterns. This will involve inspection of various fields in addition to streamfunction, such as velocity potential, outgoing longwave radiation (OLR), and sea-surface temperature (SST). This analysis, we think, will be an important advance in the diagnosis and monitoring of subseasonal teleconnection evolution.

2. Data and methods

For this analysis, 200-hPa streamfunction is utilized for the reasons just discussed. A time-extended EOF analysis is utilized to capture the spatio-temporal variability of the 200-hPa streamfunction field at pentad resolution. The analysis period is 35 winter seasons from 1979-2014, and the spatial domain consists of the entire Northern Hemisphere. This analysis focuses on December, January, and February (DJF), the three months that together make up meteorological winter. Winter is therefore taken to be the 19 pentads that span those three months. The data are extended using a five pentad window, and two pentads on each side of the 19-pentad season are allowed into the analysis so that the principal components (PCs) are defined for each of the 19 pentads. The leading eight modes are subject to varimax rotation to allow for more spatial discrimination. The number of rotated modes was selected using a scree test and by using the North *et al.* (1982) criteria. In this framework, a substantial break in the eigenvalues between modes eight and nine occur, beyond which all patterns are likely within the sampling error range. However, to be sure, variants of the

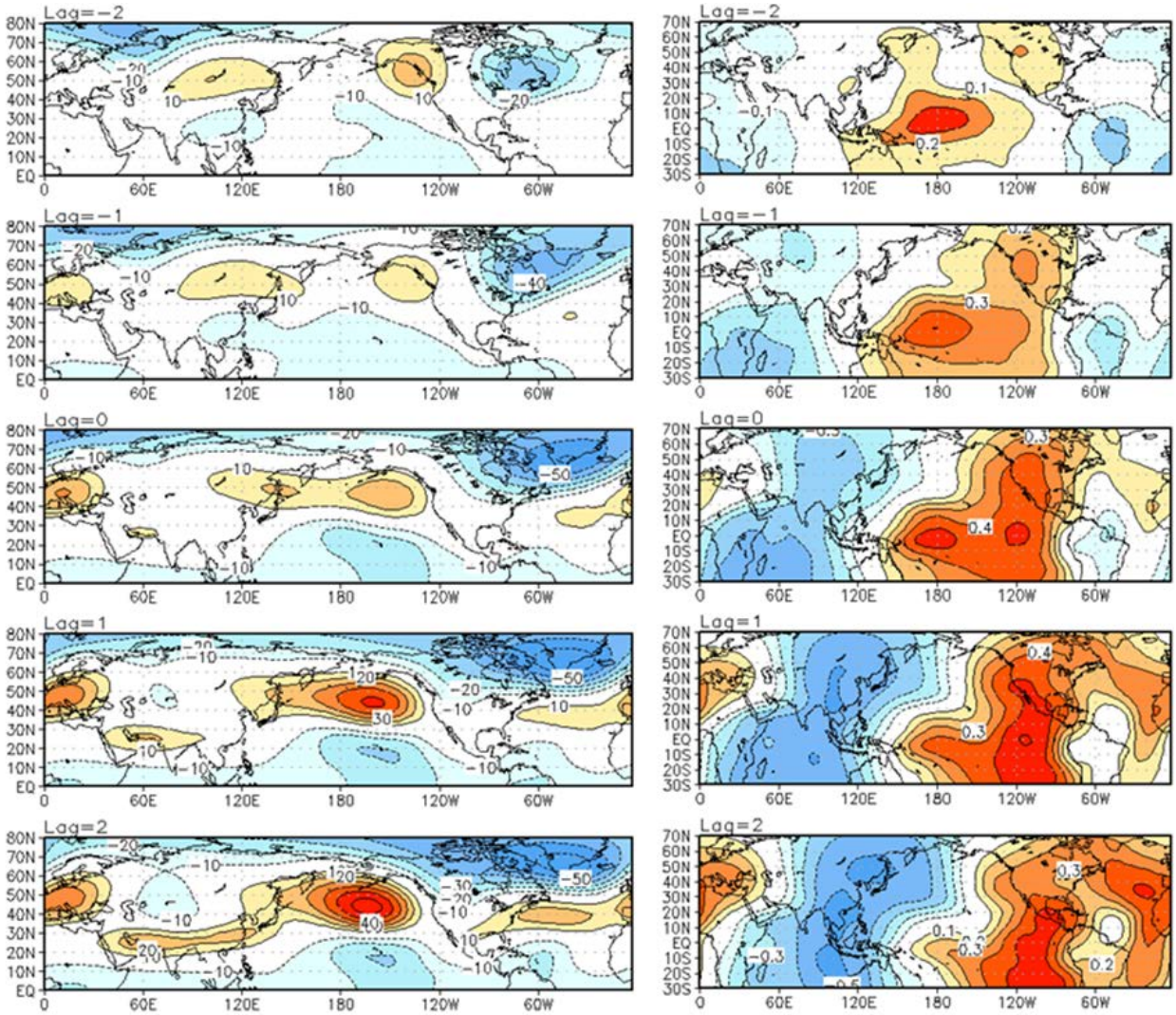

Fig. 1 Regressions of the 2nd PC (9.8% of explained variance) onto 200-hPa geopotential height (left) and correlations with 200-hPa velocity potential (right). This pattern constitutes development of the MJO extratropical response, leading the 1st PC by three pentads (r=0.9).

analysis are performed rotating as many as ten and as few as six modes. The main results of this analysis are independent of the number of rotated modes, and so the optimal eight modes are retained for this analysis.

The 200-hPa streamfunction, 200-hPa velocity potential, and OLR fields, are all from the latest Climate Forecast System Reanalysis (CFSR, Saha *et al.* 2010). SST data is obtained from a weekly Optimal Interpolation V2 (Reynolds *et al.* 2002) dataset that has been interpolated to pentad resolution. The seasonal cycle is removed from all data where appropriate.

3. Results

The results of the rotated, extended EOF analysis of streamfunction reveal the spatio-temporal evolution of several key patterns of subseasonal climate variability. The patterns that are readily identified are the MJO extratropical response, the ENSO response, the North Pacific Oscillation/West Pacific pattern (NPO/WP), the NAO, and the PNA.

The leading two principal components together comprise the MJO response, and together explain 19.9% of the total variance. Figure 1 shows the time evolution from -2 to +2 pentads of the 200-hPa geopotential

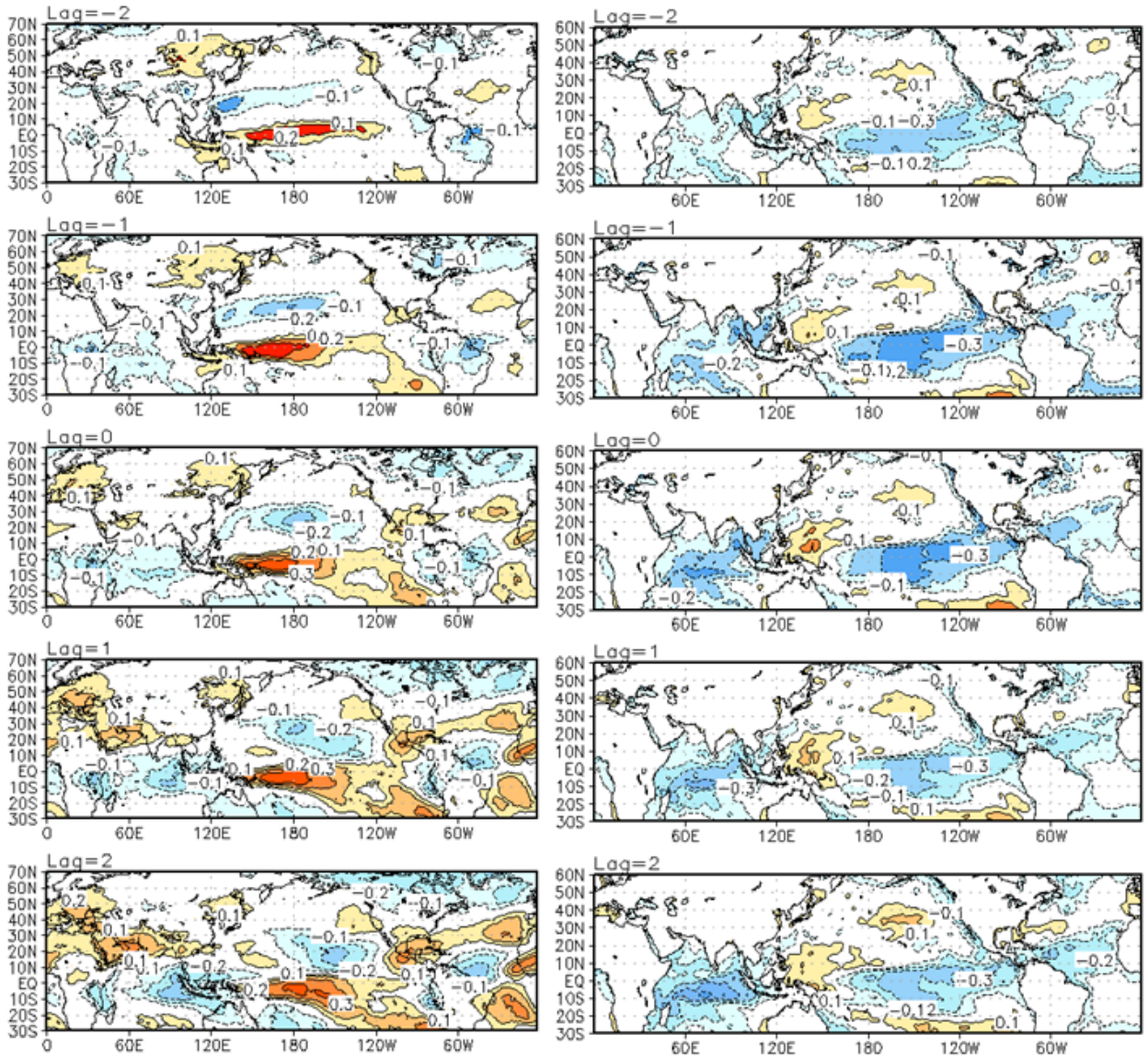

Fig. 2 Correlations of the 2nd PC (9.8% of explained variance), which constitutes the development of the MJO extratropical response, with OLR (left) and SST (right).

height regressions alongside the velocity potential footprints of PC2. PC2 is best characterized as the development of the response pattern, while PC1 (not shown) targets the decay. Not surprisingly, these patterns are highly correlated (r=0.9) at a lag of three pentads, with PC2 leading PC1.

These patterns are notable for their robust velocity potential footprints in the tropics, and the development of the MJO extratropical response is associated with, and preceded, by anomalous upper-level convergence (divergence) over the Pacific (Indian Ocean). The development of positive (negative) 200-hPa height anomalies over South Asia (central, subtropical Pacific) is consistent with the anomalous upper-level divergence (convergence) to the south. This is consistent with tropical forcing via the advection of absolute vorticity by the anomalous meridional divergent wind (not shown). Figure 2 shows the OLR and SST footprints associated with the 2nd PC, and reveals a dipole of anomalous convection between the Indian Ocean and the west-central Pacific, consistent with this being associated with the MJO. There is some small, but likely significant, relationship with equatorial Pacific SSTs, suggesting some low frequency variability is at play.

It is not surprising that there exists a strong relationship between the leading PCs of this streamfunction analysis and those that intentionally target MJO activity. The correlation between either of the leading PCs and the CPC MJO index (Baxter *et al.* 2014) peaks at r=0.62, with PC2 leading CPC MJO index 1(refer to Chapter 2) by one pentad. The final evidence in favor of solidifying the argument that PCs 1 and 2 comprise the MJO extratropical response is a direct, quantitative comparison between the regression pattern obtained in

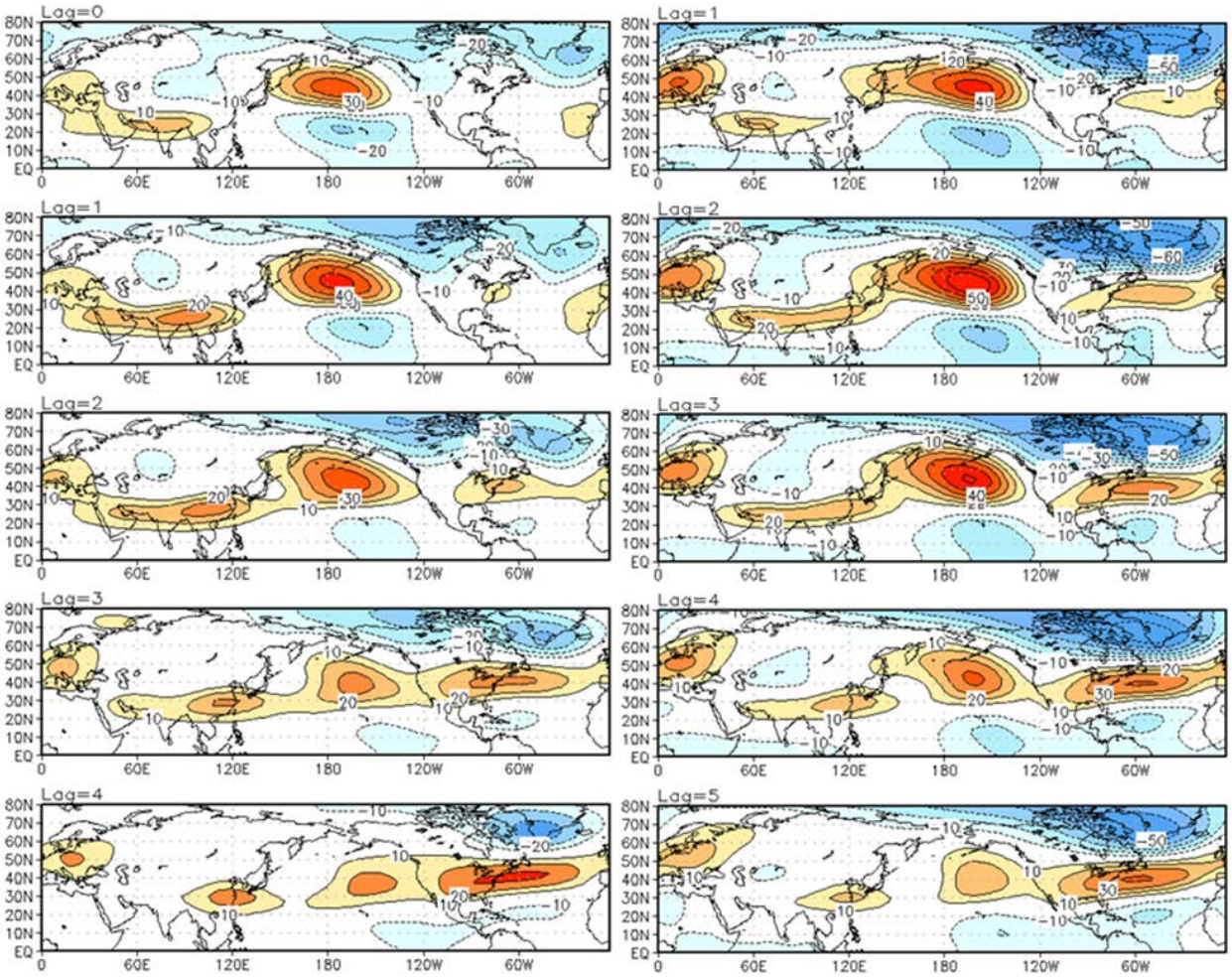

Fig. 3 Left: Lag regression (lag=0 to lag=4) between CPC MJO Index 1 and the 200-hPa geopotential height. Contour interval is 10m, with the zero contours suppressed. Right: Same as left, but for the 2nd PC from the current analysis (lag=1 to lag=5). Spatial correlations are 0.82, 0.82, 0.84, 0.88, and 0.92.

Figure 1 and the regression of CPC MJO index 1 onto the same 200-hPa geopotential height field. Figure 3 shows the regression of CPC MJO index 1 onto the 200-hPa height field from lag=0 to lag=4 pentads. This is plotted alongside the regression of PC2 onto the same height field at lag=1 to lag=5 pentads. The offset is made to put the two indices on par given the one-pentad lag between them. This analysis reveals a striking similarity between the patterns, with spatial correlations from top to bottom of 0.82, 0.82, 0.84, 0.88, and 0.92, respectively. Additionally, the amplitudes of the regressions based on PC2 are higher than in the case of the CPC MJO index (this comparison can be made since both indices are normalized). This is a welcome result, and shows that the MJO extratropical response can be effectively deduced from the data without even direct knowledge of the divergent circulation.

In addition to the MJO circulation response, this analysis also captures the low-frequency ENSO response, manifest on subseasonal timescales. Figure 4 shows the 200-hPa geopotential height and SST patterns associated with the 3rd PC. This PC also exhibits the lowest frequency temporal variability, by far, of the eight PCs retained in this analysis. Beyond subseasonal tropical-extratropical teleconnections related the MJO and ENSO, the analysis reveals spatiotemporal variability related to teleconnection more internal to the extratropical atmosphere, including the NAO, the NPO/WP, and the PNA. Further analysis (not shown here) shows that these patterns are not likely generated by anomalous tropical divergent circulations.

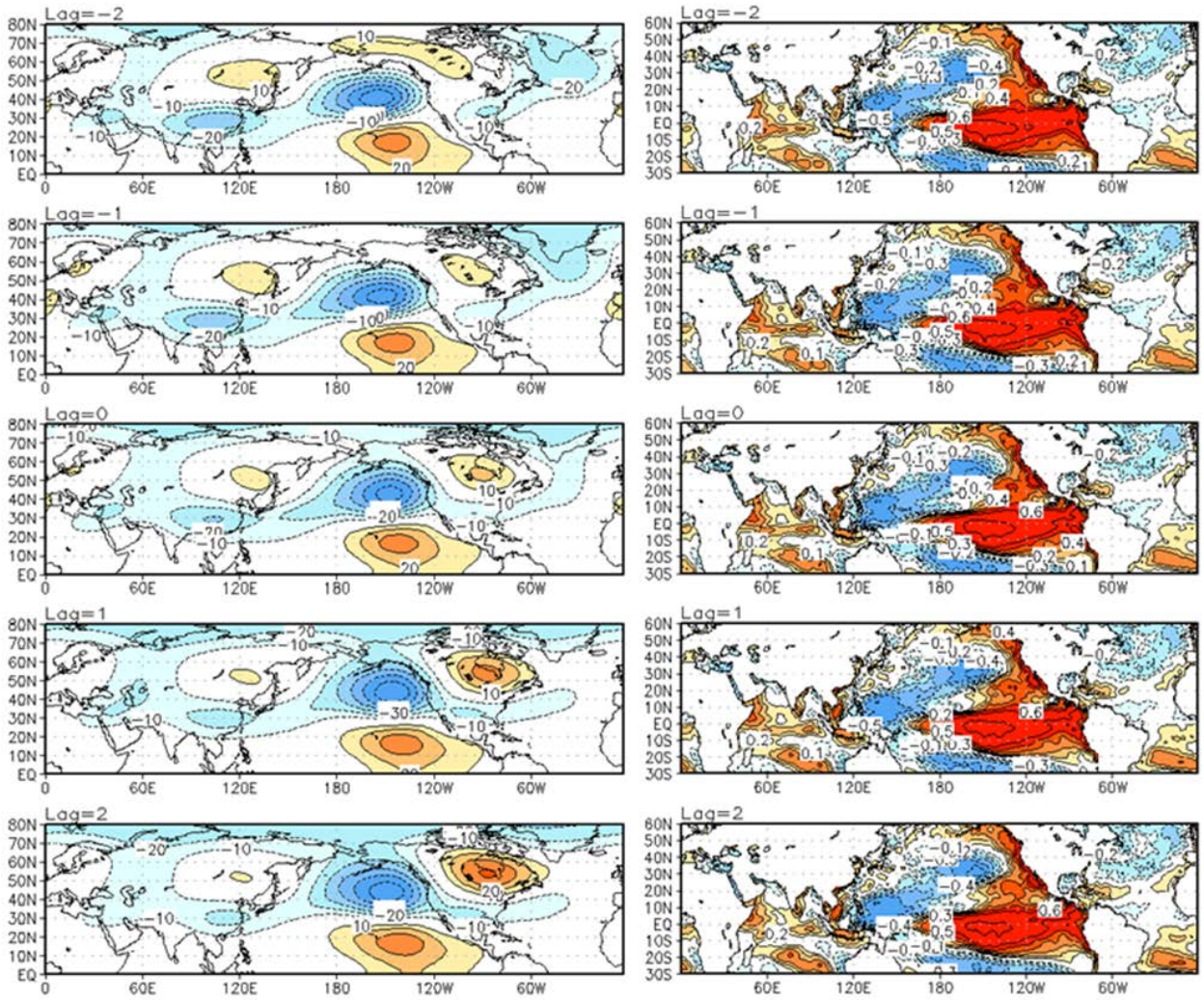

Fig. 4 Regressions of the 3rd PC onto 200-hPa geopotential height (left) and correlations with SST (right). This pattern is clearly recognizable as the extratropical ENSO response.

4. Conclusions

Teleconnection analysis is useful for reconstructing climate anomalies, including quantifying the roles of various patterns in generating climate extremes. Tropical-extratropical teleconnections are of particular interest because of the predictability implied by understanding the mechanisms of subseasonal climate pattern evolution, as they relate to readily observable precursor fields. To this end, analysis of upper-tropospheric streamfunction allows for the identification of the MJO teleconnection within the wide spectrum of tropical-extratropical variability. Subseasonal streamfunction analysis, therefore, is a preferred method for real-time diagnostics and attribution of subseasonal climate variability.

References

Barnston, A., and R. Livezy, 1987: Classification, seasonality, and persistence of low-frequency atmospheric circulation patterns. *Mon. Wea. Rev.*, **115**, 1083–1126.

Baxter, S., S. Weaver, J. Gottschalck, and Y. Xue, 2014: Pentad Evolution of Wintertime Impacts of the Madden–Julian Oscillation over the Contiguous United States. *J. Climate*, **27**, 7356–7367.

Nigam, S., 2003: *Teleconnections. Encyclopedia of Atmospheric Sciences,* J. R. Holton, J. A. Pyle, and J. A. Curry, Eds., Academic Press, 2243–2269.

Nigam, S., and S. Baxter, 2014: *Teleconnections. Encyclopedia of Atmospheric Sciences*, 2nd ed. G. North, Ed., Elsevier Science, 90–109.

North, G.R., Thomas L. Bell, Robert F. Cahalan, and Fanthune J. Moeng, 1982: Sampling Errors in the Estimation of Empirical Orthogonal Functions. *Mon. Wea. Rev.*, **110**, 699–706.

Reynolds, R.W., Nick A. Rayner, Thomas M. Smith, Diane C. Stokes, and Wanqiu Wang, 2002: An Improved In Situ and Satellite SST Analysis for Climate. *J. Climate,* **15**, 1609–1625.

Saha, S., and Coauthors, 2010: The NCEP Climate Forecast System Reanalysis. *Bull. Amer. Meteor. Soc*., **91**, 1015–1057.

Wallace, J., and D. Gutzler, 1981: Teleconnections in the geopotential height field during the Northern Hemisphere winter. *Mon. Wea. Rev.*, **109**, 784–804.

Wheeler, M. C., and H. H. Hendon, 2004: An all-season real-time multivariate MJO index: Development of an index for monitoring and prediction. *Mon. Wea. Rev.*, **132**, 1917–1932.

Science and Technology Infusion Climate Bulletin
NOAA's National Weather Service
41st NOAA Annual Climate Diagnostics and Prediction Workshop
Orono, ME, 3-6 October 2016

Variations of Mid-Atlantic Trough and Associated American-Atlantic-Eurasian Climate Anomalies

Mengmeng Lu[1], Kaiqiang Deng[1], Song Yang[1, 2, 3], Guojun Zhou[4], and Yaheng Tan[1]

[1]*School of Atmospheric Sciences, Sun Yat-sen University, Guangzhou, China*

[2] *Guangdong Province Key Laboratory for Climate Change and Natural Disaster Studies, Sun Yat-sen University, Guangzhou, China*

[3]*Institute of Earth Climate and Environment System, Sun Yat-sen University, Guangzhou, China*

[4]*Xinhua College of Sun Yat-sen University, Dongguan, China*

ABSTRACT

The mid-Atlantic trough (MAT) is one of the most prominent circulation systems over the mid-Atlantic during the boreal summer, which is viewed as an atmospheric bridge linking the American-Atlantic-Eurasian climate. On interannual time scale, the variation of MAT is significantly associated with the North Atlantic Oscillation and a southeastward propagating stationary wave that originates from the northeastern Pacific (Fig. 1(a)-(b)). The associated sea surface temperature (SST) pattern shows a meridional quadripole structure over the tropical Atlantic and the North Atlantic, which is similar to the negative Atlantic meridional mode (AMM; Fig. 1(c)). Moreover, the correlation coefficient between the interannual variability of MAT (MAT_IAV) and the AMM index significantly exceeds the 99% confidence level. The strong trough is associated with the warmer surface temperature over central-northern North America and the North Atlantic, which might be related to the higher pressure over these regions. Similarly, corresponding to the lower pressure over the Arctic region, the subtropical North Atlantic and the northeastern Pacific, the colder surface temperature appears over these areas (Fig. 2(a)). When the trough is strong, significant negative precipitation anomalies occur over the north of the Mediterranean Sea and the Black Sea, as well as the northeastern Atlantic because of the low-level northeasterly winds over these areas (Fig. 2(b)). On interdecadal time scale, there exists a significant negative correlation between the MAT and the Atlantic Multidecadal Oscillation (AMO; Fig. 3). When the trough is weak, the warmer surface temperature appears over almost entire North Atlantic (the feature is similar to the AMO), South Europe, East Asia and the North Pacific (Fig. 4(a)). The weak trough is associated with a dipole structure of anomalous rainfall over the North Atlantic and the Greenland (Fig. 4(b)).

This work will be submitted to the Canadian journal *Atmosphere-Ocean* in 2017.

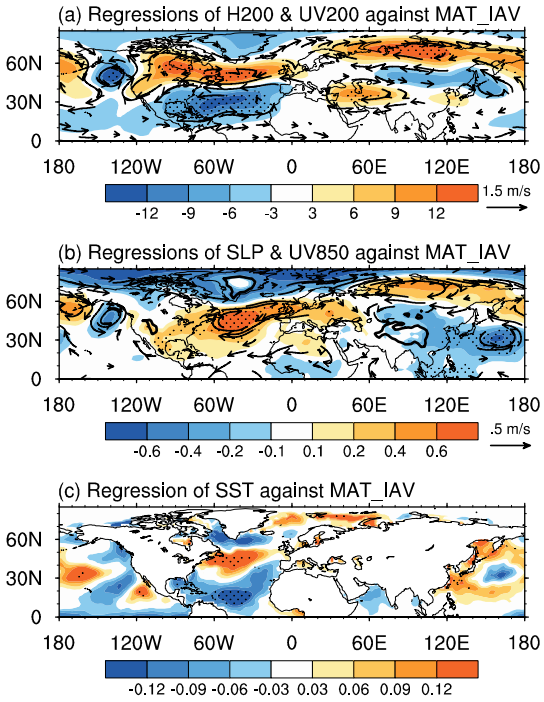

Fig. 1 (a) Regressions of 200-hPa geopotential height (shadings, units: m) and horizontal winds (vectors, units: m s^{-1}) against the MAT_IAV. (b) Same as (a), but for sea level pressure (shadings, units: hPa) and 850-hPa horizontal winds (vectors, units: m s^{-1}). (c) Same as (a), but for SST (units: °C). The dots indicate the values that are significantly above the 95% confidence level. The regressed winds smaller than 0.3 m s^{-1} and 0.1 m s^{-1} are masked out in (a) and (b), respectively. In (b), the topography higher than 2000 meters is marked with thick lines.

Correspondence to: Song Yang, School of Atmospheric Sciences, Sun Yat-sen University, 135 West Xingang Road, Guangzhou 510275, China; E-mail: yangsong3@mail.sysu.edu.cn

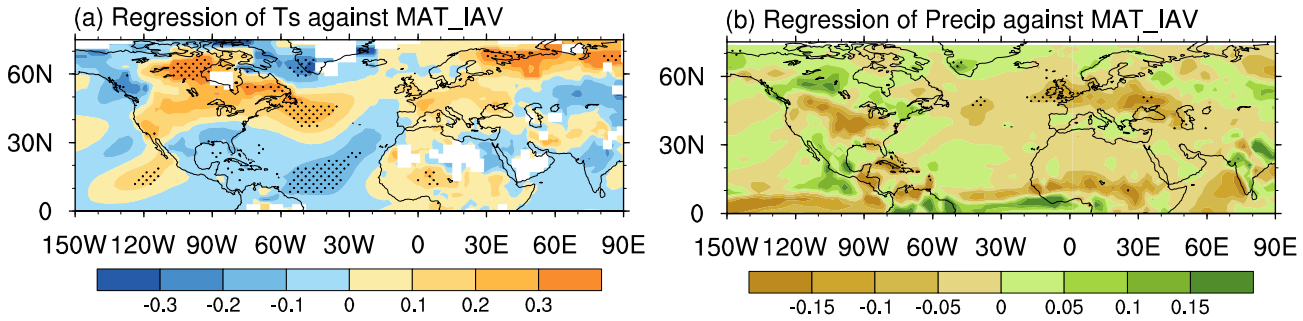

Fig. 2 Same as Fig. 1, but for (a) surface temperature (units: °C) and (b) precipitation (units: mm day^{-1}). The dots indicate the values that are significantly above the 95% confidence level.

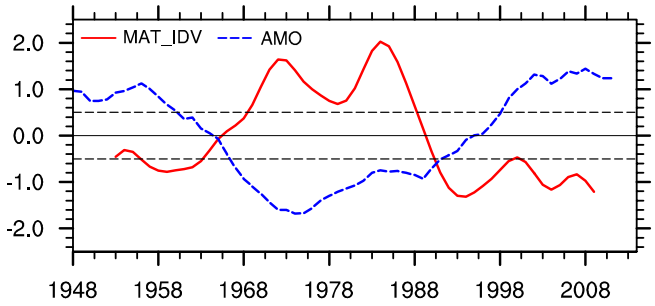

Fig. 3 Standardized interdecadal variation of MAT (MAT_IDV; red curve) that is calculated by a 10-year low-pass filter and standardized AMO index (blue curve). The dashed black lines represent the values of 0.5 standard deviations.

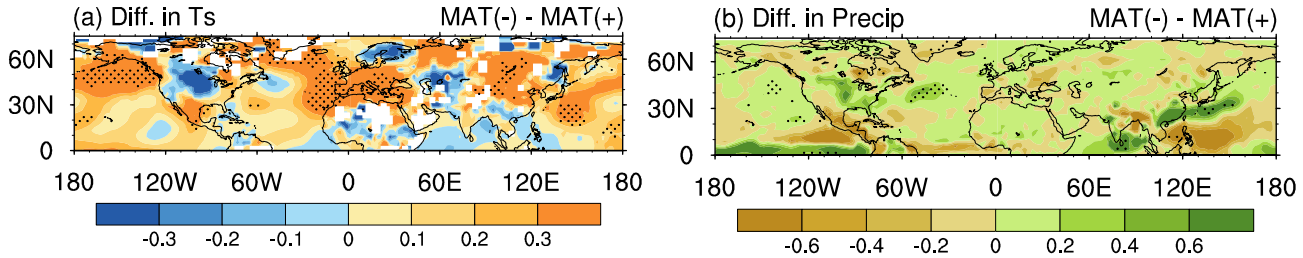

Fig. 4 (a) Composite differences of surface temperature (units: °C; in which the long-term trend is removed) between the negative phase (1991-2009) and the positive phase (1969-1988) of MAT. (b) Same as (a), but for precipitation (units: mm day^{-1}). The dots indicate the values that are significantly above the 95% confidence level.

Science and Technology Infusion Climate Bulletin
NOAA's National Weather Service
41st NOAA Annual Climate Diagnostics and Prediction Workshop
Orono, ME, 3-6 October 2016

A Preliminary Examination of a Conventional EnKF Atmospheric Reanalysis

Wesley Ebisuzaki[1], Arun Kumar[1], Jeffrey Whitaker[3], Jack Woollen[4],
Hyun-Chul Lee[2], and Leigh Zhang[2]

[1]*Climate Prediction Center, NOAA/NWS/NCEP, College Park, Maryland*
[2]*Innovim LLC., Greenbelt, Maryland*
[3]*Physical Sciences Division, NOAA/OAR/ESRL, Boulder, Colorado*
[4]*Environmental Modeling Center, NOAA/NWS/NCEP, College Park, Maryland*

1. Introduction

Atmospheric reanalyses can be optimized to produce the most accurate reanalysis by assimilating all observations including satellite observations. However, this type of reanalysis often shows discontinuities in various time series with the introduction of new satellite systems (*ex.*, Zhang *et al.* 2012). Another approach was taken by the 20th Century Reanalysis (Compo *et al.* 2011), the time series were made more homogeneous by only assimilating surface pressure observations. However, the cost of homogeneity is a less accurate reanalysis because much fewer observations were assimilated. The Climate Prediction Center (CPC) wanted a NCEP/NCAR Reanalysis (R1) replacement that would be between these two extremes. The replacement reanalysis had to have accuracy of R1, eliminate the gross artifacts from the introduction of various satellites and span from the 1950's to the present.

There is a hierarchy of reanalyses (few to more observations, potentially few to more artifacts caused by changes in the observational systems):

0) Observed SST is used to force an atmospheric model, *ex.* AMIP
1) Surface observations are assimilated, *ex.* 20th Century Reanalysis (surface pressure), ERA-20C (surface pressure and surface winds)
2) Conventional observations (non-satellite) observations are assimilated, *ex.* JRA-55C
3) Conventional and satellite observations are assimilated, ex. R1, ERA-interim, MERRA2, JRA-55
4) Conventional, satellite and marine observations are used in a coupled atmospheric-ocean assimilation system, *ex.* CFSR

Can we replace R1 with a conventional-observation based reanalysis and satisfy the accuracy requirements? To answer this question, we ran several decades with a newly developed analysis system, CORe.

2. Details of CORe (Conventional Observation Reanalysis)

The CORe system is an ensemble-Kalman-filter atmospheric data assimilation system (Jeff Whitaker *et al.*, CDWP 2016). The system uses an 80-member ensemble using a recent version of the T254 L64 semi-Lagrangian GFS model (NCEP's Global Forecast System). The CORe was run from 1950 to mid-2010 in 6 streams using a 1 year overlap between the streams. CORe assimilated conventional observations, cloud track winds, and GPS-RO (COSMIC) data. The last two items use satellite data but they are relatively insensitive to the biases in the satellite sensors. (GPS-RO is based on timing information and should not suffer from biases in the radiance measurements. The cloud track winds use radiance for the height assignment but a 0.5 degree Celsius error will only give a 51 m height error assuming an adiabatic lapse rate.)

3. Evaluation of CORe in the mid-latitudes

A common method of evaluating the performance of a data-assimilation system is to find the skill of a forecast run from the analyses. Figure 1 shows the anomaly correlation of the 5-day 500 mb height forecast

Correspondence to: Wesley Ebisuzaki, Climate Prediction Center, NOAA/NWS/NCEP, 5830 University Research Court, College Park, MD; E-mail: wesley.ebisuzaki@noaa.gov

in the Northern Hemisphere. The red line shows that the R1 anomaly correlation starts at 0.5 and reaches 0.72 at the end of the time series. The multicolored line shows the skill of the various streams of CORe which starts at 0.62 and ends at 0.82. For the period, the forecasts using the CORe model from the CORe analyses as initial conditions were superior the R1 forecasts using the R1 analyses.

Figure 2 is similar to Fig. 1 except it is for the Southern hemisphere. The Southern hemisphere is expected to be more difficult for CORe because there are fewer conventional observations and R1 assimilates satellite data. R1 has much higher forecast skill in the first 6 years and roughly the same skill in the last decade. We speculate that the R1's skill in the first 6 years is artificial, caused by a lack of Southern hemisphere observations in the early period. Assuming the skill is artificial, CORe was similar or better than R1 in this case. The behavior in the last 7 years is examined in more detail in the section, “Unusual Behavior”.

The forecast skill scores are suggestive but not proof that CORe analyses are better than the R1 analyses. The CORe forecasts were done using a much better model. For example, the CORe model had 4x the horizontal resolution (T254 *vs.* T62) and 2.3x the vertical resolution (64 levels *vs.* 28 levels). In addition, the CORe model is based on a 20-year newer version of the NCEP global model. So some of the improved skill is undoubtedly from the improved CORe model.

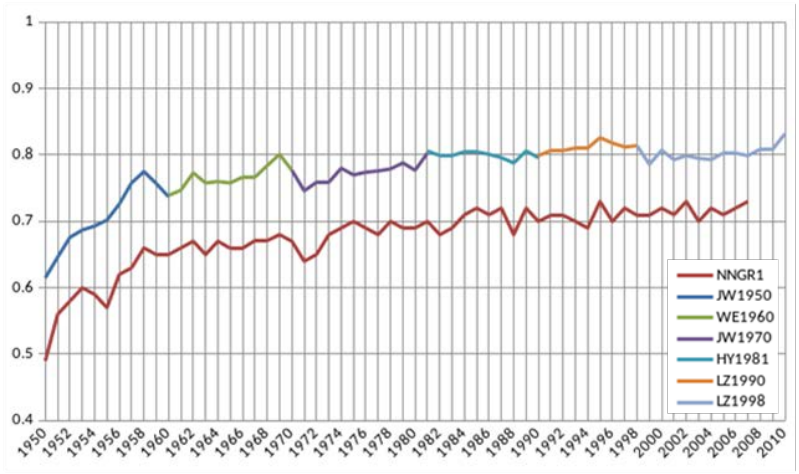

Fig. 1 Anomaly Correlation of Northern Hemisphere 500 mb height 5-day forecast (see text for details).

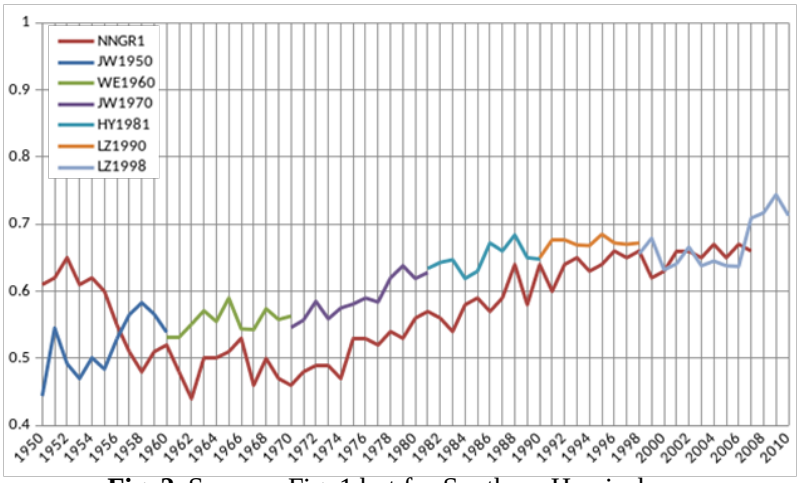

Fig. 2 Same as Fig. 1 but for Southern Hemisphere.

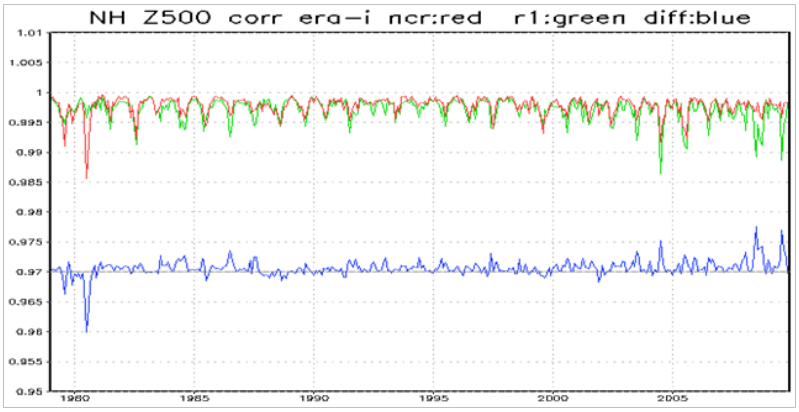

Fig. 3 Northern Hemisphere monthly mean 500 mb height anomaly correlation of CORe and ERA-interim vs. R1 and ERA-interim (see text for details).

Another approach is to assume that a modern reanalysis that assimilates conventional and satellite data is the “truth”. For “truth”, we will be using the well-regarded ERA-interim. The red line in Fig. 3 shows the anomaly correlation of the monthly mean 500 mb height of CORe and ERA-interim for 30°-60°N. The green line is similar to the red line except it shows the anomaly correlation of R1 and ERA-interim. Most of the time, the red line is higher than the green line showing that CORe more resembles ERA-interim than R1. The difference between the red and green lines is shown by the difference between the blue and horizontal black lines.

There is an unusual dip in the CORe skill in the early 1980's. In this period, the various analyses shows some uncertainty. For example, if you correlate CORe and the MERRA1 reanalyses, you do not get the dip and CORe more resembles MERRA1 than R1 resembles the MERRA1 for period of the dip.

Figure 4 is similar to Fig. 3 except it for the Southern Hemisphere (60°-30°S). Both R1 and CORe have high correlations but not as high as in the Northern hemisphere. More often than not, CORe is closer to ERA-interim than R1 is to ERA-interim. The 2000-2007 period is an exception.

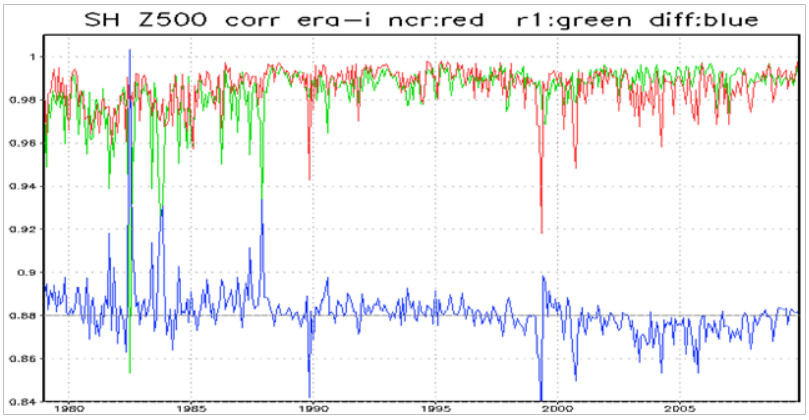

Fig. 4 Same as Fig. 3 but for Southern Hemisphere (60°-30°S).

4. Evaluation of CORe in the tropics

Figure 5 is like Fig. 3 except it shows the anomaly correlation for the 500 mb temperature in the 20°S-20°N band. The improvement by CORE is about 0.1 (blue line – black line) even though R1 assimilated satellite temperature retrievals. CORe's improved skill may be from a better model: higher resolution, modeled vs diagnostic clouds and better moist parameterizations.

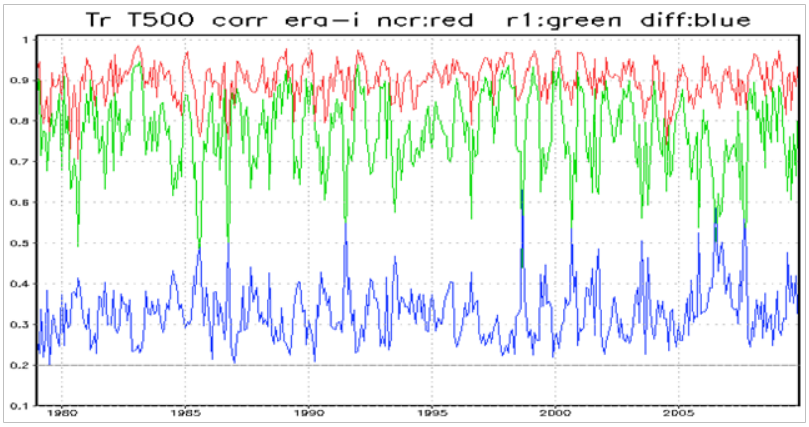

Fig. 5 Same as Fig. 3 but for 500 mb temperature in the tropics.

Figure 6 is like Fig. 5 except it is for the 200 mb zonal wind. Generally CORe did better than R1. The skill scores of CORe showed a smaller drop in the early period than R1. This suggests that CORe is better at handling low observation densities.

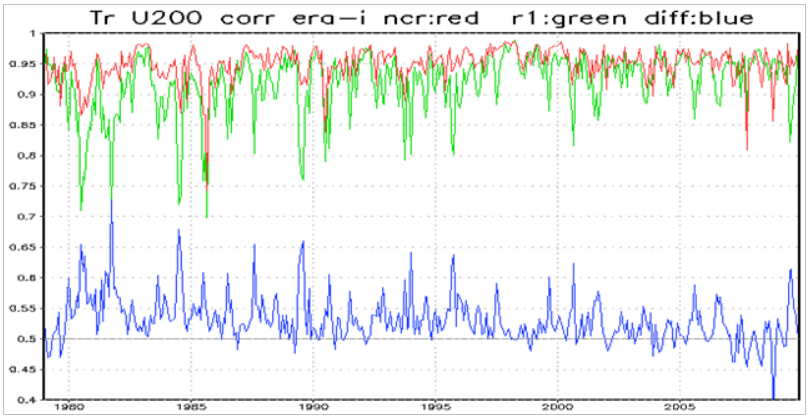

Fig. 6 Same as Fig. 5 but for 200 mb zonal wind.

5. Evaluation of CORe in the stratosphere

Modern stratosphere analyses are heavily influenced by the satellite observations because aircraft and many sondes don't go higher than the lower stratosphere. However, the stratospheric fields tend to smoother than their tropospheric counterparts, so an advanced system may not need as many observations to make a good analysis. Figure 7 is like Fig. 6 except for the tropical 50 mb zonal wind. CORe's anomaly correlation is about 0.15 better than R1 (blue line – black line). CORe's hybrid pressure-sigma vertical coordinates and ensemble Kalman filtering system may be the major factors for the improvement of CORe.

Figure 8 is like Fig. 7 except for the 60°-30°S band. Even though there are few sonde stations in the 60°-30°S band, CORe was usually more skillful than R1.

6. Unusual behavior

This is the first long-term test of the CORe system, so it expected that some problems would be found. Zhang (CDPW 2016) shows some problems. We also found that some of the tropical radiative fluxes were off, suggesting that the forecast model needed to be retuned for the T254 resolution. Some of the skill scores shows some artifacts. Figure 9 is like Fig. 4 (SH 500 mb height) except for using 00Z daily analyses and using JRA-55 instead of ERA-interim. The plot shows that the CORe skill rapidly declines (7/2000) and recovers (8/2007). Perhaps some erroneous data slipped through the QC.

7. Summary

A mostly conventional observation based reanalysis is attractive because it eliminates the "climate shifts" caused by new satellites. CORe demonstrates that such an analysis can have similar or better skill than R1. The "unusual behavior" is probably caused by something in the assimilated observations. These observations need to be identified and removed if erroneous.

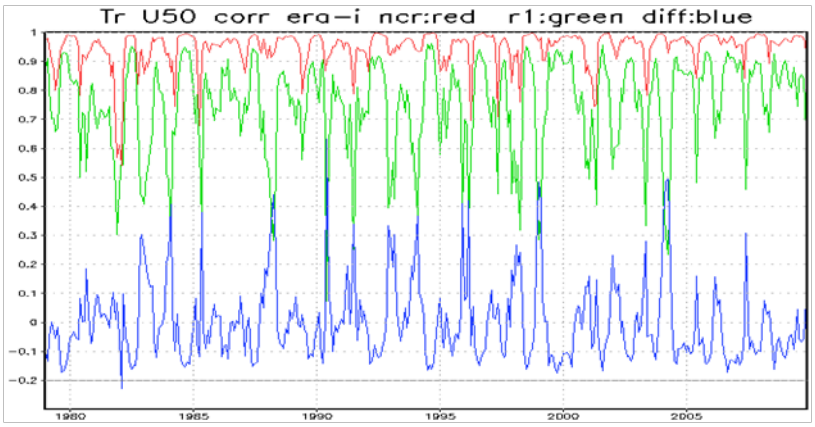

Fig. 7 Same as Fig. 6 but for tropical 50 mb zonal wind.

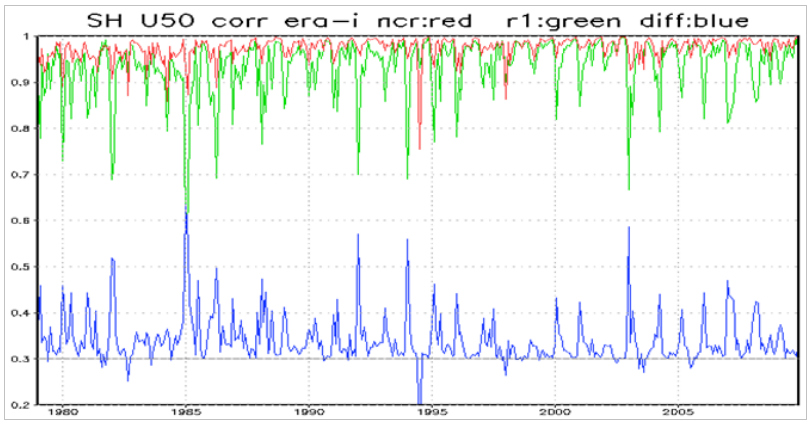

Fig. 8 Same as Fig. 7 but for Southern Hemisphere 60°-30°S band.

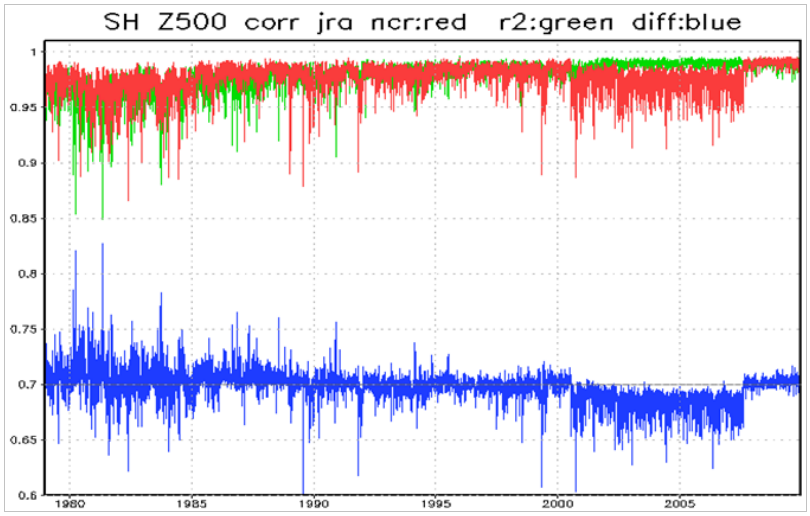

Fig. 9 Same as Fig. 4 but for using 00Z daily analyses and using JRA-55 instead of ERA-interim.

References

Compo, G. P., J. S. Whitaker, P. D. Sardeshmukh, N. Matsui, R. J. Allan, X. Yin, B. E. Gleason, R. S. Vose, G. Rutledge, P. Bessemoulin, S. Brönnimann, M. Brunet, R. I. Crouthamel, A. N. Grant, P. Y. Groisman, P. D. Jones, M. C. Kruk, A. C. Kruger, G. J. Marshall, M. Maugeri, H. Y. Mok, Ø. Nordli, T. F. Ross, R. M. Trigo, X. L. Wang, S. D. Woodruff, and S. J. Worley, 2011: The Twentieth Century Reanalysis Project. *Q.J.R. Meteorol. Soc.*, **137**, 1–28. doi:10.1002/qj.776.

Zhang, L., A. Kumar, and W. Wang, 2012: Influence of changes in observations on precipitation: A case study for the Climate Forecast System Reanalysis (CFSR), *J. Geophys. Res.*, **117**, D08105, doi:10.1029/2011JD017347.

Science and Technology Infusion Climate Bulletin
NOAA's National Weather Service
41st NOAA Annual Climate Diagnostics and Prediction Workshop
Orono, ME, 3-6 October 2016

Initial Assessment of the Conventional Observation Reanalysis

Li Zhang[1, 2], Arun Kumar[1], Jeffrey Whitaker[3], Jack Woollen[4, 5],
Wesley Ebisuzaki[1], and Hyun-Chul Lee[4, 5]

[1]*Climate Prediction Center, NOAA/NWS/NCEP, College Park, Maryland*
[2]*Innovim LLC., Greenbelt, Maryland*
[3]*Physical Sciences Division, NOAA/OAR/ESRL, Boulder, Colorado*
[4]*Environmental Modeling Center, NOAA/NWS/NCEP, College Park, Maryland*
[5]*IMSG at EMC, College Park, Maryland*

1. Introduction

The Conventional Observation Reanalysis (CORe) was recently completed at the National Centers for Environmental Prediction (NCEP), for the period of 1950 to 2009. The CORe is an atmospheric reanalysis based on the latest Semi-Lagrangian Global Forecast System (GFS) T254 L64 model using Ensemble Kalman Filter (EnKF) data assimilation system (Ebisuzaki *et al.* 2016).

The purpose of this work is to test feasibility of the ENKF based analysis over periods with different densities and time-varying qualities of conventional observed data, and to compare the performance of CORe against the NCEP/NCAR Reanalysis (R1) to assess whether this could be a suitable replacement.

2. Data

We use monthly mean fields from Jan. 1951 to Dec. 2009 to analyze CORe climate variability and trend. CORe was produced by running six simultaneous streams of analyses with one year overlap. The six streams of CORe are the following periods: Jan1950 to Dec1960; Jan1960 to Dec1970; Jan1970 to Dec1981; Jan1981 to Dec1990; Jan1990 to Dec1998; Jan1998 to Dec2009.

For a comparison with other reanalyses, temporal changes from MERRA2 (Molod *et al.* 2015), JRA55c (reanalysis using conventional observations) (Kobayash *et al.* 2014), ECMWF Reanalysis Interim (ERAI) (Dee *et al.* 2011), R1 (Kalnay *et al.* 1996) and CFSR (Saha *et al.* 2010) are also analyzed.

3. Results

The Hovmollver diagram showed the interannual variability of the 200mb heights at the equator (Fig 1) for the various reanalyses. The CFSR heights are lower than all other reanalyses,

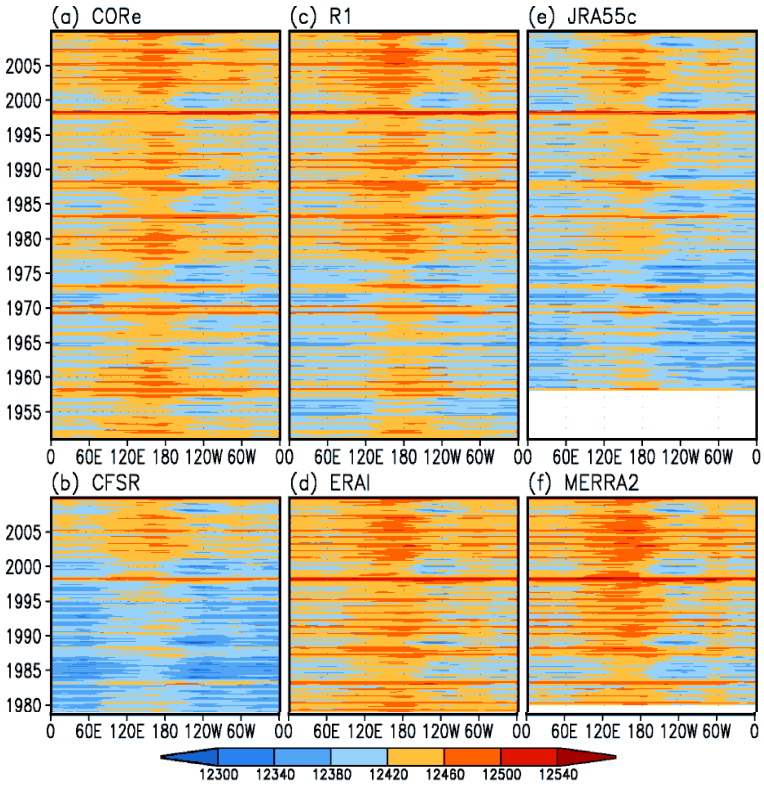

Fig. 1 Hovmoller cross section of monthly mean geopotential height in meter at 200mb along equator in a) CORe, b) CFSR, c) R1, d) ERAI, e) JRA55c and f) MERRA2.

Correspondence to: Li Zhang, Climate Prediction Center, NOAA/NWS/NCEP, 5830 University Research Court, College Park, MD, and Innovim LLC, Greenbelt, MD; E-mail: leigh.zhang@noaa.gov

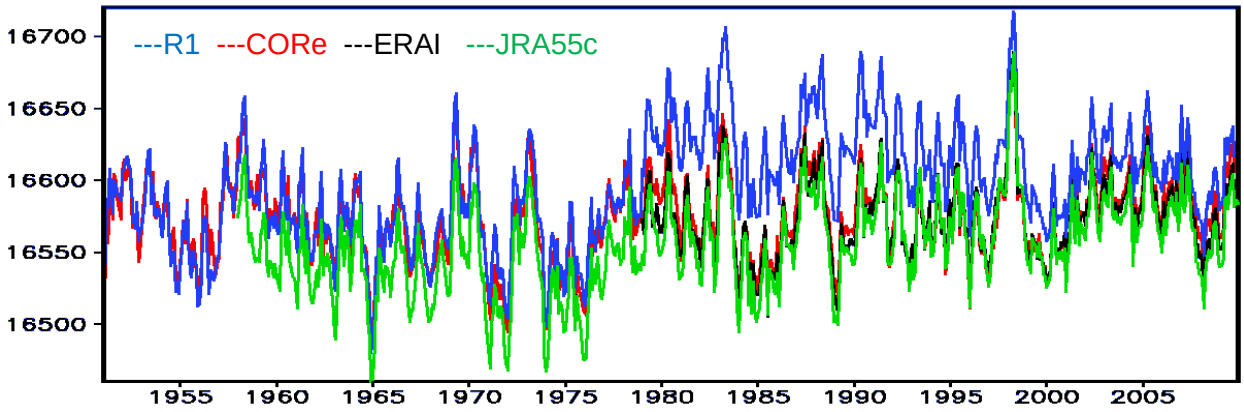

Fig. 2 100mb monthly temperature zonal mean averaged over 10°S-10°N for R1 (blue), CORe (red), ERAI (black) and JRA55c (green).

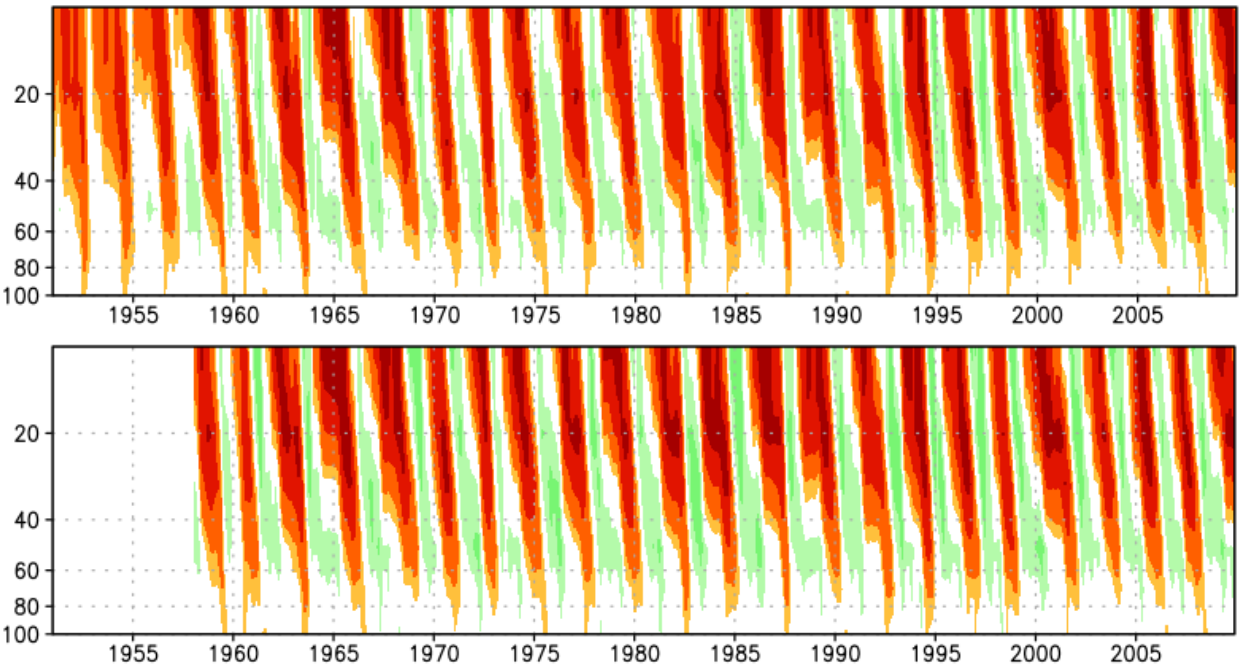

Fig. 3 Tropical monthly zonal mean zonal wind on pressure levels from 100mb to 10mb for CORe (upper panel) and JRA55c (lower panel).

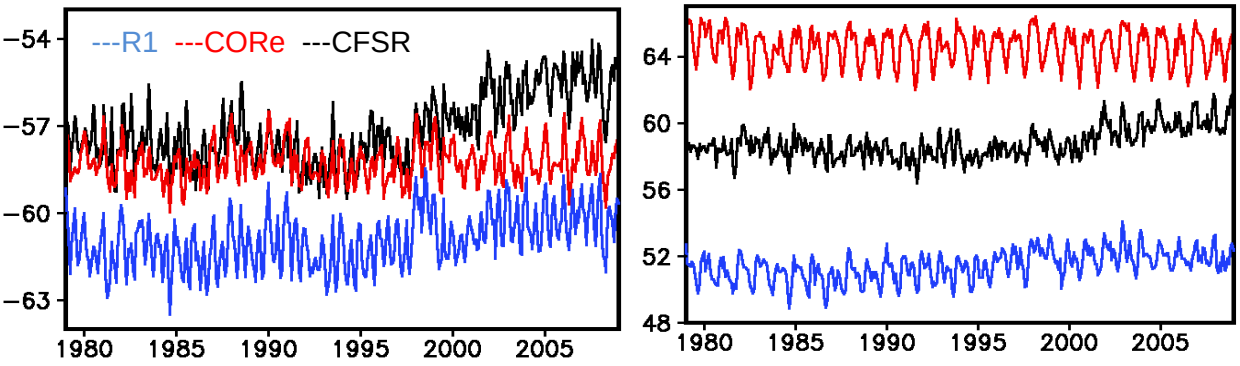

Fig. 4 Global monthly mean of surface downward long wave (left panel) and total cloud cover (right panel) for R1 (blue), CORe (red) and CFSR (black).

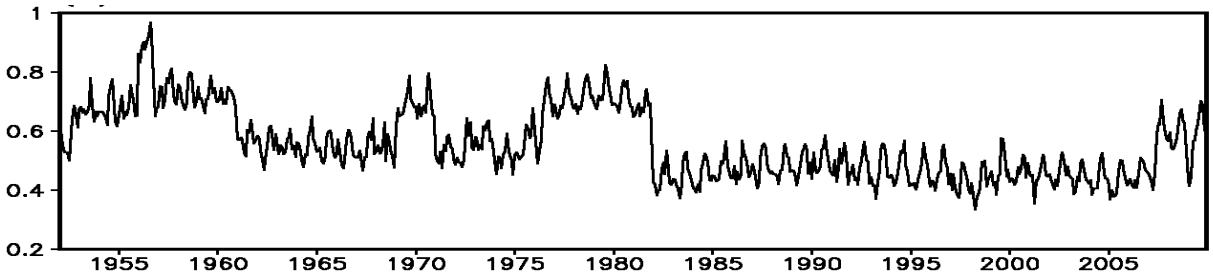

Fig. 5 Global monthly mean of precipitation minus evaporation.

particularly in the 1980s and 1990s as we already know, while the CORe height has comparable amplitude and pattern compared with ERAI and MERRA2 particularly post 1979. Before 1979, CORe is closer to R1, while JRA55c height seems lower than height in CORe and R1. R1 has the coldest 850mb temperature in the eastern equatorial Pacific; while CORe agrees very closely with the other reanalyses (picture not shown)

The zonal mean temperature averaged over tropics (10°S-10°N) at 100 mb in Fig. 2 shows that R1 has major temperature change after 1979, while CORe, ERAI and JRA55c agree post 1979 and consistent with pre-1979 values.

Figure 3 illustrates the monthly zonal mean of zonal wind on pressure levels above 100mb. Apparently, CORe (upper) and JRA55c (lower) Quasi-biennial Oscillation (QBO) winds have very good agreement at all QBO levels.

Both CFSR (black) and R1 (blue) in Fig.4 have increasing trends for surface long wave (left) and total cloud cover (right), especially after 1999, while CORe (red) has more consistent structure, though higher amount of cloud cover.

4. Discussion

In general, CORe seems competitive with R1 in the modern era and better than R1 in the earlier years. For many cases CORe appears to have fewer artifacts than other newer reanalyses. However, there are serval significant changes over the long time series of global monthly mean precipitation minus evaporation (P-E), which may be related to sea surface temperature and/or is likely affected by changes in data formats and data volumes increases: ON20 data from 1962-1972, while 1968 has upgrade format, and 1973 transition to ON23 format; 1976 transition to ON126 for surface observation; 1982 transition to updated WMO GTS character codes for surface data; 2007 may be related to introduction of COSMIC data into CORe. We will look into this further.

References

Dee, D.P., and Co-authors, 2011: The ERA-Interim reanalysis: configuration and performance of the data assimilation system. *Quart. J. R. Meteorol. Soc.*, **137**, 553-597, doi: 10.1002/qj.828

Ebisuzaki, W., A. Kumar, J. Whitaker, J. Woollen, H.-C. Lee, L. Zhang, 2016: A preliminary examination of a conventional ENKF atmospheric reanalysis. *Climate S&T Digest*, 41st NOAA Climate Diagnostics and Prediction Workshop, Orono, ME.

Kalnay, E., and Co-authors, 1996: The NCEP/NCAR 40-year reanalysis project. *Bull. Amer. Meteor. Soc.*, **77**, 437-471.

Kobayashi, C., and Co-authors, 2014: Preliminary results of the JRA-55C, an atmospheric reanalysis assimilating conventional observations only. *Sci. Online Lett. on the Atmos.*, **10**, 78-82, doi: 10.2151/sola.2014-016

Molod, A., Takacs, L., Suarez, M., and Bacmeister, J., 2015: Development of the GEOS-5 atmospheric general circulation model: evolution from MERRA to MERRA2, *Geosci. Model Dev.*, **8**, 1339-1356, doi:10.5194/gmd-8-1339-2015

Saha, S., and Co-authors, 2010: The NCEP Climate Forecast System Reanalysis. *Bull. Amer. Meteor. Soc.*, **91**, 1015-1057, doi: 10.1175/2010BAMS3001.1

Science and Technology Infusion Climate Bulletin
NOAA's National Weather Service
41st NOAA Annual Climate Diagnostics and Prediction Workshop
Orono, ME, 3-6 October 2016

A Process-based Attribution of the Difference in the Annual Variation of Surface Temperature between the Monsoon and Non-monsoon Regions

Yana Li[1], Song Yang[1], Yi Deng[2], and Xiaoming Hu[1]
[1]*School of Atmospheric Sciences, Sun Yat-sen University, Guangzhou, China*
[2]*School of Earth and Atmospheric Sciences, Georgia Institute of Technology, Atlanta*

1. Data and methodology

The primary dataset used is the European Centre for Medium-Range Weather Forecasts (ECMWF) Re-Analysis Interim (ERA-Interim, Uppala *et al.* 2008; Dee *et al.* 2011) covering the period of 1979 to present with a horizontal resolution of 1° longitude × 1° latitude and 37 pressure levels in the vertical ranging from 1000 hPa to 1 hPa.

We have adopted the same package of a climate feedback-response analysis method (CFRAM), which is based on the total energy balance within an atmosphere-surface column at a given horizontal grid point that consists of M atmospheric layers and a surface layer (Cai and Lu, 2009; Lu and Cai, 2009). Following Deng *et al.* (2012), we write the total energy balance equation separately for a month (*i.e.* March) and its latter month (*i.e.* April), take the difference (Δ) between the two months (*e.g.* April-March), and we obtain

$$\Delta\frac{\partial E}{\partial t} = \Delta S - \Delta R + \Delta Q^{non-radiative} \quad (1)$$

where R (S) is the vertical profile of the net convergence (divergence) of short-wave (long-wave) radiation flux within each layer. For all layers above the surface, $\Delta Q^{non-radiative}$ is the vertical profile of the convergence of total energy due to atmospheric turbulent, convective, and advective motions.

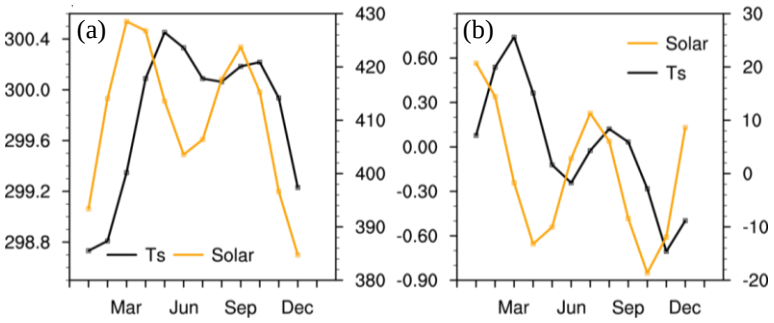

Fig. 1 (a) Climatology of annual variations of the solar radiation at the top of troposphere (TOA) (yellow solid line, corresponding to the right Y-axis, unit: W/m**2) and the surface temperature (black solid line, corresponding to the left Y-axis, unit: K) average over the monsoon region (15°S-15°N, 105°-150°E). (b) The increment between two months of the solar radiation (yellow solid line) and the surface temperature (the black solid line), and the corresponding Y-axis is same as in (a).

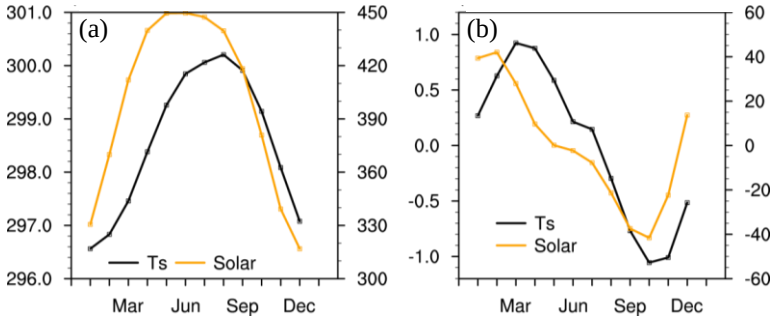

Fig. 2 Same as Fig. 1, but for the non-monsoon region (5°N-30°N, 260°-300°E).

By neglecting the interactions among various radiative feedback processes thus linearizing the radiative energy perturbation, following Hu et al. (2016), we may express ΔS and ΔR as

$$\Delta S \approx \Delta S^{solar} + \Delta S^{wv} + \Delta S^{c} + \Delta S^{\alpha} \text{ and } \Delta R \approx \Delta R^{wv} + \Delta R^{c} + \frac{\partial R}{\partial T}\Delta T \quad (2)$$

In Eq. (2), superscripts, "solar", "wv", "c", and "α", indicate solar insolation, water vapor, cloud, and surface albedo, respectively. Elements of ΔT are the vertical profile of temperature differences in each layer between months, and ∂R/∂T is the Planck feedback matrix. Substituting Eq. (2) into Eq. (1), we obtain,

Correspondence to: Yana Li, School of Atmospheric Sciences, Sun Yat-sen University, Guangzhou, China;
E-mail: liyana@mail2.sysu.edu.cn

$$\Delta T = \left(\frac{\partial R}{\partial T}\right)^{-1}\left\{\Delta S^{solar} + \Delta(S-R)^{wv} + \Delta(S-R)^{c} + \Delta S^{\alpha} + \Delta Q^{atmos\_dyn} + \Delta Q^{surface}\right\} \quad (3)$$

From (3), we can separate the temperature change between two months, for example, March-to-April, to all the dynamical and thermodynamical processes.

Additionally, a temporal pattern-amplitude projection (TPAP) method, is applied to quantify the relative contribution of each process annual variaiton to the annual cycle of observations,

$$TPAP_i = \frac{\sum_1^{12}(\Delta T_{in} * \Delta T_n)}{\sum_1^{12}(\Delta T_n)^2} \quad (5)$$

where i and n refer to the ith feedback process and nth month from January to December, and ΔT is the observation.

2. Results

The South China Sea (SCS) and the southern North America (SNA) are representative of the monsoon and non-monsoon regions, respectively. The annual variation of areal average surface temperature in SCS is bimodal (Fig. 1a), and that in SNA peaks at August (Fig. 2a). The rapid warming month over both regions is March to April (Fig. 1b and Fig. 2b).

For the monsoon region, main positive contributors to the annual variation of surface temperature are the quick feedback processes in the atmosphere such as the changes in cloud cover, water vapor and atmospheric dynamics, while the incident solar radiation at the top of the atmosphere, and the oceanic dynamical processes with the land/ocean heat storage are two greatest factors, from the perspective of contribution magnitude (Fig. 3 and Fig. 5a).

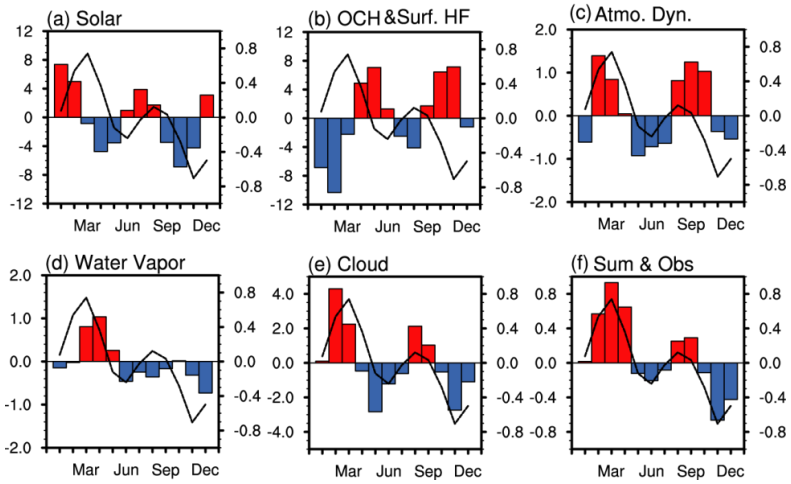

Fig. 3 Annual cycle of partial temperature changes (K) of surface temperature average over (15°S-25°N, 105°-150°E) due to changes in (a) solar radiation at the TOA, (b) oceanic dynamic and ocean/land heat storage (OCH) and surface heat flux, (c) the atmospheric dynamics, (d) water vapor, (e) cloud, (f) sum of all individual feedback processes. The black solid lines in (a-f) refer to the observation (K).

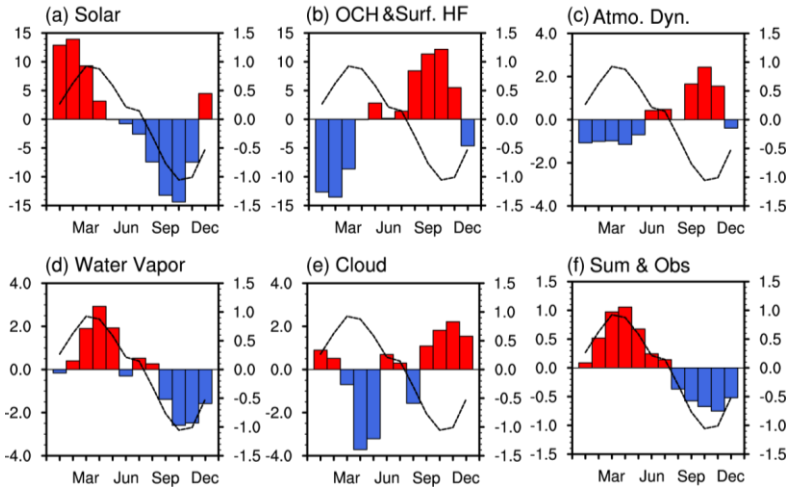

Fig. 4 Same as Fig. 3, but for the non-monsoon region (5°N-30°N, 260°-300°E).

For non-monsoon regions, the main contributor for the annual cycle of surface temperature is solar insolation. The quick feedback processed in the atmosphere contributes little, only water vapor contributing positively (Fig. 4 and Fig. 5b). Ocean is the largest negative contributor in both monsoon and non-monsoon regions, which delays the direct effect of solar radiation on the surface temperature. However, more enhanced air-sea interaction in monsoon region counteracts the oceanic negative contribution by the positive contribution of surface latent heat flux.

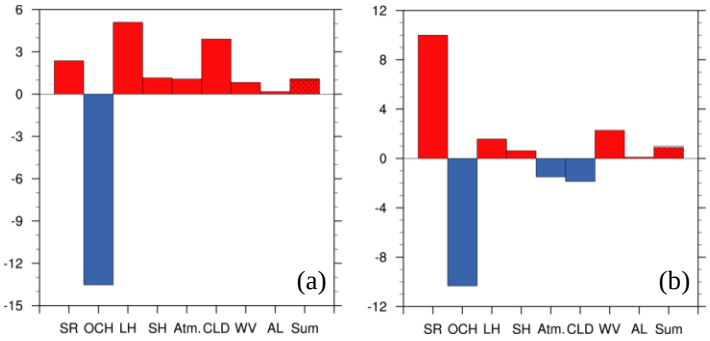

Fig. 5 Temporal pattern-amplitude projection coefficients (TPAPs) associated with each radiative and non-radiative forcing of the areal averaged surface anomalies over (a) (15°S-25°N, 105°-150°E) and (b) (5°N-30°N, 260°-300°E). The box with black dots over "Sum" refers to the observation.

References

Cai, M, and J.-H. Lu, 2009: A new framework for isolating individual feedback processes in coupled general circulation climate models. Part II: method demonstrations and comparisons. *Clim. Dyn.*, **32**, 887-900.

Dee, D.P., and Coauthors, 2011: The ERA-Interim reanalysis: configuration and performance of the data assimilation system. *Q. J. Roy. Meteor. Soc.*, **137,** 553-597.

Deng, Y., T.W. Park, and M. Cai, 2012: Process-based decomposition of the global surface temperature response to El Niño in boreal winter. *J. Atmos. Sci.*, **69**, 1706–1712.

Hu, X.M., S. Yang, and M. Cai, 2016: Contrasting the eastern Pacific El Niño and the central Pacific El Niño: Process-based feedback attribution. *Clim. Dyn.*, **47**, 2413. doi: 10.1007/s00382-015-2971-9.

Lu, J.H., and M. Cai, 2009: A new framework for isolating individual feedback process in coupled general circulation climate models. Part I: Formulation. *Clim. Dyn.*, **32**, 873-885.

Uppala S.M., D. Dee, S. Kobayashi, P. Berrisford, and A. Simmons, 2008: Towards a climate data-assimilation system: Status update of ERA–Interim. *ECMWF Newletter*, **115**, 12-18.

Science and Technology Infusion Climate Bulletin
NOAA's National Weather Service
41st NOAA Annual Climate Diagnostics and Prediction Workshop
Orono, ME, 3-6 October 2016

An Analysis of the MJO Influence on the Rainfall in Subtropical Coastal Areas of East Asia

Yun-Lan Chen[1,2], Chung-Hsiung Sui[2], Chih-Pei Chang[2], and Wanqiu Wang[3]
[1]*Central Weather Bureau, Taiwan*
[2]*National Taiwan University, Taiwan*
[3]*Climate Prediction Center, NOAA/NWS/NCEP, College Park, Maryland*

1. Introduction

The Madden-Julian Oscillation (MJO) has been found to affect weather and climate over the globe at different time scales, including the tropical cycle, Indian and Australian summer monsoons, North and South American climate, Arctic and North Atlantic Oscillations, and El Nino Southern Oscillation. In this study, we analyze its impact on the rainfall in the subtropical coastal areas of East Asia during northern winter and spring seasons. While previous studies have shown that rainfall over this area is affected by the MJO, locations of the tropical convection that is associated with this influence are not certain. Further, physical processes that link the MJO and the rainfall remain unclear.

Our analysis aims to address the following questions: (1) What is the temporal relationship between evolution of the MJO and the rainfall in the East Asia (EA) subtropical coastal areas; (2) Does such a relationship depend on the use of different MJO indices, and (3) What are the

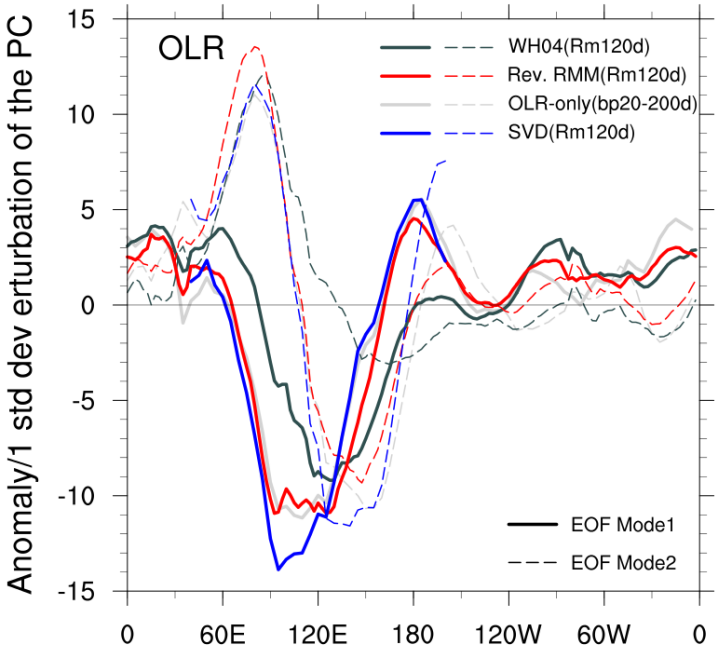

Fig 1 The leading two EOF modes for OLR variable in 4 MJO indices. The comparison shows the revised RMM index and SVD-based index are similar with the OLR-only index, which has two centers of anomaly, while the RMM index more depicts just one center.

Table 1 MJO indices used in this study: (1) WH04 RMM index, (2) Revised RMM index, (3) OLR-only index, (4) SVD-based index

	Ref /related Paper	Season	parameter	Data filter	EOF matrix	Domain longitude	Domain latitude
WH04	W&H_RMM (2004)	All-season	OLR+U8U2	Remove 120d_runningM	C-EOF/ Cov scaled	Global Tropics	1D Ave(15S-15N)
Rev. RMM	P. Liu et al. (2016)	All-season	OLR+U8U2	Remove 120d_runningM	C-EOF/ Rev. scaled	Global Tropics	1D Ave(15S-15N)
OLR-only	Matthews (2008)	DJFM	OLR-only	20-200-day filtered	EOF / Cov	Global Tropics	2D (30S-30N)
SVD	Chang et al. (2005)	DJFM	OLR+U8U2	Remove 120d_runningM	SVD/ Cov scaled	IO – MC -WNP	2D (30S-30N)

Correspondence to: Yun-Lan Chen, Central Weather Bureau, Taipei, Taiwan; E-mail: yunlan.chen@cwb.gov.tw

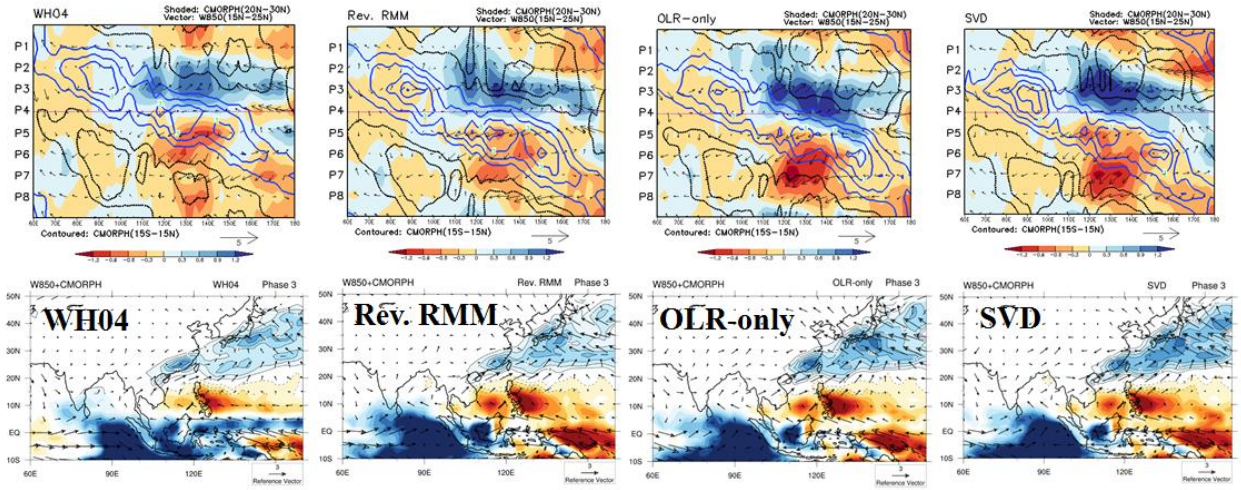

Fig 2 Phase-longitude composite diagram (upper), and 2D composite map for phase3 (lower) for 4 MJO indices, from left to right : (1) WH04 RMM index (2) Revised RMM index (3) OLR-only index (4) SVD-based index.

physical processes that relate the MJO and the rainfall variations and, in particular, what is the role of the convection and atmospheric circulation condition in the tropical western Pacific?

2. Data and approaches

The analysis is based on the NCEP atmospheric reanalysis, outgoing longwave radiation (HIRS OLR, 1979-2015) and satellite rainfall estimation (CPC CMORPH, 1998-2015). We composite rainfall evolution following the tropical MJO phases by 4 MJO indices (Fig. 1): (1) RMM index (Wheeler and Hendon, 2004), which has been shown more dominated by dynamics. (2) Revised RMM index (Liu *et al.* 2016), which was designed to enhance the contribution from OLR, (3) OLR-only index (Matthews 2008), a convection-centric index, (4) SVD-based index, an MJO index proposed by Chang *et al.* (2005) and redesigned in this study to emphasize regional domain and seasonal dependency (Table 1). According to the results from the composite analysis, two types of MJO events are separated to investigate the impact of the detailed spatial convection pattern and its evolution on East Asia rainfall, and the connection between tropical MJO convection and the subtropical responses.

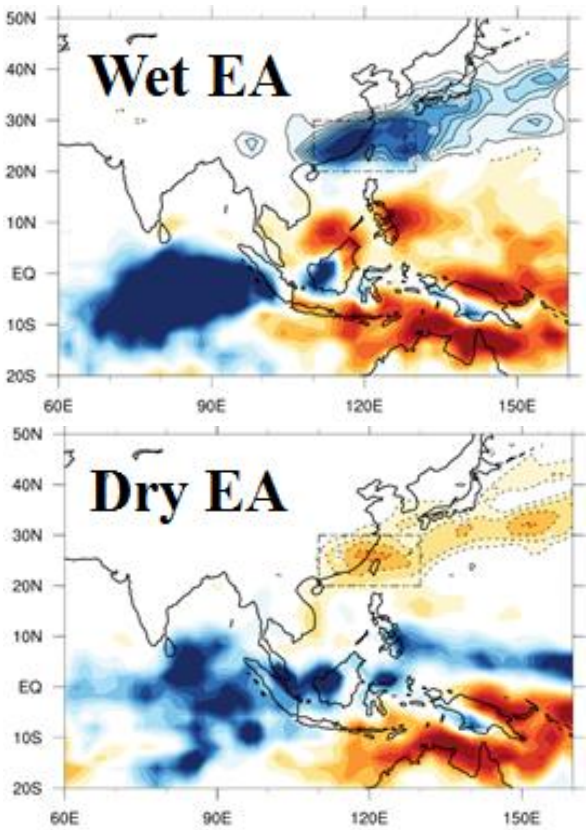

Fig 3 The CMORPH rainfall composite map for RMM MJO phases 2. (upper: the first one-third EA wet cases composite; lower: the first one-third EA dry cases composite)

3. Results

3.1 Relationship between tropical MJO and East Asian rainfall

Composite of CMORPH data show the rainfall variation in the EA subtropical coastal is modulated by MJO, consistent with previous studies (Jia *et al.* 2011, Hung 2014). All 4 MJO indices show robust wet/dry flip sign over EA during the MJO cycle. Although the main feature is similar among the 4 MJO indices, rainfall

variation over subtropical EA is better captured by OLR-only index and regional SVD-based index (Fig. 2). Taking phase 3 composite value for example, the rainfall variance over subtropical EA (20°-30°N, 110°-130°E) are 1.46 and 1.54 (mm/hr)2 for WH04 and Revised RMM indices, and are 2.63, 2.93 $(mm/hr)^2$ for OLR-only and SVD-based indices. Differences in the spatial tropical convection pattern are found between the WH04 index and the other three, which are more convection-centric. The 4 indices all show clear wetness over Indian Ocean (IO) during the MJO phase 3, while only the WH04 index produces wetness over the equatorial west Pacific (WP).

Composite maps for abnormal conditions of subtropical EA rainfall are also calculated to study its connection with the tropical convection pattern. For the same MJO phase, a dry or wet pattern over EA can exist. One such an example is shown in Fig. 3 for RMM phase 2 which also show some differences in tropical area. This suggests an analysis of more detailed spatial convection pattern is needed to understand the connection between tropical convection and subtropical rainfall.

3.2 Connection between tropical convection and subtropical responses

The fact that the subtropical rainfall variance is better captured by convection-centric MJO indices suggests that detailed tropical convection patterns may be crucial in determining the impact on EA rainfall from the MJO. We separate MJO events that correspond to strong convection into 2 groups: ISO-A and ISO-B. Group ISO-A is for cases with significant dry condition over Maritime Continent (MC), and ISO-B is for the others. We use OLR-only index for the selection of MJO cases and define the day0 as the time when active convection is over IO. The phase diagram (Fig. 4) and the time evolution of the tropical convection (Fig. 5) show the ISO-A type cases correspond to successive MJO events, while ISO-B type cases belong more to primary events.

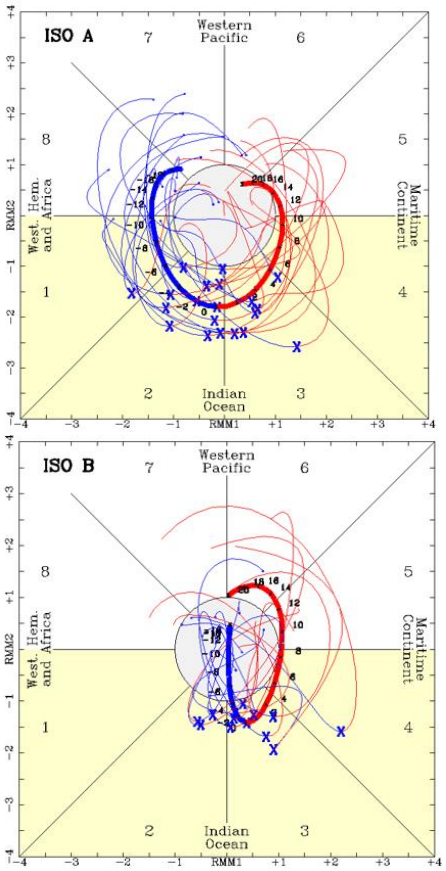

Fig 4 The MJO phase diagram for ISO-A (upper, 19 cases) and ISO-B (lower, 12 cases).

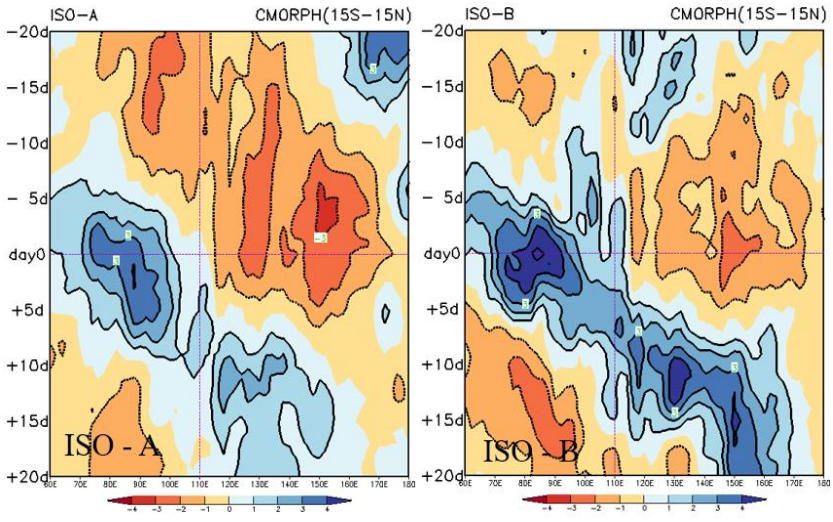

Fig 5 The propagation of tropical convection for ISO-A (left) and ISO-B (right).

Comparison of the evolution of the two MJO types shows the ISO-A type has much stronger wet response over EA than ISO-B (Fig. 6 and Fig. 7). A significant local high-level trough was established before the day0 for ISO-A in association with the evolution of the tropical convection. We speculate that this is the dynamical reason for favoring the EA wetness. Another interesting finding for ISO-A is the southward movement of the EA wetness after the day0, which is in association with the getting-stronger southwest flow near 15°-25°N (Fig. 7). It looks like the high-level trough and the southwest flow together form a long period of unstable weather and cause

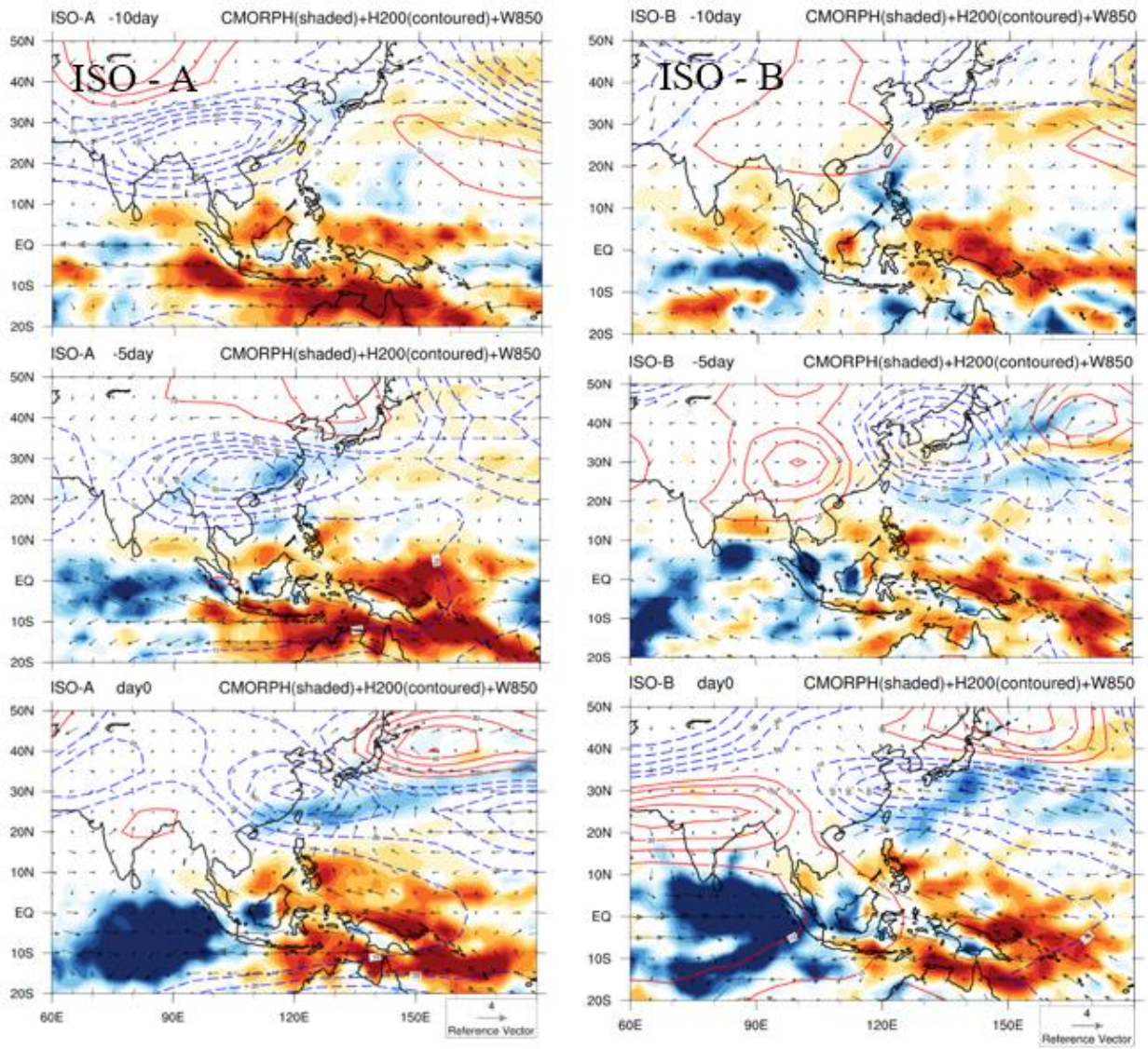

Fig 6 Evolution for ISO-A (left) and ISO-B (right): 10-day before (upper), 5-day before (middle), day 0 (lower).

rainfall over EA, and they both could be related to the MJO tropical heating and its eastward movement. From the evolution of ISO-A, the high-level trough over EA is after the eastward of cyclonic circulation anomalies, which is consistent with a response of dry phase MJO over IO-MC. The increased southwest flow is a feature frequent seen when a low-level anticyclone sits over Philippines. With a dry phase in advance, the ISO-A type tends to have a low-level anticyclone lingering Philippines area while the tropical convection over IO moves eastward into WP.

4. Summary

This study analyzes East Asia rainfall variation related to the MJO during northern winter and spring seasons. The robustness of wet/dry flip sign show EA rainfall variation is clearly modulated by MJO, suggesting that it is a source of the predictability for EA intraseasonal variations. Among the MJO indices, the convection-centric MJO index and reginal SVD MJO index are found to better capture the connection between the MJO and its subtropical rainfall responses. Our results suggest the EA rainfall response depends on the detailed spatial pattern of tropical convection. Development of a high-level trough corresponding to MC dry condition may be a key component for the EA wetness, suggesting the importance of the MC dry phase before the active convection over the IO.

References

Chang, C.-P., P. A. Harr, and H.-J. Chen, 2005: Synoptic disturbances over the equatorial South China Sea and western maritime continent during boreal winter. *Mon. Wea. Rev.*, **133**, 489–503.

Hung, Chih-Wen, Ho-Jiunn Lin, Huang-Hsiung Hsu, 2014: Madden–Julian Oscillation and the winter rainfall in Taiwan. *J. Climate*, **27**, 4521-4530.

Jia, X., L. J. Chen, F. M. Ren, and C. Y. Li, 2011: Impacts of the MJO on winter rainfall and circulation in China. *Adv. Atmos. Sci.*, **28**, 521–533

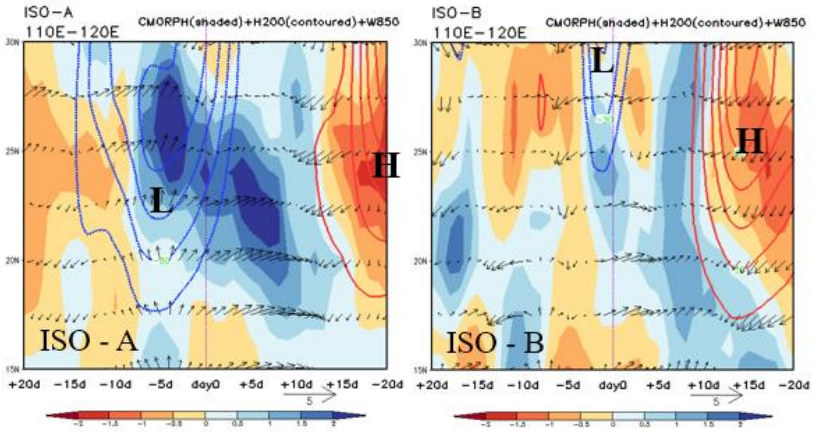

Fig 7 Time-longitude section over 110°-120°E for ISO-A (left) and ISO-B (right).

Liu, P., Q. Zhang, C. Zhang, Y. Zhu, M. Khairoutdinov, H.-M. Kim, C. Schumacher, and M. Zhang, 2016: A revised real-time multivariate MJO index. *Mon. Wea. Rev.*, **144**, 627–642.

Matthews, A. J., 2008: Primary and successive events in the Madden-Julian Oscillation. *Quart. J. Roy. Meteor. Soc.*, **134**, 439–453.

Wheeler, M. C., and H. H. Hendon, 2004: An all-season real-time multivariate MJO index: Development of an index for monitoring and prediction. *Mon. Wea. Rev.*, **132**, 1917–1932.

APPENDIX

Photo Gallery

41th NOAA Annual Climate Diagnostics and Prediction Workshop

3-6 October 2016, Orono, Maine

For complete album
http://www.nws.noaa.gov/ost/climate/STIP/41CDPW/photos.htm

In Session

Invited Talk

Spot Q & A

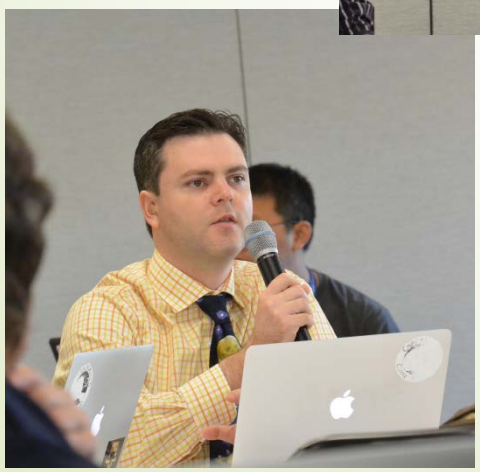

Poster Exchange

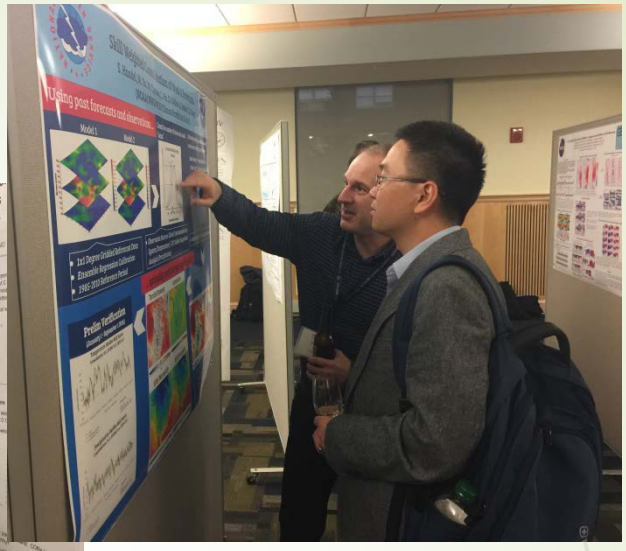

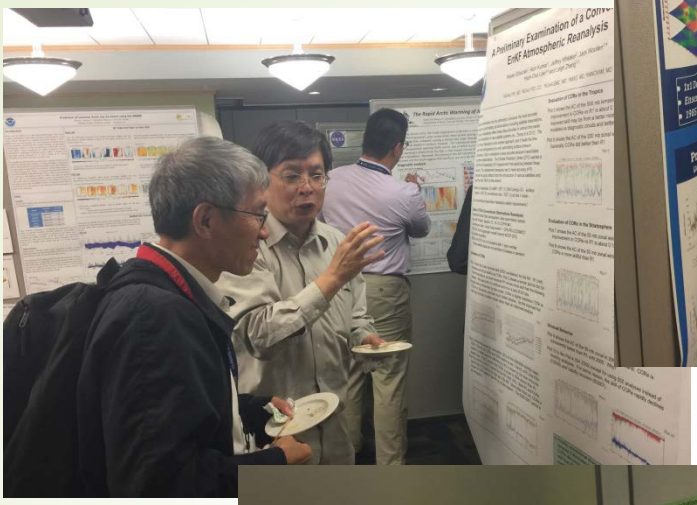

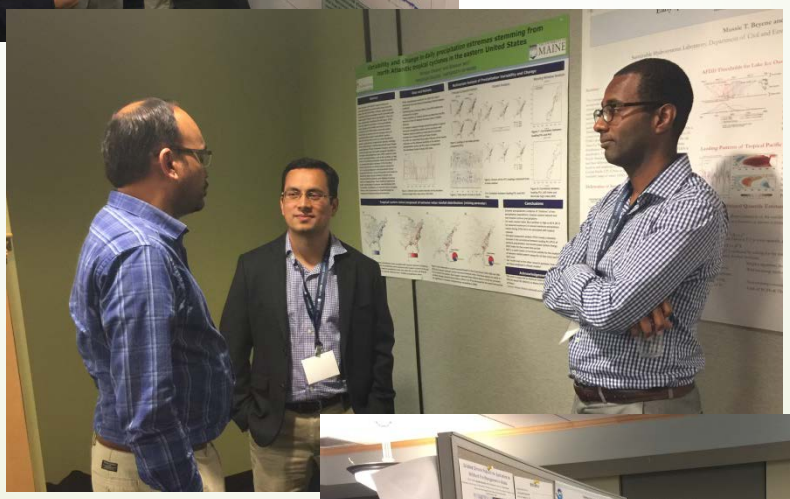

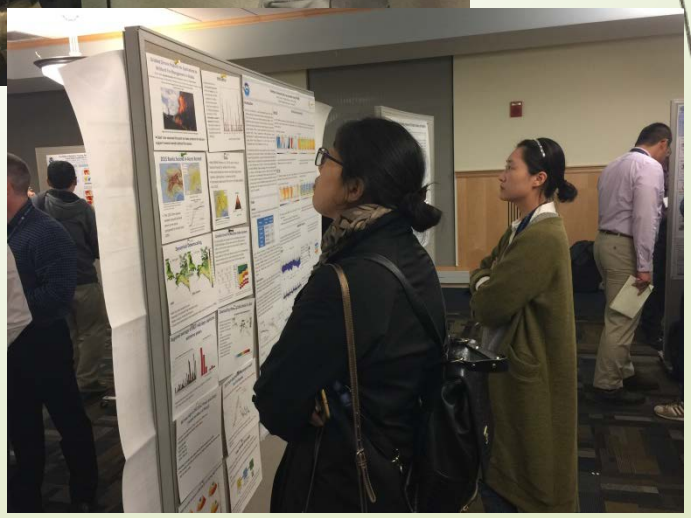

Session Break

NWS Science and Technology Infusion Climate Bulletin

Featured Special Collections

(http://www.nws.noaa.gov/ost/climate/STIP/Collections.htm)

Climate Prediction Science and Technology Digest

NOAA Climate Test Bed Joint Seminar Series Extended Summaries Collection Volume

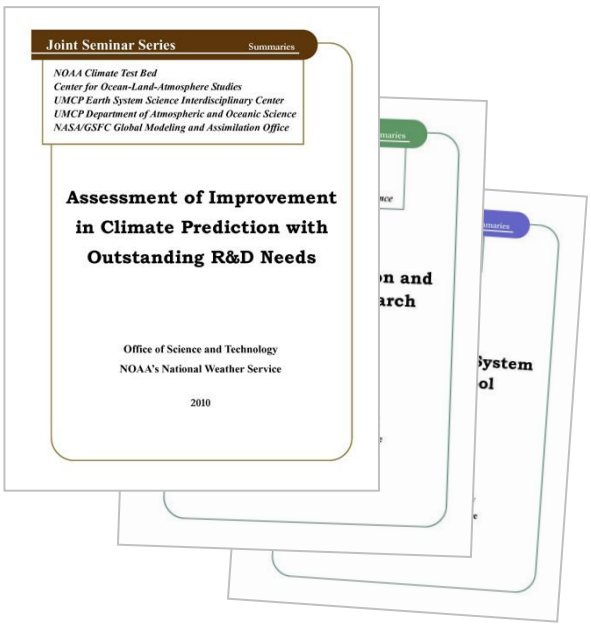

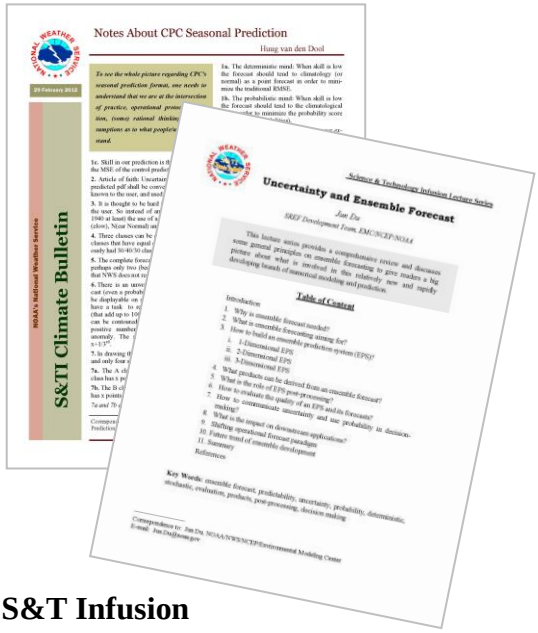

S&T Infusion Lecture Series & Notes